SYNTHESIS AND CHARACTERIZATION OF BULK GLASS-FORMING IRON-BORON BASED ALLOY SYSTEMS

A THESIS SUBMITTED TO
THE GRADUATE SCHOOL OF NATURAL AND APPLIED SCIENCES
OF
MIDDLE EAST TECHNICAL UNIVERSITY

BY

SELEN NIMET GÜRBÜZ

IN PARTIAL FULFILLMENT OF THE REQUIREMENTS
FOR
THE DEGREE OF MASTER OF SCIENCE
IN
METALLURGICAL AND MATERIALS ENGINEERING

JUNE 2004

Approval of the Graduate School of Natural and Applied Sciences

Prof. Dr. Canan ÖZGEN

Director

I certify that this thesis satisfies all the requirements as a thesis for the degree of Master of Science.

Prof. Dr. Bilgehan ÖGEL

Head of Department

This is to certify that we have read this thesis and that in our opinion it is fully adequate, in scope and quality, as a thesis for the degree of Master of Science.

Prof. Dr. Amdulla O. MEKHRABOV	Prof. Dr. M. Vedat AKDENIZ
Co-Supervisor	Supervisor

Examining Committee Members

Prof.Dr.Ali KALKANLI	(METU,METE)	
Prof.Dr.M.Vedat AKDENIZ	(METU,METE)	
Prof.Dr.Amdulla MEKHRABOV	(METU,METE)	
Prof.Dr.Ayhan ELMALI	(ANKARA UNV.)	
Assoc.Prof.Dr.C. Hakan GÜR	(METU,METE)	

I hereby declare that all information in this document has been obtained and presented in accordance with academic rules and ethical conduct. I also declare that, as required by these rules and conduct, I have fully cited and referenced all material and results that are not original to this work.

Name, Last name : Selen Nimet Gürbüz

Signature :

ABSTRACT

SYNTHESIS AND CHARACTERIZATION OF BULK GLASS-FORMING IRON-BORON BASED ALLOY SYSTEMS

Gürbüz, Selen Nimet
M.Sc. Department of Metallurgical and Materials Engineering
Supervisor: Prof.Dr. Vedat Akdeniz
Co-Supervisor: Prof.Dr. Amdulla Mekhrabov
June 2004, 207

The aim of this study, which was carried out in two main parts, is to investigate the glass forming ability of Fe-based systems. The first part involves the theoretical modeling to cover the requirement of a predictive model to identify the Fe-based alloy families that have high glass forming ability in the frame of atomistic and thermodynamic approach. The second part involves the experimental investigations to prove the results of the conducted theoretical modeling studies. For this purpose, in the first part, theoretical investigations were performed to identify the third alloying elements that will lead to an increase in the glass forming ability on the base of electronic theory of alloys in pseudopotential approximation for selected Fe- based systems, Fe - (B, Zr, Nb, C, W).

In the experimental part, in the frame of the theoretical investigation results, one of the theoretically modeled binary system, and the third alloying elements that were predicted to lead an increase in the glass forming ability of the selected binary system, were determined. As a first step, designated compositions were synthesized by using low grade conventional Fe-B alloy as a raw material by using centrifugal casting technique and copper mold casting method. To compare the results, same compositions were also cast from the high purity elements by using the same technique and method. For the characterization of these cast specimens, DSC, XRD, SEM, EDS and metallographic examination techniques were used. Amorphous structure was successfully obtained in the thin sections of the wedge-cast samples for Fe-B-Nb and Fe-B-W ternary systems.

Keywords: Fe-based alloys, Bulk metallic glasses, Glass forming ability, Commercial Fe-B alloy, Centrifugal casting method

ÖZ

DEMIR-BORON BAZLI IRI VE HACIMLI METALIK CAMLARIN SENTEZI VE KARAKTERIZASYONU

Gürbüz, Selen Nimet
Y. Lisans, Metalurji ve Malzeme Mühendisligi Bölümü
Tez Yöneticisi: Prof.Dr. Vedat Akdeniz
Ortak Tez Yöneticisi: Prof.Dr. Amdulla Mekhrabov
Haziran 2004, 207 sayfa

Iki ana kisimdan olusan bu çalismanin amaci Fe-bazli sistemlerin cam olusturabilme egilimlerini incelemektir. Ilk kisim, atomistik ve termodinamik yaklasimlar çerçevesinde, yüksek cam olusturma egilimi gösteren Fe-bazli alasim sistemlerinin belirlenmesi için ihtiyaç duyulan teorik modelleme çalismasini içermektedir. Ikinci kisim yapilan teorik modelleme çalismalarinin sonuçlarini degerlendirmek ve desteklemek amaciyla yapilan deneysel arastirmalari kapsamaktadir. Bu amaçla, ilk kisimda, psüdopotansiyel yaklasimi içerisinde alasimlarin elekronik teorisi bazinda, belirlenmis demir bazli aday sistemlerin, Fe-(B, Zr, Nb, C, W), cam olusturma egilimini arttiran üçüncü alasim elementlerini saptamak için teorik çalismalar yapilmistir.

Deneysel kisimda, teorik çalisma sonuçlari çerçevesinde, teorik modellemesi yapilan ikili sistemlerden bir tanesi ve bu ikili sistemin cam olusturma egiliminde artis saglayan üçüncü alasim elementleri belirlenmistir. Ilk olarak, belirlenen kompozisyonlar düsük safliga sahip konvansiyonel Fe-B alasimi ile hazirlanmis, bu kompozisyonlar savurmali döküm yöntemi ve bakir kalip kullanilarak üretilmistir. Elde edilen sonuçlarin karsilastirilmasi için ayni kompozisyonlar saf elementlerden hazirlanarak, ayni döküm teknigi ve kalip kullanilarak üretilmistir. Döküm numunelerinin incelenmesinde DSC, XRD, SEM, EDS ve mikroyapi inceleme teknikleri kullanilmistir. Fe-B-Nb ve Fe-B-W üçlü alasim sistemlerinde, bakir kaliba balta agzi biçiminde dökülen alasimlarin ince kisimlarinda camsi faz elde edilmistir.

Anahtar Kelimeler: Demir bazli alasimlar, Iri ve hacimli metalik camlar, Cam olusturma egilimi, Konvansiyonel Fe-B alasimi, Savurmali döküm yöntemi

To my family;

Semra F. Gürbüz- Ahmet Gürbüz

Ceren Gürbüz- Özen Gürbüz

&

Memory of my grandmother Nimet Orbeyi

ACKNOWLEDGEMENTS

I would like to express my sincere appreciation to Prof. Dr. Vedat Akdeniz and Prof. Dr. Amdulla Mekhrabov for their constant supervision, patience, guidance and motivation in the course of this thesis.

I am sincerely greateful to Prof.Dr. Bilgehan Ögel and Prof.Dr. Ayhan Elmali for their valuable intelligence, help and support.

I must also thank to Fatih Güner for his neverending patience, motivation and support in the completion of this thesis. I must also express my special thanks to Hülya Arslan, Ali Abdelal, Emrah Erdiller for their endless guidance, motivation and support over the years.

I would like to thank Can Ayas, Gül Çevik, Ziya Esen, Ilkay Saltoglu, Tufan Güngören, Süha Tirkes for their help and support.

I would also like to thank Prof. Dr. Sakir Bor, Dr. Kaan Pehlivanoglu and Dr. Elif Tarhan for their advices and moral support.

I owe a depth to my family Ahmet, Semra F., Ceren, Özen Gürbüz and Nimet Orbeyi for their neverending devotion, support and encouragements.

This study was supported by BAP-2002-07-02-00-111 project.

TABLE OF CONTENTS

LIST OF SYMBOLS

$\mathbf{I_S}$	Saturation magnetization
$\mathbf{H_C}$	Coercive field
μ_e	Magnetic permeability
$\mathbf{R_C}$	Critical cooling rate
$\mathbf{t_{max}}$	Maximum thickness attained in amorphous form
$\mathbf{d_{max}}$	Maximum diameter attained in amorphous form
$\mathbf{T_C}$	Curie temperature
$\mathbf{B_S}$	Saturation induction
l_s	Magnetostrictive coefficient
$\Delta\mathbf{T_x}$	Supercooled liquid region
$\mathbf{T_x}$	Crystallization temperature
$\mathbf{T_g}$	Glass transition temperature
$\mathbf{T_l}$	Liquidus temperature
$\mathbf{T_{rg}}$	Reduced glass transition temperature
X	Time dependent volume fraction of crystalline phase
I	Homogenous nucleation rate
U	Growth rate
K	Boltzman constant
$\mathbf{A_0}$	Mean atomic diameter
$\mathbf{N_A}$	Avagadro number
R	Gas constant
η	Viscosity
σ	Liquid/solid interface energy
$\Delta\mathbf{H_f}$	Enthalpy of fusion
$\Delta\mathbf{S_f}$	Entropy of fusion

$\mathbf{V}$	Atomic volume, molar volume
$\mathbf{G^L}$	Gibbs free energy of liquid
$\mathbf{G^S}$	Gibbs free energy of solid
$\Delta\mathbf{G^M}$	Free energy of mixing
Scc(0)	Concentration fluctuation in the long wavelength limit
$\mathbf{V_{AB}\ (r)}$	Effective interatomic potential
$\mathbf{W_{AB}}$	Partial ordering energy between A and B atoms
w	Interchange energy
α_1	Short-range order parameter at the first coordination shell
$\mathbf{P_{A,B}}$	Probability that an A atom exists at site 2 as nearest neighbour of a given B atom at site 1
$\mathbf{c_i}$	Concentration of the i atom
Q	Configurational partition function
$\mathbf{g_r}$	Function for degeneracy of the state
$\mathbf{E_r}$	Configuration energy
$\mathbf{N_i}$	Number of i atoms
$\mathbf{V_{ij}}$	Mutual energy of a pair of nearest neighbours
F	Helmoltz free energy
T	Temperature
$\Delta\mathbf{H^M}$	Heat of mixing
$\Delta\mathbf{S^M}$	Enthalpy of mixing
$\overline{\mathbf{N}}_{\mathbf{AB}}$	Equilibrium or average value of A–B pairs of atoms
$\Delta\mathbf{S^{conf.}}$	Configurational entropy
g	Lattice sites
W	Atomic volume
Z	Coordination number
t	Incubation time for crystallization
$\mathbf{Z_1}$	Constant of $2x10^{-6}$
F	Rate constant in jumps/s unit associated to diffusion or viscosity
$\mathbf{T_m}$	Melting temperature

f_1	Parameter for calculating critical cooling rate
f_2	Parameter for calculating critical cooling rate
A_i	Atomic weight of element i
C_A	Andrade coefficient
V_i	Molar volume of element i
S^s	Mismatch entropy
ΔS^{ideal}	Ideal entropy of mixing
W_{ij}	Regular solution interaction paremeter
x_1	Packing fraction
d_i	Atomic diameter i^{th} element
h_0	Pre-exponential term for viscosity
h_A	Viscosity of A element
ψ_i	Individual electron wave function
U_0	Volume dependent electronic contributions to total energy of crystal
U_{bs}	Structure dependent electronic contribution to total energy of crystal
E_F^0	Fermi energy
Ω	Volume of the crystal
$U_{lattice}$	Coulomb repulsion between the ion cores
$X(q)$	Function arising from perturbation theory
$\alpha(q)$	Ratio of the original potential of the ions to the crystal potential
$W(q)$	Form factor
R_1, r	Radius of the first coordination shell or interatomic distance
$\varepsilon(q)$	Dielectric constant
$\varepsilon^*(q)$	Modified dielectric constant
$W^\circ(q)$	Form factor of unscreened potential
Z^*	Effective valance
$\overline{\Omega}$	Average atomic volume
V/A	Casting modulus
T_p	Peak Temperature

Bi	Biot Number
Nu	Nusselt Number
l	Half plate thickness
h	Heat transfer coefficient
k	Thermal conductivity
a	Heat transfer coefficient
$\mathbf{C_p}$	Specific heat
r	Density
$\frac{\mathbf{dT}}{\mathbf{dt}}$	The rate of the temperature change of the liquid prior to solidification
$\mathbf{T_0}$	Mold temperature
T	Liquid temperature
R	Cooling rate
V	Growth rate
t	Thickness
D$\mathbf{H_x}$	Enthalpy of crystallization
D$\mathbf{H_m}$	Enthalpy of melting

CHAPTER 1

INTRODUCTION

The atomic structure of ordinary or conventional crystalline metals and alloys exhibit long-range atomic ordering, where the layout of atomic elements shows repeating patterns over an extended range. These structures can be obtained from the molten state under normal cooling conditions, by giving time to the atoms for diffusion and long-range atomic rearrangements.

On the contrary, metallic glasses (amorphous alloys or glassy alloys) have a high degree of dense random packed atomic configurations, exhibiting only short range or medium range ordering. These materials are formed when certain multi-component alloys are cooled very rapidly, so that the atoms do not have enough time for long-range atomic rearrangements and freeze into a non-crystalline, liquid like structure.

Formerly, to overcome tendency of conventional alloys to crystallize, between the melting temperature and the glass transition temperature during solidification, usually extremely high cooling rates are required, that can be attainable only by rapid quenching techniques. These required high cooling rates, on the order of 10^5-10^7, restrict the maximum attainable product thickness, product geometry and so the application areas of these materials. [1]

Later on, these issues are obviated by synthesizing special multi-component alloy systems with a high stability of supercooled liquid against crystallization and high glass forming ability (GFA). These alloys are called as bulk amorphous alloys and

can vitrify at lower cooling rates (10^2-10^3 K/s) from the molten state and consequently, they can be cast in bulk shapes (several millimeters) by conventional casting techniques. However, high vacuum, high purity of raw materials, which cause a high cost, are generally required for the fabrication of these materials. [2]

The attraction of these materials lies in the unique properties that are not obtainable in conventional crystalline alloys, such as high corrosion resistance, high strength, high hardness, good wear resistance and good workability etc. Beside all these properties, Fe-based amorphous alloys also exhibit good electrical and soft magnetic properties at room temperature such as high electrical ressistivity, high saturation magnetization (I_S), low coercive fields (H_C), and high magnetic permeabilities (μ_e). As a result of these, over the past several decades, Fe-based amorphous alloys have been investigated for applications in magnetic devices requiring magnetically soft materials. However, alloy discovery progresses by empiricism [3, 4]. The development of a predictive model that identifies the alloy families that form bulk metallic glasses remains a great scientific challenge.

In this thesis, Fe-based amorphous alloys are selected because of their unique properties and industrial application potential. This study carried out in two main parts, which are complementary to each other. The first part involves the theoretical modeling to cover the requirement of a predictive model to identify the Fe-based alloy systems that have high glass forming ability in the frame of atomistic and thermodynamic approach, and the second part involves the experimental investigations. In the first part, theoretical investigation of the glass forming ability for the selected compositions of binary Fe-based systems, Fe-B, Fe-Zr, Fe-Nb, Fe-C and the Fe-W, were performed on the base of electronic theory of alloys in pseudopotential approximation. In addition to these, the effect of the third element addition on glass forming ability and its related parameters of these systems were also examined.

On the basis of the theoretical investigation results, Fe-B binary system among the predescribed systems, and the third elements, Nb and W, that increase the glass forming ability of the selected binary system, were selected for experimental investigations. First, selected binary and ternary systems were tried to synthesis by using a conventional grade alloy as a raw material, to prepare Fe-based amorphous alloy more economically. Then, for comparison, the same binary and ternary systems were synthesized by using high purity elements. All casting experiments were performed, by using centrifugal casting machine and Cu-mold casting method under controlled atmosphere. For designating the solidification behavior and to compare the data, the same compositions were synthesized under near equilibrium solidification conditions. For the characterization of these cast specimens, DSC, XRD, SEM, EDS and metallographic examination techniques were used.

Based on the results of the experimental investigations, it appears that for binary Fe-B alloy, formation of an amorphous structure could not be detected, however, for all ternary systems, obtained by the addition of 5 at% of Nb or W elements to the Fe-B binary system, at least partial amorphous structure was obtained. This result proved the fact that addition of Nb and W elements increases the GFA of the selected binary system as predicted by the results of the theoretical modeling and computer simulations.

This thesis study covers five chapters. In the first chapter, a brief introduction to amorphous alloys is presented. In the second chapter, the historical development and the theoretical approaches are described. Third chapter includes experimental procedure for both theoretical modeling of glass forming ability and the experimental investigations of Fe-based alloys. In the next chapter, chapter four, results and the discussions of the theoretical and the experimental investigations are presented. In the last chapter, the crucial points, obtained during the study, are summarized.

CHAPTER 2

IRON-BASED BULK AMORPHOUS ALLOYS

2.1 Historical Development of Bulk Amorphous Alloys

Four decades ago the synthesis of glasses were extended to metallic systems. The first liquid alloy to be vitrified by cooling from the molten state was Au-Si in 1960 (Duwez, Willens and Klement) [5, 6]. In 1969, Chen and Turnbull were able to make amorphous spheres of ternary Pd-Si-N with N=Ag, Cu or Au. In some ternary Pd-Cu-Si and Pd-Ag-Si alloys, the supercooled liquid range extended to 40 K, which enabled to perform the first detailed studies of crystallization in metallic glasses. In addition, Chen made systematic investigations on Pd-T-P (T=Ni, Co, Fe) in 1974 and obtained critical casting thicknesses on the order of 1 mm in these alloys [7].

In the beginning of 1980s, the Turnbull group revisited Pd-Ni-P alloys by subjecting the specimens to surface etching followed by a succession of heating and cooling cycles; they decreased the heterogeneous nucleation and were thus able to make glassy ingots with a diameter of 5 mm. In 1984, the same group could extend the critical casting thickness to 1 cm by processing the Pd-Ni-P melt in a boron oxide flux. Pd-Ni-P may be considered as the first bulk metallic glass (critical cooling rate, $R_C < 10^2$-10^3 K/s) to be developed [7]. During the late 1980s, the Inoue group discovered high GFA in Ln-Al-TM (Ln: lanthanide metal, TM: transition metal) alloys (cylindrical samples with diameters up to 5 mm and critical cooling rate, $R_C >$ 1-500 K/s) [8]. Subsequently, in 1990 and 1991, the same

research group developed a family of Zr-based Zr-Al-TM [9] and Zr-Al-Ni-Cu alloys [10] having a high GFA and thermal stability. The critical casting thicknesses in these alloys ranged up to 10 mm. In 1993, they developed glassy Mg-Ln-TM alloys [11].

The development of these alloys demonstrated that bulk metallic glass compositions were not a laboratory curiosity and could be quite interesting for engineering applications. The Johnson group started the search for bulk metallic glass compositions in the early 1990s. In 1993, Peker and Johnson developed the quinary alloy Zr-Ti-TM-Be with a critical casting thickness of several centimeters and critical cooling rate values of 1-10 K/s. This work together with the work of the Inoue group could be considered as the starting point for the use of bulk glassy alloys in structural applications [7, 12].

After these developments, several the new multi-component glassy alloys were synthesized in bulk form, in Fe- [13-34], Ti-, Ni-, Hf- and Cu- based systems. In these systems, by choosing compositions which possess high glass forming ability, the critical sample thickness is reached as large as above 20 mm and the critical cooling rate is decreased 1,2 to 10 K/s. These alloys have been synthesized by conventional single roller melt spinning and more traditional copper mold casting [24, 35].

2.1.1 Fe-Based Bulk Amorphous Alloys and Their Properties

First Fe-based amorphous system, Fe-P-C alloys, was synthesized in 1967 [21]. Subsequently, (Fe, Co)-Si-B amorphous alloys with engineering importance have been developed in 1974, followed by the development of (Fe, Co, Ni)-(Cr, Mo, W)-C, (Fe, Co, Ni)-Zr-Hf and then (Fe, Co, Ni)-(Zr, Hf, Nb)-B amorphous alloys [3]. Formation of these amorphous alloys requires very high cooling rates, to suppress the crystallization and long range ordering, and the sample thicknesses have usually been limited to maximum 50 μm for sheet form and 120 μm

diameters for wire form. These limitations of geometry and the thickness restrict the application areas for these alloys [14].

In 1995, first synthesis of Fe-based bulk glassy alloy in a Fe- (Al, Ga)-P-C-B [13] system was performed. Since then, a number of bulk glassy alloys have been developed with sample thicknesses of 1-15 mm in Fe-(Nb, Mo)-(Al, Ga)-(P, Si,B)[14, 15, 16, 36], (Fe, Co, Ni)-(Zr, Hf, Nb)-B [21, 22, 37], (Fe, Co)-(Zr, Hf)-(Nb, Ta)-(Mo, W)-B [23], (Fe, Co)-Ln-B [38](Ln = lanthanide metal) and Fe-(Nb, Cr, Mo)-(P, B, C) [39] systems. Successive examples of the Fe-based bulk amorphous alloy systems, synthesized after 1995, synthesized from high purity elements by Cu-mold casting is presented in Table 2.1.

Table 2.1 Successive examples of Fe-based bulk amorphous alloy systems synthesized from high purity elements, together with the maximum thickness (t) or diameter (d) attained, since 1995.

Alloy	t or d	Production Technique	Ref. No.
Fe-Al-Ga-P-C-B	t =1 mm	Cu-Mold Casting	[13]
Fe-Al-Ga-P-C-B-Si	t =3 mm	Cu-Mold Casting	[14, 28]
Fe-Al-P-C-B-Ge	t =1 mm	Cu-Mold Casting	[15]
Fe-Nb-Al-Ga-P-C-B	t =1mm	Cu-Mold Casting	[16]
Fe-(Co, Ni)-Zr-B	t =2 mm	Cu-Mold Casting	[24]
Fe-(Co, Ni)-Zr-Nb-B	t =2 mm	Cu-Mold Casting	[24]
Fe-Co-Zr-Mo-W-B	t =6 mm	Cu-Mold Casting	[24]
Fe-Co-Ni-Zr-Nb-B	t =1,6mm	Cu-mold Casting	[25, 27]
Fe-Co-Ni-Zr-Nb-Ta-B	t =3mm	Cu-mold Casting	[25, 27]
Fe-Co-Ni-Zr-Nb-Ti-B	t =3mm	Cu-mold Casting	[25, 27]
Fe-Co-Ni-Zr-Nb-Mo-B	t =3mm	Cu-mold Casting	[25, 27]
Fe-Ni-P-B	d=1-2mm	Water Quenching	[29]
Fe-Cr-Mo-(C,B,P)	t=1-2,7mm	Cu-mold Casting	[31]
Fe-Al-Ga-P-C-B-Si	d=2mm	Cu-mold Casting	[33]
(Fe-Mn-Cr)-Zr-Nb-B	d=~2- 3mm	Cu-mold casting	[34]
(Fe-Mn-Cr)-Zr-C-B	d=~2- 3mm	Cu-mold casting	[34]
(Fe-Mn-Mo)-Zr-Nb-B	d=~2- 3mm	Cu-mold casting	[34]
(Fe-Mn-Mo)-Zr-Nb-B-Si	d=~2- 3mm	Cu-mold casting	[34]

These Fe-based bulk metallic glasses are extremely attractive for subsequent development of basic science and applications because of their high electrical resistivity and good soft magnetic properties such as high saturation magnetization (M_S), low coercive fields (H_C), low core losses, and high magnetic permeabilities (μ_e) [3, 40]. Table 2.2 illustrates experimental observations of soft magnetic properties of various Fe-based bulk metallic glasses. This includes curie temperature (T_C), saturation induction (B_S), magnetic permeability (μ_e), coercivity (H_C), magnetostrictive coefficient, for these Fe-based bulk amorphous materials.

Table 2.2 Soft magnetic characteristics, curie temperature (T_C), saturation induction (B_S), magnetic permeability (μ_e), coercivity (H_C), magnetostrictive coefficient (λ_s), of various Fe-based bulk metallic glasses.

Alloy	**T_C (K)**	**B_S (T)**	**m_e ($x10^3$)**	**H_C (A/m)**	**l_s ($x10^{-6}$)**	**Ref.**
Fe72Al5Ga2P11C6B4	605	1,07	9	5,1	21	[13, 41]
Fe72Al5Ga2P11C5B4Si1	590-600	1,14	3,2	1,5-12,7		[18]
Fe73Al5Ga2P11C5B4	~600	1,07	3,6	12,7	2	[13, 17]
Fe80P12B4Si4		1,1	5,8	1,3		[18, 44]
Fe76Al4P12B4Si4		0,96	2,6	12,7		[18, 44]
Fe74Al4Ga2P12B4Si4		0,91	1,9	19,1		[18, 44]
Fe56Co7Ni7Zr2Nb8B20	508	0,71	20	1,7	14	[20]
Fe56Co7Ni7Zr2Ta8B21	538	0,85	17,4	1,5		[20]
Fe56Co7Ni7Zr10B20	567	0,96	17,7	2,4		[21]
Fe56Co7Ni7Zr10B20	594		19,1	1,1	10	[24]
Fe56Co7Ni7Zr8Nb2B20	531	0,75	25	1,1	13	[24]
Fe56Co7Ni7Zr6Nb2,5B20	554		21,5	9,5	7	[27,42]
Fe56Co7Ni7Zr6Ta1,5Nb2,5B20	560		18	6,06	10	[27,42]
Fe56Co7Ni7Zr6Ti1,5Nb2,5B20	603		19	6,1	10	[27,42]
Fe56Co7Ni7Zr6Mo1,5Nb2,5B20	560		17	7,43	10	[27,42]
Fe70Al5Ga2P9,65C5,75B4,6Si3	~600	1,19	1,19	2,2		[28]

In addition to soft magnetic properties, the experiments show that if the alloy composition of the Fe-based bulk amorphous materials is suitably determined, these materials exhibit passive behavior under extremely severe corrosive environments, indicating that they have high corrosion resistance [1].

Up to recent years, to synthesize these attractive Fe-based bulk amorphous alloys, high purity raw materials are used. However, usage of these materials cause a high cost for production and restricts the application areas of these amorphous alloys. Therefore, the search for Fe-based bulk amorphous materials prepared from low cost raw materials becomes an important issue for practical applications. In recent years, few researches demonstrate the successful production of these materials with high glass forming ability using raw materials of low purity [2, 45]. These researches are presented in Table 2.3.

Table 2.3 New Fe-based bulk amorphous alloys synthesized from low purity raw materials, calendar years, together with the maximum diameter (d) attained.

Composition	Raw Materials	d(mm)	Method	Year	Ref. No.
(Cast Iron FC20)(1-x)Bx (x=0,3-2 in wt %)	Commercial FC20 (Fe81,1C13,77Si5,05Mn0,18 P0,015Si0,02 in at. %) and pure B crystal	2	Cu-mold Casting	2000	[43]
Fe79,25C13,8Si5,1B1,5Mn0,18 P0,15S0,02 (in at. %)	Commercial FC20 (Fe80,46C14,01Si5,18Mn0,18 P0,15S0,02 in at. %) and pure B crystal		Melt Spinning	2000	[44]
Fe61Co7Zr10Mo5W2M(15+x) (x=0-1,2) (in at. %)	Fe-B Alloy (Fe79,8 wt%, 18,3 wt% B and rest is Al, Si, C, S, P) and pure Co, Zr, Mo and W	1-2	Cu-mold Casting	2003	[2]
Fe60Co8Zr10Mo5W2B15 (in at. %)	Fe-B Alloy (Fe79,74 wt%, 17,89 wt% B and rest is Al, Si, C, P) and pure Co, Zr, Mo and W	1,5	Cu-mold Casting	2004	[45]

As it can be realized from Table 2.1 and Table 2.2, most of the Fe-based bulk amorphous alloys have been synthesized from Fe-B system by the addition of metal or metalloid elements.

On these account, several researches and also our study especially was focused on Fe-B system. This system shows significant glass forming ability for compositions close to the Fe-rich eutectic and it's often used as a model system for the understanding of glass formation and crystallization in metallic materials.

The crystallization product of these metallic glasses generally contains solid solution α-Fe, and two intermediate compounds Fe_2B, Fe_3B [14, 15, 21, 35, 45-50]. However, according to the Fe-B binary phase diagram, Figure 2.1 (continuous line), it can be seen that Fe_3B phase does not exist under equilibrium conditions.

The researches, focused on the Fe-B system, indicate that Fe_3B is generally considered as metastable phase and appears to be the one of the crystallization products of Fe-B metallic glasses. In these studies, a metastable phase diagram has been calculated, for Fe-B system, using the estimated thermodynamic properties for Fe_3B [46-47]. The result is shown in Figure 2.1. According to the experimental findings, Fe_3B phase becomes stable at a low temperature and shows a eutectic decomposition at 18 at. % B and turns out to melt peritectically at 1433 K [47].

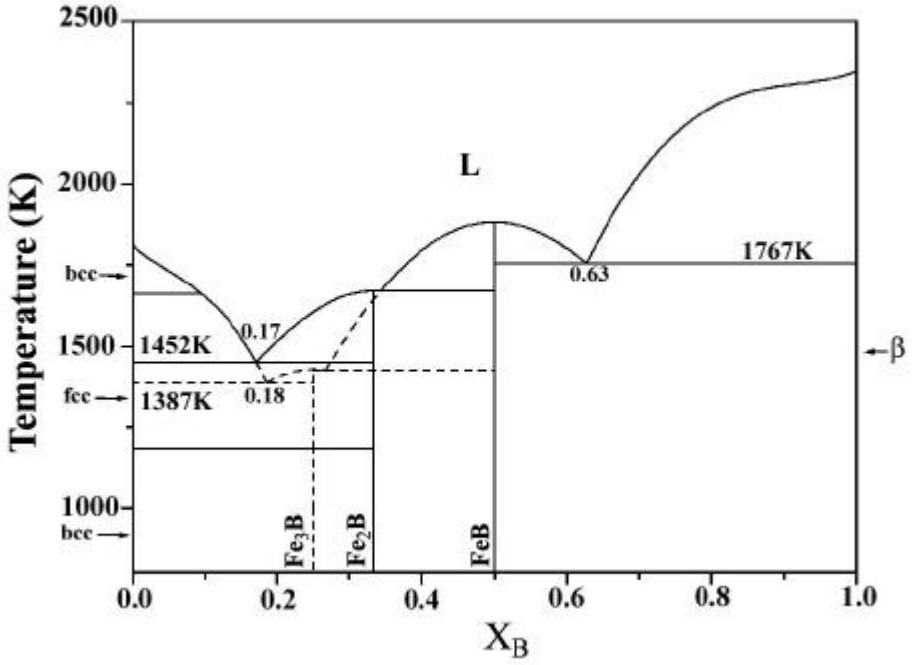

Figure 2.1 Fe-B stable (continuous line) and metastable (dashed line) phase diagrams [46].

2.2 Theory of Glass Formation

2.2.1 Bulk Glass Forming Ability and Related Key Parameters

The glass forming ability can be defined as the degree of ready glass formation to avoid nucleation and growth of crystals. Glass forming ability (GFA) is characterized by the critical cooling rate R_c, but it is difficult to measure. Thus several key parameters have been used to predict the GFA, most often used are;

I. Supercooled liquid region,

II. Reduced glass transition temperature.

2.2.1.1 Supercooled Liquid Region

Supercooled liquid region before crystallization, ΔT_x, can be defined by:

$$\Delta T_x = T_x - T_g \qquad \textbf{(2.1)}$$

where, T_x is the crystallization temperature and T_g is the glass transition temperature. The existence of a wide supercooled liquid region denotes a high thermal stability of the supercooled liquid against crystallization, so that high GFA [26, 51-53].

2.2.1.2 Reduced Glass Transition

The reduced glass transition temperature, T_{rg} can be defined as:

$$T_{rg} = \frac{T_g}{T_l} \qquad \textbf{(2.2)}$$

where, T_g and T_l are the glass transition and liquidus temperatures, respectively. Generally T_g has a weak dependence of composition. On the contrary T_l often decreases strongly as the alloy composition increases. Thus, in general the interval between the T_l and T_g decreases and the value of T_{rg} increases with increasing alloying concentration so that the probability of being able to cool through the interval between T_l and T_g without crystallization is enhanced, so that the GFA is increased. The ratio T_g/T_l also arises from the requirement that the viscosity must be large at temperatures between the melting point and the glass transition temperature. The viscosity at T_g being the constant, the higher the ratio T_g/T_l, the higher will be the viscosity and hence the smaller will be the critical cooling rate for glass formation. Accordingly, alloy systems for which the glass forming ability

is higher, are those with near or at eutectic compositions or low-lying T_l compared with the melting points of host metals, thus leading to high T_{rg} [54, 55].

2.2.2 Approaches to Glass Formation

2.2.2.1 Semi-Empirical Approach

It has been suggested that the most multinary metallic alloys that can vitrify easily (high GFA) are seen to share several common features based on the several empirical rules. These rules state that:

(i) Alloy systems must be composed of three or more constituent elements,

(ii) The atomic size ratios of the components must be sufficiently different (typically exceeding ~13 %), and

(iii) Heat of mixing between the components must be negative.

It is suggested that the multinary alloy systems, which have above stated features, have enhanced short range orderings, higher degree of dense random packed structure and new local atomic configurations different from the competing crystalline phases. The higher degree of dense random packing of the larger, medium and smaller atomic sizes also result in the homogeneous mixture of the different types of elements on a long range scale.

Formation of the liquid with specific atomic configurations and the multicomponent interactions on a short-range scale has been suggested to increase the liquid/solid interface energy and decrease the atomic diffusivity and increase the viscosity, which in turn, leads to the suppression of nucleation and growth of crystalline phases.

Although, the crystallized structure are composed of the multicomponent phases on the progress of crystallization requires the redistribution of the constituent elements on a long range scale. The necessity is thought to cause the high thermal stability of the supercooled liquid against crystallization that result in the large glass forming ability. The suppression of crystal nucleation, atomic diffusivity and crystal growth gives rise to a deep eutectic point through a significant decrease in T_m due to the increase in the thermal stability of the liquid [1, 3, 8-11, 56]. Figure 2.2 summarizes of mechanism for the stabilization of supercooled liquid and the formation of bulk glassy alloys according to the semi-empirical approach.

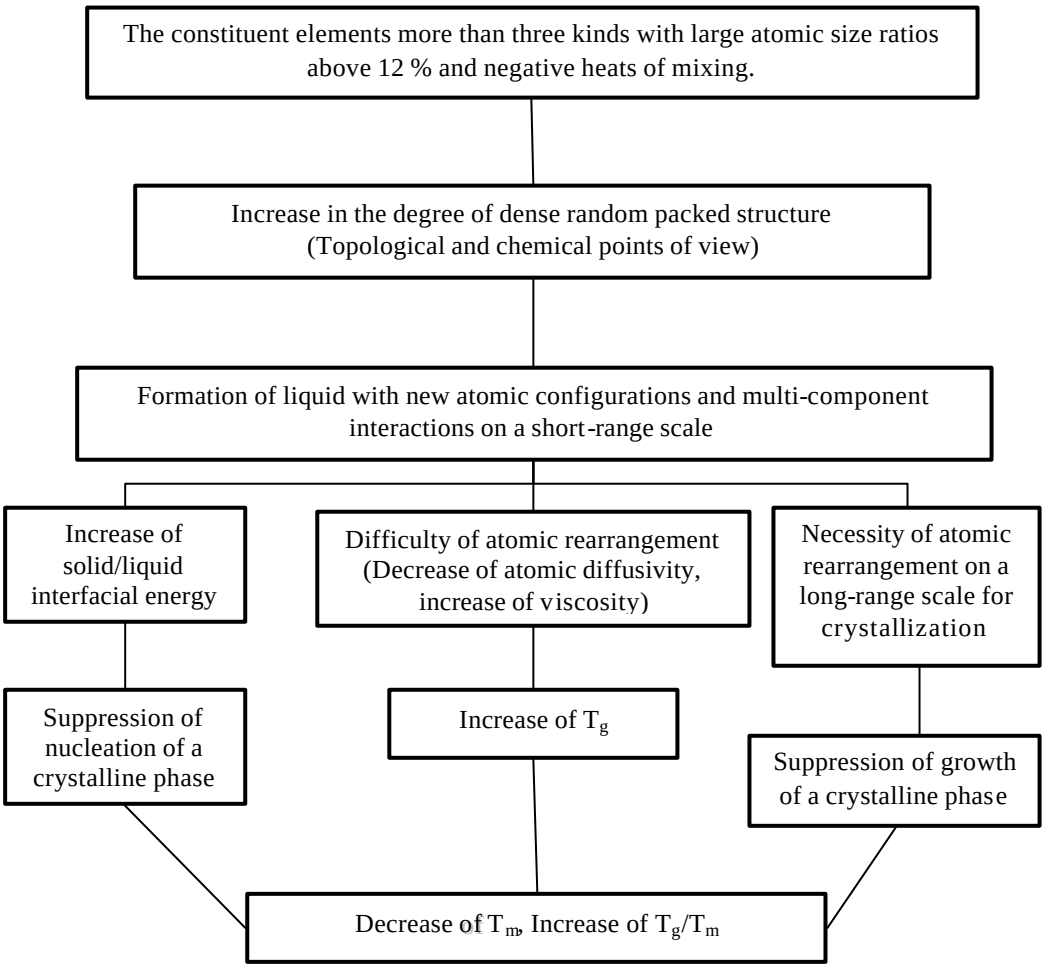

Figure 2.2 Summary of mechanism for the stabilization of supercooled liquid and the formation of bulk glassy alloys according to the semi-emprical approach [1].

2.2.2.2 Kinetic Approach

Formation of an amorphous phase by solidification from liquid phase requires suppression of the nucleation and growth of a crystalline phase in the supercooled liquid region. As a result it is important to investigate the high GFA from the kinetic point of view.

When the liquid is cooled from above the liquidus temperature T_l to a temperature below T_g at a constant cooling rate R, the time dependent volume fraction of crystalline phase X can be given based on non-isothermal crystallization kinetics [57, 58]:

$$X(T) = \frac{4\pi}{3R^4}\int_{T_l}^{T_g} I(T')\left[\int_{T}^{T_g} U(T')dT'\right]^3 dT' \qquad \textbf{(2.3)}$$

where, I and U are the steady-state nucleation and growth rate, respectively. The homogenous nucleation (I) and growth (U) rates of a crystalline phase with spherical morphology from supercooled liquid are known to be expresses by the relations [57, 58]:

$$I = \frac{10^{30}}{\eta}\exp\left[\frac{-16\pi}{3}\frac{\Delta S_f \alpha^3 T^2}{N_A k(T_l - T^2)}\right] \qquad \textbf{(2.4)}$$

$$U = \frac{kT}{3\pi a_0^2 \eta}\left[1 - \exp\left[-\frac{(T_l - T)\Delta S_f}{RT}\right]\right] \qquad \textbf{(2.5)}$$

where, T_l is the liquidus temperature, k is Boltzman constant, a_0 is the mean atomic diameter, N_A is Avogadro number, R is gas constant, and η is viscosity. α is dimensionless parameter related to the liquid/solid interface energy (σ), and ΔH_f can be expressed as:

$$\alpha = \left(\frac{(N_A V)^{1/3} \sigma}{\Delta H_f} \right) \qquad \textbf{(2.6)}$$

where, V is the atomic volume.

From these entire relations one can know that the improvement of the GFA can be achieved by increasing viscosity of the supercooled liquid, entropy and by decreasing the liquidus temperature and the enthalpy.

On the other hand, the microscopic reasons for glass formation tendency in metallic alloys have not been understood well by any above approaches to metallic glasses. More atomistic approach to the amorphous structure formation is required to resolve and to understand the formation of glassy state by investigating the interactions and interatomic relations by the help of pseudopotential theory applying to amorphous state of the metallic alloys [57, 58].

2.2.2.3 Thermodynamic Approach

As the amorphous alloys are undercooled liquids, the ease of obtaining this state depends on two main factors of influence.

- **i.** The free energy difference between the undercooled liquid and the more stable solid phases, G^L-G^S, at the temperature of freezing, should be comparatively small or negative.
- **ii.** The rate of formation of the crystalline phases should be smaller than the amorphous phase.

These conditions have two main consequences. They limit the range of composition in which the glass state can be achieved all together. Additionally, the alloy design according to these criteria is limiting the freedom of choice of components and compositions [58, 59].

Consequently, to analyze solidification and glass forming ability of a system, investigation of the free energy difference between the solid and liquid state is generally required. However, for multi-component systems, it is impossible to estimate the energies accurately as a function of composition and temperature. For this reason, Takeuchi and Inoue [60] propose an assumption: $G^L - G^S$ at a composition is proportional to ΔG^M of the liquid phase.

In this frame, more detailed studies were performed in order to investigate the thermodynamic properties of liquid alloys, such as heat of mixing, entropy of mixing and free energy of mixing. These studies make it possible to calculate the critical cooling rate in order to obtain amorphous structure for binary and multi-component alloys. In the following parts, theoretical background of these studies will be presented.

2.2.2.3.1 Binary Alloys

2.2.2.3.1.1 Order in Liquid Alloys

From the point of view of interatomic interactions, a binary alloy is either:

- **i.** An ordered alloy, where unlike atoms are preferred as nearest neighbours over like atoms, or
- **ii.** A segregated alloy, where like atoms are preferred to pairs as nearest neighbours over unlike atoms.

Unfortunately, there is no direct way to distinguish the constituent atoms and hence the identification of a nearest-neighbour pair of atoms is problematic. In this case either the structural data or the observed thermodynamic functions (such as activity, heat of mixing, excess Gibbs energy of mixing, excess heat capacity, etc) or other thermophysical data (such as viscosity, diffusivity, density, surface tension, electrical resistivity, etc) are considered to extract information associated

with interatomic interactions. Some of the empirical criteria as well as microscopic parameters, which are used to identify ordered alloys, are summarized below [61].

(a) Alloys exhibiting negative deviations from Raoult's law.

(b) The heat of formation and the excess Gibbs energy of mixing are negative.

(c) The concentration fluctuation in the long wavelength limit (Scc (0)) is less than the ideal value.

(d) If V_{AB} (r) (i, j=A, B) are the effective interatomic potential, then one can define the radial form of the order potential, i.e.

$$W_{AB}(r) = V_{AB}(r) - \frac{V_{AA}(r) + V_{BB}(r)}{2} \qquad \textbf{(2.7)}$$

For ordered alloys, one requires that W_{AB} (r) > 0 around the nearest-neighbour distances [61].

(e) In the framework of regular solution theory, the interchange energy ω $(= -\frac{Z}{2} W_{AB}) < 0$.

(f) The Warren–Cowley short-range order parameter α should be less than 0. $(-1 \leq \alpha \leq 0)$

2.2.2.3.1.1.1 Short-Range Order Parameter

Consider that two liquid metals, say A and B, at standard state are mixed together to form an alloy. On mixing, if A and B atoms prefer to remain heterocoordinated (i.e. A–B pair) over the self-coordinated (i.e. A–A pair or B–B pair), then we call it an ordering alloy. In order to quantify it, let us consider the Warren–Cowley short-range order parameter, α_1, for the first-neighbour shell which is defined in terms of the conditional probability, $P_{A,B}$ [61].

$$P_{A,B} = c_A (1 - \alpha_1) \qquad \textbf{(2.8)}$$

where $P_{A,B}$ defines the probability that an A atom exists at site 2 as a nearest neighbour of a given B atom at site 1. Equation (2.8) provides an immediate insight into the local arrangement of atoms in the mixture. For a random distribution of atoms, $P_{A,B} = c_A$, then $\alpha_1 = 0$. If $\alpha_1 < 0$, then A–B pairs of atoms are preferred over A–A or B–B pairs as nearest neighbours. By taking a probabilistic approach one can easily show that the limiting values of α_1 lie in the range,

$$-\frac{c_A}{c_B} \le \alpha_1 \le 1 \qquad \text{for } c_A \le ½ \qquad \textbf{(2.9)}$$

$$-\frac{c_B}{c_A} \le \alpha_1 \le 1 \qquad \text{for } c_A = ½$$

For $c_A = c_B = ½$

$$-1 \le \alpha_1 \le 1 \qquad \textbf{(2.10)}$$

The minimum possible value $\alpha_{1,\,min} = -1$, means complete ordering of A–B pairs in the melt, whereas the maximum value, $\alpha_{1,\,max} = 1$, suggests that the A–A and B–B pairs in the melt are totally segregated. For ordering α_1 varies from -1 to 0.

Later, Bhatia and Singh used lattice model theory to obtain expressions for short range order parameter, α_1 [61], i.e.

$$\alpha_1 = \frac{s-1}{s+1} \qquad (\textbf{2.11})$$

with

$$s = \left[1 + 4c_A c_B \left(e^{-W/Zk_BT} - 1\right)^{\frac{1}{2}}\right] \qquad \textbf{(2.12)}$$

It is obvious that for $W/(k_BT) \rightarrow 0$, equation (2.12) implies $a_l = 0$, i.e. a completely random distribution of atoms in the alloy. If $W/(k_BT) < 0$, a_l is positive, i.e. like atoms (A–A or B–B) tend to pair as nearest neighbours and for $W/(k_BT) > 0$, a_l is negative which shows a preference for unlike atoms (A–B) to pair in the alloy [61-62].

2.2.2.3.1.1.2 Quantitative Evaluation of Free Energy of Mixing

Thermodynamic properties of binary systems can be investigated in the light of two simple theoretical models [61, 62];

(i) by taking into consideration only energetic effect

(ii) by taking into consideration both energetic and size effect

For the first model, let us start with the configurational partition function, Q, which can be expressed as

$$Q = \sum_r g_r e^{-E_r/k_BT} \qquad \textbf{(2.13)}$$

where g_r stands for degeneracy of the state r, E_r is the configuration energy. The basic task is to obtain g_r and E_r for a binary alloy consisting of N_A ($= N_{C_A}$) atoms of element A and N_B ($= N_{C_B}$) atoms of element B.

It is assumed that:

(i) The constituent atoms A and B are sufficiently similar in size and shape so that they are interchangeable on the lattice and

(ii) All configurations of atoms, whether in pure state A or pure state B, or in the alloy A–B, have equal energy. It is equivalent to saying that the mixing of atoms leaves this energy unchanged, i.e. there is no energetic effect. Therefore, we have

$$Q_A = Q_B \tag{2.14}$$

$$V_{AB} = \frac{V_{AA} + V_{BB}}{2} \tag{2.15}$$

where V_{ij} is the mutual energy of a pair of nearest neighbours. Within these approximations, one readily writes

$$g_r = \frac{N!}{N_A! N_B!} \tag{2.16}$$

$$E_r = c_A (N_{AA}\ V_{AA}) + c_B (N_{BB}\ V_{BB}) \tag{2.17}$$

The bracketed terms in Equation (2.17) represent the energy of pure substances A and B, respectively. For solid and liquid phases

$$F \sim G = -k_B T \ln Q \tag{2.18}$$

one obtains

$$\Delta G^{M} = c_A (N_{AA} V_{AA}) + c_B (N_{BB} V_{BB}) + RT \sum_i c_i \ln c_i \qquad \textbf{(2.19)}$$

or

$$\Delta G^{M} = RT \sum_i c_i \ln c_i \qquad \textbf{(2.20)}$$

$$\Delta S^{M} = -\left(\frac{\partial G^{M}}{\partial T}\right) = -R\sum_i c_i \ln c_i \qquad \Delta H^{M}=0 \qquad \textbf{(2.21)}$$

It is also concluded that if the size and the enthalpic effects are absent, systems behave as an ideal mixture.

Lets now incorporate the 'energetic effect' and consider that there will be contributions to the potential energy from A–B pairs of neighbours as well as from A–A and B–B pairs. Now assume that

$$V_{AB} = \frac{V_{AA} + V_{BB}}{2} + \frac{1}{2} W \qquad \textbf{(2.22)}$$

where W is usually known as ordering energy. In effect A–A, B–B and A–B pairs of atoms are now energetically distinguishable. Therefore the configurational energy, E, becomes

$$E_r = c_A (N_{AA} V_{AA}) + c_B (N_{BB} V_{BB}) - \frac{1}{2} \overline{N}_{AB} W \qquad \textbf{(2.23)}$$

where $\overline{N}_{AB}$ represents the equilibrium or average value of A–B pairs of atoms. In the simplest approximation where the atoms N_A and N_B are distributed completely randomly, N_{AB} can be given by

$$\overline{N}_{AB} = \frac{N_A N_B}{N_A + N_B} \tag{2.24}$$

By substituting these values into Equations (2.13) and (2.18),

$$\Delta G^M = RT \sum_i c_i \ln c_i - \frac{1}{2} N c_A c_B W \tag{2.25}$$

Hence

$$\Delta S^M = -R \sum_i c_i \ln c_i + \frac{1}{2} N c_A c_B \left(\frac{dW}{dT} \right) \tag{2.26}$$

$$\Delta H^M = -\frac{N}{2} c_A c_B W + T c_A c_B \frac{N}{2} \left(\frac{dW}{dT} \right) \tag{2.27}$$

For the second model, the size effect is also taken into consideration to calculate the heat of mixing, entropy of mixing and free energy of mixing. The help of the quasi-lattice theory of liquid mixtures examines the role of the size effect in conjunction with interchange energy. Quasi-lattice theory allows one to write an explicit expression for ΔS^M and ΔH^M.

The configurational entropy, $\Delta S^{conf.}$, arises due to the specific distribution of the components. Let N_A be the number of A atoms, i.e., N_A occupy a group of γ_1-lattice sites and N_B occupy γ_2-lattice sites. For all possible arrangements of atoms (if there is no energetic effect, $\Delta H^M = 0$) the entropy of mixing can be expressed as

$$\frac{\Delta S^M}{R} = -c_A \ln\left(\frac{c_A}{c_A + \gamma c_B}\right) - c_B \ln\left(\frac{\gamma c_B}{c_A + \gamma c_B}\right) - \frac{1}{2} Z q_A c_A \ln\left(\frac{c_A + \gamma c_B}{c_A + q c_B}\right)$$

$$- \frac{1}{2} Z q_B c_B \ln\left(\frac{c_B + \frac{c_A}{\gamma}}{c_B + \frac{c_A}{q}}\right) \quad \textbf{(2.28)}$$

where c_A and c_B are the compositions, R is the gas constant and γ can be expressed ($\Omega_B > \Omega_A$, and Ω is the atomic volume) as

$$\gamma = \frac{\gamma_B}{\gamma_A} = \frac{\Omega_B}{\Omega_A} \quad \textbf{(2.29)}$$

$$q = \frac{q_B}{q_A} \quad \textbf{(2.30)}$$

q_i is related to Z (the coordination number) and γ_i by

$$\frac{1}{2} Z(\gamma_i - q_i) = \gamma_i - 1, \quad i = A,B \quad \textbf{(2.31)}$$

$$\frac{1}{2} Z(\gamma_A - q_A) = \gamma_A - 1, \quad \gamma_A = \Omega_A \quad \textbf{(2.32)}$$

$$\frac{1}{2}Z(\gamma_B - q_B) = \gamma_B - 1, \qquad \gamma_B = \Omega_B \tag{2.33}$$

On the other hand, if one considers the energetic effect of the binary mixture (i.e. $\Delta H^M \neq 0$) then quasi-lattice theory provides an explicit expression for ΔH^M [61]

$$\frac{\Delta H^M}{N k_B T} = \frac{2 c_A c_B q_A q_B}{(h+1)(c_A q_A + c_B q_B)}\left(\frac{\omega}{k_B T}\right) \tag{2.34}$$

where k_B is the Boltzman constant with

$$h = \left(1 + \frac{4 c_A c_B q_A q_B}{(c_A q_A + c_B q_B)^2}(k^2 - 1)\right)^{1/2} \tag{2.35}$$

where k is defined as

$$k = \exp\left(\frac{\omega}{Z k_B T}\right) \tag{2.36}$$

where

$$\frac{2\omega}{Z} = -(2V_{AB} - (V_{AA} + V_{BB})) \tag{2.37}$$

ω is the interchange energy. V_{ij} is the effective interatomic potential of ij pairs of atoms.

The Gibbs free energy establishes a relation between ΔH^M and the thermal degrees of freedom as [61];

$$\Delta G^M = \Delta H^M - T\Delta S^M \tag{2.38}$$

When we substitute both Equations (2.28) and (2.34) into Equation (2.38), we obtain for binary liquid alloys

$$\frac{\Delta G^{M}}{Nk_B} = \frac{2c_A c_B q_A q_B}{(h+1)(c_A q_A + c_B q_B)}\left(\frac{\omega}{Nk_B}\right)$$

$$-T\left\{c_A \ln\left(\frac{c_A}{c_A+\gamma c_B}\right) - c_B \ln\left(\frac{\gamma c_B}{c_A+\gamma c_B}\right) - \frac{1}{2}Zq_A c_A \ln\left(\frac{c_A+\gamma c_B}{c_A+q c_B}\right) - \frac{1}{2}Zq_B c_B \ln\left(\frac{c_B+\frac{c_A}{\gamma}}{c_B+\frac{c_A}{q}}\right)\right\}$$

(2.39)

2.2.2.3.1.1.3 Quantitative Evaluation of Critical Cooling Rate

The tendency, or glass-forming ability (GFA), is frequently estimated by critical cooling rate (R_C); the systems with R_C less than approximately 10^5 K/s are regarded as high glass forming alloys. Critical cooling rate can be evaluated by using the thermodynamic functions [60].

Since a dimensional unit of R_C is K/s, it is reasonable to assume that R_C is in proportion to melting temperature and in inverse proportion to incubation time to crystallize *t*. Under this assumption, Equation (2.40) was proposed to evaluate R_C:

$$R_C = Z_1 \frac{T_m}{\tau} = Z_1 f T_m \qquad \textbf{(2.40)}$$

where R_C is the critical cooling rate, Z_1 the constant of $2x10^{-6}$, *f* the rate constant in jumps/s unit associated to diffusion or viscosity, and T_m the melting

temperature. The rate constant f is expressed by Eyring's relation with k_B the Boltzmann constant, a is the interatomic distance, and η the viscosity:

$$f = \frac{k_B T}{a^3 \eta} \tag{2.41}$$

Substitution of Equation (2.41) at T_m in Equation (2.40) leads to Equation (2.42):

$$R_C = Z \frac{k_B T_m^2}{a^3 \eta_{T=T_m}} \tag{2.42}$$

where

$$\eta(T_m) = C_A \frac{\sqrt{AT_m}}{V^{2/3}} \tag{2.43}$$

C_A is Andrade coefficient, A the atomic weight, and V the molar volume. The C_A values are, with few exceptions, closely grouped. The value is 1,85 x 10^{-7} $(J/Kmol^{1/3})^{1/2}$ and adopted for glass-forming systems. The exceptions, all having anomalously high values of C_A, are some semi conducting compounds such as Se_2Ge, and some compounds close to relatively easy glass-forming compositions such as Fe_2B (C_A=4,6 x 10^{-7} $(J/Kmol^{1/3})^{1/2}$). For eutectics, it is clear that the values of C_A fall into two groups. For "normal" eutectics C_A has a value of 1,85 x 10^{-7} $(J/Kmol^{1/3})^{1/2}$, very similar to the behavior for pure metals. For "deep" eutectics, associated with glass-formation, the values of C_A much higher, 5,3 x 10^{-7} $(J/Kmol^{1/3})^{1/2}$ for $Fe_{83}C_{17}$ [63]. Molar volume, V and atomic weight, A can be calculated as:

$$V = c_A V_A + c_B V_B \tag{2.44}$$

$$A = c_A A_A + c_B A_B \tag{2.45}$$

Where V_A and V_B are the molar volumes and A_A and A_B are the atomic weights of A and B elements.

The evaluation of R_C on the basis of Equation (2.42) was first carried out for typical metallic glasses. It is obvious that all the values of R_C calculated by Equation (2.42) are higher than 10^7 K/s.

Thus, the decrease in R_C by over 10^5, which is required for fabrication of metallic glasses, does not cause even if all the physical and thermodynamic parameters change on alloying as far as Equation (2.42) is used for the evaluation of R_C. This indicates that the decrease in R_C is only achieved by modification of constant Z in Equation (2.42). Consequently, a modified probability Z_1 in addition to Z was assumed as shown in Equation (2.46) [60]:

$$Z_1 = \exp\left(\frac{\Delta G^M}{RT}\right) \qquad \textbf{(2.46)}$$

Note the sign in the exponential term is defined to be plus, so that the system with a large negative value of ΔG^M has a large tendency to decrease R_C. Combining Equations (2.42) and (2.46), eventually, Equation (2.47) was obtained for the evaluation of R_C. Equation (2.47) is, thus, taken into account the effect of decrease in R_C on alloying [60]:

$$R_C = A_1 \frac{k_B T_m^2}{a^3 \eta_{T=T_m}} \exp\left(\frac{\Delta G^M}{RT}\right) \qquad \textbf{(2.48)}$$

2.2.2.3.2 Multi-component Alloys

2.2.2.3.2.1 Quantitative Evaluation of Free Energy of Mixing

In this part, ΔG^M consisting of multi-component systems will be introduced [60]. ΔG^M is defined in terms of its enthalpy of mixing, ΔH^M and entropy of mixing ΔS^M as expressed in Equation (2.38) previously.

For entropy of mixing, ideal configurational entropy ΔS^{ideal} and mismatch term of entropy S^σ resulting from atomic size were considered:

$$\Delta S^{ideal} + S^\sigma = \Delta S^M \quad \textbf{(2.49)}$$

Regular Solution Model

According to the regular solution model, ΔH^M and ΔS^{ideal} are defined as equations (2.50) and (2.51) for the multi-component systems with N elements [60]:

$$\Delta H^M = \sum_{i=1, i\neq j}^{N} \omega_{ij} c_i c_j \quad \textbf{(2.50)}$$

$$\Delta S^{ideal} = -R\sum_{i=1}^{N} (c_i \ln c_i) \quad \textbf{(2.51)}$$

where ω_{ij} is the regular solution interaction parameter between i and j elements, and R is the gas constant. ω_{ij} is assumed to be independent of both the composition and temperature and it can be expressed as:

$$\omega_{ij} = -\frac{ZW}{2} \quad \textbf{(2.52)}$$

where Z is the coordination number. Substitution of Equation (2.52) in to Equation (2.50) leads to:

$$\Delta H^{M} = -\frac{Z}{2}\sum_{i=1,i\neq j}^{N} W_{ij} c_i c_j \qquad \textbf{(2.53)}$$

Mismatch term in entropy of mixing term is taken into account to describe the entropy of mixing concerning the differences in atomic radii. S^{σ} is expressed as:

$$S^{\sigma} = k_B \left\{ \frac{3}{2}(\zeta^2 - 1) y_1 + \frac{3}{2}(\zeta - 1)^2 y_2 - \left[\frac{1}{2}(\zeta - 1)(\zeta - 3) + \ln \zeta \right](1 - y_3) \right\} \qquad \textbf{(2.54)}$$

where ζ is defined as

$$\zeta = \frac{1}{(1 - \xi_1)} \qquad \textbf{(2.55)}$$

ξ_1 is the packing fraction (=0,64) and, y_1, y_2 and y_3 are parameters having a relation of $y_1+y_2+y_3=1$.

$$y_1 = \frac{1}{\sigma^3}\sum_{j\rangle i=1}^{n} (d_i + d_j)(d_i - d_j)^2 c_i c_j \qquad \textbf{(2.56)}$$

$$y_2 = \frac{\sigma^2}{(\sigma^3)^2}\sum_{j\rangle i=1}^{n} d_i d_j (d_i - d_j)^2 c_i c_j \qquad \textbf{(2.57)}$$

$$y_3 = \frac{(\sigma^2)^3}{(\sigma^3)^2} \qquad \textbf{(2.58)}$$

$$\sigma^k = \sum_{i=1}^{n} c_i d_i^k, \quad k=2, 3 \qquad \textbf{(2.59)}$$

where d_i is the atomic diameter of i^{th} element. By Equations (2.54)-(2.59), mismatch term of entropy of mixing of the multi-component system consisting of N elements can be calculated as a function of atomic diameter, composition and packing fraction.

2.2.2.3.2.2 Quantitative Evaluation of Critical Cooling Rate

As mentioned above, ΔG^M of the multi-component alloy systems consists of two terms, regular solution model term and misfit excess entropy term. In order to evaluate the critical cooling rate for multi-component metallic glasses, Inoue and Takeuchi [60] derive an equation:

$$R_C = Z\frac{k_B T_m^2}{a^3 \eta_{T=T_m}} \exp\left[f_1\left(\frac{\Delta H^M - T_m \Delta S^{ideal}}{300R} \right) - f_2\left(\frac{T_m S^\sigma}{300R} \right) \right] \qquad \textbf{(2.60)}$$

where f_1 and f_2 are the fitting parameters. By the method of least squares f_1 and f_2 were calculated to be 0,75 and 1,2, respectively.

2.2.2.3.3 Quantitative Evaluation of Viscosity for Binary and Multi-component Alloys

Viscosity (η) of liquid alloys is equally important in the understanding of the atomic level structure and interactions. As in the case of thermodynamic functions, the composition dependence of η of liquid alloys is also found to exhibit either a linear variation, or positive or negative deviations from the additive rule of mixing ($\eta = c_A \eta_A + c_B \eta_B$) [61, 64].

In the light of conformal solution results, Singh, Sommer and Akinlade propose an equation for $\Delta\eta$ as [64]:

$$\frac{\eta - \eta_0}{\eta_0} = \frac{\Delta\eta}{\eta_0} = -\frac{\Delta H^M}{RT} \qquad \textbf{(2.61)}$$

where R is the ideal gas constant and ΔH^M is the enthalpy of mixing.

2.2.3 Pseudopotential Theory

2.2.3.1 Principles of The One-electron Theory

In principle, it is possible to find out everything about a structure by solving Schrödinger's equation for a system of interacting nuclei and electrons that form the structure. This problem, however, is too hard to solve and some simplifications are therefore unavoidable. Following simplifications are adopted to solve the problem in the basis of one electron theory:

(i) First, it is generally assumed that the nuclei are too massive to follow the rapidly changing spatial distribution of the electrons (the adiabatic approximation). For this reason, two Schrödinger's equations will be considered one for the electrons and the other for the nuclei. In the following, the one with the behavior of electrons will be concerned.

(ii) It is further assumed that instead of treating the electronic subsystem as a whole, it is possible to consider separately the motions of individual electrons. Each of them is then thought of as moving in the effective field of the (stationary) nuclei and all the other electrons (hence the name – the effective field approximation). Accordingly, the total electron wave function is expressed in terms of individual electron wave functions, ψ_i.

(iii) Further approximations are made in the actual evaluation of the total function and in the consequent determination of the effective potential as seen by a single electron (Pauli- exclusion principle). This leads to a system of one-electron Schrödinger equation in the Hartree-Fock approximation including both Coulomb and exchange interactions between the electrons.

The one electron theory is the primitive or basis. It has been worked detaily by several times, however it will be surveyed in some detail through, first of all, nearly-free electron model.

2.2.3.2 Nearly-free Electron Model (NFE)

One electron theory can be taken as a basis for a more detailed model, 'Nearly Free Electron Model'. As stated by the electron theory, total crystal energy can be given as follows:

$$\Sigma_{str} = U_0 + U_{bs} + U_{lattice} \qquad \textbf{(2.62)}$$

Here, the $U_{lattice}$ involves the Coulomb repulsion between the ion cores, the U_0 is the volume dependent electronic contribution and U_{bs} is the structure dependent electronic contribution to the total energy. The values for U_0 and U_{bs} can be calculated from following equations:

$$U_0 = 2 * \frac{\Omega}{(2\pi)^3} * \int_{\substack{\text{inside}\\ \text{the}\\ \text{Fermi}\\ \text{sphere}}} \left(K^2 + \left\langle \vec{K} \middle| V \middle| \vec{K} \right\rangle \right) d^3K \qquad \textbf{(2.63)}$$

$$U_{bs} = -2 * \frac{\Omega}{(2\pi)^3} * \sum_q \left| S\left(\vec{q}\right) \right|^2 \int_{\substack{\text{inside}\\ \text{the}\\ \text{Fermi}\\ \text{sphere}}} \frac{\left| \left\langle \vec{K}+\vec{q} \middle| V \middle| \vec{K} \right\rangle \right|^2}{\left(\vec{K}+\vec{q}\right)^2 - K^2} d^3K - U_{el}^{int} \qquad \textbf{(2.64)}$$

The g_n vectors are replaced with the ordinary position vectors of q. The wave vector is designates as k, where Ω and V stands respectively for volume of the crystal and crystal potential.

Above, U_0 describes a 'free' electron gas with the inclusion of electron-electron interaction. Moreover, U_{bs} is associated with band characteristics and named as "Band Structure Energy". Lastly, when calculating E(k), interaction energy of each electron pair contributes to the energy of each electron, meaning that the electron-electron interaction energy is counted twice while calculating the total energy of the crystal. The term U_{el}^{int} is used in order to get rid of this additional energy calculated by subtracting it from the equation.

If the potential V is local, its form factor K is independent and can be taken out of the K integral that appears then in U_{bs}. This solution is known as Lindhard's function:

$$\chi\left(\vec{q}\right) = -2 * \frac{\Omega}{(2\pi)^3} * \frac{1}{N} * \int_{\substack{\text{inside} \\ \text{the} \\ \text{Fermi} \\ \text{sphere}}} \frac{d^3k}{\left(\vec{k}+\vec{q}\right)^2 - \vec{k}^2} \qquad \textbf{(2.65)}$$

If Fermi surface is assumed spherical, then the Equation (2.65) becomes:

$$\chi(q) = -\frac{Z}{4}\left(\frac{2}{3}E_F^{\circ}\right)^{-1}\left(1 + \frac{1-x^2}{2x}\ln\left|\frac{1+x}{1-x}\right|\right) \qquad \textbf{(2.66)}$$

In Equation (2.66), $x = k/2k_F$ and $E_F^0 = (3\pi^2 z/\Omega_0)^{2/3}$.

The electron-electron interaction energy U_{el}^{int} may be represented [65] as a result of interactions between the non-uniform part of the crystal electron density and the potential, which is the difference between the crystal potential, ϑ^{cr} and the initial

potential ϑ^{ion} of the system of ions. U_{el}^{int} can be expressed in terms of the form factor of V^{cr} (q), if a function, $\alpha(\vec{q}) = \vartheta^{ion}/\vartheta^{cr}$, is set up in order to characterize this potential.

$$U_{el}^{int} = \sum_{q} |S(q)|^2 |V(q)|^2 \chi(q)(1-\alpha(q)) \qquad \textbf{(2.67)}$$

and;

$$U_{bs} = \sum_{q} |S(q)|^2 |V(q)|^2 \chi(q) - U_{el}^{int} = \sum_{q} |S(q)|^2 |V(q)|^2 \chi(q)\alpha(q) \qquad \textbf{(2.68)}$$

where $S(q) = \frac{1}{N}\sum_{i} e^{-iqt_i}$

Note that, no assumptions about the nature of potential except the locality of the potential or about the way in which the crystal potential is composed of the ionic potentials (that is, about the screening mechanism) has been made while deriving this equation. $\chi(q)$ is a function arising from perturbation theory whereas $\alpha(\vec{q})$ is the ratio of the original potential of the ions to the crystal potential.

A frequently used characteristic function Φ_{bs} (q) is defined as:

$$\Phi_{bs}(q) = \sum_{q} |V(q)|^2 \chi(q)\alpha(q) \qquad \textbf{(2.69)}$$

Using the Eq. (2.69), U_{bs} can be rewritten as a sum, over the lattice sites, of Fourier transforms Φ_{bs} (R_i) where transforms can be defined as follows:

$$\Phi_{bs}(R) = 2\frac{\Omega}{(2\pi)^3}\int \Phi_{bs}(q) e^{iqR} d^3q \qquad \textbf{(2.70)}$$

$\Phi_{bs}(R)$ may be thought of as the potential of the interaction between ions through the electron gas (the same electron is simultaneously attracted by all the ions, hence their mutual attraction). It is this interaction that must compensate for the direct Coulomb repulsion of the ions.

The total interatomic interaction potential has the form of

$$\Phi(R) = \frac{Z^2 e^2}{r} + \frac{2\Omega}{(2\pi)^3}\int \left[V^{str}(q)\right]^2 \chi(q)\varepsilon^*(q)e^{i\vec{q}\vec{r}}d^3q \qquad \textbf{(2.71)}$$

When it is given that the systems volume is constant, $\Phi(R)$ in Eq. (2.71) describes the interaction between the atoms. In other words, it is the redistribution of the atoms within the crystal systems.

2.2.3.3 Calculation of Ordering Energies and Pairwise Interatomic Interactions for Ternary Alloys

According to the electronic theory of alloys in the pseudopotential approximation [66-70], the ordering potential itself is

$$W_{\alpha\beta}(R_i) = V_{AA}(R_i) + V_{BB}(R_i) - 2V_{AB}(R_i) \qquad \textbf{(2.72)}$$

will take the form

$$W_{\alpha\beta}(R_i) = \frac{2}{N}\sum_{q}^{i} F_p(q)e^{i\vec{q}\vec{g}_i} \qquad \textbf{(2.73)}$$

or

$$W(R_i) = \frac{\overline{\Omega}}{\pi^2}\int dq * q^2 F_p(q)\frac{\sin qR_i}{qR_i} \qquad \textbf{(2.74)}$$

here

$$F_p(q) = \frac{\overline{\Omega}}{8\pi}\left|\Delta W^b(q)\right|^2 q^2 \frac{1-\varepsilon(q)}{\varepsilon^*(q)} + \frac{2\pi}{\overline{\Omega}}(\Delta Z)^2 \frac{1}{q^2}\exp\left(-\frac{q^2}{4\eta}\right) = F_{bs}(q) + F_{es}(q) \qquad \textbf{(2.75)}$$

It is easy matter to show that $W_{a\beta}(R_i)$ may be written as

$$W_{\alpha\beta}(R_i) = \frac{\overline{\Omega}}{\pi^2}\int dq * q^2 \frac{\sin qR_i}{qR_i}\left\{\frac{\overline{\Omega}}{8\pi}q^2\frac{1-\varepsilon(q)}{\varepsilon^*(q)}\left|W_B^b(q)\right|^2 + \frac{2\pi}{q^2}\left(Z_B^*\right)^2\exp\left(-q^2/4\xi\right)\right\}$$

$$-\frac{2\overline{\Omega}}{\pi^2}\int dq * q^2 \frac{\sin qR_i}{qR_i}\left\{\frac{\overline{\Omega}}{8\pi}q^2\frac{1-\varepsilon(q)}{\varepsilon^*(q)}W_A^b(q)W_B^b(q) + \frac{2\pi}{q^2}Z_A^* Z_B^*\exp\left(-q^2/4\xi\right)\right\}$$

$$+-\frac{\overline{\Omega}}{\pi^2}\int dq * q^2 \frac{\sin qR_i}{qR_i}\left\{\frac{\overline{\Omega}}{8\pi}q^2\frac{1-\varepsilon(q)}{\varepsilon^*(q)}\left|W_A^b(q)\right|^2 + \frac{2\pi}{q^2}\left(Z^*\right)^2\exp\left(-q^2/4\xi\right)\right\} \qquad \textbf{(2.76)}$$

Interatomic interaction potentials between different ionic pairs in the alloys can be calculated in a similar way;

$$V_{\alpha\beta}(R_i) = \frac{\overline{\Omega}}{\pi^2}\int F_{\alpha\beta}^1(q)\frac{\sin qR_i}{qR_i}q^2 dq \qquad \textbf{(2.77)}$$

here $F_{\alpha\beta}^1$ is,

$$F_{\alpha\beta}^1(q) = -\frac{\overline{\Omega}}{8\pi}\left|W_\alpha^\circ(q)W_\beta^\circ(q)\right|q^2\frac{\varepsilon(q)-1}{\varepsilon^*(q)} + \frac{2\pi}{\overline{\Omega q^2}}\left|Z_\alpha^* Z_\beta^*\right|\exp\left(-\frac{q^2}{4\xi}\right) \qquad \textbf{(2.88)}$$

a, ß≡A, B, C and $\overline{\Omega}$ is the average atomic volume of the ternary alloy

$$\overline{\Omega} = c_A\Omega_A + c_B\Omega_B + c_C\Omega_C \qquad \textbf{(2.89)}$$

$\varepsilon(q)$ is the dielectric constant, $\varepsilon^*(q)$ is the modified dielectric constant which takes in to account the correlation and exchange effects. $W_\alpha^\circ(q)$ and $W_\beta^\circ(q)$ are the form factors of an unscreened pseudopotential of a and β ions respectively, $Z_\alpha^\circ(Z_\beta^\circ)$ is the effective valency of the a (β) component atoms,ξ is the Ewald parameter.

For ternary alloys, ordering energy values $W_{a\beta}(R_i)$ and pairwise interaction potentials, $V_{a\beta}(R_i)$ can be calculated by the help of the equations (2.68)-(2.89) as a function of the interatomic distance, R_i when the form factor of unscreened potentials, $W^\circ(q)$, and effective valances, Z^*, are provided.

CHAPTER 3

EXPERIMENTAL PROCEDURE

This study carried out in two main parts, as pointed previously, which are complementary to each other. The first part involves the theoretical modeling of the glass forming ability of Fe-based alloy systems by using atomistic and thermodynamic approach, and the second part involves the experimental investigations.

In this chapter, stages of the theoretical modeling of the glass forming ability of Fe-based alloys will be presented. Also, selected binary systems, compositions and the selected ternary elements for theoretical investigations will be stated. All alloy compositions are expressed in terms of atomic percentages throughout the chapter unless otherwise stated.

In addition, for the experimental investigations, the designated binary system, third elements, the background of these selections and, the experimental technique for the synthesizing of the specimens will be mentioned.

3.1 Theoretical Investigation of Glass Forming Ability of Fe-based Alloys

Since the first synthesis of amorphous alloys in 1960, great deal of experimental investigations has been performed. Up to date, the alloy discovery progress by the help of the empirical approaches and, there is a requirement for the development of a predictive model that identifies the alloy systems that will lead to the formation of metallic glasses. The present study, aims to cover this requirement by modeling the glass forming ability of Fe-based alloys in the frame of the atomistic view and to perform binary and ternary liquid alloy investigations and also to clarify the relations between the ordering energy and factors corresponding to glass forming ability.

3.1.1 Calculation of Ordering Energy Using Electronic Theory of Alloys In Pseudopotential Approximation

For the theoretical modeling of the glass forming ability of Fe-based systems, binary supercooled liquid investigations were performed theoretically by calculating the ordering energy values using electronic theory of alloys in pseudopotential approximation.

For binary supercooled liquid investigations, the FORTRAN program, Meh 7, which has been formulated by Prof. Dr. A. O. MEKHRABOV, on the base of Equations (2.71)-(2.89), were executed for the various selected binary Fe- based systems to calculate the ordering energy value at the first coordination shell, W_{AB}, between the constituent atoms, A – B.

In order to calculate the ordering energy values of ternary systems and to investigate the effect of the selected third alloying element addition, interactions between the main constituent elements and third alloying element were also taken into consideration beside the interactions between the main constituent elements. For this purpose, FORTRAN programs, MEH 1, MEH2, and MEH 3, which have

been formulated by Prof. Dr. A. O. MEKHRABOV, on the base of Equations (2.71)-(2.89), were run to calculate partial ordering energies at the first coordination shell, W_{AB}, W_{AC}, W_{BC}, respectively for the various ternary Fe- based systems. W_{AB}, W_{AC}, W_{BC} are the partial ordering energies for A-B, A–C and B-C atomic pairs in the ternary alloy, respectively. These calculations are performed for each of the selected systems and the compositions when 1 at % of selected third alloying element substituted for 1 at % of the each constituent element that forms the binary alloy. In addition, by using the results of the ordering energy calculations and equation (2.37), interchange energy values was also calculated for binary and ternary systems.

Selected binary systems and third alloying elements will be presented in the next sections of this chapter together with radius of the first coordination shell (R), used in the calculations. The interatomic distances at the first coordination shell were determined from the literature for some compositions. For other systems, these values were obtained by summing the radius of the constituent elements, taken from the paper of Senkov and Miracle [71], assuming that in liquid state these atoms are touching to each other.

3.1.2 Quantitative Evaluation of Heat of Mixing, Entropy of Mixing, Free Energy of Mixing, Critical Cooling Rate, Short Range Order and Viscosity

By using the results of the ordering energy calculations and thermodynamic approaches for glass forming ability, quantitative evaluation of heat of mixing, entropy of mixing, free energy of mixing, critical cooling rate, short range order parameter and viscosity were performed for selected Fe-based binary and ternary systems.

For the calculation of these thermodynamic, thermo physical and kinetic parameters, two different approaches, which relate the ordering energy values and these parameters, were used. First approach, which was presented in detail in section 2.2.2.3.1, has been studied by Sommer and Singh [61, 62], and valid for

only binary liquid alloys. The second approach, which was presented in section 2.2.2.3.2, has been studied by the Inoue [60] and can be used for multi-component liquid alloys.

In order to compare these two approaches, heat of mixing, critical cooling rate and related other empirical parameters were calculated by using the ordering energy values between the constituent elements for Fe-based binary systems. The tabulated result of this comparison will be given in the next chapter.

For the calculation of heat of mixing, entropy of mixing and critical cooling rate the second approach was used, as it is applicable to both binary and ternary systems, to investigate the effect of the 1 at % of third element substitution for each of the constituent elements on these parameters. These calculations were performed for each of the binary and the ternary systems. For the calculation of the short-range order parameter, first approach was used. The results of all these calculations together with the results of the ordering energy calculations will be also presented in the next chapter.

3.1.3 Selection of Fe-based Binary Systems and Third Alloying Elements

For selecting the binary systems, the previously studied Fe-based bulk amorphous alloy systems were considered. Selection of the compositions was performed on the base of the binary phase diagrams of these systems, which were given in Appendix A. For selection of the compositions, mainly the following points were taken into consideration.

Firstly, in selection, compositions that possess growth problems, and hence favor the glass formation, were especially considered, such as intermetallics, eutectics and off-eutectics. Intermetallics exhibit faceted growth morphology; hence their growth is problematic and requires very high undercoolings. Eutectic compositions also exhibit growth problems as they are characterized by the simultaneous growth

of two phases from the liquid, called diffusion-coupled growth, and require very high undercoolings, especially when one component is faceted, so growth of a eutectic phase mixture is difficult and slow. When both phases possess non-faceted morphology, the eutectic will exhibit a regular morphology, whereas if one phase exhibits anisotropic growth characteristics (faceted type growth), the eutectic morphology becomes irregular. The coupled growth of the irregular eutectic is more problematic than the regular one [72].

Furthermore, the crystallization products of the previously studied Fe-based amorphous systems and the compositions that reflect general solidification behavior of binary alloy systems were taken into account.

In the light of these considerations, the selected binary Fe-based systems and compositions are presented in Table 3.1 together with the interatomic distances (R) used in ordering energy calculations for these systems.

Table 3.1 Selected binary Fe-based systems and compositions, radius of the first coordination shell used in the ordering energy calculations.

Binary System	Composition	Radius of First Coordination Shell (R, A°)	Reference No.
Fe-Zr	Fe73Zr27	2,83	
	Fe67Zr33		
	Fe33Zr67		
Fe-B	Fe83B17	2,22	
	Fe75B25	2,21	[74]
	Fe67B33	2,14	[74]
Fe-Nb	Fe87.9Nb12.1	2,67	
	Fe57Nb43		
Fe-C	Fe83C17	1,93	[73]
	Fe75C25	1,95	
Fe-W	Fe80W20	2,61	
	Fe67W33		
	Fe60W40		

For selection of the third alloying elements, beside the previous studies, atomic size and the electronic structure of these elements were considered. The selected third alloying elements are stated, on the periodic table, in Table 3.2.

Table 3.2 Selected third alloying elements that have been used for theoretical modeling studies.

1A												3A	4A	5A	6A	7A	8A
1 **H**	2A																2 **He**
3 **Li**	4 **Be**											5 **B**	6 **C**	7 **N**	8 **O**	9 **F**	10 **Ne**
11 **Na**	12 **Mg**	3B	4B	5B	6B	7B		8B		1B	2B	13 **Al**	14 **Si**	15 **P**	16 **S**	17 **Cl**	18 **Ar**
19 **K**	20 **Ca**	21 **Sc**	22 **Ti**	23 **V**	24 **Cr**	25 **Mn**	26 **Fe**	27 **Co**	28 **Ni**	29 **Cu**	30 **Zn**	31 **Ga**	32 **Ge**	33 **As**	34 **Se**	35 **Br**	36 **Kr**
37 **Rb**	38 **Sr**	39 **Y**	40 **Zr**	41 **Nb**	42 **Mo**	43 **Tc**	44 **Ru**	45 **Rh**	46 **Pd**	47 **Ag**	48 **Cd**	49 **In**	50 **Sn**	51 **Sb**	52 **Te**	53 **I**	54 **Xe**
55 **Cs**	56 **Ba**	57 **La**	72 **Hf**	73 **Ta**	74 **W**	75 **Re**	76 **Os**	77 **Ir**	78 **Pt**	79 **Au**	80 **Hg**	81 **Tl**	82 **Pb**	83 **Bi**	84 **Po**	85 **At**	86 **Rn**
87 **Fr**	88 **Ra**	89 **Ac**															

58 **Ce**	59 **Pr**	60 **Nd**	61 **Pm**	62 **Sm**	63 **Eu**	64 **Gd**	65 **Tb**	66 **Dy**	67 **Ho**	68 **Er**	69 **Tm**	70 **Yb**	71 **Lu**
90 **Th**	91 **Pa**	92 **U**	93 **Np**	94 **Pu**	95 **Am**	96 **Cm**	97 **Bk**	98 **Cf**	99 **Es**	100 **Fm**	101 **Md**	102 **No**	103 **Lr**

Main Constituent Element

Selected Third Element

Elements that are used both as Main Constituent Element and Selected Third Element

3.2 Experimental Investigation of Fe-based Amorphous Alloys

In this study, production of Fe-based alloys, that were predicted to have high glass forming ability, were performed by using centrifugal casting machine and Cu-mold casting method under protective argon atmosphere. For the preparation of determined alloy compositions, both high purity raw materials and low purity raw materials were used. For the elemental analysis of low purity raw material of Fe-B alloy, X-ray fluorescence (XRF) technique was used. The solidification structure of the cast specimens was examined by X-ray diffractometry, optical and scanning electron microscopy. The existence of the glass transition and thermal stability of the cast specimens were analyzed by differential scanning calorimeter (DSC).

3.2.1 Alloy Selection and Preparation

As previously mentioned, experimental studies performed up to now indicate that B is a major element for the Fe-based bulk amorphous alloys and, Fe-B system was used as a model system for the understanding of glass formation and crystallization of metallic materials in literature.

Depending on the base of the theoretical modeling studies and by taking into account the previous experimental studies, Fe-B system was selected for experimental investigations. For this system, the theoretical modeling was performed for the compositions of Fe83B17, Fe75B25 and Fe67B33, as mentioned previously. Among these systems, Fe83B17 composition was selected since this composition corresponds to the Fe-rich eutectic in the Fe-B phase diagram, which is given in Figure 2.1 of the previous chapter, and the previously performed investigations indicate that Fe-B system shows significant glass forming ability for compositions close to Fe-rich eutectic.

For the following stages of the study, niobium and tungsten elements were determined as a ternary alloying element, by taking into consideration of the theoretical modeling studies, their availability and price.

As indicated previously, to produce Fe-based bulk glassy alloys, high purity of raw materials is generally required, which cause a high cost, and restricts their applications. For this reason, first of all, the determined binary and ternary alloy compositions were tried to be synthesized by using low purity industrial grade Fe-B alloy, the compositional analysis of which will be given in the next section of this chapter, and conventional copper mold casting method. The compositions that were tried in study with the mold that was used are given in Table 3.4.

Table 3.4 Alloy compositions prepared from low purity industrial Fe-B alloy.

System	Code	Mold	Nominal Compositions (in wt.%)	Nominal Compositions (in at.%)
Fe-B	S1	M1	Fe 96,19B 3,81	Fe83B17
Fe-B-Nb	S2	M2	Fe 87,73 B 3,48 Nb 8,79	Fe79B16Nb5
Fe-B-Nb	S2	M1	Fe 87,73 B 3,48 Nb 8,79	Fe79B16Nb5
Fe-B-W	S3	M1	Fe 87,73 B 3,48 W 8,79	Fe79B16W5

In the next stages of experimental investigations, to compare the results, the following compositions were also synthesized from the high purity elements, given in Table 3.3 with the mold that was used.

Table 3.3 Alloy compositions prepared from high purity elements.

System	Code	Mold	Nominal Composition (in wt. %)	Nominal Composition (in at. %)
Fe-B	S4	M1	Fe 96,19 B 3,81	Fe83B17
Fe-B-Nb	S5	M1	Fe 87,73 B 3,48 Nb 8,79	Fe79B16Nb5

3.2.1.1 Alloy Preparation

After determination of the alloy systems and compositions, to eliminate the melting problems during induction heating of the alloying composition, the form of the elements were treated. The purity and form of the elements are given in Table 3.5.

Table 3.5 The purity and form of the elements.

Elements	Purity	Shape
Fe-B Alloy	Low	Coarse Grains (crushed)
Fe	99,97+	Irregular Pieces (forged and cut into smaller pieces)
B	99,9	Crystalline Pieces (crushed)
Nb	99.6	Turnings (forged and cut into pieces)
W	99.9	Rods (crushed)

The weight percent boron content of low purity industrial Fe-B alloy was determined as 19,11 wt % by boron analysis method and spectrophotometric instrumentation's of constituents, other than boron, was examined by X-ray fluorescence (XRF) technique in ETI BOR Holding before experiments were performed. Beside these, also composition determination, except boron that cannot be determined, was also performed by using Energy Dispersive Analysis, in METE, METU. For both, XRF and EDS analysis, boron content was taken as 19,11 wt % and the weight percentages of the other constituents were normalized according to the boron content. The results of these analyses were given in Table 3.6, together with the compositional analysis given by the manufacturer.

Table 3.6 The results of the Fe-B alloy analysis.

Element	Analysis given by the manufacturer wt%	XRF results wt%	EDS results wt %
Fe	74,8-79,8	75,1860	73,0760
B	15-20	19,1100	19,1100
Si	2	2,8919	4,6916
Cr	-	0,6199	0,4934
Mn	-	0,5165	0,6957
Al	3	0,5065	1,2134
Ca	-	0,2883	0,7118
Cu	-	0,1990	-
Ni	-	0,1938	-
P	-	0,1595	-
Mg	-	0,1594	-
Mo	-	0,1128	-
Ti	-	0,0564	-
C	0,20	-	-

For all experiments, conducted by using low purity Fe-B alloy, preparation of the alloys was performed by taking into consideration of the XRF results.

3.2.2 Melting and Casting

In this study, to perform the melting and casting of Fe-based alloys, following equipments, centrifugal casting machine, copper molds, alumina crucibles, were used.

3.2.2.1 Production of Alumina Crucibles

Castable alumina crucibles with conic geometry were produced from steel dies for melting and casting of alloying elements into copper wedge molds centrifugally. The reason for choosing the castable alumina as a raw material for making the crucibles was to eliminate the contaminations that may be resulted from the reactions of the alloying elements and the crucible. Table 3.7 shows the elemental analysis of the castable alumina.

Table 3.7 Elemental analysis of the castable alumina.

Element	Weight %
Al_2O_3	97.0 (app)
SiO_2	0.2 (max.)
Fe_2O_3	0.1 (max.)
CaO	1.6 (max.)

In the production of alumina crucibles, effort was given to preserve the size distribution of the castable alumina particles because it is known that the size distribution is very important, due to the fact that big alumina particles have binding effect and small size particles increase the thermal shock resistance of the castable alumina.

The raw material was prepared as ceramic mud from water and alumina in a plastic cup by stirring to achieve good wetting and de-aeration and cast into desired crucible geometry of steel dies. After casting, air-drying was applied for 24 hours and alumina crucible was separated from steel dies. In order to obtain high strength and high thermal shock resistant alumina crucible, firing of the ceramic crucibles was conducted with controlled temperature increase in the furnace with specified time intervals. Table 3.8 shows the firing procedure of the crucibles.

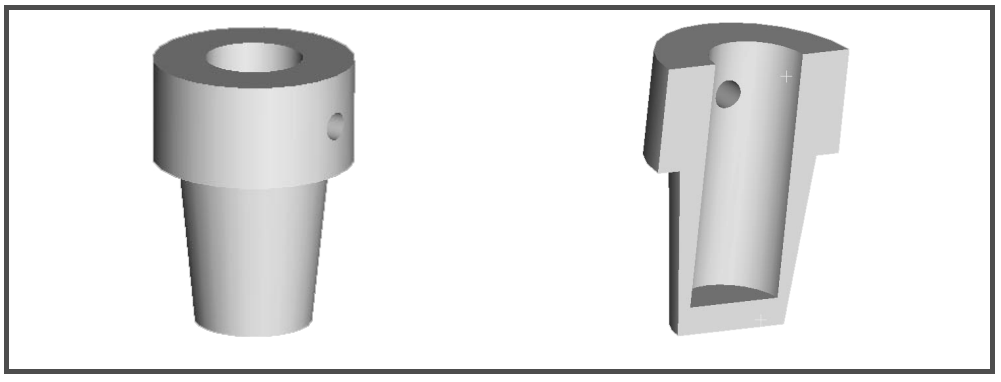

Figure 3.1 Schematic view of crucible.

Table 3.8 Firing procedure of the crucibles: temperatures and corresponding times.

Temperature	Time
~100° C	24 hours
~200° C	1-2 hours
~300° C	1-2 hours
~400° C	1-2 hours
~500° C	1-2 hours
~600° C	12 hours
~700° C	1-2 hours
~800° C	1-2 hours
~900° C	1-2 hours
~1000° C	1-2 hours

The furnace was shut down after the firing and, crucibles were allowed to cool in the furnace to room temperature. The thermal shock resistance of the produced crucibles was quite high, so each crucible could be used for approximately six or seven experiments.

3.2.2.2 Copper Mold

To cast the molten metal alloy, Cu-molds, which have a wedge-shape cavity, were used. As a mold material, copper was selected because of its high thermal conductivity, so that the heat removal from the melt is high which provides to attain high cooling rates. Moreover, the wedge-shaped inner cavity of these molds provides different thicknesses along the specimens' length. Figure 3.2 shows schematic view of Cu-molds and specimens.

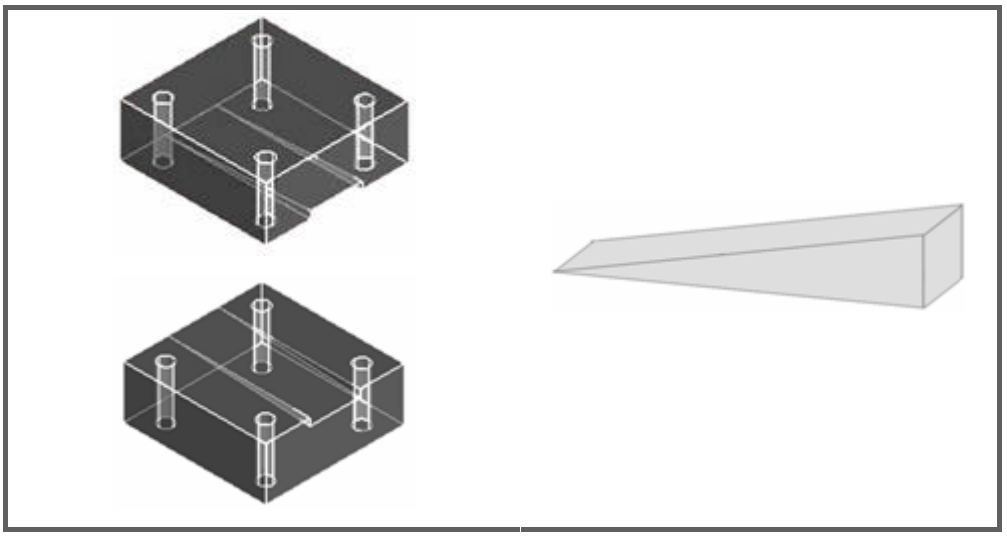

Figure 3.2 Schematic view of Cu-mold together with view of the wedge shaped cast sample.

The wedge-shaped cast specimens' geometry is consent to illustrate the influence of the different cooling rates on the solidification structures, with higher cooling rates in thin sections and lower cooling rate in thicker sections.

For casting, three different Cu-molds were used with identical wedge-shape geometry, but differ in sizes. The outer dimension of the Cu-molds, together with dimensions and the volume of the mold cavity are presented in Table 3.9.

Table 3.9 Dimensions of the Cu-molds and the mold cavity.

Mold	Outer Dimensions (mm)	Dimensions of the Mold Cavity (mm)	Surface area of the Mold Cavity (mm^2)	Volume of the Mold Cavity (mm^3)
M1	40 x 40 x 80	3x 13 x 55	1596	1072
M2	80 x 80 x 80	8x 30 x 70	4760	8400

3.2.2.3 Centrifugal Casting Machine

Centrifugal casting method is an important process for the extension of application field of amorphous alloy. Based on the principle of centrifugal force and taking into account the high glass-forming ability (GFA) of Fe-based alloys, centrifugal casting method was used in this study.

Before melting and casting operation, calculated amounts of alloying elements were weighed by SARTORIUS precision weighing balance and nearly 10-20 g amounts of the alloying elements, which amounts depend on the used mold capabilities, were mixed and put into the alumina crucible.

Melting and casting of the sample alloys was achieved in MANFREDI Multihertz Neutromag Digital centrifugal casting machine for production of bulk amorphous samples by forcing melt metal through inside of rotating copper wedge mold. The machine is capable of melting alloys whose melting temperature is lower than 2000°C by offering opportunity of melting and casting either in natural atmosphere, vacuum or neutral atmosphere (argon gas) by choosing a cycle by means of the special selector.

Alloying elements were heated to a melting temperature in the machine by induction heating under vacuumed condition that was created by blowing argon gas. During the heating, observation of the alloy was done from outside of machine and temperature was increased until the alloying elements were melted. The inside temperature of alumina crucible was read by the help of the pyrometer, which is assembled on the machine.

After melting of alloying elements, melt is injected into copper wedge mold generally to have high cooling rates necessary for formation of bulk amorphous alloy.

In the study, also, alumina crucible was used to see the near-equilibrium solidification microstructures of these alloys. After melting of alloying elements in alumina crucible, melt alloy was left in crucible without injection to copper wedge mold and cooled slowly until solidification temperature of alloy was passed over in casting machine. Then crucible was left to cool to room temperature.

3.2.3 Structural Characterization of Cast Alloys

After Fe-based alloys synthesized, microstructural and structural characterization of specimens, taken from the casting multi-component system, were performed by the help of the metallographic examination techniques, Differential Scanning Calorimeter (DSC), X-ray Diffraction Analysis (XRD) and Scanning Electron Microscope (SEM).

3.2.3.1 Microstructural Examination

Samples were cut from each cast alloy of different sections and mounted in a Bakelite support with diameter of 30 mm under the conditions of 3500-4000 psi pressure and 140°C temperatures. The samples were placed in a metallic disc for grinding and polishing. Table 3.10 and Table 3.11 show the details of grinding and polishing steps, respectively. After polishing, the samples were washed in water, cleaned with ethyl alcohol and dried. Various etching solutions were tried and, 2% and 5% of Nital solutions were determined for etching of cast alloys.

Table 3.10 Details of grinding steps.

Grinding	SiC-Paper #80	SiC-Paper #120	SiC-Paper #320	SiC-Paper #500	SiC-Paper #800
Speed (rpm)	250	250	250	250	250
Time (min)	~5	~3	~3	~3	~3

Table 3.11 Details of polishing steps.

Polishing	Diamond Paste 6mm	Diamond Paste 3mm	Diamond Paste 1mm
Lubricant	Blue	Blue	Blue
Speed(rpm)	200	200	200
Time (min)	~6	~6	~3

After the metallographic preparation, microstructures of the cast samples were examined both in optical microscope and JEOL JSM-6400 scanning electron microscope equipped with NORAN Series VI Micro analyzer system to learn compositional and structural information about the specimen.

By the help of the NORAN Six X-ray Micro analyzer System, the compositions of the phases were also examined both in terms of atomic and weight percentages of the elements that form the phase.

3.2.3.2 X-Ray Diffraction Analysis

In this study, PHILIPS PW 1320 DY 871 X-ray diffraction equipment was used at 30kV, 8 mA with 100 cps. Small fragments, taken from the thinner sections of the wedge cast specimens were investigated under Co K_α radiation.

Peak outputs of the X-ray diffraction technique for each sample were examined and existence of an amorphous structure was investigated. For crystalline or partially amorphous samples, each peak was investigated to identify the possible compound formation and crystalline phases.

3.2.3.3 Thermal Analysis

Thermal Analysis of the cast samples was conducted by using Differential Scanning Calorimetry (DSC) technique to determine the existence and extent of the amorphous phase.

In the experiments, SETARAM SETSYS 16/18 differential scanning calorimeter was used. 20-25 mg of representative samples was prepared. Then these samples were put into small high temperature Al_2O_3 crucible and heated with a rate of 20 ^{0}C/min under Ar gas purge to a temperature above the melting. Then, cooling was applied to a room temperature, which was followed by a second heating above melting temperature to determine various properties, such as melting temperature (T_m), crystallization temperature (T_x), glass transition temperature (T_g) and thermal stability of the cast specimens, reduced glass temperature (T_{rg}), supercooled liquid region (ΔT_x).

CHAPTER 4

RESULTS AND DISCUSSION

This study was carried out under two main part. First part covers the theoretical modeling of GFA of candidate Fe-based systems. By the help of these investigations, the potential candidates of Fe-based systems that have high glass forming ability were determined. Second part involves the experimental investigation to prove the results of the conducted theoretical modeling studies. In this chapter the results of these investigations will be presented and evaluated.

4.1 Theoretical Investigation of Glass Forming Ability of Fe-Based Alloys

In this study, in order to cover the requirement of a predictive model that identifies the alloy families, theoretical modeling of the glass forming ability of Fe-based alloys, in the frame of the atomistic and thermodynamic approach, was performed. This modeling was applied for 13 different binary compositions and, for each of these compositions, the effect of approximately 33 different ternary elements were investigated by the substitution of 1 at % of third alloying element for each of the constituent elements that form the binary system. The stages of the theoretical modeling studies were presented in section 3.1 of the Chapter 3. In the next sections the result of these studies will be presented.

4.1.1 Ordering Energy Investigations

As mentioned in section 2.2.2.3.1.1, a liquid alloy can be either an ordered alloy, where unlike atoms are preferred as nearest neighbours over like atoms, or a segregated alloy, where like atoms are preferred to pairs as nearest neighbours over unlike atoms. The formation of ordering in a liquid alloy, with high interatomic interactions between the A and B atoms, increase the tendency of compound formation, i.e intermetallic phase formation, which exhibits growth problems, and hence increase the glass forming ability. However, formation of segregating, which results from the high interactions between the A – A atoms and B – B atoms, favors the formation of clusters composed of A and B atoms separately, and hence may lead to a decrease in the glass forming ability by forming convenient sites for heterogeneous nucleation.

In addition, formation of the liquid with high ordering energies, and with high interatomic interactions on a short-range scale leads increase in packing density, decrease in the atomic diffusivity and increase in the viscosity, which results in high stability against crystallization of competiting crystalline phases and hence high glass forming ability.

By taking these into consideration and, the relations, mentioned in section 2.2.2.3, between the ordering energy and parameters related to glass forming ability, such as heat of mixing, viscosity, and critical cooling rate, it is consistent that an increase in the ordering energy of the alloy also increase the glass forming ability.

In these account, ordering energy investigations were performed to predict the glass forming ability of Fe-based systems. The ordering energy and interchange energy values of the binary Fe-B, Fe-Zr, Fe-Nb, Fe-C and Fe-Zr systems were calculated using electronic theory of alloys in pseudopotential approximation. In order to investigate the effect of the third alloying element addition, partial

ordering energy between the A – B, A – C, and B – C atomic pairs, and the interchange values of the ternary systems were also calculated.

In this section only the results of theoretical modeling studies for Fe-B system, which was selected for experimental investigations, are given, in atomic unit, from Table 4.1 to Table 4.6 and in SI units from Table 4.7 to Table 4.12. For other systems, the results will be given in Appendix B. In these tables, results of the ordering energy and regular interaction parameter calculations of the binary system were presented in first row, and for ternary systems these results were given in the consequent rows. In these tables, M denotes the third alloying element.

Table 4.1 Results of the ordering energy and interchange energy calculations for Fe82B17M1, in atomic unit (1 a.u. = 2 Ry = 27,2 eV).

Fe82B17M1						
M	W_{Fe-B} **a.u.**	W_{Fe-M} **a.u.**	W_{B-M} **a.u.**	$^{W}Fe-B$ **a.u.**	$^{W}Fe-M$ **a.u.**	$^{W}B-M$ **a.u.**
None	0,0480	-	-	-0,2882	-	-
Al	0,0486	-0,0009	0,0729	-0,2913	0,0051	-0,4375
Bi	0,0472	0,0928	0,1853	-0,2831	-0,5570	-1,1119
C	0,0485	0,0283	-0,0039	-0,2912	-0,1695	0,0233
Ca	0,0462	0,2183	0,4154	-0,2773	-1,3096	-2,4926
Co	0,0479	0,0037	0,0307	-0,2872	-0,0223	-0,1842
Cr	0,0480	0,0010	0,0521	-0,2881	-0,0060	-0,3128
Cu	0,0477	-0,0073	0,0135	-0,2859	0,0439	-0,0813
Ga	0,0476	-0,0051	0,0479	-0,2857	0,0305	-0,2876
Ge	0,0476	-0,0041	0,0650	-0,2859	0,0244	-0,3898
Hf	0,0477	0,0400	0,1983	-0,2860	-0,2402	-1,1898
K	0,0447	-0,0054	0,0474	-0,2682	0,0325	-0,2841
Mg	0,0472	0,0141	0,0848	-0,2835	-0,0846	-0,5086
Mo	0,0484	0,0562	0,3124	-0,2904	-0,3370	-1,8741
Na	0,0463	0,0207	0,0649	-0,2779	-0,1242	-0,3893
Nb	0,0481	0,0643	0,2731	-0,2885	-0,3860	-1,6383
P	0,0479	-0,0219	0,0407	-0,2872	0,1313	-0,2442
Pb	0,0473	0,0588	0,1105	-0,2836	-0,3526	-0,6632
Pd	0,0477	0,0021	0,0695	-0,2861	-0,0126	-0,4168
Pt	0,0477	0,0021	0,0046	-0,2860	-0,0125	-0,0277
Re	0,0486	0,0947	0,3348	-0,2918	-0,5681	-2,0090
Se	0,0478	-0,0018	0,0788	-0,2867	0,0109	-0,4726
Si	0,0478	-0,0115	0,0628	-0,2867	0,0691	-0,3771
Ta	0,0481	0,0562	0,2571	-0,2885	-0,3370	-1,5429
W	0,0484	0,1029	0,3288	-0,2903	-0,6172	-1,9728
Y	0,0469	0,0137	0,1474	-0,2816	-0,0820	-0,8843
Zr	0,0476	0,0514	0,2320	-0,2857	-0,3081	-1,3919

Table 4.2 Results of the ordering energy and interchange energy calculations for Fe83B16M1, in atomic unit.

Fe82B17M1						
M	**W_{Fe-B} a.u.**	**W_{Fe-M} a.u.**	**W_{B-M} a.u.**	**$^{W}Fe-B$ a.u.**	**$^{W}Fe-M$ a.u.**	**$^{W}B-M$ a.u.**
None	0,0480	-	-	-0,2882	-	-
Al	0,0483	-0,0008	0,0728	-0,2900	0,0048	-0,4368
Bi	0,0470	0,0923	0,1850	-0,2818	-0,5536	-1,1100
C	0,0485	0,0282	-0,0039	-0,2912	-0,1689	0,0236
Ca	0,0460	0,2166	0,4125	-0,2761	-1,2994	-2,4749
Co	0,0477	0,0037	0,0304	-0,2859	-0,0223	-0,1825
Cr	0,0478	0,0010	0,0518	-0,2868	-0,0059	-0,3105
Cu	0,0474	-0,0074	0,0133	-0,2846	0,0441	-0,0796
Ga	0,0474	-0,0051	0,0479	-0,2844	0,0306	-0,2871
Ge	0,0474	-0,0041	0,0649	-0,2846	0,0245	-0,3895
Hf	0,0475	0,0400	0,1983	-0,2847	-0,2400	-1,1900
K	0,0445	-0,0059	0,0460	-0,2671	0,0354	-0,2761
Mg	0,0470	0,0141	0,0844	-0,2822	-0,0847	-0,5064
Mo	0,0482	0,0909	0,3126	-0,2891	-0,5455	-1,8754
Na	0,0461	0,0206	0,0642	-0,2767	-0,1233	-0,3849
Nb	0,0481	0,0645	0,2733	-0,2885	-0,3870	-1,6400
P	0,0476	-0,0220	0,0407	-0,2859	0,1318	-0,2444
Pb	0,0471	0,0584	0,1103	-0,2823	-0,3501	-0,6619
Pd	0,0475	0,0019	0,0686	-0,2848	-0,0112	-0,4116
Pt	0,0475	0,0020	0,0046	-0,2847	-0,0120	-0,0275
Re	0,0484	0,0947	0,3351	-0,2904	-0,5684	-2,0109
Se	0,0476	-0,0021	0,0787	-0,2854	0,0124	-0,4725
Si	0,0476	-0,0115	0,0628	-0,2854	0,0689	-0,3770
Ta	0,0479	0,0563	0,2574	-0,2872	-0,3378	-1,5444
W	0,0482	0,1029	0,3290	-0,2890	-0,6173	-1,9741
Y	0,0467	0,0137	0,1474	-0,2803	-0,0822	-0,8845
Zr	0,0474	0,0514	0,2321	-0,2844	-0,3085	-1,3926

Table 4.3 Results of the ordering energy and interchange energy calculations for Fe74B25M1, in atomic unit.

Fe74B25M1						
M	W_{Fe-B}	W_{Fe-M}	W_{B-M}	w_{Fe-B}	w_{Fe-M}	w_{B-M}
	a.u.	**a.u.**	**a.u.**	**a.u.**	**a.u.**	**a.u.**
None	0,0497	-	-	-5,7583	-	-
Al	0,0503	-0,0010	0,0751	-5,8243	0,1148	-8,7043
Bi	0,0488	0,0988	0,1917	-5,6494	-11,4473	-22,2098
C	0,0502	0,0292	-0,0038	-5,8201	-3,3818	0,4437
Ca	0,0477	0,2286	0,4333	-5,5321	-26,4905	-50,2065
Co	0,0495	0,0040	0,0320	-5,7394	-0,4581	-3,7049
Cr	0,0497	0,0012	0,0550	-5,7566	-0,1354	-6,3769
Cu	0,0493	-0,0072	0,0137	-5,7122	0,8308	-1,5851
Ga	0,0493	-0,0051	0,0494	-5,7067	0,5936	-5,7290
Ge	0,0493	-0,0041	0,0669	-5,7092	0,4734	-7,7571
Hf	0,0493	0,0418	0,2030	-5,7124	-4,8385	-23,5236
K	0,0461	-0,0062	0,0475	-5,3420	0,7130	-5,4998
Mg	0,0489	0,0146	0,0876	-5,6606	-1,6898	-10,1460
Mn	0,0495	-0,0005	0,0406	-5,7329	0,0599	-4,7087
Mo	0,0501	0,0956	0,3217	-5,8023	-11,0743	-37,2731
Na	0,0479	0,0212	0,0666	-5,5451	-2,4544	-7,7185
Nb	0,0497	0,0667	0,2800	-5,7632	-7,7242	-32,4452
Ni	0,0495	0,0041	0,0316	-5,7404	-0,4715	-3,6580
P	0,0495	-0,0223	0,0423	-5,7358	2,5836	-4,9009
Pb	0,0489	0,0628	0,1139	-5,6614	-7,2799	-13,1936
Pd	0,0493	0,0029	0,0731	-5,7157	-0,3320	-8,4699
Pt	0,0493	0,0025	0,0049	-5,7134	-0,2912	-0,5708
Re	0,0503	0,0997	0,3455	-5,8301	-11,5549	-40,0390
Se	0,0494	-0,0005	0,0821	-5,7257	0,0636	-9,5174
Si	0,0494	-0,0119	0,0648	-5,7260	1,3790	-7,5062
Sn	0,0490	0,0142	0,1207	-5,6818	-1,6440	-13,9876
Ta	0,0497	0,0584	0,2638	-5,7632	-6,7642	-30,5632
Ti	0,0496	-0,0024	0,0436	-5,7422	0,2834	-5,0474
V	0,0500	-0,0076	0,0490	-5,7896	0,8826	-5,6721
W	0,0501	0,1074	0,3384	-5,8004	-12,4461	-39,2099
Y	0,0485	0,0141	0,1502	-5,6202	-1,6386	-17,4060
Zn	0,0493	0,0051	0,0248	-5,7132	-0,5889	-2,8768
Zr	0,0492	0,0530	0,2373	-5,7059	-6,1448	-27,4949

Table 4.4 Results of the ordering energy and interchange energy calculations for Fe75B24M1, in atomic unit.

Fe75B24M1						
M	**W_{Fe-B} a.u.**	**W_{Fe-M} a.u.**	**W_{B-M} a.u.**	**$^{W}Fe-B$ a.u.**	**$^{W}Fe-M$ a.u.**	**$^{W}B-M$ a.u.**
None	0,0497	-	-	-0,2194	-	-
Al	0,0500	-0,0009	0,0750	0,0041	0,0041	-0,3310
Bi	0,0485	0,0982	0,1913	-0,4334	-0,4334	-0,8448
C	0,0500	0,0291	-0,0039	-0,1284	-0,1284	0,0172
Ca	0,0475	0,2268	0,4301	-1,0012	-1,0012	-1,8988
Co	0,0493	0,0039	0,0317	-0,0174	-0,0174	-0,1398
Cr	0,0494	0,0011	0,0546	-0,0051	-0,0051	-0,2411
Cu	0,0491	-0,0072	0,0134	0,0318	0,0318	-0,0590
Ga	0,0490	-0,0051	0,0494	0,0227	0,0227	-0,2179
Ge	0,0490	-0,0041	0,0669	0,0181	0,0181	-0,2953
Hf	0,0491	0,0417	0,2030	-0,1841	-0,1841	-0,8964
K	0,0459	-0,0067	0,0460	0,0295	0,0295	-0,2033
Mg	0,0486	0,0146	0,0872	-0,0644	-0,0644	-0,3848
Mn	0,0492	-0,0005	0,0404	0,0023	0,0023	-0,1782
Mo	0,0498	0,0955	0,3219	-0,4217	-0,4217	-1,4212
Na	0,0476	0,0210	0,0658	-0,0928	-0,0928	-0,2906
Nb	0,0495	0,0668	0,2803	-0,2951	-0,2951	-1,2375
Ni	0,0493	0,0041	0,0313	-0,0179	-0,0179	-0,1380
P	0,0493	-0,0224	0,0423	0,0989	0,0989	-0,1869
Pb	0,0486	0,0624	0,1136	-0,2754	-0,2754	-0,5017
Pd	0,0491	0,0026	0,0722	-0,0116	-0,0116	-0,3186
Pt	0,0491	0,0024	0,0049	-0,0107	-0,0107	-0,0216
Re	0,0501	0,0998	0,3459	-0,4405	-0,4405	-1,5271
Se	0,0492	-0,0008	0,0821	0,0036	0,0036	-0,3626
Si	0,0492	-0,0119	0,0648	0,0524	0,0524	-0,2859
Sn	0,0488	0,0142	0,1206	-0,0625	-0,0625	-0,5325
Ta	0,0495	0,0585	0,2640	-0,2583	-0,2583	-1,1657
Ti	0,0493	-0,0025	0,0435	0,0110	0,0110	-0,1920
V	0,0497	-0,0076	0,0488	0,0338	0,0338	-0,2155
W	0,0498	0,1074	0,3386	-0,4743	-0,4743	-1,4950
Y	0,0483	0,0142	0,1503	-0,0626	-0,0626	-0,6634
Zn	0,0491	0,0051	0,0247	-0,0224	-0,0224	-0,1088
Zr	0,0490	0,0531	0,2374	-0,2344	-0,2344	-1,0482

Table 4.5 Results of the ordering energy and interchange energy calculations for Fe66B33M1, in atomic unit.

Fe66B33M1						
M	**W_{Fe-B} a.u.**	**W_{Fe-M} a.u.**	**W_{B-M} a.u.**	**$^{W}Fe-B$ a.u.**	**$^{W}Fe-M$ a.u.**	**$^{W}B-M$ a.u.**
None	0,0514	-	-	-0,2210	-	-
Al	0,0520	-0,0007	0,0795	-0,2237	0,0029	-0,3420
Bi	0,0503	0,1074	0,2041	-0,2164	-0,4617	-0,8777
C	0,0520	0,0305	-0,0044	-0,2235	-0,1312	0,0189
Ca	0,0492	0,2359	0,4454	-0,2116	-1,0145	-1,9154
Co	0,0512	0,0045	0,0321	-0,2202	-0,0193	-0,1379
Cr	0,0514	0,0014	0,0580	-0,2209	-0,0060	-0,2493
Cu	0,0510	-0,0072	0,0107	-0,2191	0,0310	-0,0461
Ga	0,0509	-0,0048	0,0526	-0,2188	0,0205	-0,2261
Ge	0,0509	-0,0043	0,0714	-0,2189	0,0185	-0,3069
Hf	0,0509	0,0454	0,2155	-0,2190	-0,1954	-0,9268
K	0,0474	-0,0141	0,0317	-0,2038	0,0606	-0,1364
Mg	0,0505	0,0160	0,0908	-0,2169	-0,0688	-0,3905
Mn	0,0511	-0,0004	0,0407	-0,2199	0,0019	-0,1749
Mo	0,0518	0,1064	0,3479	-0,2227	-0,4573	-1,4960
Na	0,0493	0,0208	0,0626	-0,2122	-0,0894	-0,2693
Nb	0,0514	0,0743	0,3012	-0,2211	-0,3193	-1,2953
Ni	0,0512	0,0046	0,0316	-0,2203	-0,0198	-0,1361
P	0,0512	-0,0245	0,0468	-0,2200	0,1053	-0,2012
Pb	0,0504	0,0687	0,1197	-0,2169	-0,2952	-0,5149
Pd	0,0510	0,0021	0,0721	-0,2192	-0,0090	-0,3100
Pt	0,0510	0,0025	0,0054	-0,2191	-0,0109	-0,0230
Re	0,0521	0,1127	0,3765	-0,2238	-0,4844	-1,6191
Se	0,0511	-0,0004	0,0905	-0,2195	0,0015	-0,3892
Si	0,0511	-0,0126	0,0697	-0,2196	0,0542	-0,2996
Sn	0,0506	0,0155	0,1277	-0,2178	-0,0667	-0,5493
Ta	0,0514	0,0652	0,2839	-0,2211	-0,2805	-1,2206
Ti	0,0512	-0,0029	0,0466	-0,2203	0,0124	-0,2005
V	0,0517	-0,0081	0,0528	-0,2222	0,0349	-0,2272
W	0,0518	0,1189	0,3652	-0,2226	-0,5112	-1,5706
Y	0,0501	0,0156	0,1583	-0,2152	-0,0671	-0,6805
Zn	0,0510	0,0057	0,0251	-0,2191	-0,0245	-0,1078
Zr	0,0509	0,0579	0,2525	-0,2188	-0,2492	-1,0856

Table 4.6 Results of the ordering energy and interchange energy calculations for Fe67B32M1, in atomic unit.

Fe67B32M1						
M	**W_{Fe-B} a.u.**	**W_{Fe-M} a.u.**	**W_{B-M} a.u.**	**w_{Fe-B} a.u.**	**w_{Fe-M} a.u.**	**w_{B-M} a.u.**
None	0,0514	-	-	-0,2210	-	-
Al	0,0518	-0,0006	0,0794	-0,2225	0,0026	-0,3412
Bi	0,0501	0,1067	0,2038	-0,2153	-0,4587	-0,8762
C	0,0517	0,0304	-0,0044	-0,2223	-0,1307	0,0191
Ca	0,0490	0,2338	0,4418	-0,2105	-1,0054	-1,8996
Co	0,0509	0,0045	0,0317	-0,2191	-0,0192	-0,1365
Cr	0,0511	0,0014	0,0575	-0,2197	-0,0059	-0,2473
Cu	0,0507	-0,0073	0,0104	-0,2180	0,0312	-0,0446
Ga	0,0506	-0,0053	0,0525	-0,2177	0,0230	-0,2256
Ge	0,0506	-0,0043	0,0713	-0,2178	0,0186	-0,3066
Hf	0,0507	0,0454	0,2155	-0,2179	-0,1952	-0,9268
K	0,0472	-0,0146	0,0302	-0,2028	0,0629	-0,1298
Mg	0,0502	0,0160	0,0903	-0,2158	-0,0688	-0,3884
Mn	0,0509	-0,0004	0,0404	-0,2188	0,0019	-0,1735
Mo	0,0515	0,1063	0,3482	-0,2216	-0,4571	-1,4971
Na	0,0491	0,0206	0,0617	-0,2111	-0,0887	-0,2655
Nb	0,0512	0,0744	0,3015	-0,2200	-0,3201	-1,2965
Ni	0,0510	0,0046	0,0313	-0,2191	-0,0198	-0,1346
P	0,0509	-0,0246	0,0468	-0,2188	0,1058	-0,2013
Pb	0,0502	0,0681	0,1195	-0,2158	-0,2930	-0,5139
Pd	0,0507	0,0018	0,0710	-0,2181	-0,0078	-0,3055
Pt	0,0507	0,0024	0,0053	-0,2180	-0,0105	-0,0228
Re	0,0518	0,1127	0,3769	-0,2227	-0,4847	-1,6207
Se	0,0508	-0,0007	0,0905	-0,2184	0,0028	-0,3891
Si	0,0508	-0,0126	0,0696	-0,2185	0,0541	-0,2995
Sn	0,0504	0,0155	0,1276	-0,2166	-0,0666	-0,5487
Ta	0,0512	0,0654	0,2841	-0,2200	-0,2812	-1,2218
Ti	0,0510	-0,0029	0,0465	-0,2191	0,0127	-0,2001
V	0,0514	-0,0081	0,0527	-0,2211	0,0350	-0,2265
W	0,0515	0,1189	0,3655	-0,2215	-0,5113	-1,5715
Y	0,0498	0,0156	0,1583	-0,2141	-0,0672	-0,6806
Zn	0,0507	0,0057	0,0249	-0,2180	-0,0245	-0,1069
Zr	0,0506	0,0580	0,2526	-0,2176	-0,2495	-1,0861

Table 4.7 Results of the ordering energy and interchange energy calculations for Fe82B17M1, in SI units.

Fe82B17M1						
M	**W_{Fe-B} J/mol x10^5**	**W_{Fe-M} J/mol x10^5**	**W_{B-M} J/mol x10^5**	**$^{W}Fe-B$ J/mol x10^5**	**$^{W}Fe-M$ J/mol x10^5**	**$^{W}B-M$ J/mol x10^5**
None	1,2606	-	-	-7,5634	-	-
Al	1,2743	-0,0224	1,9138	-7,6461	0,1342	-11,4830
Bi	1,2381	2,4366	4,8634	-7,4286	-14,6196	-29,1805
C	1,2736	0,7414	-0,1020	-7,6415	-4,4485	0,6122
Ca	1,2131	5,7283	10,9028	-7,2789	-34,3695	-65,4169
Co	1,2564	0,0977	0,8056	-7,5387	-0,5863	-4,8335
Cr	1,2602	0,0263	1,3683	-7,5612	-0,1581	-8,2098
Cu	1,2506	-0,1921	0,3556	-7,5039	1,1525	-2,1335
Ga	1,2498	-0,1336	1,2578	-7,4987	0,8015	-7,5469
Ge	1,2505	-0,1069	1,7052	-7,5028	0,6415	-10,2314
Hf	1,2511	1,0507	5,2044	-7,5067	-6,3043	-31,2261
K	1,1733	-0,1420	1,2427	-7,0395	0,8521	-7,4562
Mg	1,2400	0,3701	2,2248	-7,4399	-2,2208	-13,3485
Mo	1,2702	1,4741	8,1977	-7,6213	-8,8447	-49,1861
Na	1,2157	0,5431	1,7027	-7,2943	-3,2587	-10,2163
Nb	1,2619	1,6883	7,1663	-7,5713	-10,1298	-42,9979
P	1,2561	-0,5742	1,0683	-7,5368	3,4454	-6,4098
Pb	1,2405	1,5422	2,9008	-7,4428	-9,2532	-17,4049
Pd	1,2515	0,0550	1,8232	-7,5091	-0,3302	-10,9391
Pt	1,2510	0,0546	0,1211	-7,5062	-0,3274	-0,7266
Re	1,2762	2,4850	8,7875	-7,6569	-14,9100	-52,7248
Se	1,2542	-0,0477	2,0671	-7,5251	0,2864	-12,4026
Si	1,2540	-0,3022	1,6494	-7,5237	1,8131	-9,8965
Ta	1,2619	1,4741	6,7488	-7,5713	-8,8447	-40,4929
W	1,2698	2,6996	8,6295	-7,6188	-16,1974	-51,7768
Y	1,2317	0,3585	3,8678	-7,3902	-2,1509	-23,2070
Zr	1,2498	1,3477	6,0882	-7,4985	-8,0862	-36,5294

Table 4.8 Results of the ordering energy and interchange energy calculations for Fe83B16M1, in SI units.

Fe83B16M1						
M	W_{Fe-B} **J/mol x10^5**	W_{Fe-M} **J/mol x10^5**	W_{B-M} **J/mol x10^5**	w_{Fe-B} **J/mol x10^5**	w_{Fe-M} **J/mol x10^5**	w_{B-M} **J/mol x10^5**
None	1,2606	-	-	-7,5634	-	-
Al	1,2685	-0,0209	1,9105	-7,6108	0,1255	-11,4633
Bi	1,2325	2,4217	4,8553	-7,3952	-14,5300	-29,1316
C	1,2736	0,7388	-0,1034	-7,6415	-4,4331	0,6204
Ca	1,2077	5,6837	10,8253	-7,2464	-34,1022	-64,9521
Co	1,2507	0,0976	0,7983	-7,5042	-0,5853	-4,7899
Cr	1,2544	0,0259	1,3582	-7,5266	-0,1554	-8,1492
Cu	1,2449	-0,1930	0,3481	-7,4695	1,1580	-2,0884
Ga	1,2441	-0,1337	1,2559	-7,4645	0,8025	-7,5352
Ge	1,2448	-0,1073	1,7037	-7,4688	0,6437	-10,2223
Hf	1,2454	1,0496	5,2052	-7,4727	-6,2977	-31,2313
K	1,1682	-0,1550	1,2079	-7,0090	0,9299	-7,2474
Mg	1,2344	0,3703	2,2152	-7,4062	-2,2217	-13,2915
Mo	1,2645	2,3863	8,2034	-7,5867	-14,3176	-49,2203
Na	1,2103	0,5394	1,6837	-7,2617	-3,2365	-10,1021
Nb	1,2619	1,6926	7,1737	-7,5713	-10,1557	-43,0420
P	1,2504	-0,5766	1,0692	-7,5026	3,4594	-6,4151
Pb	1,2349	1,5315	2,8951	-7,4092	-9,1888	-17,3706
Pd	1,2458	0,0490	1,8002	-7,4747	-0,2938	-10,8013
Pt	1,2453	0,0524	0,1202	-7,4719	-0,3145	-0,7212
Re	1,2704	2,4863	8,7958	-7,6221	-14,9178	-52,7748
Se	1,2485	-0,0544	2,0667	-7,4911	0,3263	-12,4002
Si	1,2483	-0,3014	1,6490	-7,4895	1,8087	-9,8939
Ta	1,2562	1,4775	6,7556	-7,5369	-8,8650	-40,5338
W	1,2640	2,7001	8,6348	-7,5842	-16,2007	-51,8091
Y	1,2262	0,3593	3,8691	-7,3570	-2,1561	-23,2146
Zr	1,2441	1,3496	6,0914	-7,4645	-8,0974	-36,5484

Table 4.9 Results of the ordering energy and interchange energy calculations for Fe74B25M1, in SI units.

Fe74B25M1						
M	W_{Fe-B} **J/mol x10^5**	W_{Fe-M} **J/mol x10^5**	W_{B-M} **J/mol x10^5**	w_{Fe-B} **J/mol x10^5**	w_{Fe-M} **J/mol x10^5**	w_{B-M} **J/mol x10^5**
None	1,3042	-	-	-5,7583	-	-
Al	1,3192	-0,0260	1,9715	-5,8243	0,1148	-8,7043
Bi	1,2796	2,5928	5,0305	-5,6494	-11,4473	-22,2098
C	1,3182	0,7660	-0,1005	-5,8201	-3,3818	0,4437
Ca	1,2530	6,0001	11,3718	-5,5321	-26,4905	-50,2065
Co	1,3000	0,1038	0,8392	-5,7394	-0,4581	-3,7049
Cr	1,3039	0,0307	1,4444	-5,7566	-0,1354	-6,3769
Cu	1,2938	-0,1882	0,3590	-5,7122	0,8308	-1,5851
Ga	1,2926	-0,1345	1,2976	-5,7067	0,5936	-5,7290
Ge	1,2931	-0,1072	1,7570	-5,7092	0,4734	-7,7571
Hf	1,2939	1,0959	5,3281	-5,7124	-4,8385	-23,5236
K	1,2100	-0,1615	1,2457	-5,3420	0,7130	-5,4998
Mg	1,2821	0,3827	2,2981	-5,6606	-1,6898	-10,1460
Mn	1,2985	-0,0136	1,0665	-5,7329	0,0599	-4,7087
Mo	1,3142	2,5083	8,4424	-5,8023	-11,0743	-37,2731
Na	1,2560	0,5559	1,7482	-5,5451	-2,4544	-7,7185
Nb	1,3054	1,7495	7,3488	-5,7632	-7,7242	-32,4452
Ni	1,3002	0,1068	0,8285	-5,7404	-0,4715	-3,6580
P	1,2992	-0,5852	1,1101	-5,7358	2,5836	-4,9009
Pb	1,2823	1,6489	2,9884	-5,6614	-7,2799	-13,1936
Pd	1,2946	0,0752	1,9184	-5,7157	-0,3320	-8,4699
Pt	1,2941	0,0659	0,1293	-5,7134	-0,2912	-0,5708
Re	1,3205	2,6172	9,0689	-5,8301	-11,5549	-40,0390
Se	1,2969	-0,0144	2,1557	-5,7257	0,0636	-9,5174
Si	1,2969	-0,3123	1,7002	-5,7260	1,3790	-7,5062
Sn	1,2869	0,3724	3,1682	-5,6818	-1,6440	-13,9876
Ta	1,3054	1,5321	6,9226	-5,7632	-6,7642	-30,5632
Ti	1,3006	-0,0642	1,1432	-5,7422	0,2834	-5,0474
V	1,3113	-0,1999	1,2847	-5,7896	0,8826	-5,6721
W	1,3138	2,8191	8,8811	-5,8004	-12,4461	-39,2099
Y	1,2730	0,3712	3,9425	-5,6202	-1,6386	-17,4060
Zn	1,2940	0,1334	0,6516	-5,7132	-0,5889	-2,8768
Zr	1,2924	1,3918	6,2276	-5,7059	-6,1448	-27,4949

Table 4.10 Results of the ordering energy and interchange energy calculations for Fe75B24M1, in SI units.

Fe75B24M1						
M	**W_{Fe-B} J/mol x10^5**	**W_{Fe-M} J/mol x10^5**	**W_{B-M} J/mol x10^5**	**$^{W}Fe-B$ J/mol x10^5**	**$^{W}Fe-M$ J/mol x10^5**	**$^{W}B-M$ J/mol x10^5**
None	1,3042	-	-	-5,7583	-	-
Al	1,3128	-0,0244	1,9679	-5,7961	0,1079	-8,6882
Bi	1,2736	2,5766	5,0219	-5,6228	-11,3758	-22,1718
C	1,3119	0,7631	-0,1020	-5,7919	-3,3693	0,4502
Ca	1,2471	5,9517	11,2874	-5,5061	-26,2766	-49,8340
Co	1,2937	0,1036	0,8312	-5,7117	-0,4575	-3,6699
Cr	1,2976	0,0302	1,4334	-5,7289	-0,1332	-6,3282
Cu	1,2876	-0,1891	0,3509	-5,6848	0,8349	-1,5494
Ga	1,2864	-0,1347	1,2954	-5,6794	0,5946	-5,7194
Ge	1,2870	-0,1076	1,7553	-5,6820	0,4750	-7,7497
Hf	1,2877	1,0946	5,3289	-5,6852	-4,8325	-23,5270
K	1,2044	-0,1751	1,2085	-5,3176	0,7730	-5,3354
Mg	1,2760	0,3828	2,2876	-5,6336	-1,6903	-10,0997
Mn	1,2923	-0,0137	1,0591	-5,7053	0,0606	-4,6759
Mo	1,3080	2,5069	8,4483	-5,7746	-11,0679	-37,2994
Na	1,2488	0,5519	1,7276	-5,5135	-2,4368	-7,6273
Nb	1,2991	1,7539	7,3565	-5,7357	-7,7436	-32,4791
Ni	1,2940	0,1066	0,8206	-5,7129	-0,4708	-3,6231
P	1,2930	-0,5877	1,1111	-5,7085	2,5945	-4,9054
Pb	1,2762	1,6373	2,9824	-5,6346	-7,2287	-13,1673
Pd	1,2884	0,0687	1,8936	-5,6882	-0,3032	-8,3603
Pt	1,2879	0,0637	0,1283	-5,6860	-0,2812	-0,5664
Re	1,3142	2,6185	9,0778	-5,8022	-11,5607	-40,0783
Se	1,2907	-0,0215	2,1553	-5,6986	0,0951	-9,5159
Si	1,2907	-0,3115	1,6997	-5,6987	1,3754	-7,5040
Sn	1,2808	0,3718	3,1654	-5,6549	-1,6415	-13,9755
Ta	1,2991	1,5355	6,9297	-5,7357	-6,7793	-30,5947
Ti	1,2944	-0,0655	1,1414	-5,7148	0,2890	-5,0395
V	1,3050	-0,2007	1,2808	-5,7618	0,8861	-5,6549
W	1,3075	2,8195	8,8867	-5,7727	-12,4479	-39,2348
Y	1,2670	0,3719	3,9436	-5,5937	-1,6418	-17,4111
Zn	1,2878	0,1333	0,6470	-5,6857	-0,5884	-2,8564
Zr	1,2862	1,3936	6,2308	-5,6787	-6,1526	-27,5091

Table 4.11 Results of the ordering energy and interchange energy calculations for Fe66B33M1, in SI units.

Fe66B33M1						
M	**W_{Fe-B} J/mol x10^5**	**W_{Fe-M} J/mol x10^5**	**W_{B-M} J/mol x10^5**	**w_{Fe-B} J/mol x10^5**	**w_{Fe-M} J/mol x10^5**	**w_{B-M} J/mol x10^5**
None	1,3487	-	-	-5,7993	-	-
Al	1,3655	-0,0177	2,0872	-5,8715	0,0761	-8,9749
Bi	1,3207	2,8181	5,3572	-5,6790	-12,1180	-23,0358
C	1,3642	0,8009	-0,1152	-5,8662	-3,4438	0,4955
Ca	1,2915	6,1920	11,6907	-5,5535	-26,6256	-50,2702
Co	1,3440	0,1175	0,8418	-5,7794	-0,5054	-3,6199
Cr	1,3482	0,0369	1,5218	-5,7975	-0,1586	-6,5437
Cu	1,3373	-0,1894	0,2813	-5,7505	0,8143	-1,2096
Ga	1,3356	-0,1252	1,3798	-5,7430	0,5384	-5,9333
Ge	1,3361	-0,1129	1,8731	-5,7451	0,4856	-8,0545
Hf	1,3368	1,1927	5,6565	-5,7484	-5,1287	-24,3228
K	1,2437	-0,3697	0,8324	-5,3478	1,5898	-3,5795
Mg	1,3241	0,4198	2,3833	-5,6935	-1,8051	-10,2480
Mn	1,3424	-0,0113	1,0674	-5,7723	0,0488	-4,5900
Mo	1,3593	2,7913	9,1311	-5,8451	-12,0027	-39,2635
Na	1,2950	0,5459	1,6438	-5,5684	-2,3475	-7,0682
Nb	1,3496	1,9488	7,9056	-5,8031	-8,3797	-33,9942
Ni	1,3443	0,1210	0,8305	-5,7806	-0,5201	-3,5710
P	1,3426	-0,6430	1,2278	-5,7732	2,7649	-5,2795
Pb	1,3239	1,8019	3,1427	-5,6928	-7,7483	-13,5136
Pd	1,3380	0,0549	1,8923	-5,7536	-0,2359	-8,1367
Pt	1,3375	0,0665	0,1405	-5,7511	-0,2859	-0,6043
Re	1,3662	2,9567	9,8822	-5,8747	-12,7137	-42,4933
Se	1,3399	-0,0094	2,3753	-5,7616	0,0403	-10,2138
Si	1,3403	-0,3310	1,8286	-5,7634	1,4235	-7,8631
Sn	1,3291	0,4072	3,3525	-5,7151	-1,7510	-14,4156
Ta	1,3496	1,7122	7,4500	-5,8031	-7,3625	-32,0350
Ti	1,3444	-0,0759	1,2236	-5,7809	0,3263	-5,2616
V	1,3563	-0,2130	1,3866	-5,8320	0,9159	-5,9624
W	1,3589	3,1202	9,5858	-5,8431	-13,4169	-41,2190
Y	1,3136	0,4096	4,1535	-5,6486	-1,7613	-17,8602
Zn	1,3374	0,1496	0,6578	-5,7508	-0,6433	-2,8285
Zr	1,3352	1,5207	6,6261	-5,7413	-6,5392	-28,4921

Table 4.12 Results of the ordering energy and interchange energy calculations for Fe67B32M1, in SI units.

Fe67B32M1						
M	**W_{Fe-B} J/mol x10^5**	**W_{Fe-M} J/mol x10^5**	**W_{B-M} J/mol x10^5**	**w_{Fe-B} J/mol x10^5**	**w_{Fe-M} J/mol x10^5**	**w_{B-M} J/mol x10^5**
None	1,3487	-	-	-5,7993	-	-
Al	1,3583	-0,0160	2,0825	-5,8406	0,0688	-8,9549
Bi	1,3139	2,7998	5,3479	-5,6498	-12,0393	-22,9959
C	1,3571	0,7975	-0,1167	-5,8353	-3,4294	0,5020
Ca	1,2849	6,1364	11,5941	-5,5251	-26,3864	-49,8547
Co	1,3370	0,1174	0,8329	-5,7491	-0,5048	-3,5814
Cr	1,3412	0,0363	1,5093	-5,7671	-0,1560	-6,4899
Cu	1,3303	-0,1903	0,2723	-5,7204	0,8184	-1,1707
Ga	1,3286	-0,1403	1,3771	-5,7132	0,6034	-5,9216
Ge	1,3291	-0,1133	1,8711	-5,7152	0,4872	-8,0458
Hf	1,3299	1,1913	5,6569	-5,7186	-5,1225	-24,3245
K	1,2375	-0,3840	0,7922	-5,3212	1,6512	-3,4063
Mg	1,3172	0,4197	2,3708	-5,6639	-1,8045	-10,1943
Mn	1,3354	-0,0115	1,0590	-5,7421	0,0496	-4,5538
Mo	1,3522	2,7901	9,1373	-5,8147	-11,9974	-39,2903
Na	1,2883	0,5415	1,6205	-5,5398	-2,3283	-6,9684
Nb	1,3425	1,9537	7,9134	-5,7729	-8,4010	-34,0274
Ni	1,3373	0,1208	0,8215	-5,7503	-0,5194	-3,5323
P	1,3356	-0,6455	1,2288	-5,7433	2,7757	-5,2840
Pb	1,3171	1,7885	3,1364	-5,6635	-7,6906	-13,4864
Pd	1,3310	0,0477	1,8646	-5,7235	-0,2050	-8,0176
Pt	1,3305	0,0642	0,1393	-5,7210	-0,2760	-0,5991
Re	1,3591	2,9585	9,8917	-5,8441	-12,7218	-42,5342
Se	1,3330	-0,0171	2,3750	-5,7318	0,0737	-10,2123
Si	1,3334	-0,3301	1,8278	-5,7334	1,4193	-7,8594
Sn	1,3222	0,4066	3,3492	-5,6855	-1,7484	-14,4015
Ta	1,3425	1,7161	7,4572	-5,7729	-7,3793	-32,0661
Ti	1,3374	-0,0773	1,2215	-5,7508	0,3322	-5,2527
V	1,3492	-0,2138	1,3824	-5,8015	0,9195	-5,9443
W	1,3518	3,1209	9,5916	-5,8127	-13,4199	-41,2438
Y	1,3069	0,4104	4,1542	-5,6196	-1,7647	-17,8632
Zn	1,3304	0,1495	0,6525	-5,7207	-0,6428	-2,8056
Zr	1,3283	1,5227	6,6289	-5,7115	-6,5475	-28,5043

The third elements that lead to increase of the ordering energy compared to binary system are presented in Table 4.13, for Fe-B, Fe-Zr, Fe-Nb, Fe-C and Fe-Zr systems.

From these results, it can be noticed that, the third alloying elements of *Re, Al, B, C, Mo, W, Ta, Zr* and *Nb,* affect the ordering characteristics of binary Fe-based systems, whatever the system and the composition is, by increasing the ordering energy, and therefore these elements are potential candidates to increase the glass forming ability of Fe-based systems. These elements can be grouped in two different classes, in Table 4.14.

Table 4.14 Classification of third alloying elements.

Class 1 **Transition Metal Elements**	**Class 2** **Metalloid Elements**
Re	B
W	Al
Mo	C
Nb	
Ta	
Zr	

The literature analysis, summarized in Table 2.1 and Table 2.3 of Chapter 2, indicates that these metal and metalloid elements are used in production of bulk amorphous Fe-based alloys. Consequently, it is worthy to state that the results of the ordering energy calculation studies are in good agreement with the experimental studies reported in literature.

Table 4.13 Third alloying elements, given in descending order, which leads to an increase in the ordering energy value of binary systems.

System	Composition	Elements 1 at. % substituted for Fe	Elements 1 at. % substituted for B, Zr, Nb, C or W
Fe-B	Fe83B17	Re, Al, C, Mo, W, Ta	C, Re, Al, Mo, W, Nb
	Fe75B25	Re, Al, C, Mo, W, V,Ta, Nb	Re, Al, C, Mo, W, V
	Fe67B33	Re, Al, C, Mo, W, V, Ta, Nb	Re, Al, C, Mo, W, V
Fe-Zr	Fe73Zr27	B, Bi, Se, Mo, Co, Mn, Re, Ge, Ga, W, C, Y	Re, C, Al, W, Mo, B, Ta, Nb, V, P, Cr, Se, Ti, Si, Ni, Co, Mn, Ge, Hf
	Fe67Zr33	Re, C, W, Al, Mo, V, B, Nb, Ta, P, Se, Cr	Re, C, W, Al, Mo, V, B, Nb, Ta, P, Se,Cr, Ti, Si, Ni, Co, Ge, Mn, Hf
	Fe33Zr67	Re, C, W, Mo, Al, B, Nb, Ta, Se, P, Cr, Ti	Re, C, W, Mo, Al, V, B, Nb, Ta, Se, P, Cr, Ti, Si, Ge, Ni, Co, Hf
Fe-Nb	Fe87,9Nb12,1	Re, C, Al, W, Mo, V, B, Ta, P, Se, Cr	Ta, Re, C, Al, W, Mo, V, B
	Fe57Nb43	Zr, Re, C, Al, W, Mo, V, B, Ta, P, Cr, Se	Re, C, Al, W, Mo, V, B, Ta, P, Cr, Se, Ti, Si, Ni, Co, Ge, Mn, Hf, Ga, Zr
Fe-C	Fe83C17	Re, Al, Mo, W, V, B, Nb, Ta	Re, Al
	Fe75B25	Al, Re, Mo, W, B, V	Al, Re
Fe-W	Fe80W20	Re, C, Al, W, Mo, V, B, Ta, Nb, P, Cr	Re, C, Al
	Fe67W33	Re, C, Al, W, B, Mo, V, Ta, Nb, P, Cr	Re, C, Al
	Fe60W40	Re, Al, W, B, V, Mo, P, Ta, Nb, Cr, Si, Ti	Re, C, Al

4.1.2 Quantitative Evaluation of Heat of Mixing, Entropy of Mixing, Gibbs Free Energy of Mixing, Critical Cooling Rate, Short Range Order and Viscosity

By using the results of the ordering energy calculations and relations, theoretical background of which were given in section 2.2.2.3 of Chapter 2 in detail, it was possible to deduce various parameters, which are supposed to be an indication of glass forming ability.

As mentioned previously, there are two theoretical approaches that relate the ordering energy values with heat of mixing and so, critical cooling rate and $\Delta\eta/\eta_0$ for binary liquid alloys. First approach has been studied by Sommer and Singh [61, 62], and valid for only binary liquid alloys. The second approach has been studied by the Inoue [60] and can be used for multi-component liquid alloys. In order to compare these two approaches, heat of mixing, critical cooling rate and related other empirical parameters were calculated. The result of this comparison is given in Table 4.15.

As it can be seen from the Table 4.15, studies of Sommer et.al. and Inoue give comparable results that the values are almost on the same order. Moreover, it was further seen that the Fe-B system can be easily distinguished among the other systems by its more negative heat of mixing, and lower critical cooling rate values that is higher predicted glass forming ability.

Table 4.15 Comparison between the Approach 1, which was studied by Sommer et al. [61, 62] and the Approach 2, which was studied by Inoue [60].

Binary System		Approach	ΔH^M J/mol (10^5)	ΔS^M J/K.mol	$\Delta h/h_0$	R_C K/s (10^7)
Fe-Zr	Fe73Zr27	Approach1	-0,099	9,694	0,624	13,119
		Approach2	-0,186	5,329	1,171	19,662
	Fe67Zr33	Approach1	-0,106	10,54	0,662	11,699
		Approach2	-0,195	5,783	1,224	18,571
	Fe33Zr67	Approach1	-0,069	10,54	0,579	8,829
		Approach2	-0,13	5,667	1,088	14,535
Fe-B	Fe83B17	Approach1	-0,643	8,335	5,344	0,07
		Approach2	-1,067	6,557	10,122	0,018
	Fe75B25	Approach1	-0,869	9,346	7,302	0,01
		Approach2	-1,23	8,616	10,326	0,007
	Fe67B33	Approach1	-1,128	10,54	8,154	0,005
		Approach2	-1,432	10,279	10,357	0,008
Fe-Nb	Fe87.9Nb12.1	Approach1	-0,062	6,131	0,455	24,867
		Approach2	-0,132	3,528	0,962	28,26
	Fe57Nb43	Approach1	-0,19	11,357	1,266	6,842
		Approach2	-0,338	6,594	2,249	9,243
Fe-C	Fe83C17	Approach1	-0,265	7,577	2,233	2,569
		Approach2	-0,265	7,144	2,234	4,886
	Fe75C25	Approach1	-0,452	9,346	2,575	2,673
		Approach2	-0,55	9,477	3,136	3,373
Fe-W	Fe80W20	Approach1	-0,407	8,317	2,562	2,685
		Approach2	-0,601	4,918	3,788	3,403
	Fe67W33	Approach1	-0,65	10,54	3,678	0,741
		Approach2	-0,864	6,276	4,888	1,434
	Fe60W40	Approach1	-0,741	11,185	3,921	0,577
		Approach2	-0,951	6,661	5,035	1,325

In order to investigate the effect of the third element addition to the binary system, when 1 at. % of third element atoms replaced with each of the constituent's atoms, the second approach was used for the rest of the calculations. By doing so, investigation of the third element effect, on the enthalpy of mixing, entropy of mixing and related critical cooling rate would be more meaningful. In this section only the results of Fe-B system is given in from Table 4.16 to Table 4.21. For other systems the results will be given in Appendix C. In these tables, results of the calculations for the binary system were presented in first row, and for ternary systems these results were given in the consequent rows. In these tables also M denotes the third alloying element. By using the results of the ΔH^M and R_C calculations, percent changes in these parameters, relative to the binary system, caused by the substitution of 1 at % of third alloying element, were plotted. These graphs are given from Figure 4.1 to Figure 4.6. In order to reveal the effect of third element addition on each of the parameters, percent changes in ΔH^M, S^σ, ΔG^M, beside the elements that decrease the critical cooling rate and percent decrease in critical cooling rate, are given from Table 4.22 to Table 4.24 for Fe-B system.

As given in Equation (2.49), entropy of mixing composed of two terms, ideal entropy of mixing and mismatch entropy. Ideal entropy of mixing term was described by the equation (Equation (2.51)) as;

$$\Delta S^{ideal} = -R\sum_{i=1}^{N}(c_i \ln c_i)$$

Accordingly, ideal entropy of mixing depends on only the composition of elements. In our study, the aim is to determine the effect of third element addition qualitatively, so the amount of the third element was taken as constant and, hence ideal entropy of mixing term gave the same value whatever the added third element is, for the same binary system and composition. On this account, in all tables, the data of mismatch entropy term, that concerns the atomic size differences, is given.

Table 4.16 Calculated values of enthalpy of mixing (ΔH^M), mismatch entropy (S^σ), entropy of mixing (ΔS^M), change in viscosity ($\Delta\eta/\eta_0$), critical cooling rate (R_c) and short range order parameter (α_1) for Fe82B17M1.

Fe82B17M1						
M	ΔH^M **J/mol x10^5**	S^s **J/mol.K**	ΔS^M **J/mol.K**	$\Delta h/h_0$	R_C **K/s x10^4**	a_1
None	-1,2172	2,7685	6,5569	8,8751	11,8712	-0,2048
Al	-1,2343	2,8392	7,0774	9,0172	10,1730	
Bi	-1,3550	3,3763	7,6145	10,0214	4,3508	
C	-1,2507	2,9550	7,1932	9,1534	9,0468	
Ca	-1,5577	3,7694	8,0076	11,7070	1,1815	
Co	-1,2139	2,7695	7,0078	8,8479	11,6290	
Cr	-1,2193	2,7693	7,0075	8,8925	11,2545	
Cu	-1,1902	2,7738	7,0121	8,6508	13,4666	
Ga	-1,2016	2,8153	7,0535	8,7452	12,4629	
Ge	-1,2080	2,7684	7,0066	8,7988	12,0496	
Hf	-1,3012	2,9731	7,2113	9,5739	6,4712	
K	-1,1370	5,0014	9,2396	8,2082	13,6405	
Mg	-1,2280	3,0023	7,2405	8,9652	10,3342	
Mo	-1,3686	2,8008	7,0391	10,1339	4,3956	
Na	-1,2109	3,4596	7,6978	8,8229	10,7653	
Nb	-1,3616	2,8374	7,0756	10,0760	4,5680	
P	-1,1833	2,7914	7,0296	8,5930	14,0747	
Pb	-1,2930	3,2344	7,4727	9,5054	6,5406	
Pd	-1,2181	2,8068	7,0450	8,8824	11,2157	
Pt	-1,2003	2,8126	7,0509	8,7345	12,4081	
Re	-1,4293	2,8066	7,0448	10,6388	2,9799	
Se	-1,2177	2,8197	7,0579	8,8796	11,2496	
Si	-1,2008	2,7700	7,0082	8,7385	12,6630	
Ta	-1,3468	2,8380	7,0763	9,9530	4,9644	
W	-1,4329	2,8028	7,0410	10,6690	2,9154	
Y	-1,2373	3,3369	7,5751	9,0422	9,2326	
Zr	-1,3237	3,0038	7,2420	9,7609	5,6496	

Table 4.17 Calculated values of enthalpy of mixing (ΔH^M), mismatch entropy (S^σ), entropy of mixing (ΔS^M), change in viscosity ($\Delta\eta/\eta_0$), critical cooling rate (R_c) and short range order parameter (α_1) for Fe83B16M1.

Fe83B16M1						
M	ΔH^M **J/mol x10^5**	S^s **J/mol.K**	ΔS^M **J/mol.K**	$\Delta h/h_0$	R_C **K/s x10^4**	a_1
None	-1,2172	2,7685	6,5569	8,8751	11,8712	-0,2048
Al	-1,1780	2,6842	6,7886	8,5493	14,8868	
Bi	-1,2993	3,2155	7,3199	9,5579	6,3523	
C	-1,2006	2,8030	6,9075	8,7371	12,7308	
Ca	-1,4993	3,6052	7,7096	11,2212	1,7546	
Co	-1,1591	2,6161	6,7206	8,3918	16,8628	
Cr	-1,1639	2,6159	6,7204	8,4315	16,3800	
Cu	-1,1357	2,6202	6,7247	8,1973	19,4909	
Ga	-1,1467	2,6607	6,7652	8,2887	18,0813	
Ge	-1,1529	2,6150	6,7195	8,3401	17,5075	
Hf	-1,2446	2,8163	6,9208	9,1032	9,4930	
K	-1,0847	4,8281	8,9326	7,7730	19,5281	
Mg	-1,1733	2,8452	6,9496	8,5097	14,9869	
Mo	-1,3551	2,6465	6,7510	10,0220	4,9248	
Na	-1,1574	3,2980	7,4025	8,3777	15,5017	
Nb	-1,3086	2,6824	6,7869	9,6355	6,5490	
P	-1,1279	2,6390	6,7435	8,1325	20,4742	
Pb	-1,2380	3,0750	7,1794	9,0482	9,5025	
Pd	-1,1624	2,6524	6,7568	8,4192	16,3546	
Pt	-1,1460	2,6581	6,7626	8,2833	17,9325	
Re	-1,3705	2,6522	6,7566	10,1499	4,4302	
Se	-1,1620	2,6650	6,7695	8,4157	16,4128	
Si	-1,1454	2,6172	6,7216	8,2783	18,4169	
Ta	-1,2893	2,6831	6,7875	9,4751	7,3198	
W	-1,3745	2,6485	6,7529	10,1837	4,3227	
Y	-1,1820	3,1764	7,2809	8,5828	13,4354	
Zr	-1,2670	2,8467	6,9511	9,2891	8,2942	

Table 4.18 Calculated values of enthalpy of mixing (ΔH^M), mismatch entropy (S^σ), entropy of mixing (ΔS^M), change in viscosity ($\Delta\eta/\eta_0$), critical cooling rate (R_c) and short range order parameter (α_1) for Fe74B25M1.

Fe74B25M1						
M	ΔH^M **J/mol x10^5**	S^s **J/mol.K**	ΔS^M **J/mol.K**	$\Delta h/h_0$	R_C **K/s x10^4**	a_1
Fe75B25	-1,2297	3,9429	8,6159	10,3263	7,3337	-0,3333
Al	-1,2484	4,0281	9,1424	10,4836	6,2065	
Bi	-1,3354	4,6166	9,7310	11,2139	3,2309	
C	-1,2506	4,1170	9,2313	10,5022	6,0526	
Ca	-1,4950	5,0392	10,1536	12,5542	1,1333	
Co	-1,2244	3,9446	9,0589	10,2822	7,2795	
Cr	-1,2319	3,9442	9,0586	10,3451	6,9501	
Cu	-1,2046	3,9506	9,0649	10,1155	8,2380	
Ga	-1,2157	4,0006	9,1150	10,2086	7,6215	
Ge	-1,2221	3,9427	9,0570	10,2626	7,3783	
Hf	-1,3014	4,1777	9,2920	10,9286	4,2778	
K	-1,1468	6,3509	11,4652	9,6299	8,4071	
Mg	-1,2351	4,2098	9,3242	10,3716	6,5775	
Mn	-1,2219	3,9774	9,0917	10,2611	7,3644	
Mo	-1,3986	3,9837	9,0981	11,7445	2,4075	
Na	-1,2133	4,7065	9,8208	10,1888	7,0227	
Nb	-1,3545	4,0260	9,1404	11,3742	3,1598	
Ni	-1,2246	3,9437	9,0580	10,2838	7,2724	
P	-1,2043	3,9577	9,0720	10,1128	8,2766	
Pb	-1,2842	4,4632	9,5775	10,7842	4,5600	
Pd	-1,2310	3,9907	9,1051	10,3376	6,9004	
Pt	-1,2106	3,9976	9,1119	10,1657	7,7660	
Re	-1,4142	3,9905	9,1049	11,8756	2,1583	
Se	-1,2326	4,0057	9,1201	10,3507	6,8391	
Si	-1,2179	3,9398	9,0541	10,2271	7,6186	
Sn	-1,2483	4,2367	9,3510	10,4824	5,9660	
Ta	-1,3427	4,0268	9,1411	11,2751	3,3706	
Ti	-1,2228	4,0523	9,1666	10,2688	7,2488	
V	-1,2287	3,9627	9,0770	10,3182	7,0735	
W	-1,4132	3,9861	9,1004	11,8675	2,1735	
Y	-1,2454	4,5741	9,6884	10,4582	5,8059	
Zn	-1,2185	4,0022	9,1165	10,2323	7,4893	
Zr	-1,3198	4,2115	9,3258	11,0830	3,8279	

Table 4.19 Calculated values of enthalpy of mixing (ΔH^M), mismatch entropy (S^σ), entropy of mixing (ΔS^M), change in viscosity ($\Delta\eta/\eta_0$), critical cooling rate (R_c) and short range order parameter (α_1) for Fe75B24M1.

Fe75B24M1						
M	**ΔH^M J/mol x10^5**	**S^s J/mol.K**	**ΔS^M J/mol.K**	**$\Delta\eta/\eta_0$ x10^1**	**R_C K/s x10^4**	**a_1**
None	-1,2297	3,9429	8,6159	10,3263	7,3337	-0,3333
Al	-1,2133	3,8848	8,9067	10,1891	7,9280	
Bi	-1,3006	4,4664	9,4883	10,9222	4,1236	
C	-1,2167	3,9774	8,9993	10,2176	7,6703	
Ca	-1,4578	4,8850	9,9069	12,2418	1,4696	
Co	-1,1903	3,8031	8,8250	9,9960	9,2397	
Cr	-1,1974	3,8028	8,8247	10,0552	8,8457	
Cu	-1,1707	3,8089	8,8308	9,8312	10,4413	
Ga	-1,1816	3,8578	8,8797	9,9222	9,6769	
Ge	-1,1878	3,8014	8,8233	9,9746	9,3769	
Hf	-1,2660	4,0323	9,0542	10,6317	5,4771	
K	-1,1142	6,1860	11,2079	9,3563	10,6055	
Mg	-1,2010	4,0640	9,0859	10,0852	8,3544	
Mn	-1,1877	3,8350	8,8569	9,9740	9,3541	
Mo	-1,3620	3,8412	8,8632	11,4371	3,1051	
Na	-1,1790	4,5553	9,5773	9,9008	8,9374	
Nb	-1,3185	3,8828	8,9047	11,0718	4,0610	
Ni	-1,1905	3,8023	8,8242	9,9977	9,2293	
P	-1,1698	3,8174	8,8393	9,8238	10,5246	
Pb	-1,2500	4,3145	9,3364	10,4973	5,7978	
Pd	-1,1962	3,8481	8,8700	10,0453	8,8002	
Pt	-1,1769	3,8548	8,8767	9,8834	9,8313	
Re	-1,3773	3,8479	8,8698	11,5659	2,7891	
Se	-1,1979	3,8628	8,8847	10,0592	8,7172	
Si	-1,1835	3,7991	8,8210	9,9381	9,6885	
Sn	-1,2137	4,0905	9,1124	10,1923	7,6000	
Ta	-1,3067	3,8835	8,9054	10,9731	4,3308	
Ti	-1,1886	3,9086	8,9305	9,9812	9,2125	
V	-1,1940	3,8207	8,8426	10,0271	9,0118	
W	-1,3766	3,8435	8,8655	11,5601	2,8037	
Y	-1,2110	4,4243	9,4462	10,1691	7,3940	
Zn	-1,1847	3,8594	8,8813	9,9486	9,4897	
Zr	-1,2843	4,0657	9,0876	10,7852	4,9042	

Table 4.20 Calculated values of enthalpy of mixing (ΔH^M), mismatch entropy (S^σ), entropy of mixing (ΔS^M), change in viscosity ($\Delta\eta/\eta_0$), critical cooling rate (R_c) and short range order parameter (α_1) for Fe66B33M1.

Fe66B33M1						
M	**ΔH^M J/mol x10^5**	**S^s J/mol.K**	**ΔS^M J/mol.K**	**$\Delta h/h_0$**	**R_C K/s x10^4**	**a_1**
None	-1,4322	5,0089	10,2789	9,2727	8,4255	-0,4925
Al	-1,4579	5,1116	10,8135	9,4587	6,9692	
Bi	-1,5429	5,7617	11,4636	10,0730	3,9159	
C	-1,4487	5,1675	10,8694	9,3923	7,2797	
Ca	-1,7012	6,2194	11,9213	11,2177	1,5851	
Co	-1,4240	5,0113	10,7132	9,2136	8,4649	
Cr	-1,4353	5,0108	10,7127	9,2952	7,9694	
Cu	-1,4011	5,0194	10,7213	9,0476	9,5707	
Ga	-1,4169	5,0799	10,7818	9,1617	8,7028	
Ge	-1,4247	5,0086	10,7105	9,2181	8,4253	
Hf	-1,5161	5,2800	10,9820	9,8794	4,8713	
K	-1,3161	7,6251	13,3270	8,4328	10,4484	
Mg	-1,4358	5,3158	11,0177	9,2985	7,6333	
Mn	-1,4220	5,0524	10,7543	9,1991	8,5106	
Mo	-1,6318	5,0600	10,7619	10,7164	2,7109	
Na	-1,4016	5,8593	11,5612	9,0514	8,4951	
Nb	-1,5814	5,1093	10,8112	10,3516	3,5400	
Ni	-1,4242	5,0100	10,7119	9,2150	8,4575	
P	-1,4066	5,0136	10,7155	9,0874	9,3338	
Pb	-1,4856	5,5943	11,2963	9,6590	5,4733	
Pd	-1,4315	5,0683	10,7702	9,2678	8,0145	
Pt	-1,4065	5,0763	10,7782	9,0865	9,0751	
Re	-1,6537	5,0680	10,7699	10,8741	2,3799	
Se	-1,4383	5,0858	10,7877	9,3168	7,7312	
Si	-1,4218	5,0002	10,7021	9,1976	8,6132	
Sn	-1,4539	5,3455	11,0474	9,4294	6,8112	
Ta	-1,5682	5,1101	10,8120	10,2563	3,7620	
Ti	-1,4243	5,1393	10,8412	9,2155	8,3093	
V	-1,4338	5,0347	10,7366	9,2844	8,0075	
W	-1,6472	5,0628	10,7647	10,8274	2,4673	
Y	-1,4508	5,7154	11,4173	9,4073	6,5883	
Zn	-1,4161	5,0817	10,7836	9,1563	8,7404	
Zr	-1,5376	5,3176	11,0195	10,0351	4,3564	

Table 4.21 Calculated values of enthalpy of mixing (ΔH^M), mismatch entropy (S^σ), entropy of mixing (ΔS^M), change in viscosity ($\Delta\eta/\eta_0$), critical cooling rate (R_c) and short range order parameter (α_1) for Fe67B32M1.

Fe67B32M1						
M	**ΔH^M J/mol x10^5**	**S^s J/mol.K**	**ΔS^M J/mol.K**	**$\Delta h/h_0$**	**R_C K/s x10^4**	**a_1**
None	-1,4322	5,0089	10,2789	9,2727	8,4255	-0,4925
Al	-1,4304	4,9827	10,6252	9,2597	8,2420	
Bi	-1,5156	5,6245	11,2669	9,8755	4,6322	
C	-1,4225	5,0432	10,6856	9,2022	8,5458	
Ca	-1,6709	6,0774	11,7199	10,9989	1,9063	
Co	-1,3974	4,8847	10,5271	9,0213	9,9574	
Cr	-1,4083	4,8842	10,5267	9,0997	9,3974	
Cu	-1,3747	4,8925	10,5349	8,8569	11,2452	
Ga	-1,3898	4,9516	10,5940	8,9660	10,2658	
Ge	-1,3978	4,8822	10,5246	9,0241	9,9241	
Hf	-1,4882	5,1486	10,7910	9,6778	5,7756	
K	-1,2907	7,4705	13,1129	8,2493	12,2598	
Mg	-1,4091	5,1839	10,8263	9,1052	8,9922	
Mn	-1,3953	4,9247	10,5671	9,0061	10,0183	
Mo	-1,6028	4,9321	10,5746	10,5062	3,2329	
Na	-1,3756	5,7211	11,3635	8,8635	9,9767	
Nb	-1,5529	4,9804	10,6229	10,1453	4,2096	
Ni	-1,3977	4,8835	10,5259	9,0228	9,9485	
P	-1,3797	4,8885	10,5310	8,8927	10,9965	
Pb	-1,4589	5,4590	11,1014	9,4659	6,4516	
Pd	-1,4041	4,9402	10,5827	9,0697	9,4716	
Pt	-1,3804	4,9481	10,5905	8,8977	10,6516	
Re	-1,6243	4,9400	10,5824	10,6620	2,8426	
Se	-1,4111	4,9574	10,5998	9,1200	9,1286	
Si	-1,3949	4,8745	10,5169	9,0028	10,1495	
Sn	-1,4268	5,2132	10,8556	9,2334	8,0417	
Ta	-1,5398	4,9813	10,6237	10,0505	4,4727	
Ti	-1,3976	5,0099	10,6523	9,0221	9,7861	
V	-1,4067	4,9074	10,5498	9,0882	9,4485	
W	-1,6181	4,9349	10,5773	10,6172	2,9427	
Y	-1,4238	5,5787	11,2211	9,2120	7,7794	
Zn	-1,3898	4,9534	10,5958	8,9660	10,2683	
Zr	-1,5096	5,1857	10,8281	9,8325	5,1682	

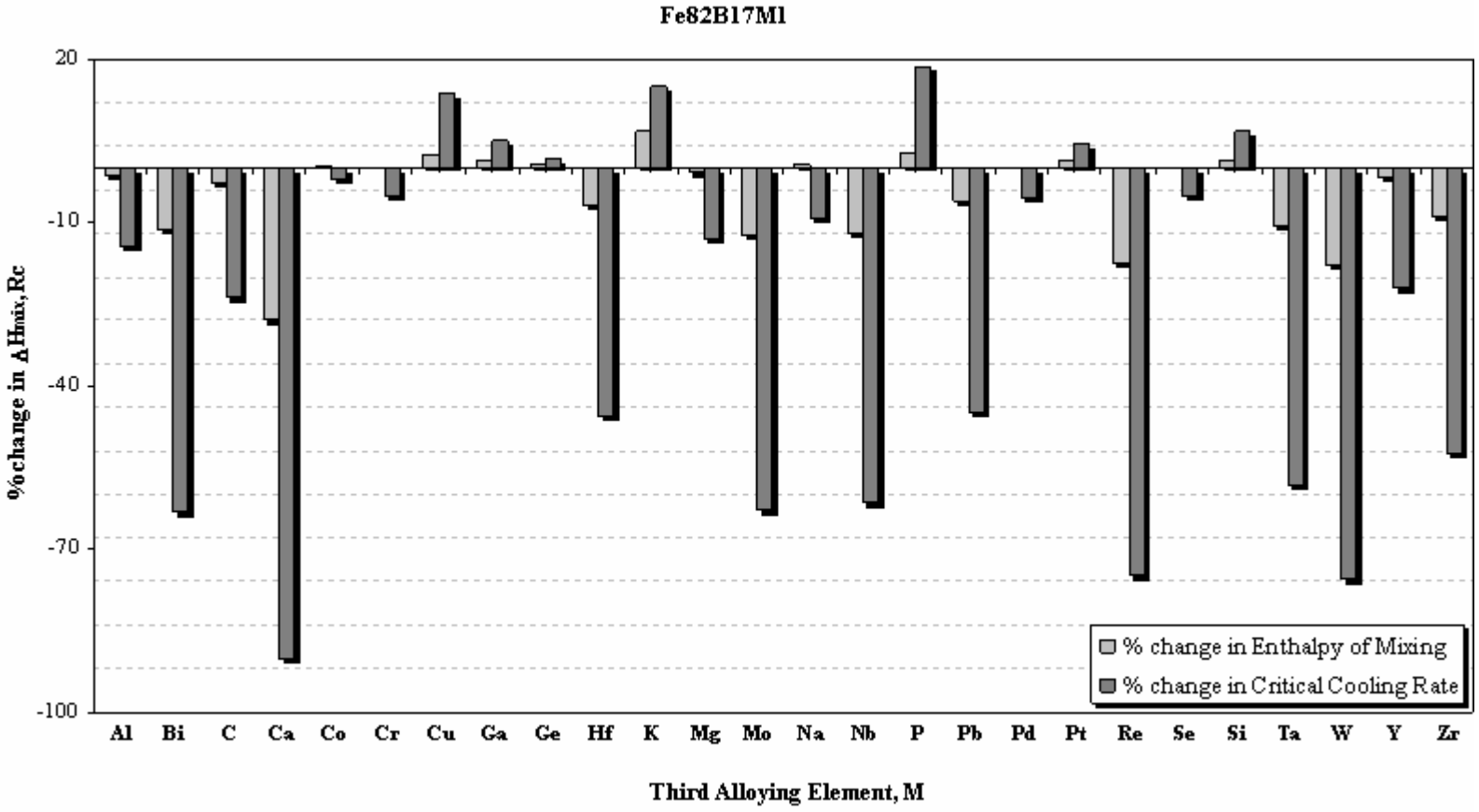

Figure 4.1 The effect of substitution of 1 at% of third element for Fe on enthalpy of mixing and critical cooling rate for Fe82B17M1.

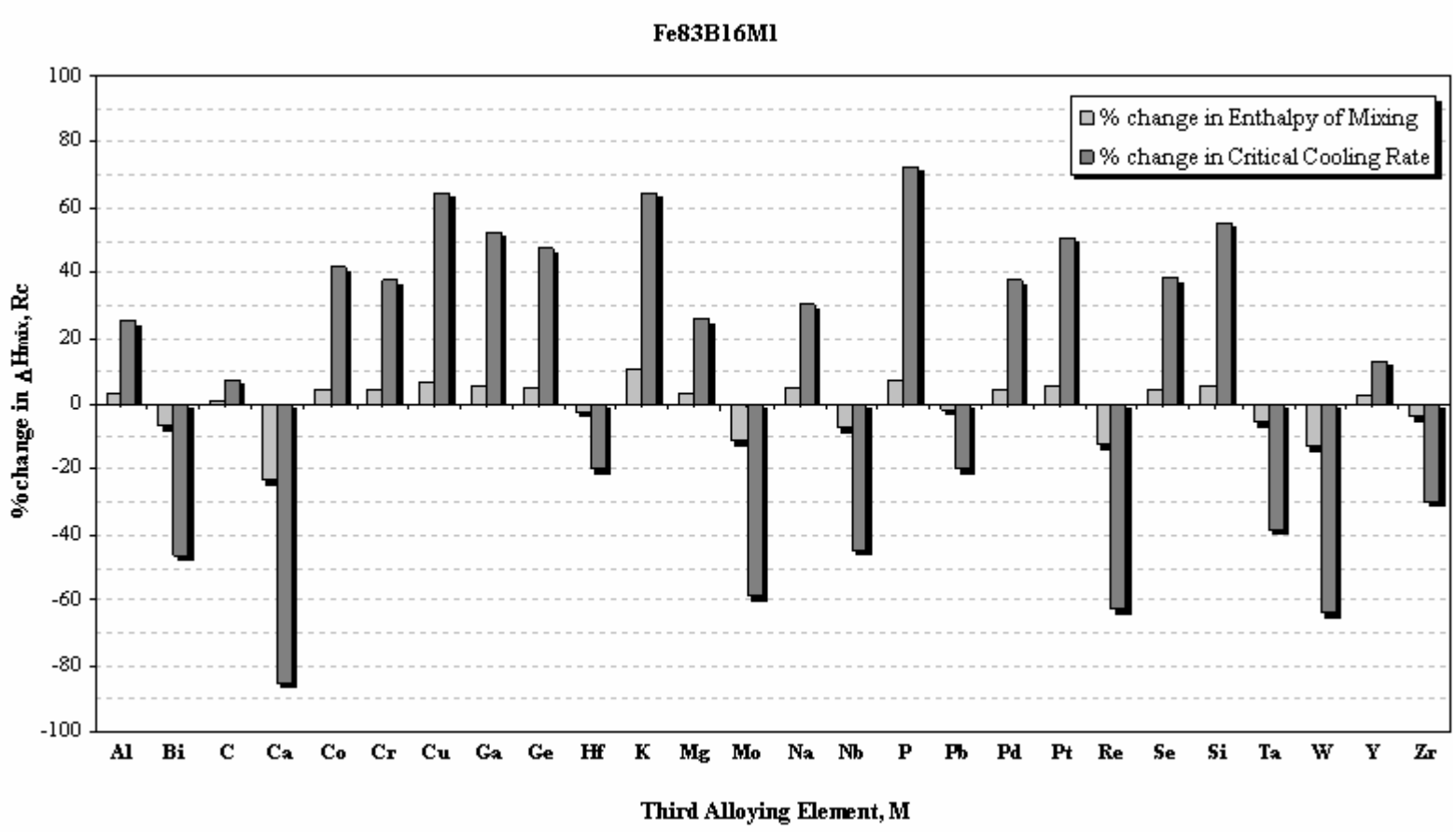

Figure 4.2 The effect of substitution of 1 at% of third element for B on enthalpy of mixing and critical cooling rate for Fe83B16M1.

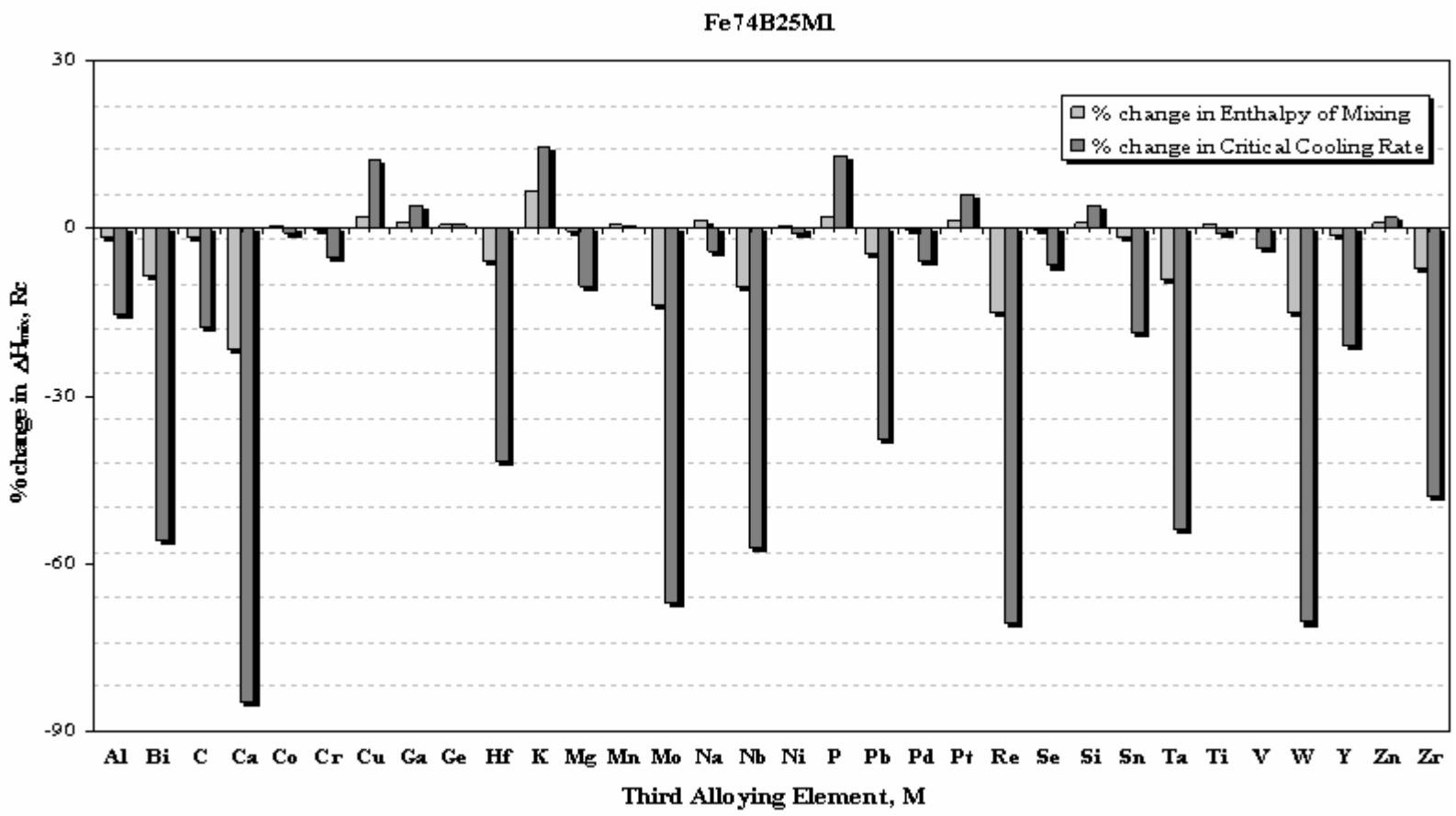

Figure 4.3 The effect of substitution of 1 at% of third element for Fe on enthalpy of mixing and critical cooling rate for Fe74B25M1.

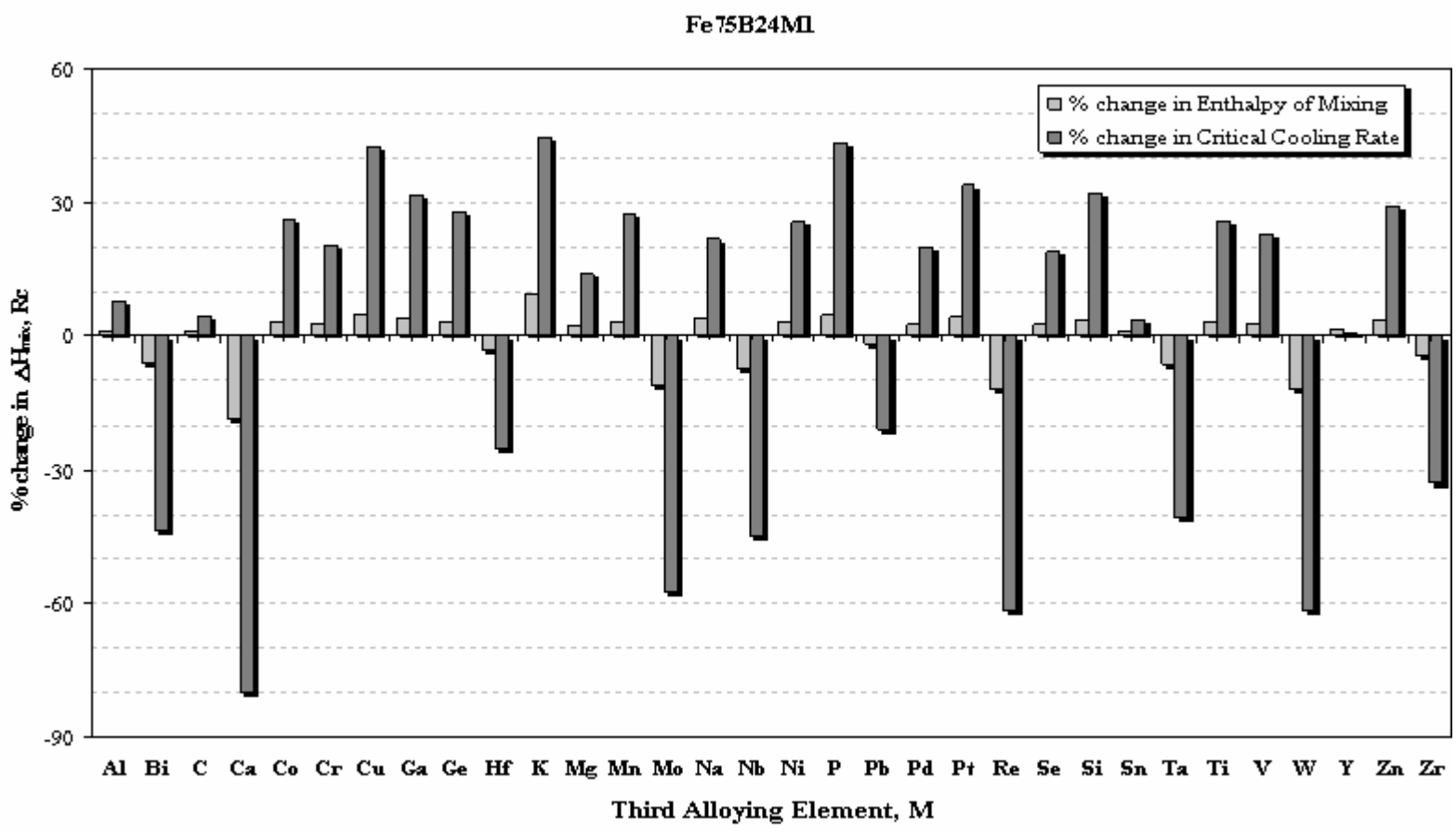

Figure 4.4 The effect of substitution of 1 at% of third element for B on enthalpy of mixing and critical cooling rate for Fe75B24M1.

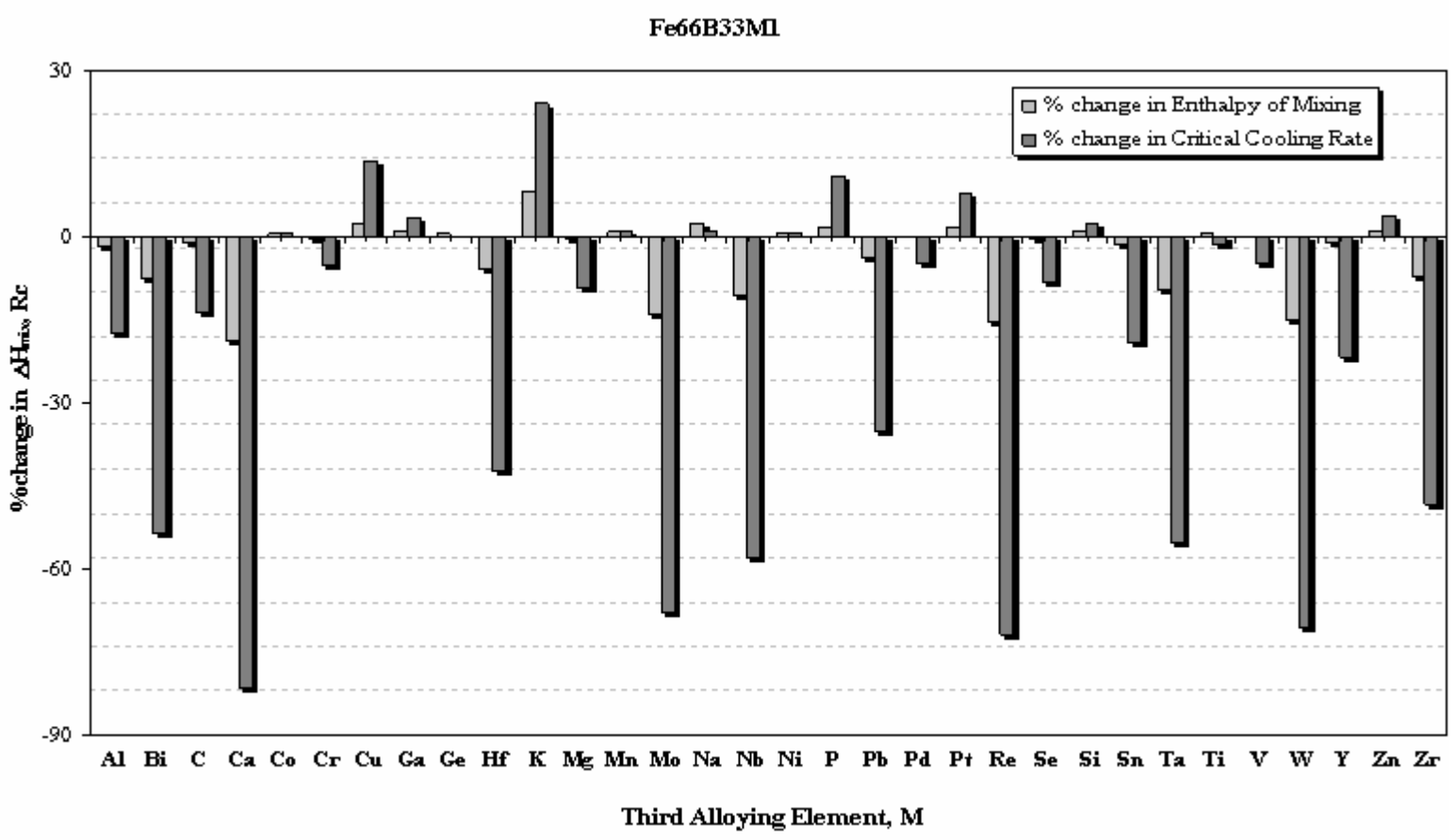

Figure 4.5 The effect of substitution of 1 at% of third element for Fe on enthalpy of mixing and critical cooling rate for Fe66B33M1.

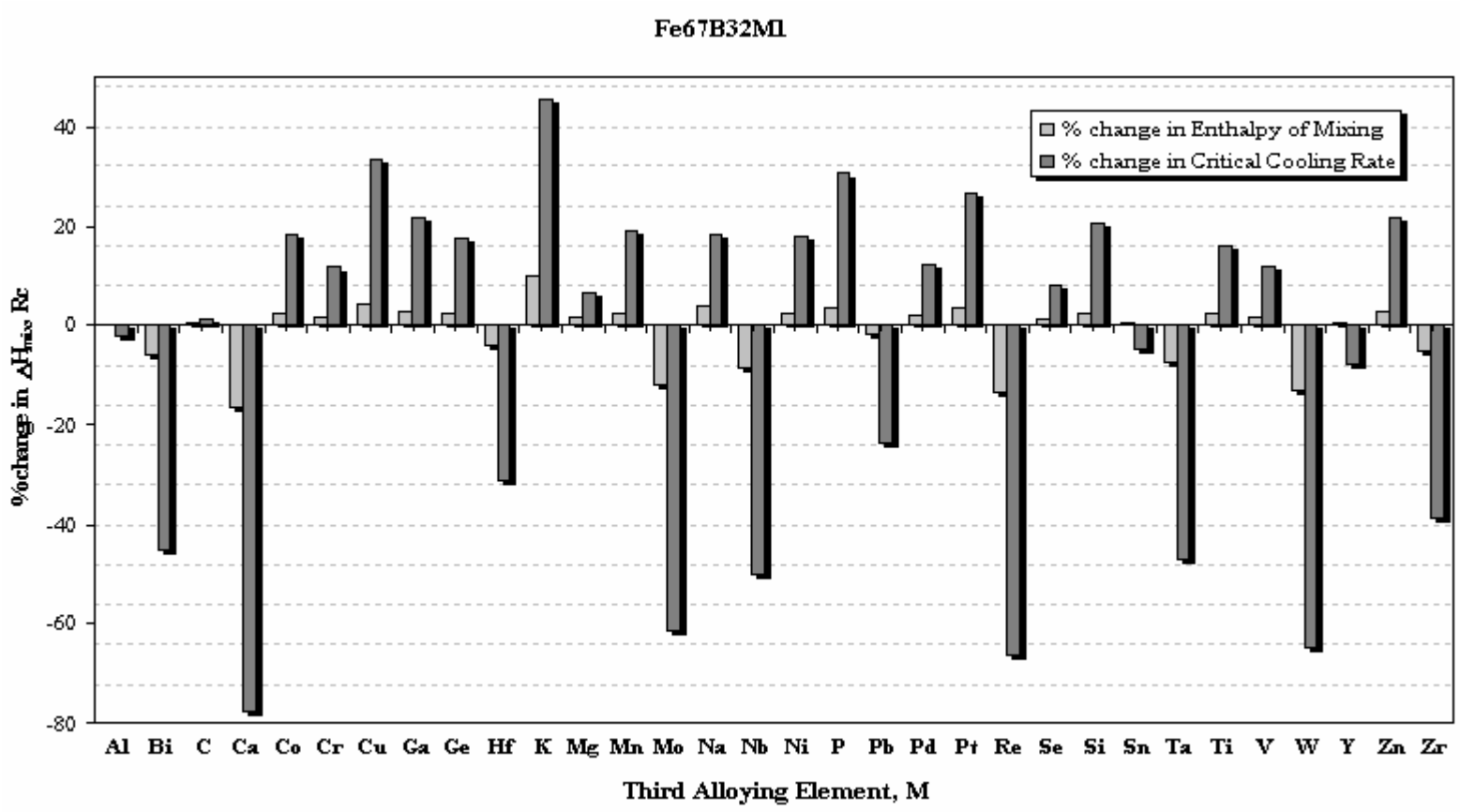

Figure 4.6 The effect of substitution of 1 at% of third element for B on enthalpy of mixing and critical cooling rate for Fe67B32M1.

Table 4.22 Third elements that decrease the critical cooling rate, % change in enthalpy of mixing, % change in S^{σ}, % change in ΔG^{M} and % decrease in R_C for Fe83B17 system.

Fe82B17M1				
Third Elements That Decrease Rc	**% change in ΔH^{M}**	**% change in S^{s}**	**% change in ΔG^{M}**	**% decrease in R_C**
Ca	-27,975	36,153	-27,552	-90,048
W	-17,722	1,241	-16,974	-75,441
Re	-17,423	1,377	-16,701	-74,898
Bi	-11,324	21,955	-11,672	-63,350
Mo	-12,435	1,169	-12,068	-62,972
Nb	-11,863	2,489	-11,578	-61,520
Ta	-10,648	2,513	-10,451	-58,181
Zr	-8,750	8,500	-8,873	-52,409
Hf	-6,903	7,390	-7,125	-45,488
Pb	-6,227	16,832	-6,786	-44,903
C	-2,750	6,737	-3,252	-23,792
Y	-1,650	20,532	-2,654	-22,227
Al	-1,404	2,554	-1,876	-14,305
Mg	-0,890	8,444	-1,580	-12,947
Na	0,516	24,964	-0,779	-9,315
Pd	-0,072	1,384	-0,605	-5,521
Se	-0,045	1,850	-0,594	-5,236
Cr	-0,172	0,030	-0,656	-5,194
Co	0,269	0,039	-0,247	-2,040
Fe83B16M1				
Third Elements That Decrease Rc	**% change in ΔH^{M}**	**% change in S^{s}**	**% change in ΔG^{M}**	**% decrease in R_C**
Ca	-23,176	30,223	-22,772	-85,220
W	-12,927	-4,334	-12,208	-63,587
Re	-12,593	-4,200	-11,903	-62,681
Mo	-11,330	-4,404	-10,725	-58,515
Bi	-6,745	16,146	-7,099	-46,490
Nb	-7,511	-3,108	-7,222	-44,833
Ta	-5,927	-3,085	-5,753	-38,339
Zr	-4,089	2,825	-4,229	-30,132
Hf	-2,253	1,728	-2,491	-20,033
Pb	-1,710	11,070	-2,273	-19,953

Table 4.23 Third elements that decrease the critical cooling rate, % change in enthalpy of mixing, % change in S^{σ}, % change in ΔG^{M} and % decrease in R_C for Fe75B25 system.

Fe74B25M1				
Third Elements That Decrease Rc	**% change in ΔH^{M}**	**% change in S^{s}**	**% change in ΔG^{M}**	**% decrease in R_C**
Ca	-21,576	27,805	-21,235	-84,547
Re	-15,004	1,208	-14,153	-70,569
W	-14,925	1,095	-14,077	-70,363
Mo	-13,734	1,036	-12,992	-67,172
Nb	-10,149	2,109	-9,778	-56,913
Bi	-8,596	17,087	-8,992	-55,944
Ta	-9,188	2,128	-8,906	-54,040
Zr	-7,329	6,812	-7,412	-47,803
Hf	-5,833	5,954	-6,017	-41,669
Pb	-4,435	13,195	-5,049	-37,821
Y	-1,277	16,008	-2,297	-20,833
Sn	-1,512	7,451	-2,153	-18,649
C	-1,704	4,415	-2,200	-17,469
Al	-1,523	2,160	-1,942	-15,369
Mg	-0,439	6,770	-1,149	-10,311
Se	-0,237	1,594	-0,749	-6,744
Pd	-0,110	1,213	-0,618	-5,909
Na	1,331	19,366	-0,067	-4,241
Cr	-0,182	0,033	-0,635	-5,230
V	0,078	0,503	-0,418	-3,548
Ti	0,556	2,774	-0,078	-1,157
Ni	0,412	0,019	-0,094	-0,835
Co	0,426	0,042	-0,082	-0,738
Fe75B24M1				
Third Elements That Decrease Rc	**% change in ΔH^{M}**	**% change in S^{s}**	**% change in ΔG^{M}**	**% decrease in R_C**
Ca	-18,550	23,894	-18,225	-79,961
Re	-12,004	-2,410	-11,178	-61,969
W	-11,948	-2,520	-11,123	-61,770
Mo	-10,758	-2,578	-10,038	-57,660
Nb	-7,220	-1,525	-6,867	-44,626
Bi	-5,771	13,277	-6,168	-43,772
Ta	-6,264	-1,506	-5,999	-40,947
Zr	-4,445	3,113	-4,539	-33,127
Hf	-2,958	2,266	-3,152	-25,316
Pb	-1,657	9,424	-2,268	-20,942

Table 4.24 Third elements that decrease the critical cooling rate, % change in enthalpy of mixing, % change in S^{σ}, % change in ΔG^{M} and % decrease in R_C for Fe67B33 system.

Fe66B33M1				
Third Elements That Decrease Rc	**% change in ΔH^{M}**	**% change in S^{s}**	**% change in ΔG^{M}**	**% decrease in R_C**
Ca	-18,779	24,167	-18,480	-81,187
Re	-15,461	1,180	-14,321	-71,754
W	-15,010	1,076	-13,913	-70,717
Mo	-13,939	1,020	-12,953	-67,825
Nb	-10,417	2,004	-9,858	-57,985
Ta	-9,496	2,021	-9,037	-55,350
Bi	-7,726	15,029	-8,132	-53,523
Zr	-7,360	6,163	-7,344	-48,295
Hf	-5,858	5,413	-5,962	-42,184
Pb	-3,730	11,688	-4,388	-35,038
Y	-1,300	14,104	-2,342	-21,806
Sn	-1,513	6,720	-2,149	-19,160
Al	-1,796	2,050	-2,159	-17,285
C	-1,154	3,166	-1,644	-13,600
Mg	-0,249	6,126	-0,989	-9,403
Se	-0,426	1,535	-0,909	-8,240
Cr	-0,217	0,038	-0,644	-5,413
V	-0,113	0,515	-0,576	-4,961
Pd	0,047	1,185	-0,468	-4,879
Ti	0,553	2,603	-0,090	-1,380
Ge	0,527	-0,005	0,023	-0,002
Fe67B32M1				
Third Elements That Decrease Rc	**% change in ΔH^{M}**	**% change in S^{s}**	**% change in ΔG^{M}**	**% decrease in R_C**
Ca	-16,666	21,333	-16,384	-77,375
Re	-13,413	-1,376	-12,297	-66,262
W	-12,981	-1,478	-11,905	-65,074
Mo	-11,909	-1,532	-10,945	-61,630
Nb	-8,425	-0,568	-7,883	-50,037
Ta	-7,509	-0,551	-7,066	-46,915
Bi	-5,820	12,290	-6,225	-45,021
Zr	-5,405	3,530	-5,399	-38,660
Hf	-3,911	2,790	-4,025	-31,451
Pb	-1,866	8,987	-2,520	-23,428
Y	0,586	11,375	-0,454	-7,668
Sn	0,379	4,079	-0,260	-4,556
Al	0,126	-0,522	-0,247	-2,179

Summary of the third elements that lead to decrease of the heat of mixing and critical cooling rate, hence increase the glass forming ability of the binary system are presented in Table 4.25, for Fe-B, Fe-Zr, Fe-Nb, Fe-C and Fe-Zr systems. As it can be realized from this table, *Ca, Re, W, Mo, Nb, Ta, C, Zr, Hf, P, Si, B, Na, K, Al, Mn, Mg, Ga* and *Co* are the potential candidate elements to improve the glass forming ability for almost all selected Fe-based systems and compositions.

In comparison of these results with the literature analysis, from Table 2.1 to Table 2.3, and results of the ordering energy calculations, Table 4.13, it can be realized that there is a good agreement between all these results.

For the experimental investigation studies, results of which will be discussed in the following section, as a starting point Fe83B17 composition was selected, as stated previously. Third elements *Nb* and *W* were selected as an alloying element among the others on the base of the theoretical modeling and computer simulation studies. As it can be seen from Table 4.13 and 4.21, these elements increase the degree of ordering, increase the mismatch entropy, decrease the heat of mixing and critical cooling rate as compared to Fe83B17 composition, hence niobium and tungsten elements are two of the best potential candidates to enhance the glass forming ability of this composition. In selection of these elements also their availability and economic reasons were taken into account.

Table 4.25 Summary of the elements that decreases both enthalpy of mixing and critical cooling rate as compared to binary system.

System	Composition	Third element that decrease ΔH^{M}	Third element that decrease R_C
Fe-B	Fe82B17M1	Ca, W, Re, Bi, Mo, Nb, Ta, Zr, Hf, Pb, C, Y, Al, Mg, Se, Cr, Co	Ca, W, Re, Bi, Mo, Nb, Ta, Zr, Hf, Pb, C, Y, Al, Mg, Na, Se, Cr, Co
	Fe83B16M1	Ca, W, Re, Mo, Bi, Nb, Ta, Zr, Hf, Pb	Ca, W, Re, Mo, Bi, Nb, Ta, Zr, Hf, Pb
	Fe74B25M1	Ca, Re, W, Mo, Nb, Bi, Ta, Zr, Hf, Pb, Y, Sn, C, Al, Mg, Se, Cr	Ca, Re, W, Mo, Nb, Bi, Ta, Zr, Hf, Pb, Y, C, Al, Mg, Pd, Na, Cr, Co
	Fe75B24M1	Ca, Re, W, Mo, Nb, Bi, Ta, Zr, Hf, Pb	Ca, Re, W, Mo, Nb, Bi, Ta, Zr, Hf, Pb
	Fe66B33M1	Ca, Re, W, Mo, Nb, Ta, Bi, Zr, Hf, Pb, Y, Al, C, Mg, Se, Cr, V	Ca, Re, W, Mo, Nb, Ta, Bi, Zr, Hf, Pb, Y, Sn, Al, C, Mg, Se, Cr, Ge
	Fe67B32M1	Ca, Re, W, Mo, Nb, Ta, Bi, Zr, Hf, Pb	Ca, Re, W, Mo, Nb, Ta, Bi, Zr, Hf, Pb, Y, Sn, Al
Fe-Zr	Fe72Zr27M1	C, B, Ta, Ni, Bi, K, Re, Na, Mo, P, Y, W, Se, Ga, Mn, Si, Al, Ca	C, B, Ta, Bi, K, Re, Na, Mo, P, Y, W, Ga, Mn, Si, Mg, Nb, Al, Hf, Ca
	Fe73Zr26M1	C, B, K, Bi, Mo, W, Hf, Re, P, Cr, Al, Ca	C, B, K, Bi, Mo, W, Hf, Re, Na, P, Ta, Nb, Y, Si, Ga, Al, Mn, Mg, Ca
	Fe66Zr33M1	C, B, K, Bi, Mo, W, Na, P, Re, Hf, Cr, Ta, Si, Ti, Ni, Nb, Al, Ca	C, B, K, Bi, Mo, W, Na, P, Re, Hf, Ta, Si, Nb, Al, Ge, Ga, Y, Mn, Mg, Ca
	Fe67Zr32M1	C, B, K, Bi, Mo, W, Na, P, Re, Hf, Cr, Ta, Si, V, Ni, Nb, Al, Ca	C, B, K, Bi, Mo, W, Na, P, Re, Hf, Ta, Si, Se, Nb, Al, Ga, Ge, Zn, Y, Mn, Mg, Ca
	Fe32Zr67M1	C, K, B, Ca, Na, P, Al, Si, Cr, Mg, Ni, W, Ti, Mo, V, Ga	C, K, B, Ca, Na, P, Al, Bi, Si, Mg, W, Mo, V, Ga, Zn, Ge, Se, Re, Hf, Mn, Ta, Nb, Y
	Fe33Zr66M1	C, B, K, Ca, Na, P, Al, Si, Cr, Mg, W, Ni, Mo,Ga, Re, Hf,Ta, Nb	C, B, K, Ca, Na, P, Al, Si, Cr, Mg, W, Ni, Mo, Ti, V, Ga, Re, Hf, Ta, Mn, Nb, Y
Fe-Nb	Fe86,9Nb12,1M1	Ca, K, Bi, B, W, Mo, Na, C, Pb, Hf, Re, Zr, Pt, Ta, Y, Se, Sn, P	Ca, K, Bi, B, W, Mo, Na, C, Pb, Hf, Re, Zr, Pt, Ta, Y, Se, P, Cr, Zn, Ga, Ni, Co
	Fe87,9Nb11,1M1	Ca, Bi, C, Ta, Hf, Pd, Pt, Sn	Ca, K, Bi, B, W, Mo, Pb, Na, C, Ta, Hf, Re, Pd, Pt, Y, Se, Sn, P
	Fe56Zr43M1	Ca, K, B, Na, C, W, Mo, Zr, P, Re, Pt, Al, Hf, Si, Ni, Co, Ta	Ca, K, B, Na, C, Pd, W, Mo, Zr, P, Re, Pt, Al, Hf, Bi, Cr, Si, Se, Ni, Co, Ta
	Fe57Nb42M1	Ca, K, B, Na, C, W, Pd, Mo, Re, P, Al, Bi, Mg, Hf, Cr, Si, Zr, Co	Ca, K, B, Na, C, W, Pd, Mo, Re, P, Pt, Al, Bi, Mg, Hf, Cr, Si, Se, Ni, Zr, Co, Ta
Fe-W	Fe79W20M1	C, B, Bi, K, Ca, Al, Na, Mo, Re, Pd, Hf, Pt, Zr, P, Ta, Nb	C, B, Bi, K, Ca, Al, Na, Mo, Re, Pd, Hf, Pt, Zr, Pb, P, Ta, Y, Nb
	Fe80W19M1	C, Ca, Ge, Na, Mg	C, B, K, Bi, Ca, Ge, Na, Al, K, Mg
	Fe66W33M1	C, B, Bi, Al, K, Ca, Cr, Na, Pd, Mo, P	C, B, Bi, Al, K, Ca, Cr, Na, Pd, Mo, P
	Fe67W32M1	C, B, Ca, K, Na	C, B, Bi, Al, Ca, K, Cr, Na
	Fe59W40M1	C, B, Al, K, Cr, Ca, Na, Pd	C, B, Bi, Al, K, Cr, Ca, Na, Pd
	Fe60W39M1	C, B, Bi, Ca, K, Al, Na	C, B, Bi, Ca, K, Al, Na
Fe-C	Fe82C17M1	Re, W, Mo, Nb, Ta, Zr, Hf, Ca, Bi, Pb, B, Al, Mg, Cr, Ni, Co	Re, W, Mo, Nb, Ta, Zr, Hf, Ca, Bi, Pb, Y, Sn, B, Al, Mg, Zn, Cr, Ni, Co, V, Si, Ga
	Fe83C16M1	Re, W, Mo, Nb, Ta, Zr, Bi, Hf, Ca, Pb, Y, Sn, B, Al	Re, W, Mo, Nb, Ta, Zr, Bi, Hf, Ca, Pb, Y, Sn, B, Al
	Fe74C25M1	Re, W, Mo, Nb, Ta, Zr, Hf, Ca, Bi, Pb, Y, Sn, B, Al, Mg, Co	Re, W, Mo, Nb, Ta, Zr, Hf, Ca, Bi, Pb, Y, Sn, Al, B, Mg, Se, V, Cr, Ge, Ni, Co, Si
	Fe75C24M1	Re, W, Mo, Nb, Ta, Bi, Zr, Pb, Hf, Ca, B	Re, W, Mo, Nb, Ta, Bi, Zr, Pb, Hf, Ca, B, Y

4.2 Experimental Investigations

For the experimental investigations, the results of the theoretical modeling studies were taken into consideration. As a starting point, Fe83B17 composition was focused on. Then, experimental studies were progressed by the addition of the selected third alloying elements, niobium and tungsten to binary system.

In the first stages of the experimental studies, the predetermined binary and ternary alloy compositions, presented in Table 3.4, were tried to synthesize by using low purity industrial grade Fe-B alloy. In the next stages, to compare the results and to analyze the effect of the other impurity elements that exist in low-grade commercial Fe-B alloy, selected compositions of Fe-B and Fe-B-Nb systems were synthesized from the high purity raw elements.

Throughout the thesis study alloy production was performed by using centrifugal casting machine and Cu-mold casting method. The characterization of the cast samples was performed by using X-ray diffraction, DSC, SEM and metallographic examination techniques. Moreover, by the help of the NORAN Six X-ray Microanalysis System, the compositional analyses of the phases were examined. However, this system can not detect the light elements such as B, consequently, the results of the elemental analysis will be given in terms of nominal composition. The results and the discussions of these investigations will be presented in the following sections.

4.2.1 Production of Fe-based Alloys by Using Low Grade Commercial Fe-B Alloy

The compositional analysis of low-grade commercial Fe-B alloy is examined by various techniques and the results were presented in Table 3.6. During the efforts in determining the chemical composition of Fe-B alloy, it was realized that the composition is not homogenous throughout the ore and changing region by region. By keeping these into mind, the compositions of the master alloys were prepared by taking the XRF results as a base and adjusting the content of the Fe to B ratio in the cast alloy by adding different amount of pure iron element for the binary system. For ternary systems, the selected compositions were prepared by adjusting the Fe/B/Nb or Fe/B/W ratio in the cast alloy by adding pure iron and third alloying elements to commercial Fe-B alloy.

4.2.1.1 Binary Fe-B Alloy

As stated previously, in literature, Fe-B system has been used as a model system for understanding the glass forming ability in amorphous materials, and this system exhibits high glass forming ability close to the Fe rich eutectic (Fe83B17). However, production of a bulk amorphous Fe83B17 alloy by using conventional Cu-mold technique has not been reported up to date.

In this study, as a starting point for experimental investigations, binary Fe83B17 composition (alloy S1) was synthesized by using conventional Cu-mold casting. The casting was performed by using mold M1 and at a temperature of 1150 °C. To examine the solidification behavior and to compare the data, the same composition was also synthesized under near equilibrium conditions. The DSC curve of the wedge-cast sample obtained at a heating rate of 20 °C/min is given in Figure 4.7. As it can be seen from this figure, the glass transition and crystallization peak cannot be observed. This result was expected due to the high critical cooling rate value of this system, for glass formation, predicted from the theoretical modeling

results. Furthermore, general melting behavior of the alloy was observed by examining the DSC curves: the essential melting occurs through one stage endothermic peak, which corresponds to the eutectic reaction. Summary of the thermal data obtained from the DSC experiments is presented in Table 4.26.

Table 4.26 Thermal data obtained from DSC experiment for alloy S1 (Fe83B17), T_l and ΔH_m denotes the melting temperature, i.e. the eutectic temperature, and enthalpy of melting, respectively.

T_l (°C)	ΔH_m (J/gr)
1165,12	3,3661

XRD studies of the both slowly cooled and wedge-cast samples, patterns are given in Figure 4.8, assigned the presence of α-Fe (with body centered cubic structure), Fe_2B (with tetragonal structure) and aluminum oxide (Al_2O_3) phases for slowly cooled sample and in addition to these, Fe_3B (with tetragonal structure) phase for the wedge-cast sample. The comparison between these two XRD patterns revealed the fact that the non-equilibrium solidification enhances the formation of metastable Fe_3B phase.

The solidification microstructures of both slowly cooled and wedge cast samples are presented in Figure 4.9, together with the EDS analysis results which indicated the presence of only Si element among the impurity elements that have been exist in low grade commercial Fe-B alloy. This was most probably resulted from the fact that the impurity elements other than Si, formed slag and rose to melt surface during induction heating and, hence could not flow into the mold during casting or could not be detected by the EDS analysis, which has an error tolerance of ±2, due to their low concentration in commercial Fe-B alloy.

In addition, from the micrographs of wedge-cast sample, the existence of Al_2O_3 particles can be easily distinguished, whereas these particles cannot be observed from the micrographs of the slowly cooled sample although the XRD pattern reveals the formation of aluminum oxides. On the base of these, it can be stated that although the melting and the castings were done under the Ar atmosphere, samples were contaminated with alumina, probably arising from the reaction between the crucible and the melt.

In analyzing the solidification structures, stable and metastable binary phase diagrams of Fe-B system, Figure 2.1, were taken into account. Special points of the Fe-B stable and metastable phase diagrams are given in Table 4.27 [47, 75-78].

Table 4.27 Special points of the stable and metastable phase diagrams of Fe-B system [47, 75-78].

Fe-B Stable Phase Diagram					
Reaction	**Composition, at. %B**			**Temperature °C**	**Reaction Type**
L Û d**Fe**		0		1538	Melting
d**Fe** Û g**Fe**		0		1394	Allotropic
g**Fe** Û a**Fe**		0		912	Allotropic
g**Fe** Û a**Fe + Fe_2B**	≅0	≅0	33,3	911 ± 10	Peritectoid
L Û g**Fe+ Fe_2B**	≅17	0	33,3	1174 ± 30	Eutectic
L + FeB Û **Fe_2B**	≅32,5	50	33,3	1389 ± 20	Peritectic
L Û **FeB**		50		1650 ± 60	Congruent
L Û **FeB + (b**B**)**	≅64	50	>98,5	1500 ± 10	Eutectic
L Û b**B**		100		209 2± 30	Melting
Fe-B Metastable Phase Diagram					
Reaction	**Composition, at. %B**			**Temperature °C**	**Reaction Type**
L Û g**Fe+ Fe_3B**	≅18,6	0	25	1113±10	Eutectic
L + FeB Û **Fe_3B**		50	25	1160	Peritectic

As it can be seen from Figure 4.9.a and b, the microstructure of the slowly cooled sample consists of interdendritic irregular eutectic phase mixture (denoted as X on the micrograph) and a dendritic primary phase (denoted as Y on the micrograph). In the first stages of the solidification, presumably primary phase forms, which has

faceted growth morphology, as seen from the micrograph. On the base of the growth morphology and XRD result, this primary phase regarded as Fe_2B. In the following stages, as the temperature decreases, the remaining liquid phase transforms to eutectic phase mixture composed of α-Fe and Fe_2B phases. The EDS analysis results taken from the eutectic phase mixture denoted the existence of Fe and Si elements, which might be resulted from the fact that either the Si element dissolved in the α-Fe phase, or Fe_2B intermetallic phase.

Furthermore, from the microstructural examinations, for slowly cooled sample, it appears that although the eutectic composition was prepared, the composition was not exactly eutectic but off eutectic. This discrepancy probably resulted from the compositional inhomogeneity of low-grade commercial Fe-B alloy.

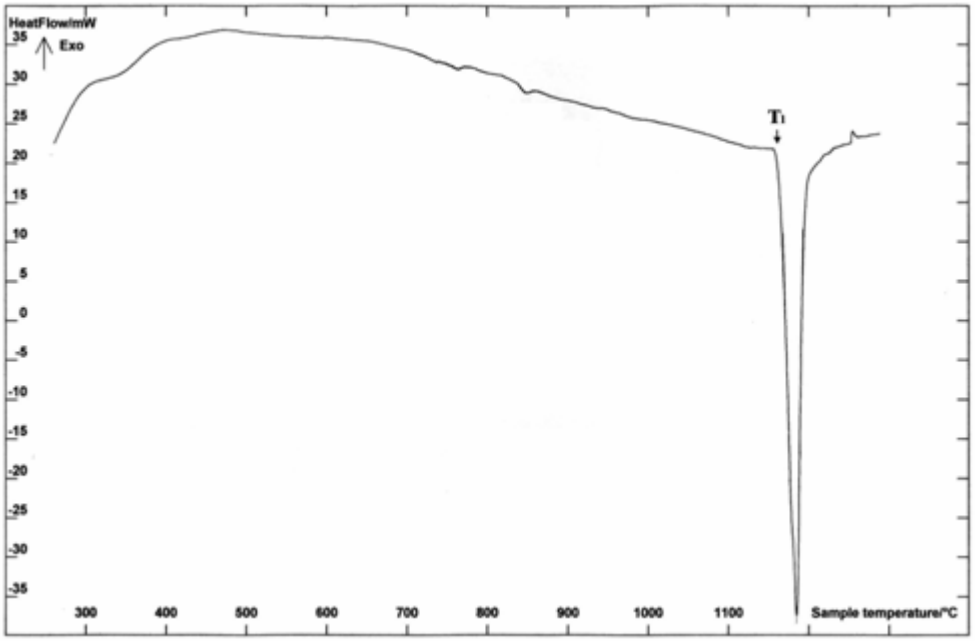

Figure 4.7 DSC pattern of alloy S1, obtained at a heating rate of 20 °C/min.

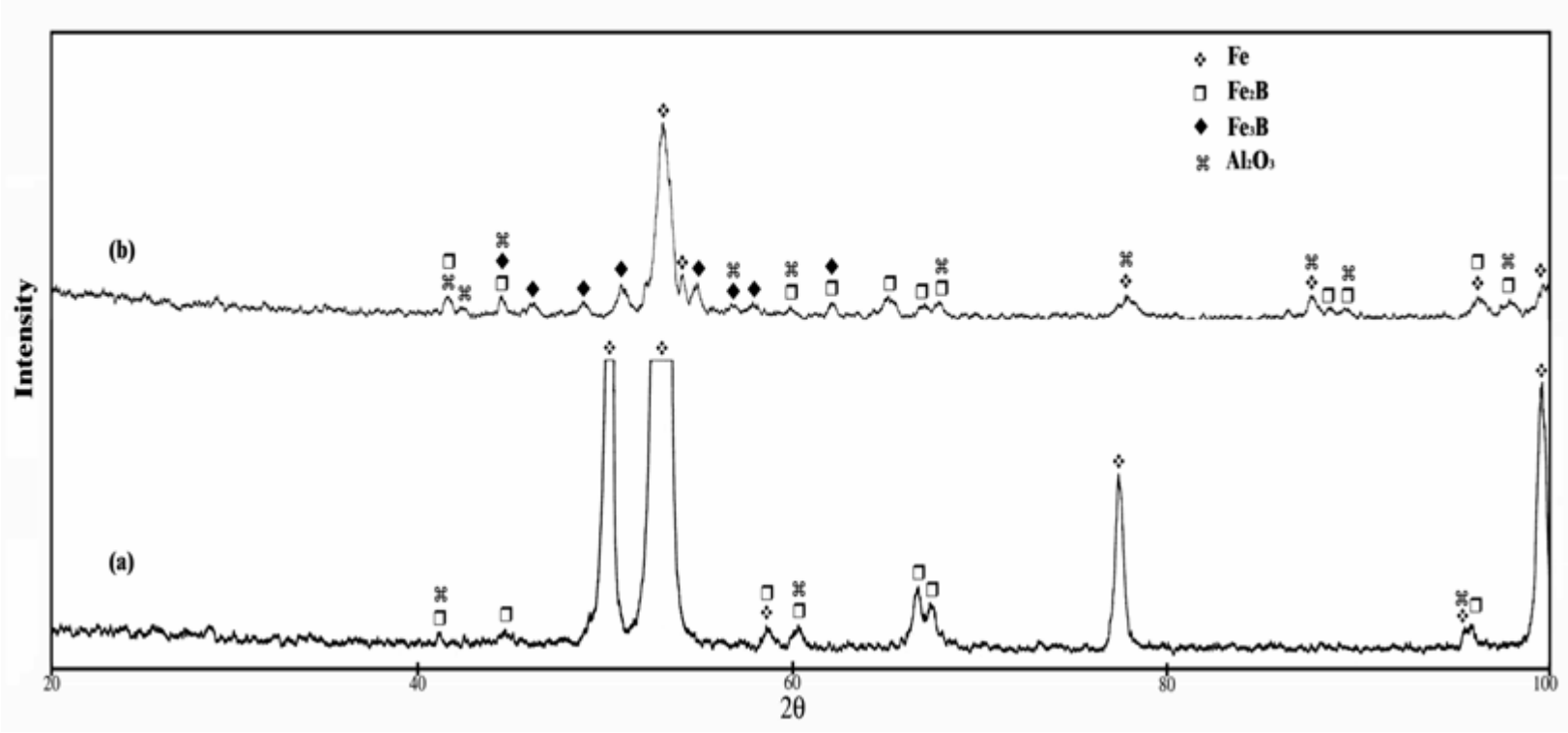

Figure 4.8 X-ray Diffraction patterns of the slowly cooled sample (a) and wedge-cast sample (b) of alloy S1 ($Fe_{83}B_{17}$).

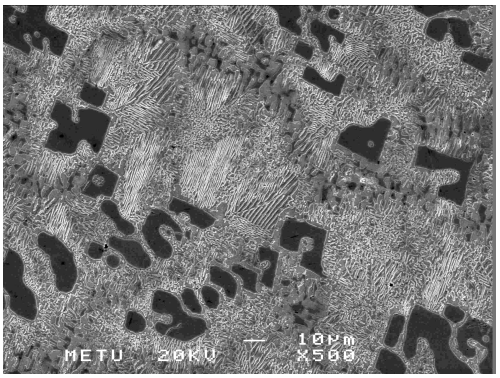

(a)

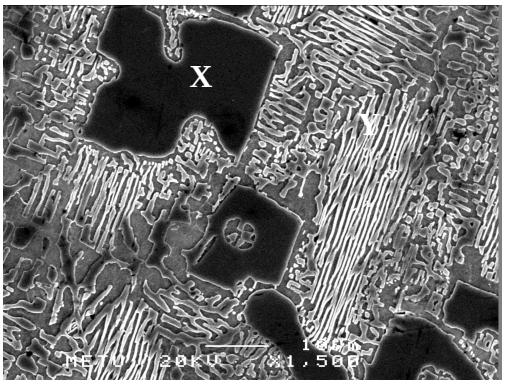

(b)

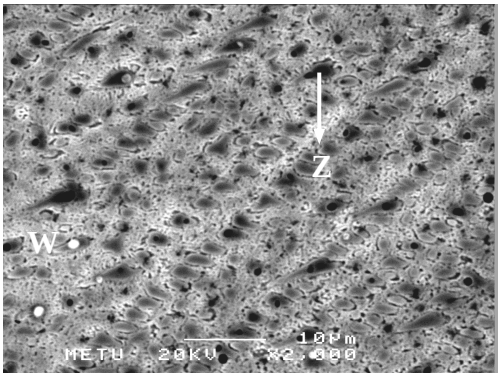

(c)

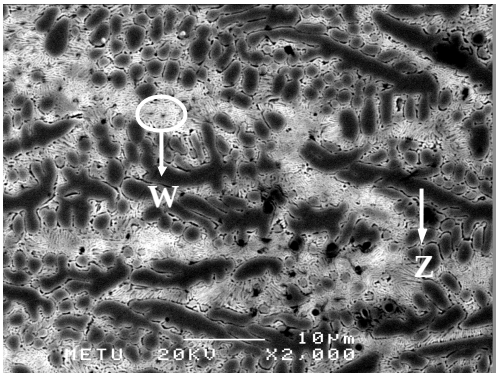

(d)

Sample	Analyzed Region	Element	Weight % (±2)	Atom % (±2)
Slowly cooled	General	Fe	99,52	99,05
		Si	0,48	0,95
Wedge-cast	General	Fe	99.56	99.12
		Si	0.44	0.88
	Dark Region (Z)	Fe	99,85	99,71
		Si	0,15	0,29

(e)

Figure 4.9 Microstructure of slowly cooled and wedge cast sample, alloy S1: a) *500, SE image of slowly cooled sample, b) *1500, SE image of slowly cooled sample, c) *2000, SE image of the thin section of wedge-cast sample, d) *2000, SE image of the thick section of wedge-cast sample and e) EDS analysis results.

The crystalline microstructure of the wedge-cast sample, Figure 4.9.c and d, reveals a structure different from the slowly cooled specimen in that the formation of the faceted primary phase that exhibits growth problems was suppressed and, instead, formation of dark contrasted phase with a non-faceted morphology (denoted as Z on the micrograph) was detected. This dark contrasted phase with dendritic morphology was identified as α-Fe phase, on the base of the XRD and EDS analysis results, containing small amounts of Si element. The matrix (denoted as W on the micrograph) is probably composed of eutectic phase mixture, whose components could not be determined exactly. However, based on the microstructural findings of slowly cooled specimen and XRD pattern of the wedge-cast specimen, it can be predicted that components of the eutectic phase mixture are α-Fe and Fe_2B or Fe_3B. Comparison between the wedge-cast and slow cooled sample further reveals the fact that formed eutectic structure in wedge-cast alloy has finer morphology as compared to the eutectic in slowly cooled sample. This result was expected, as the morphology becomes finer with increasing the rate of solidification in order to allow the diffusion to redistribute the atoms.

The difference between microstructures of the primary phases of the slowly cooled and wedge-cast samples most probably arisen from the skewed eutectic coupled zone phenomena, in the case of which, high cooling rates may lead to the formation of primary hypoeutectic dendrites even on the hypereutectic side of the eutectic composition. Skewed zones are usually associated with eutectics, which contain one phase having faceted growth morphology [72]. In section 4.2.3, skewed zone phenomena will be mentioned in a more detailed manner.

By comparing the SEM images of the thin and relatively thick sections, Figure 4.9.c and d, the effect of the cooling rate on the microstructure can be easily recognized. As the thickness of the sample increases, rate of the heat removal from the melt and hence the cooling rate decreases, so coarser structure was formed.

4.2.1.2 Ternary Fe-B-Nb Alloy

According to the modeling and computer simulation results, it was predicted that addition of the Nb element leads to an increase in the glass forming ability and a decrease in the critical cooling rate for glass formation of Fe83B17 composition. To verify this result, Nb element was selected as a third alloying element and Fe79B16Nb5 (alloy S2) composition was synthesized at a casting temperature of 1150 °C by using copper mold M2.

To compare the solidification structures, same alloy composition was also prepared under near equilibrium conditions. The XRD pattern of the slowly cooled specimen, given in Figure 4.10, indicated the formation of possible phases; α-Fe, Fe_2B, Fe_3B, FeNbB and Al_2O_3. The structure of these phases, except FeNbB that has a hexagonal structure, was mentioned previously. Figure 4.11 shows the microstructures taken from SEM together with the EDS results. When the XRD and EDS results are analyzed together, it appears that the Si and part of the Nb element probably dissolved in the other phases. Moreover, the aluminum oxide particles can be easily distinguished and denoted on the micrograph, although the general EDS analysis results do not reveal the existence of aluminum. This discrepancy most probably resulted from the low content of aluminum in alloy.

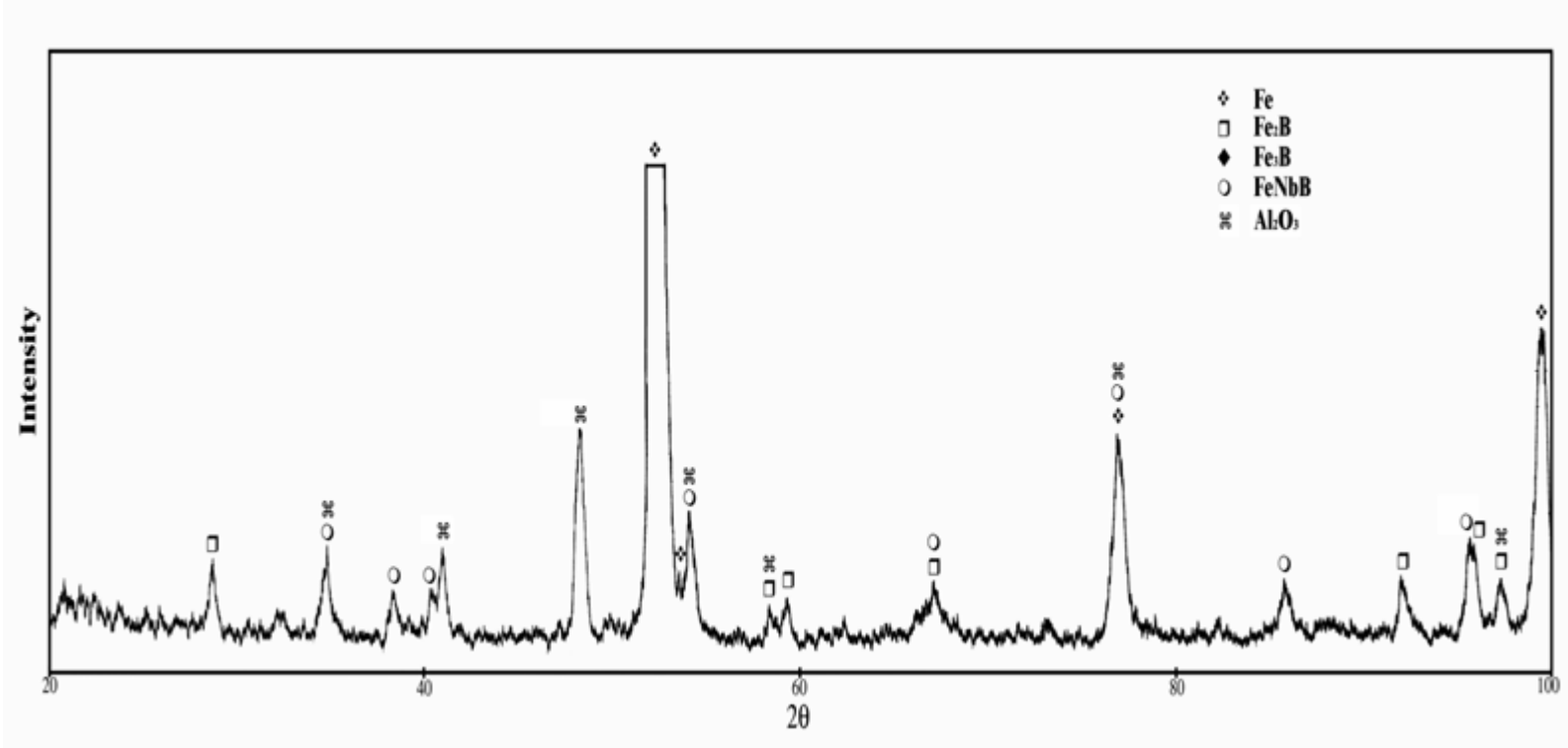

Figure 4.10 X-ray Diffraction pattern of the slowly cooled sample of alloy S2 (Fe79B17Nb5).

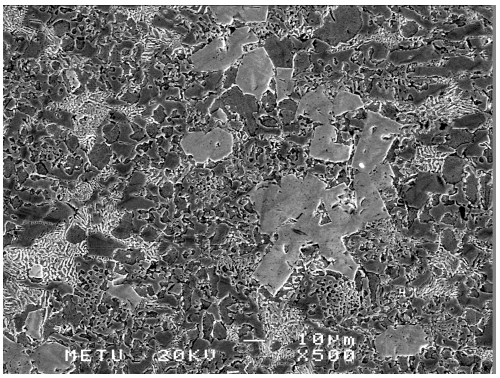

(a)

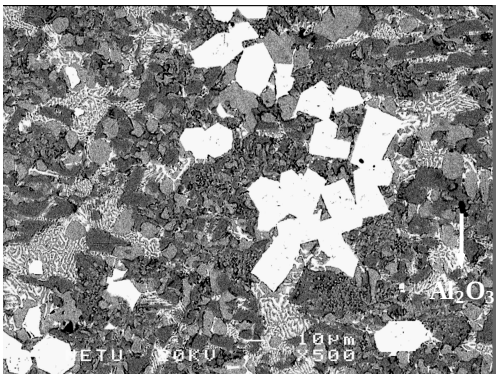

(b)

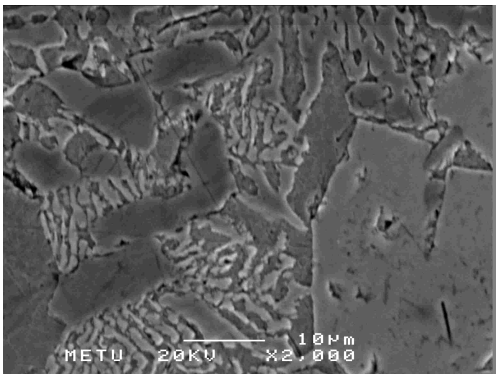

(c)

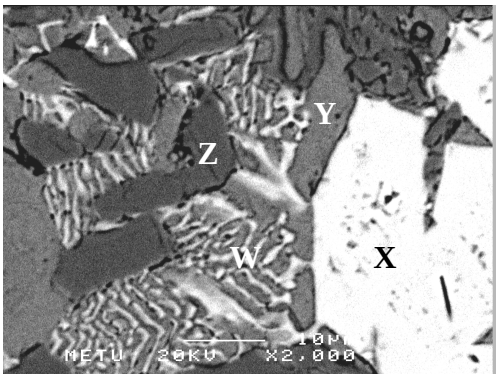

(d)

Sample	Analyzed Region	Element	Weight % (±2)	Atom % (±2)
Slowly cooled	General	Fe	88,60	92,43
		Nb	11,11	6,97
		Si	0,29	0,61
	White Region (X)	Fe	36,97	49,39
		Nb	63.03	50.61
	Light Gray Region (Y)	Fe	99,43	98,87
		Si	0,57	1,13
	Dark Gray Region (Z)	Fe	97.80	98.10
		Nb	1.79	1.08
		Si	0.41	0.82

(e)

Figure 4.11 Microstructure of slowly cooled sample, alloy S2: a) *500, SE image, b) *500, BS image, c) *2000, SE image, d) *2000, BS image and e) EDS analysis results.

The complex microstructure of the slowly cooled specimen indicates three different phases, with white, light gray and dark gray contrast (denoted as X, Y, Z on the micrograph, respectively) as can be seen in the backscatter image (BSE) more clearly, and irregular eutectic phase mixture (denoted as W on the micrograph). On the base of the morphology, Figure 4.11.b and d, EDS and XRD results, it can be proposed that white contrasted phase is most probably hexagonal FeNbB phase. When the growth morphologies and XRD results are taken into consideration, the light gray phase can be assigned to α-Fe phase, as this phase exhibits non-faceted growth morphology and, the dark gray phase to Fe_2B or Fe_3B, as the morphology seems to be faceted. However, all these phases cannot be identified exactly due to fact that the results of the compositional analysis taken from these regions do not give enough information for determination of the phases. Based on these considerations and the SEM images, it appears that the components of the irregular eutectic phase mixture are α-Fe and FeNbB intermetallic phase.

The thermal behavior of the wedge-cast sample of alloy S2 was examined by DSC. The DSC pattern, presented in Figure 4.12, reveals the existence of an amorphous phase and demonstrates that the crystallization takes place through a single stage exothermic peak. The summary of the thermal data obtained from the DSC experiments together with the GFA related parameters, T_{rg} and ΔT_x, are presented in Table 4.28. It is known from the literature that lowering of T_l upon alloying enhances the GFA [54, 55]. Comparison of Tables 4.26 and 4.28 reveals the fact that addition of ternary element, Nb, decreases the value of eutectic temperature, T_l.

Table 4.28 Thermal data compiled from DSC experiment for alloy S2 (Fe79B16Nb5); crystallization temperature (T_x), glass transition temperature (T_g), melting temperature (T_l), and enthalpy of crystallization and melting (ΔH_x and ΔH_m, respectively).

T_g (°C)	T_x (°C)	DH_x (J/gr)	T_l (°C)	DH_m (J/gr)	DT_x (°C)	T_{rg}
527,55	536,50	-0,1314	1140,34	1,8242	~ 8,95	~ 0,46

XRD pattern taken from the thin section of the wedge-cast sample indicated the formation of one broad peak and only two sharp peaks on the top of the broad peak. This result together with the DSC result designated the formation of an amorphous phase in the thinnest section of wedge-cast sample. To reveal the crystallization process, same section of the sample annealed at a temperature 800 °C, above the exothermic peak, for 3600 s in DSC. Figure 4.13 shows the XRD pattern of the annealed sample together with the XRD pattern of the as-cast sample for comparison.

The diffraction pattern of the annealed sample was identified to consist of α-Fe, Fe_3B, Fe_2B and FeNbB phases, which reveals that the single exothermic peak occurs by the simultaneous precipitation of these phases.

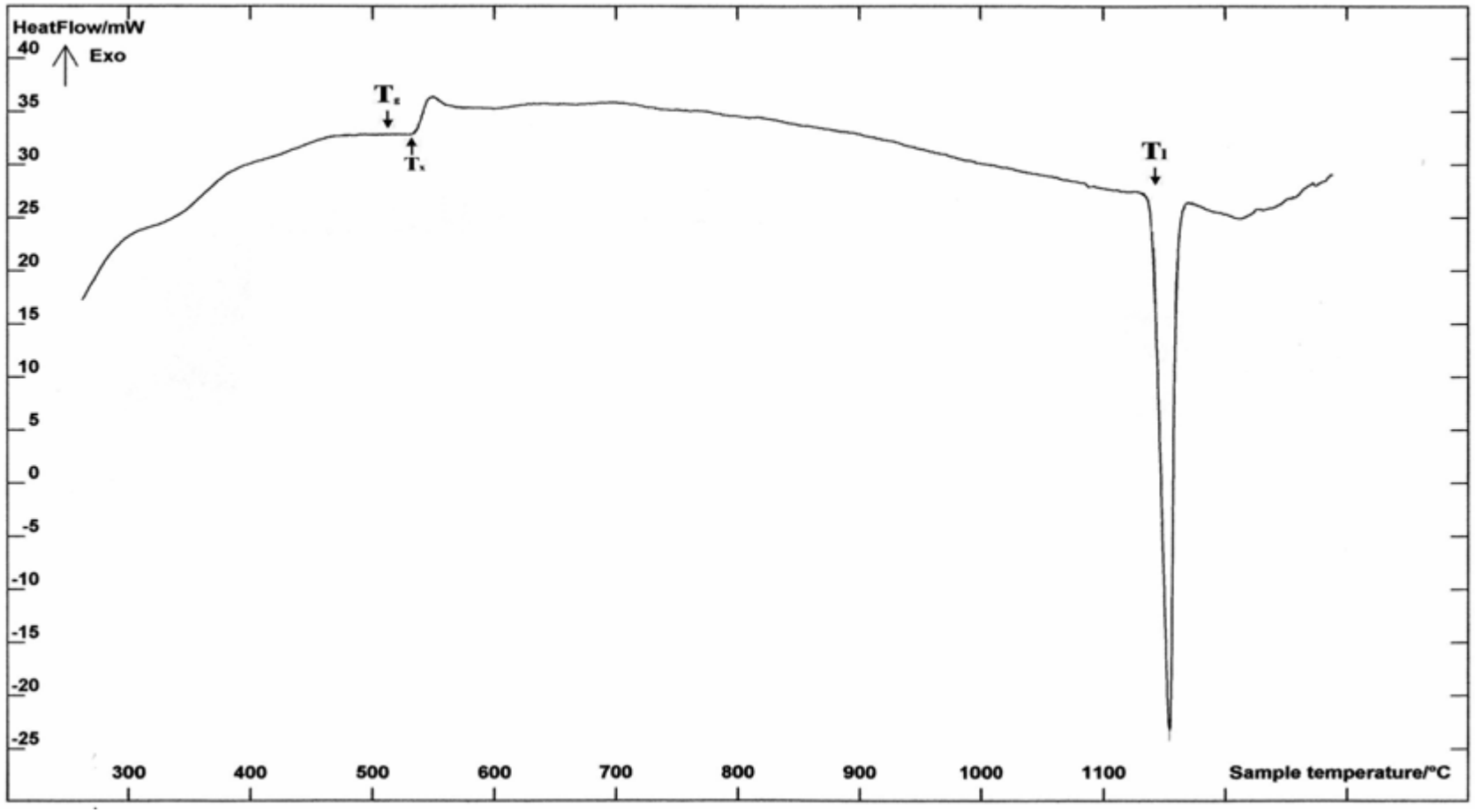

Figure 4.12 DSC pattern of alloy S2, obtained at a heating rate of 20 °C/min.

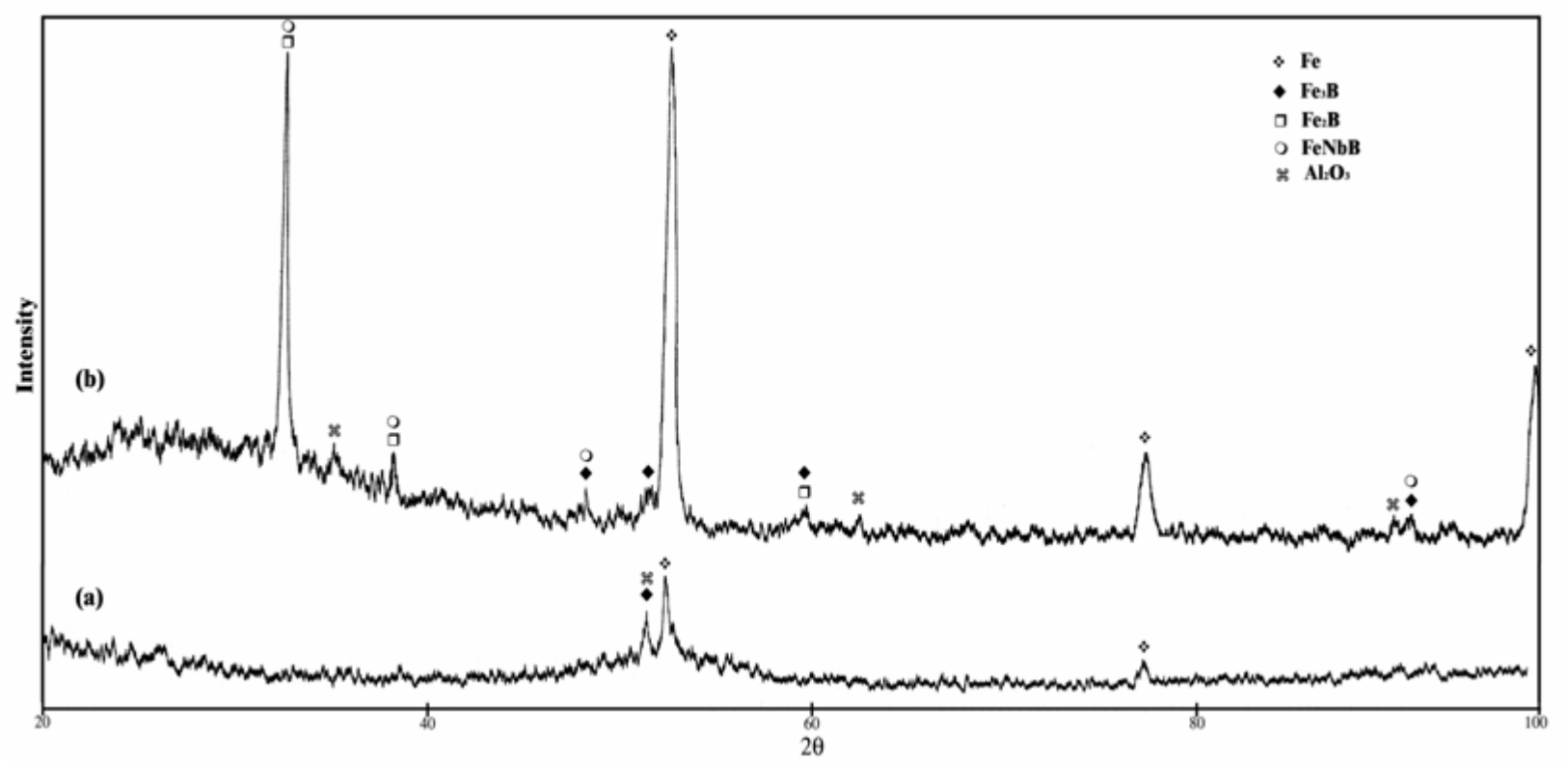

Figure 4.13 X-ray Diffraction patterns of the as cast sample, synthesized by using mold M1, (a) and heat treated (800 °C, 3600 s) sample (b) of alloy S2 ($Fe_{79}B_{17}Nb_5$).

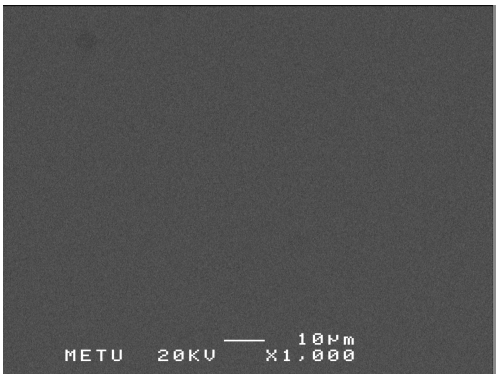

(a)

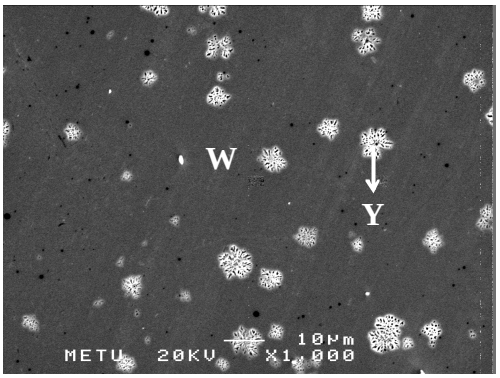

(b)

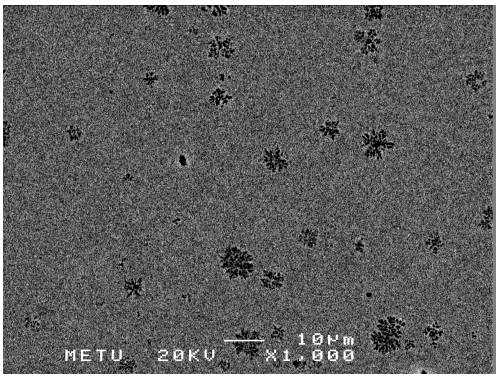

(c)

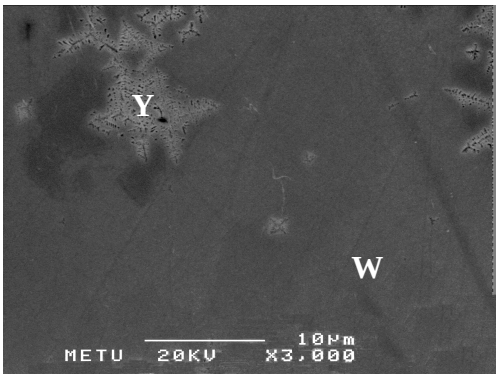

(d)

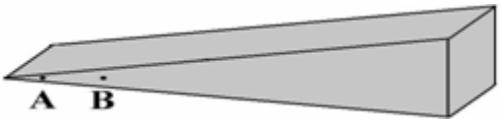

(e)

Sample	Analyzed Region	Element	Weight % (±2)	Atom % (±2)
Wedge-Cast	General	Fe	88,05	92,06
		Nb	11,66	7,33
		Si	0,29	0,61
	Section A	Fe	88,28	92,05
		Nb	11,31	7,09
		Si	0,42	0,86

(f)

Figure 4.14.a Microstructure of wedge-cast sample, S2: a) *1000, BS image of Section A, b) *1000, SE image of middle zones of Section B, c) *1000, BS image of (b), and d) *3000, SE image of zones near to the edge of Section B, e) Schematic view of the sample together with the representation of the sections, f) EDS analysis results.

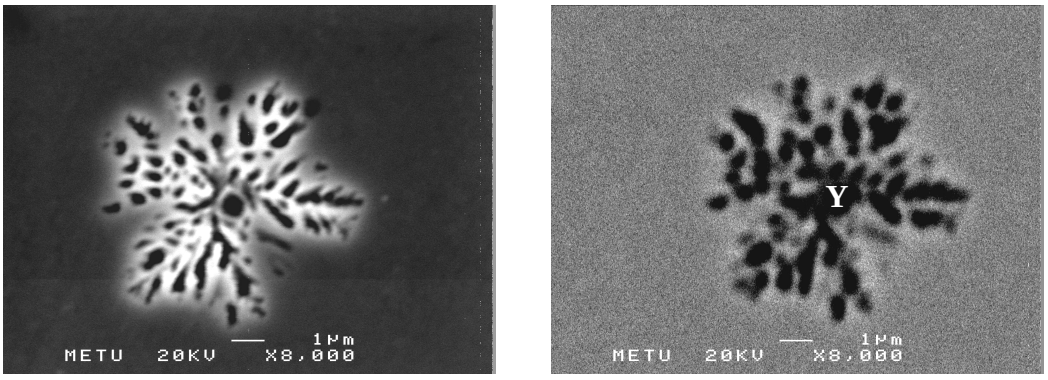

(a) **(b)**

Figure 4.15 Closer view of the dendrites (Y) in alloy S2: a) *8000, SE image, b) *8000, BS image.

The microstructures with the results of the EDS analysis of the thin sections for the wedge-cast sample of alloy S2 are presented in Figure 4.14. In the thinnest section (Section A), Figure 4.14.a, where the cooling rate was sufficiently higher, a featureless microstructure is observed which has been a typical appearance for amorphous materials. In relatively higher thickness (Section B), the microstructure of zones near to the edge of the sample is featureless, whereas in the middle, Figure 4.14.b, composed of fine dendritic phase (denoted as Y on the micrograph) embedded in a featureless matrix. In these micrographs, this dendritic phase, closer view of which is given in Figure 4.15, based on the XRD pattern and the growth morphology, was identified as a-Fe.

The microstructure of the middle and thick sections are presented in Figure 4.16 for the same sample. In middle thickness (Section C), the microstructure is similar to the microstructure of Section B, Figure 4.14.b, except formation of another phase with white contrast (denoted as X) was detected as seen in backscatter image more clearly. Based on the morphology and XRD results, this phase was identified as FeNbB. The thickest sections (Section D), $t \cong 6$ mm, exhibit quite different and

complex appearance than the microstructures of both slowly cooled and relatively thinner sections of the wedge-cast sample. In this microstructure, the eutectic structure, observed under near equilibrium conditions, could not be detected and instead, the microstructure is composed of micron scale crystallites. This variation in microstructure with cooling rate indicates the problematic growth of the irregular eutectic structure.

Furthermore, the effect of the cooling rate on the microstructures can be seen clearly by comparing the Figure 4.14.b and Figure 4.16.a, as the thickness of the sample increases the nucleation rate increases as expected due to decrease in the attained cooling rates.

On the base of the microstructural findings of the slowly cooled and wedge-cast specimens, it can be stated that the formation of featureless matrix in this alloy occurs due to the suppression of the eutectic growth under rapid cooling conditions. In the thinnest section of the wedge-cast sample, the fully featureless microstructure was observed most probably due to the fact that the achieved critical cooling rate value was higher than the required critical cooling rate for glass formation. The suppression of the eutectic phase most probably resulted from the problematic growth of the constituent FeNbB intermetallic phase.

All these findings have shown that the GFA of Fe-B-Nb ternary system is higher as compared to Fe-B binary system and, proved the results of the predicted theoretical calculations: the addition of Nb element leads to a considerable increase in GFA of the binary Fe-B system by increasing the ordering energy.

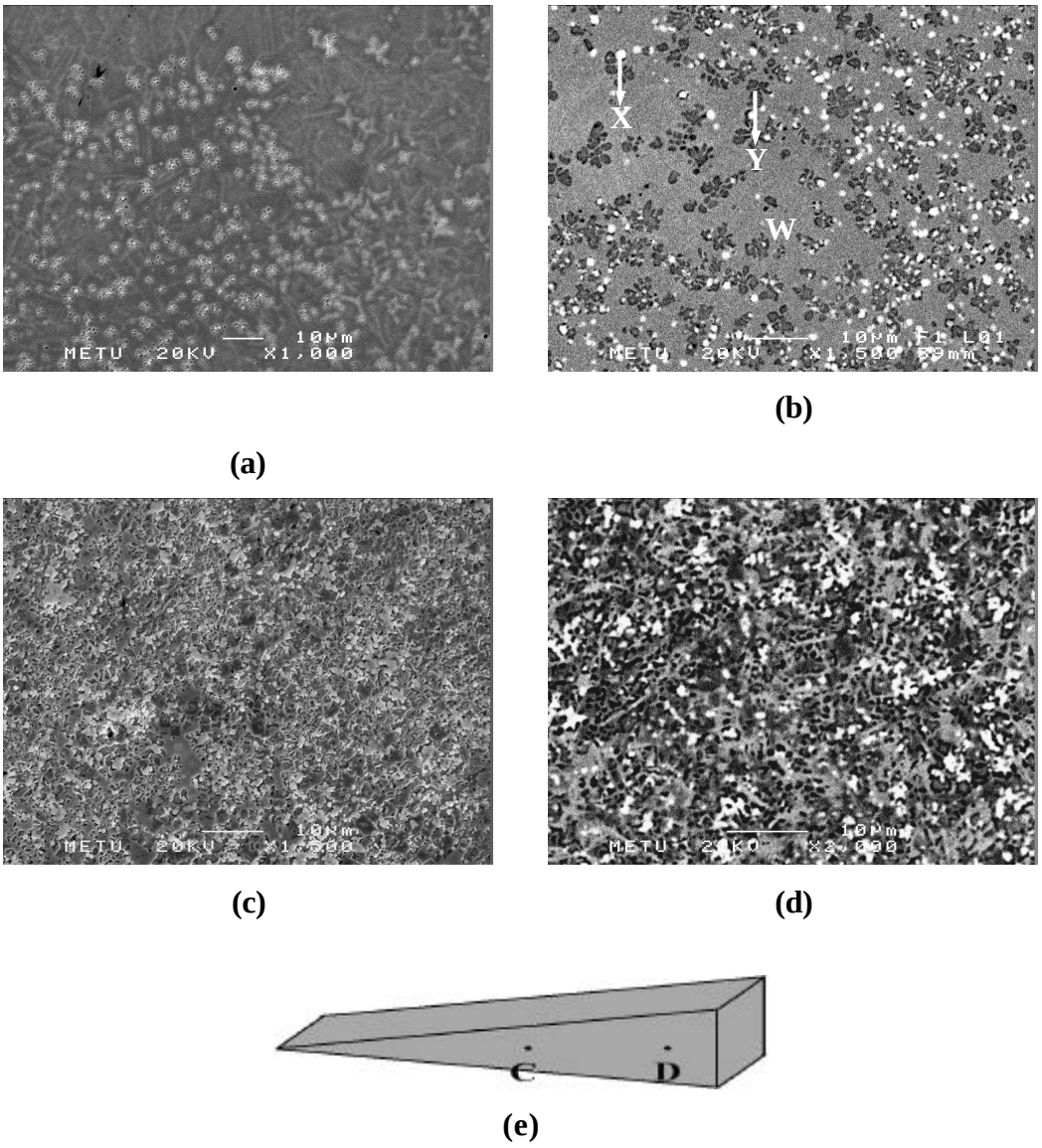

Figure 4.16 Microstructure of wedge-cast sample, S2: a) *1000, SE image and b) *1500, BS image of Section C, c) *1500, SE image and d) *2000, BS image of thickest section (Section D), e) Schematic view of the sample together with the representation of the sections.

To investigate the effect of the mold design, same composition was prepared and synthesized by using Cu-mold, M1. The only difference between mold M1 and M2 is their dimensions, given in Table 3.9. Maximum sample thickness achieved for mold M1 and M2 are 3 mm and 7 mm, respectively.

The DSC experiment gave the same result with the previous wedge-cast sample synthesized by using mold M2, Figure 4.12, and hence will not be presented here. Similarly, the microstructural examination reveals out almost same structure with Figures 4.14 and 4.16, with an exception that the thickest sections of the alloy synthesized by using mold M2 composed of micron scale crystallites, seen from Figure 4.16.d, whereas for the alloy cast into mold M1, even in the thickest sections the structure composed of α-Fe dendrites embedded in an amorphous matrix, similar to section C of the alloy cast into mold M2. This result is expected as the maximum sample thickness that can be attained for mold M1, 3mm, comes across approximately to the middle sections of sample cast into the mold M2.

The XRD pattern of the thinnest of the sample synthesized by using mold M1 is given in Figure 4.17, together with the diffraction pattern of the thickest section for comparison. Regarding to this figure, it can be realized that while the XRD pattern of the thinnest section consists of a single broad peak, which is a typical appearance for an amorphous material, the XRD pattern taken from the thickest section consists of various peaks corresponding to the a-Fe, Fe_2B, Fe_3B and FeNbB phases.

When the XRD patterns taken from the thinnest sections of the samples synthesized by using mold M2 and M1, Figure 4.14 and 4.17, respectively, are compared, it can be seen that the XRD pattern of the sample synthesized by using mold M1 consists of one broad peak, whereas the pattern of the sample synthesized by using M2 consists of one broad peak and two sharp peaks. On these account, it can be stated that the mold design is important for the production of bulk metallic glasses.

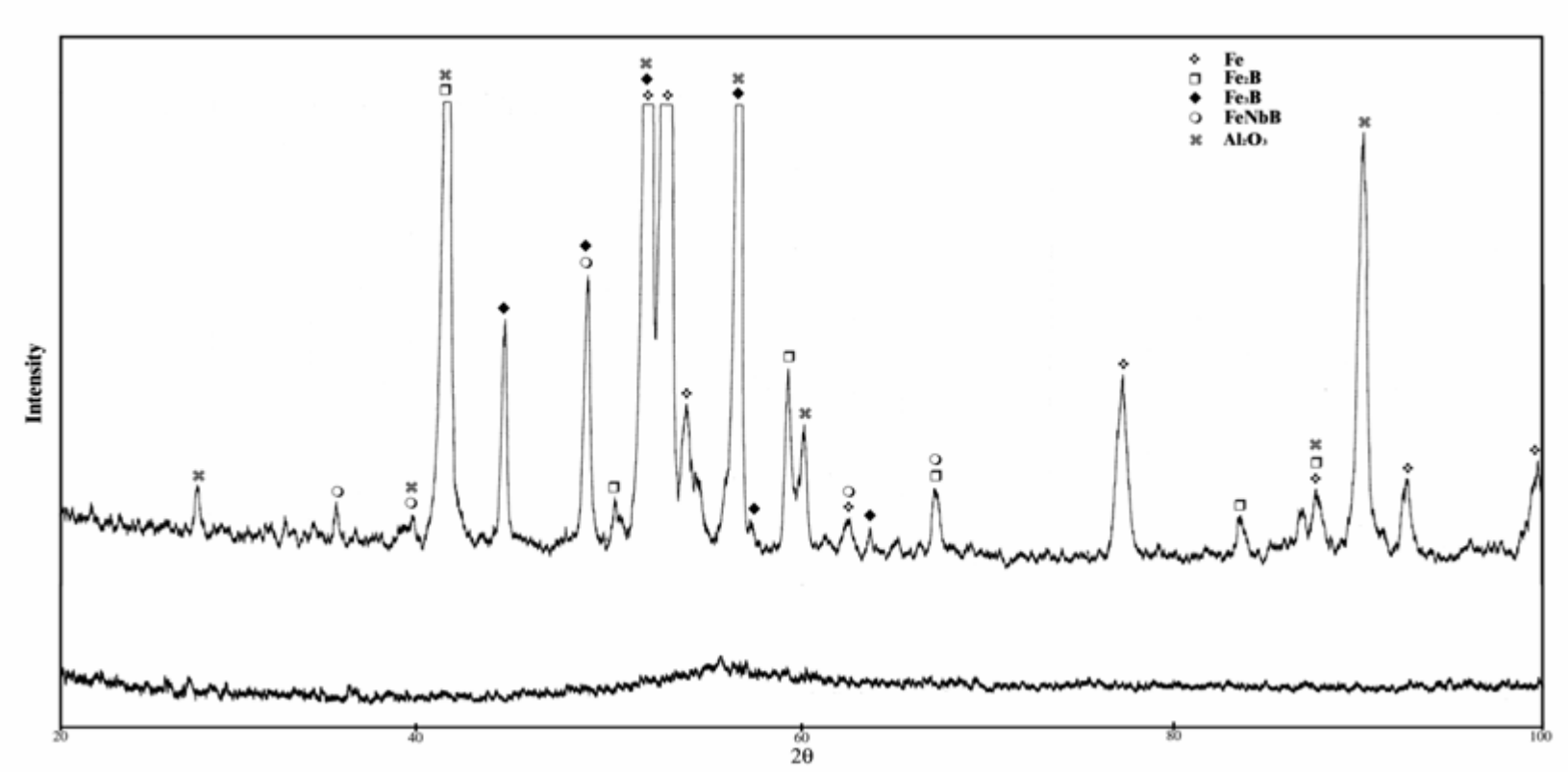

Figure 4.17 X-ray Diffraction pattern of the wedge-cast sample, synthesized by using mold M1, of alloy S2 (Fe79B17Nb5), taken from the thinnest section (a) and thickest section (b).

4.2.1.3 Ternary Fe-B-W Alloy

After investigating the effect of Nb element addition on glass forming ability for the selected Fe-B binary composition, W element was selected to verify the results of the theoretical calculations further and Fe79B16W5 (alloy S3) composition was synthesized at a casting temperature of 1250 °C by using copper mold M1. Similar to previous experiments, to understand the effect of the cooling rate on solidification behavior same alloy composition was also prepared under near equilibrium conditions. The XRD pattern of the slowly cooled specimen, given in Figure 4.18, indicates the possibility of formation of α-Fe, Fe_2W, Fe_2B phases and aluminum oxide.

As can be seen from Figure 4.19, the microstructures of the slowly cooled sample consist of two different phases, with light and dark gray contrast (denoted as X and Y on the micrograph), and irregular eutectic phase mixture (denoted as V on the micrograph). According to growth morphologies, the EDS and XRD results, the light gray phase can be assigned to Fe_2W intermetallic phase and the dark gray dendritic phase to a-Fe. The components of the irregular eutectic phase mixture are probably non-faceted a-Fe and faceted Fe_2B intermetallic phases, but exact identification could not be succeeded. Furthermore, the black spots, seen in the micrographs, were identified as small aluminum oxide particles.

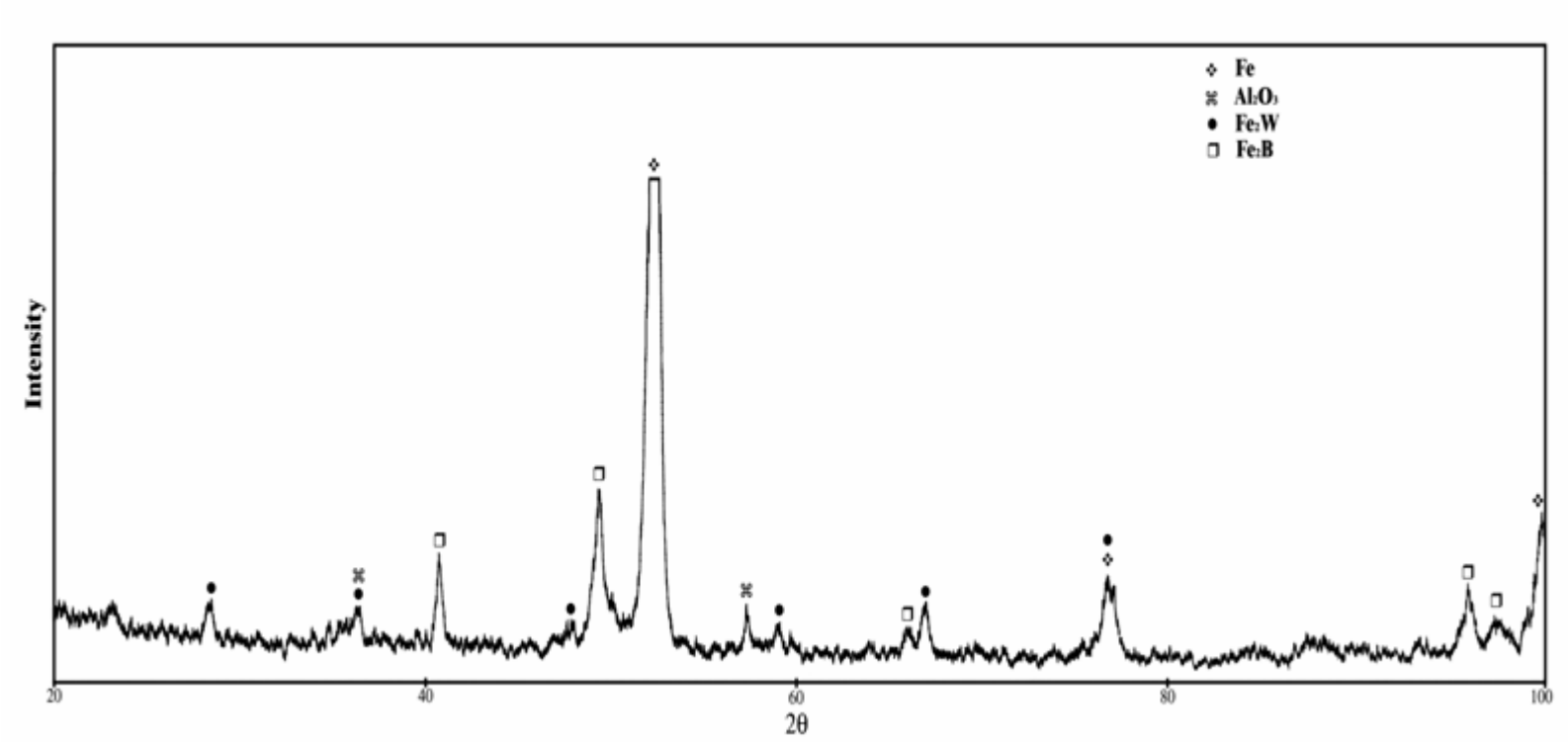

Figure 4.18 X-ray Diffraction pattern of the slowly cooled sample of alloy S3 ($Fe_{79}B_{17}W_5$).

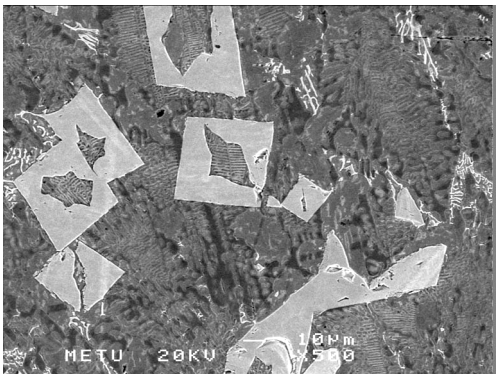

(a)

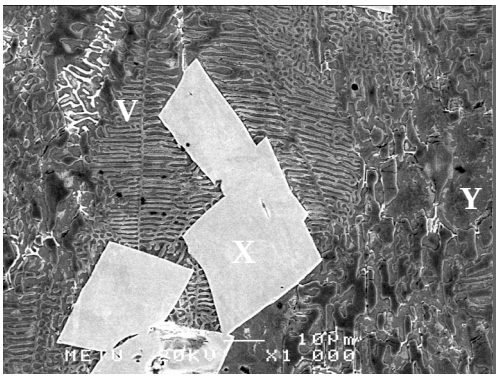

(b)

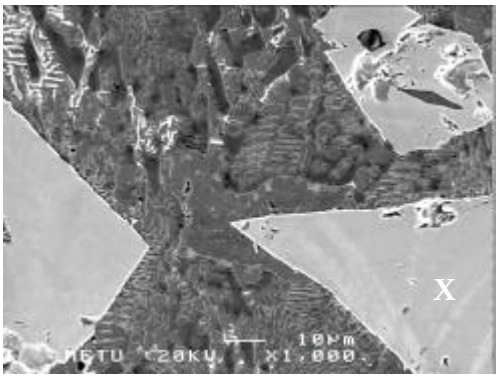

(c)

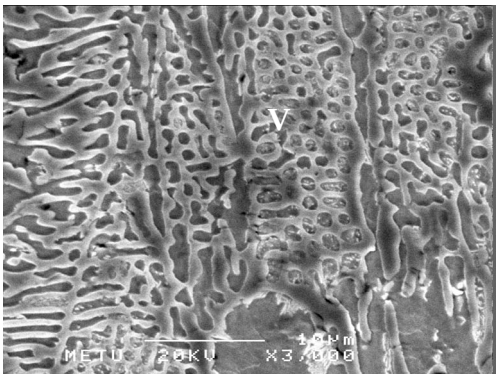

(d)

Sample	Analyzed Region	Element	Weight % (±2)	Atom % (±2)
Slowly cooled	General	Fe	84,55	94,74
		W	15,45	5,26
	Light Gray Region (X)	Fe	34,63	63,56
		W	65,37	36,44

(e)

Figure 4.19 Microstructure of slowly cooled sample, alloy S3: a) *500, SE image, b) *1000, SE image, c) *1000, SE image, d) *3000, SE image, e) EDS analysis results.

For the wedge-cast sample, the DSC pattern, presented in Figure 4.20, reveals the existence of an amorphous phase. According to this figure, the crystallization takes place through two stage exothermic peak. The summary of the thermal data obtained from the DSC experiments together with the parameters, T_{rg} and ΔT_x is shown in Table 4.29. From this table, it can be stated that the addition of W element leads to a decrease in T_l, hence increase the GFA.

Table 4.29 Summary of the thermal data of alloy S3 ($Fe_{79}B_{16}W_5$); crystallization temperature (T_x), glass transition temperature (T_g), melting temperature (T_l), and enthalpy of crystallization and melting (ΔH_x and ΔH_m, respectively).

T_g (°C)	T_{x1} (°C)	ΔH_{x1} (J/gr)	T_{x2} (°C)	ΔH_{x2} (J/gr)	T_l (°C)	$\Delta H_{m.}$ (J/gr)	ΔT_x (°C)	T_{rg}
507,09	533,20	-0,4039	758,32	-0,1199	1152,30	2,3533	~26,11	~0,44

XRD pattern, Figure 4.21, taken from the thin section of the wedge-cast sample indicated the formation of a-Fe, Fe_2W (with hexagonal structure), Fe_2B, Fe_3B phases and Al_2O_3. On the base of the XRD and DSC experiments results, it can be stated that at least partially amorphous material was obtained in thin sections.

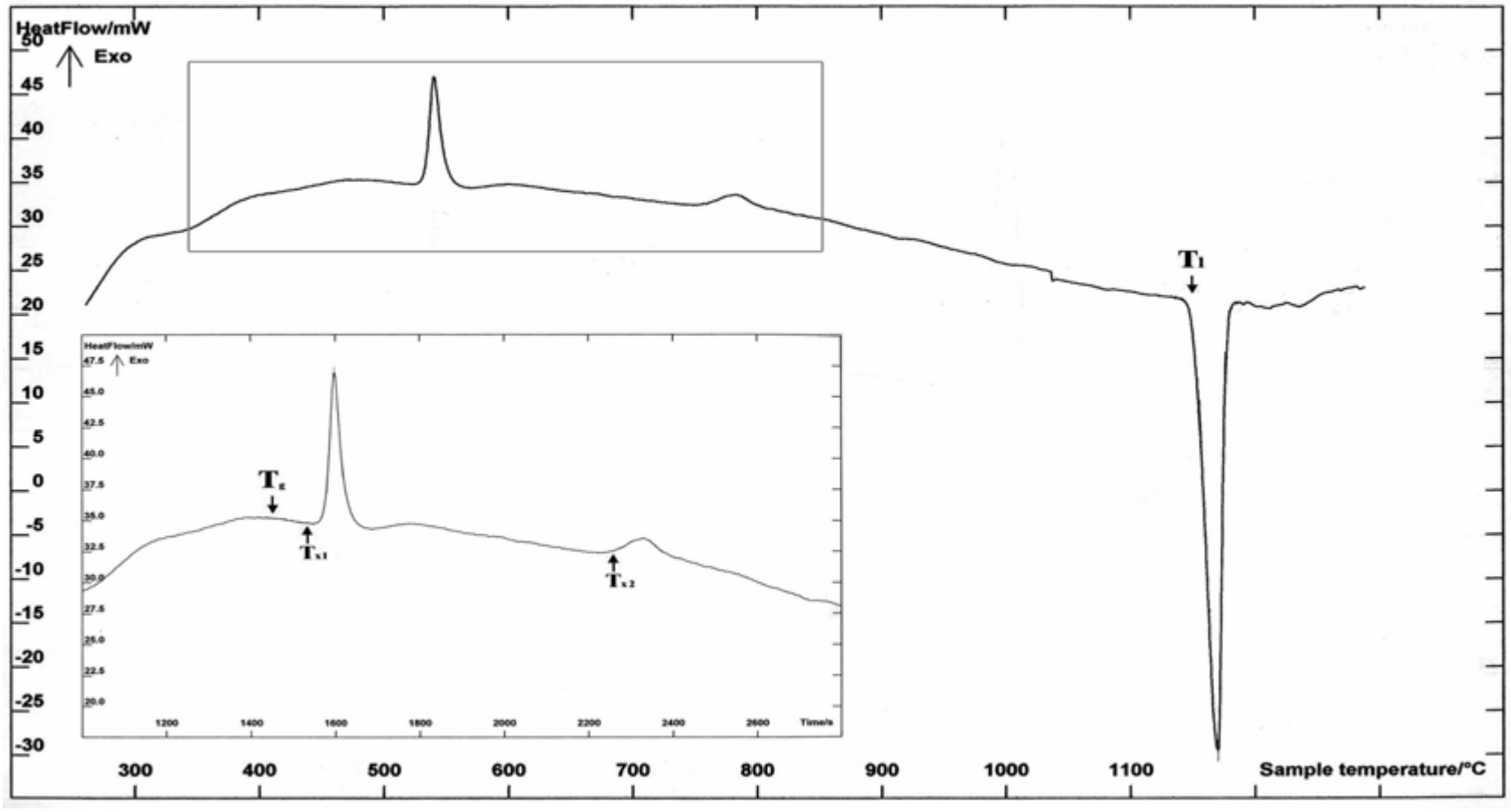

Figure 4.20 DSC pattern of alloy S3, obtained at a heating rate of 20 °C/min.

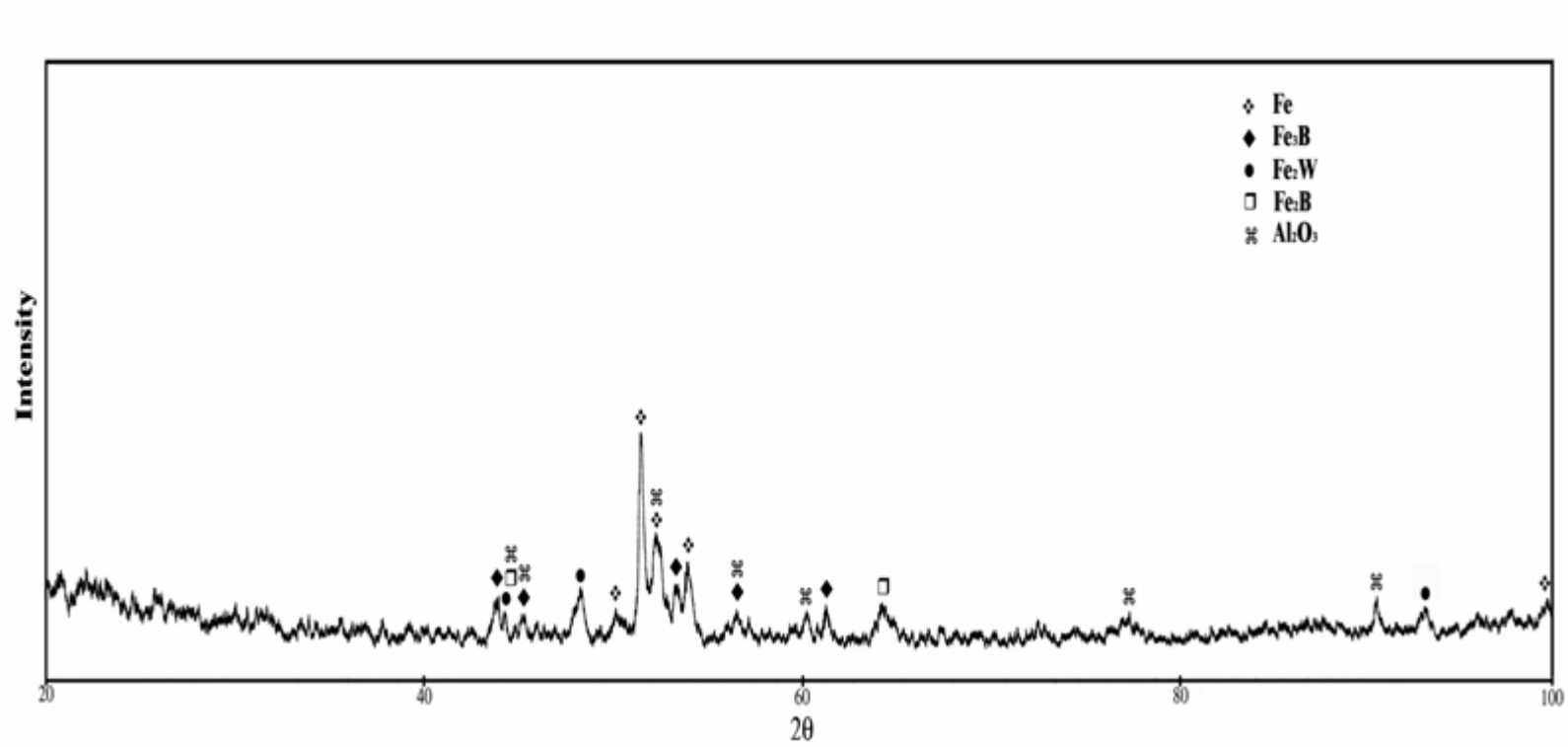

Figure 4. 21 X-ray Diffraction pattern of the wedge-cast sample of alloy S3 (Fe79B17W5).

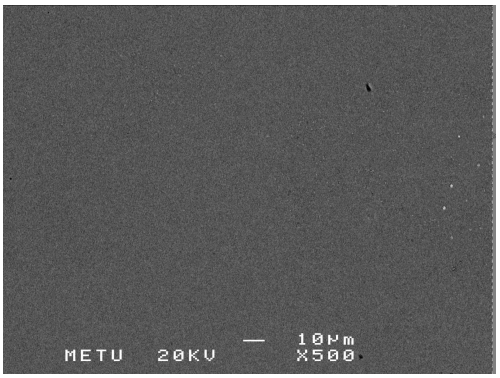

(a)

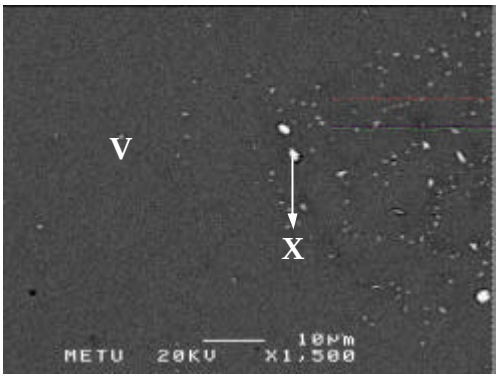

(b)

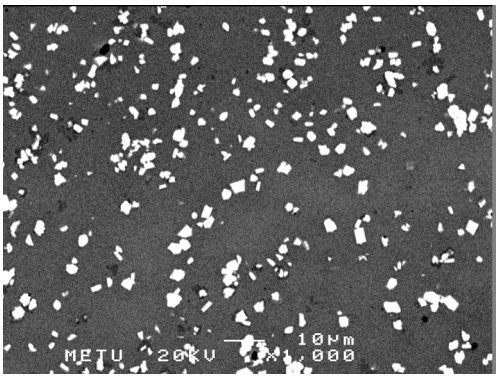

(c)

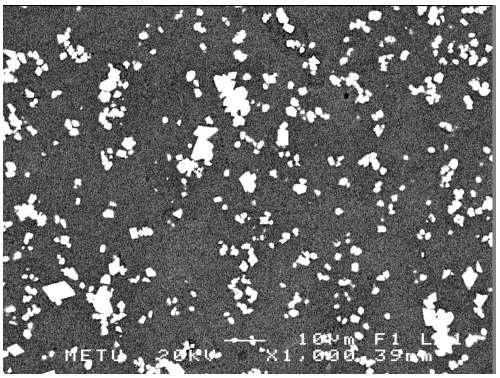

(d)

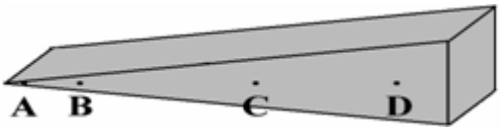

(e)

Sample	Analyzed Region	Element	Weight % (±2)	Atom % (±2)
Wedge-cast	General	Fe	84,15	94,59
		W	15,85	5,41
	Matrix (V)	Fe	81,35	93,49
		W	18,65	6,51
	Light Gray Region (X)	Fe	35,09	64,02
		W	64,91	35,98

(f)

Figure 4.22 Microstructure of wedge-cast sample, alloy S3: a) *500, BS image of section A, b) *1500, BS image of section B, c) *1000, BS image of section C, d) *1000, BS image of section D, e) Schematic view of the sample together with the representation of the sections, f) EDS analysis results.

The microstructure for the wedge cast alloy is presented in Figure 4.22. In the thinnest section (Section A), a featureless microstructure was observed which is a typical appearance of amorphous materials. In relatively higher thickness (Section B), the microstructure composed of a faceted phase (denoted as X on the micrograph), Fe_2W regarding to the EDS and XRD results, embedded in a featureless matrix. This microstructure was preserved throughout the sample with only a difference that the morphology became coarser with an increase in the sample thickness, as seen from the micrographs of section B, C and D of the sample. These microstructural findings supported the result of the DSC experiments.

When the solidification structures of slowly cooled and wedge-cast samples are compared, it can be realized that the glass formation in this alloy occurs due to the suppression of the eutectic growth under rapid cooling conditions. The ease of suppression of the eutectic phase can be understood by considering the fact that the constituent phase Fe_2B intermetallic has growth problems since exhibits faceted growth morphology.

4.2.2 Production of Fe-based Alloys by Using High Purity Raw Materials

In order to compare the results between the alloys produced by using low grade commercial Fe-B alloy and by using high purity elements and, to investigate the effect of the impurity elements that exist in the low grade commercial Fe-B, selected compositions of Fe-B and Fe-B-Nb systems were synthesized from the high purity elements as a raw material. To compare the solidification structures and the effect of the cooling rate on solidification structure, similar to previous investigations near equilibrium cooling of the same alloys were achieved by allowing the alloy to solidify completely in crucible. In this section the results of these experiments will be discussed.

4.2.2.1 Binary Fe-B Alloy

Similar to first experiment, binary eutectic composition Fe83B17 (S4) was prepared, however, high purity raw materials were used. For the rapid cooling, to obtain the same solidification conditions with alloy S1, alloy S4 was synthesized by using same mold, M1, with a casting temperature of 1150 °C.

The XRD patterns of the slowly cooled and wedge-cast samples are given in Figure 4.23.a and b, respectively. Similar to alloy S1, these XRD patterns reveal the formation of α-Fe, Fe_2B and aluminum oxide for slowly cooled and beside these phases Fe_3B intermetallic phase for the wedge-cast sample, as expected.

SEM images of slowly cooled sample of alloy S4 are given in Figure 4.24. Similar to XRD pattern, the solidification structure of the slowly cooled sample resemble to the solidification structure of slowly cooled sample of alloy S1, Figure 4.9; formation of primary Fe_2B phase (X) and a irregular eutectic phase mixture (Y) between the α-Fe and Fe_2B were detected.

The microstructure of wedge-cast sample of alloy S4, presented in Figure 4.24.c and d, reveals that the microstructure is fully eutectic with an irregular morphology. From these micrographs, it can be realized that formed eutectic phase mixture exhibits very fine morphology due to the attained higher cooling rates as compared with the near equilibrium cooling conditions.

In addition, from Figure 4.24.c, individual eutectic grains can be easily distinguished from the color contrast, resulted from the orientation difference of the eutectic phase mixture. Based on the microstructural findings and XRD pattern, it can be interpreted that the component of the eutectic phase mixture that exhibits non-faceted growth morphology is probably α-Fe phase, however the other component can be either Fe_2B or Fe_3B faceted intermetallic phases.

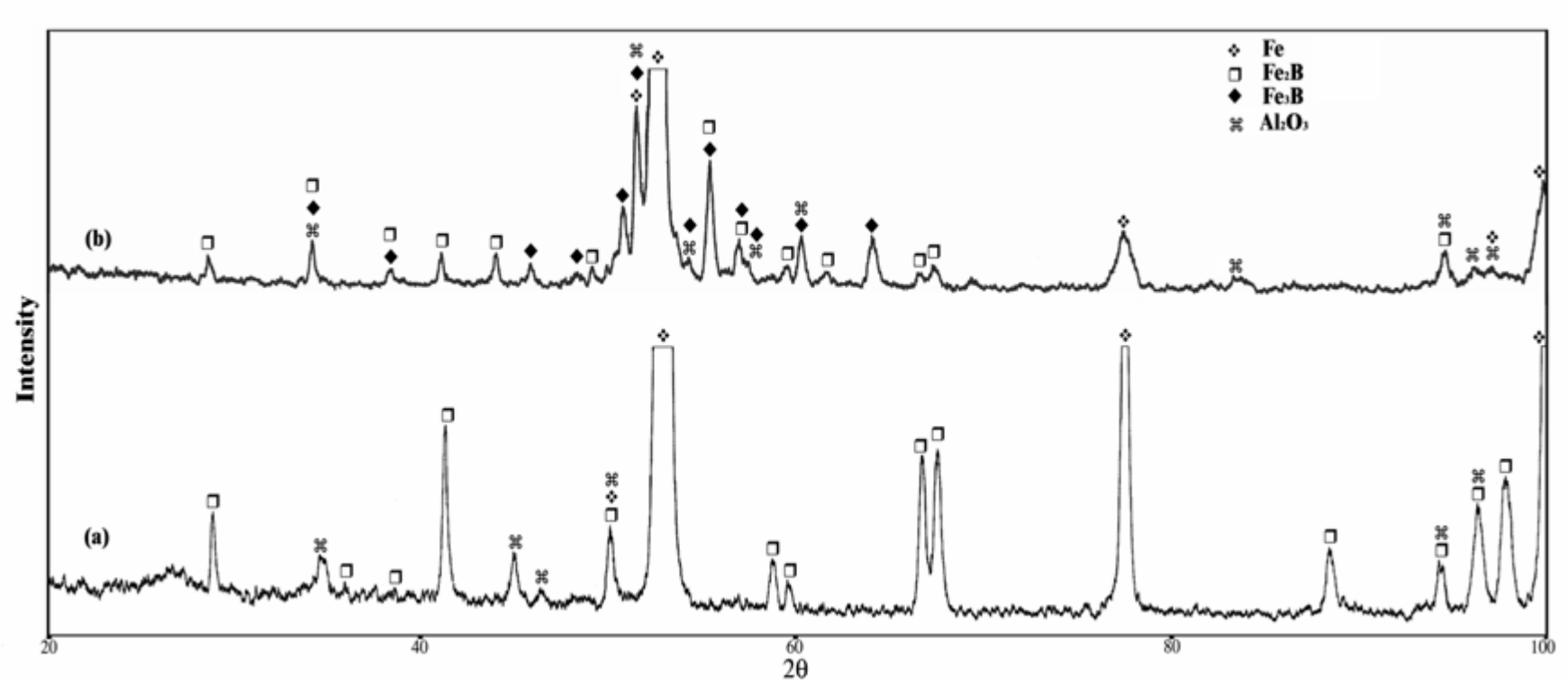

Figure 4.23 X-ray Diffraction patterns of the slowly cooled sample (a) and wedge-cast sample (b) of alloy S4 (Fe83B17).

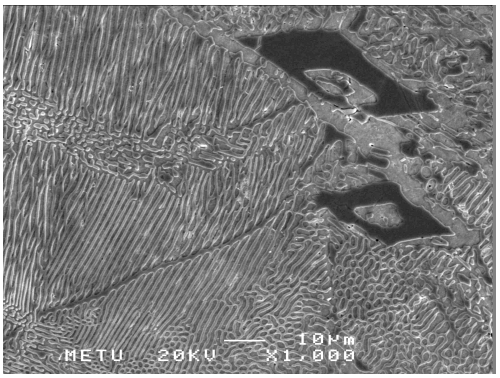

(a)

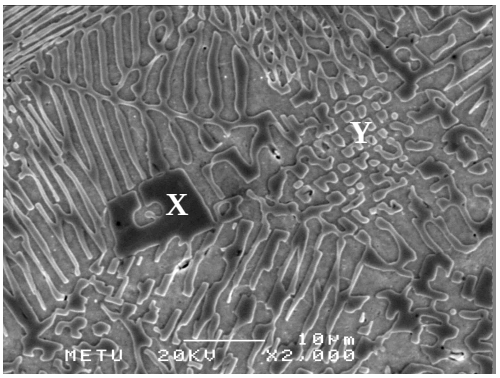

(b)

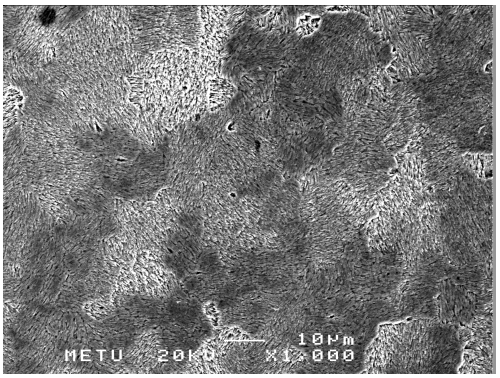

(c)

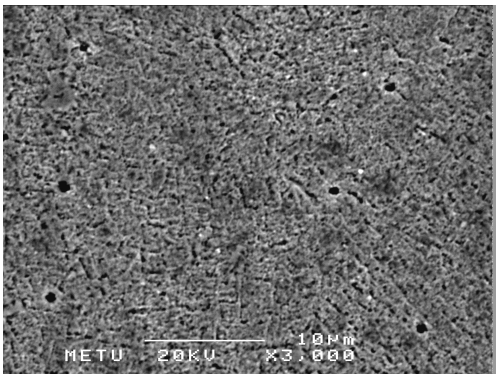

(d)

Sample	Analyzed Region	Element	Weight % (±2)	Atom % (±2)
Slowly cooled	General	Fe	100	100
Wedge-cast	General	Fe	100	100

(e)

Figure 4.24 Microstructure of slowly cooled and wedge-cast sample, alloy S4: a) *1000, SE image of slowly cooled sample, b) *2000, SE image of slowly cooled sample, c) *1000, SE image of the thin section of wedge cast sample, d) *3000, SE image of the thick section of wedge cast sample, e) EDS analysis results.

DSC pattern for the wedge-cast alloy, presented in Figure 4.25, obtained at a heating rate of 20 °C/min, gives similar result with the wedge-cast sample of alloy S1, Figure 4.7; the glass transition and crystallization peak were not appear. In this alloy, the melting occurs through a broad single-stage endothermic, eutectic melting, as seen from the figure. The summary of the thermal data, obtained from the DSC experiments, is tabulated in Table 4.30.

Table 4.30 Thermal data compiled from the DSC experiment for alloy S4 (Fe83B17); melting temperature (T_l), and enthalpy of melting (ΔH_m).

T_l (°C)	DH_m. (J/gr)
1163,32	2,9012

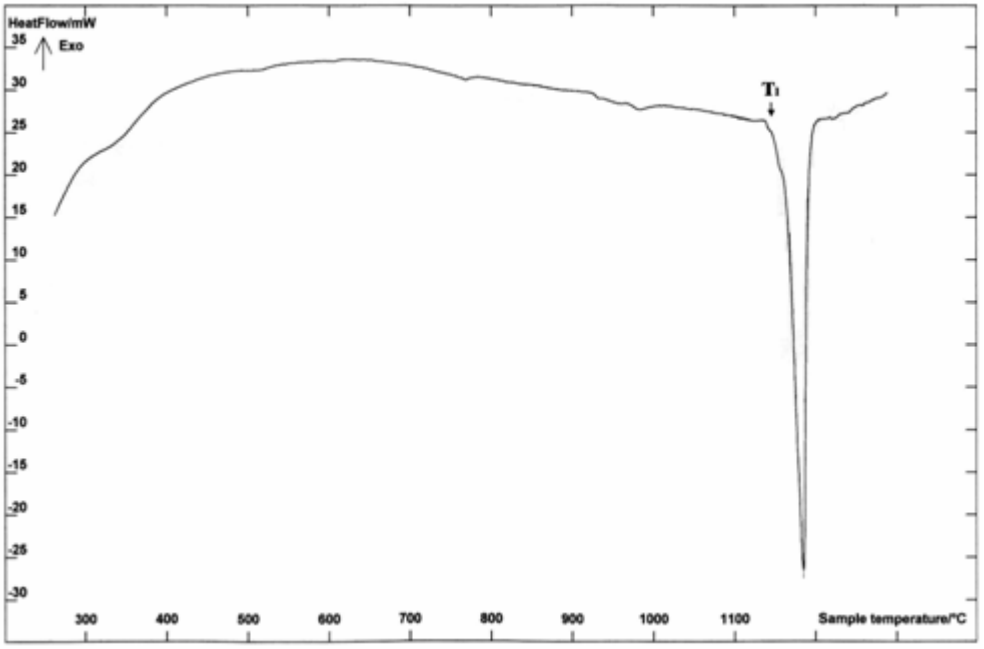

Figure 4.25 DSC pattern of alloy S4, obtained at a heating rate of 20 °C/min.

4.2.2.2 Ternary Fe-B-Nb Alloy

As a next step slowly cooled and wedge cast samples of Fe79B17Nb5 composition (alloy S5) were prepared by using the high purity elements, to compare the results with the alloy S2. The XRD pattern of the slowly cooled sample, Figure 4.26, denoted the formation of a-Fe, Fe_2B, Fe_3B, FeNbB and Al_2O_3 phases, similar to XRD pattern of the slowly cooled sample of alloy S2.

The SEM images of the slowly cooled specimen, presented in Figure 4.27, are analogous to the images of alloy S2, Figure 4.11. On the base of the microstructure findings of alloy S2, the white contrasted phase (denoted as X on the micrographs) was identified as FeNbB phase, light gray and the dark gray contrasted phases (denoted as Y and Z on the micrographs) can be assigned to a-Fe and Fe_2B or Fe_3B, respectively, but exact nature of these phases cannot be identified.

For the wedge-cast alloy, the thermal behavior was examined by DSC. The DSC pattern, presented in Figure 4.28, reveals the existence of an amorphous phase; the glass transition and crystallization peak can be seen. The melting of the alloy occurs through a single stage endothermic peak, melting of the eutectic phase mixture. When DSC patterns of alloy S2 and S4 are compared it can be realized that the crystallization peak is smaller in the DSC pattern of the alloy S4. This would tend to suggest that the volume fraction of formed amorphous phase is smaller for alloy S4. The summary of the thermal data obtained from the DSC experiments together with the parameters, T_{rg} and ΔT_x is presented in Table 4.31. Comparison between Tables 4.30 and 4.31 points out that the addition of Nb element leads to a decrease in the T_l value. The XRD pattern taken from the thinnest section of the wedge-cast sample of alloy S5 is given in Figure 4.29. This X-ray diffraction pattern, distinct from the XRD pattern of wedge-cast sample of alloy S2, pointed out the presence of possible phases; a-Fe, Fe_2B, Fe_3B, FeNbB and aluminum oxide.

Table 4.31 Summary of the thermal data of alloy S5 (Fe79B16Nb5); crystallization temperature (T_x), glass transition temperature (T_g), melting temperature (T_l), and enthalpy of crystallization and melting (ΔH_x and ΔH_m, respectively).

T_g (°C)	T_x (°C)	ΔH_x (J/gr)	T_l (°C)	ΔH_m. (J/gr)	ΔT_x (°C)	T_{rg}
490,02	501,31	-2,6040	1142,21	88,4717	~11,29	~0,43

The SEM images for the wedge cast alloy are presented in Figure 4.30. In these microstructures, the eutectic phase mixture and the intermetallic phases, observed in slowly cooled sample of the same alloy, could not be detected. Instead, the microstructure in the thinnest section consists of dendritic phase (denoted as Y on the micrographs), can be seen in Figure 4.31 more clearly, embedded in a featureless matrix. These dendrites were identified as a-Fe, on the base of the XRD results and the previous experimental findings. This microstructure was preserved throughout the sample with only a difference that the formation of a new phase with a white contrast (denoted as X on the micrographs) was detected. This phase was identified as FeNbB regarding to the XRD and EDS results. As can be seen from these micrographs, the solidification structure resembles to the structure of alloy S2, from Figures 4.14 to 4.16, with an exception that the alloy S2 exhibits fully amorphous structure in the thinnest sections.

In order to determine the reasons of the differences between the wedge-cast samples of alloys S2 and S4, synthesized by using commercial Fe-B alloy and high purity raw materials, respectively, detailed analysis are required. However, it can be interpreted that this difference arise due to the impurity elements that exist in commercial Fe-B alloy, which may possess positive effect in increasing the GFA.

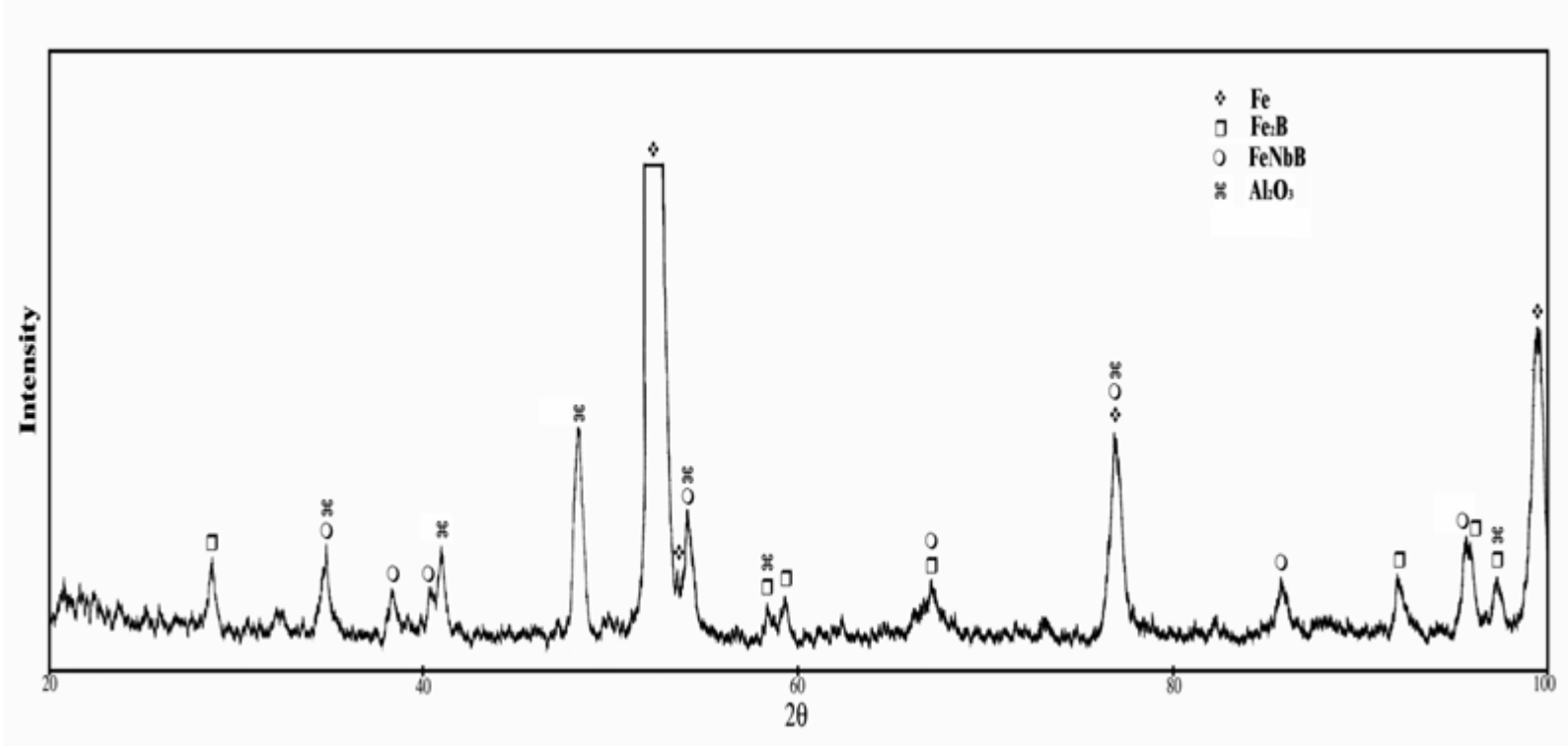

Figure 4.26 X-ray Diffraction pattern of the slowly cooled sample of alloy S5 (Fe79B16Nb5).

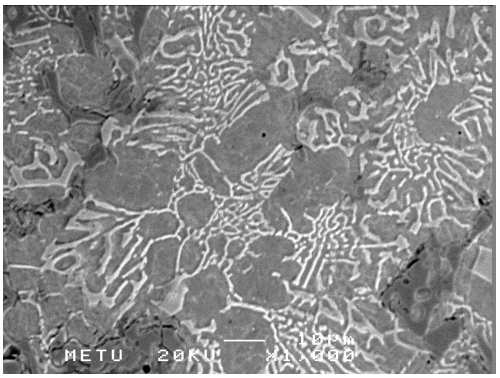

(a)

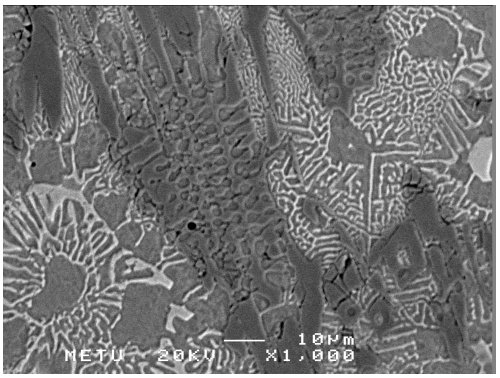

(b)

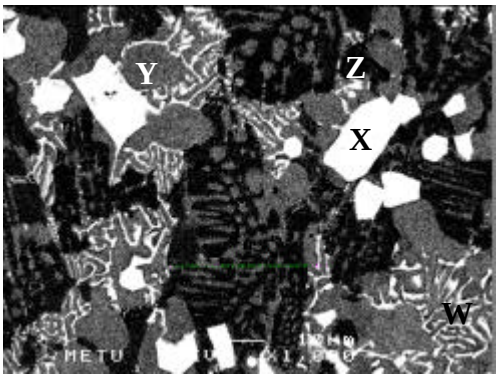

(c)

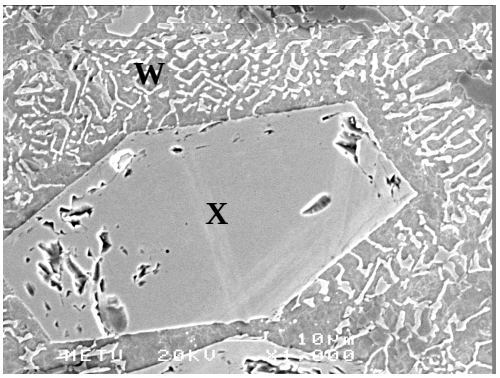

(d)

Sample	Analyzed Region	Element	Weight % (±2)	Atom % (±2)
Wedge-cast	General	Fe	88,08	92,48
		Nb	11,92	7,52
	White Region (X)	Fe	39,58	52,15
		Nb	60,42	47,85
	Light Gray Region (Y)	Fe	100	100
	Dark Gray Region (Z)	Fe	100	100

(e)

Figure 4.27 Microstructure of wedge-cast sample, Fe79B16Nb5: a) *1000, SE image, b) *1000, SE image, c) *1000, BS image, d) *1000, SE image, e) EDS analysis results.

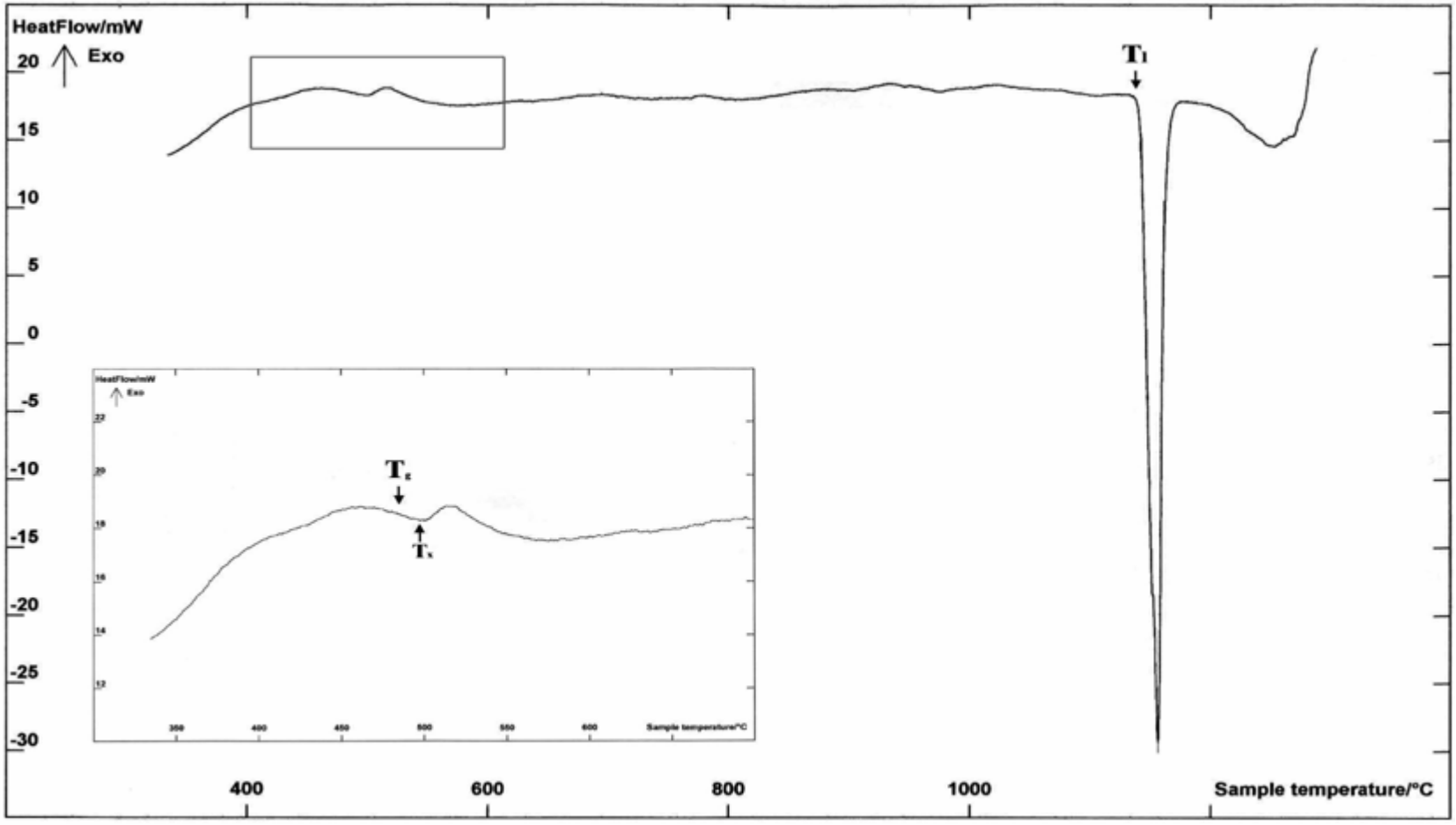

Figure 4.28 DSC pattern of alloy S5, obtained at a heating rate of 20 °C/min.

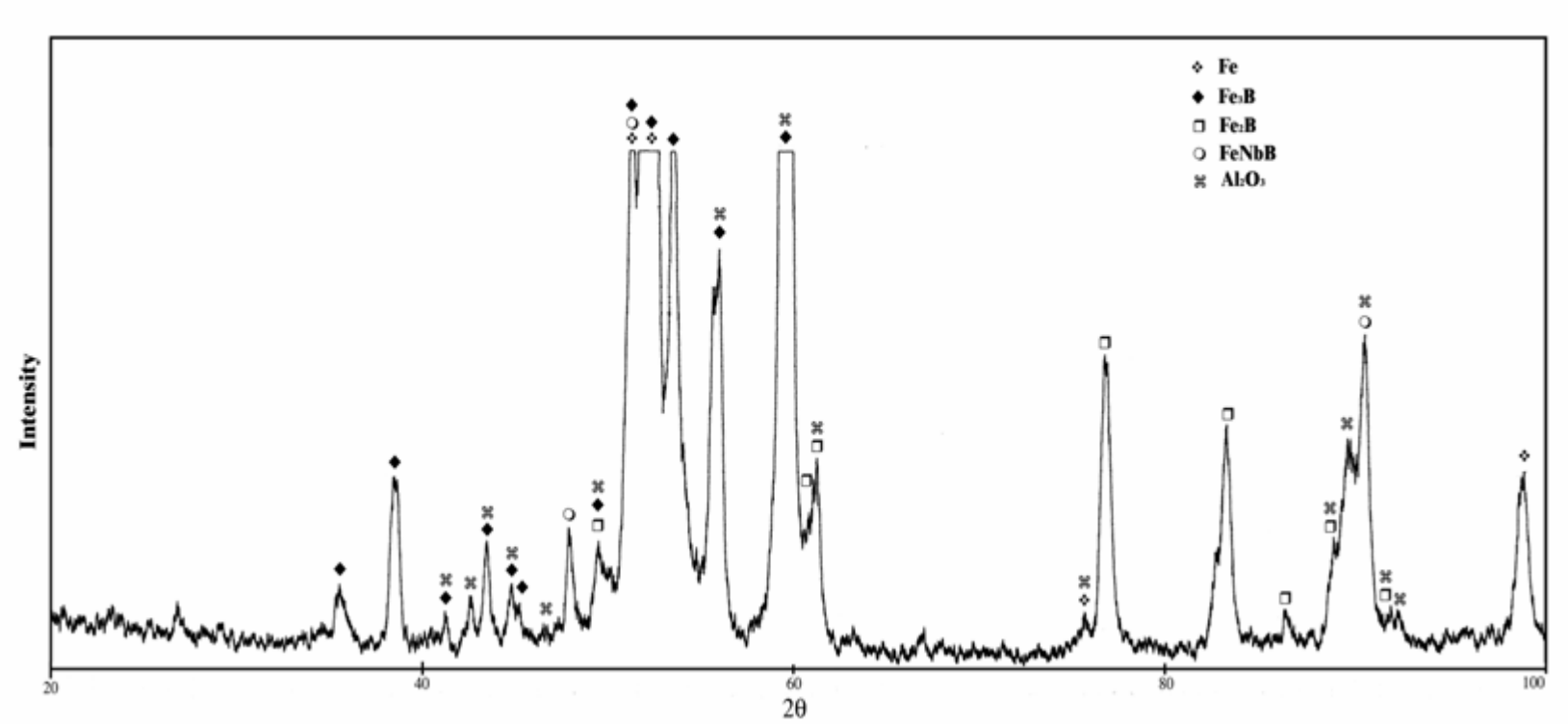

Figure 4.29 X-ray Diffraction pattern of the wedge-cast sample of alloy S5 (Fe79B16Nb5).

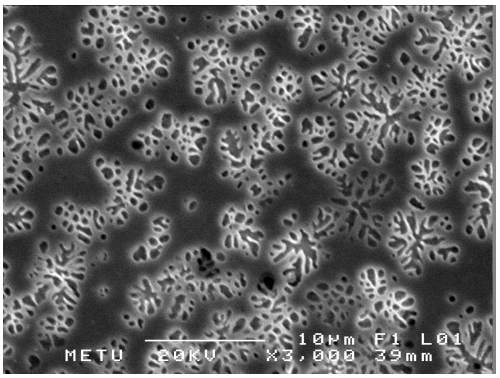

(a)

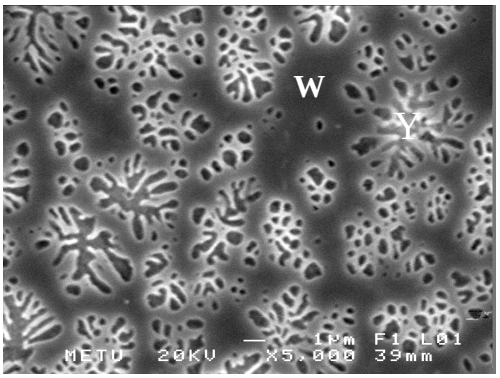

(b)

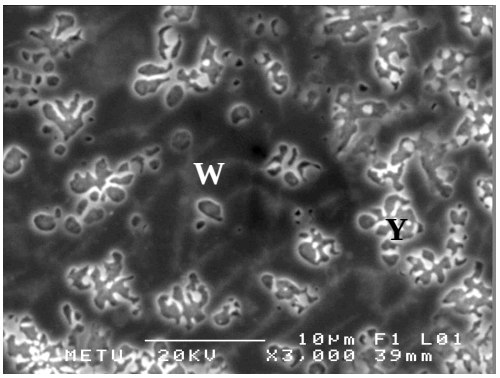

(c)

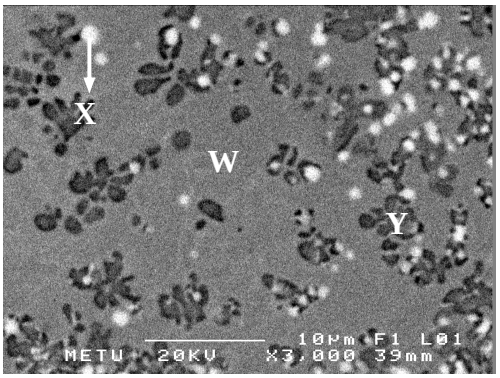

(d)

Sample	Analyzed Region	Element	Weight % (±2)	Atom % (±2)
Wedge-cast	General	Fe	84,76	90,24
		Nb	15,24	9,76
	Matrix (W)	Fe	83,42	89,33
		Nb	16,58	10,67

(e)

Figure 4.30 Microstructure of wedge-cast sample, alloy S5: a) *3000, SE image and b) *5000, SE image of the thinnest section, c) *3000, SE image and d) *3000, BS image of the thickest section, e) EDS analysis results.

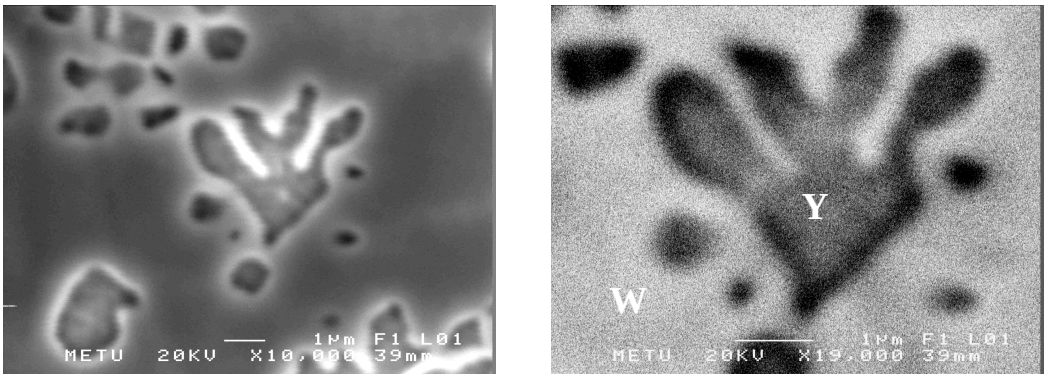

(a) **(b)**

Figure 4.31 SEM images of the dendritic phase (Y) in alloy S5: a) *10000, SE image, b) *19000, BS image.

4.2.3 General Discussions of The Experimental Investigations

In this study, Fe-B based binary and ternary systems were synthesized by using commercial Fe-B alloy and high purity elements. In the previous sections the results of the experiments were presented and discussed in a more detailed manner. In this section, the results will be evaluated in a more general frame.

In this respect, there are two important results that should be mentioned. Firstly, for Fe83B17 binary alloys, synthesized either by using commercial grade Fe-B alloy or high purity elements (S1 and S4, respectively), formation of an amorphous structure could not be detected, however, for all ternary systems, obtained by the addition of Nb or W elements to the binary system, at least partial amorphous structure was obtained. This result proves the fact that addition of Nb and W elements increases the GFA of the selected binary system as predicted by the results of the theoretical modeling and computer simulations.

Secondly, in this study, amorphous structure was successfully obtained in Fe79B16Nb5 (S2) and Fe79B16W5 (S3) alloys, prepared from the low purity commercial grade Fe-B alloy by using Cu-mold casting method, for the first time in literature. By considering these, it can be stated that the result obtained in this study is significant due to the fact that high purity of raw materials cause a high cost and, hence restrict the application areas of these materials, as mentioned previously.

All experimental findings have shown that the solidification microstructures of slowly and the rapidly cooled samples of same alloys are quite different from each other. Furthermore, experimental findings of the rapidly solidified samples indicate that scale of the microconstituents and for some alloys even formed final solidification microstructure changes as the thickness of the specimen increases for the wedge-cast sample of the same alloy. These differences introduce the effect of the thickness of the sample on the cooling rate and resultant attained cooling rate on phase selection and final solidification structure explicitly.

On this account, in this study, it was tried to calculate the cooling rate achieved during casting. The effect of the sample thickness on the attained cooling rate can be characterized by the Nusselt (Nu) or Biot (Bi) Number [79-80], through the following equation,

$$B_i = \frac{hl}{k} \qquad \textbf{(4.1)}$$

where h is heat transfer coefficient, l is the half plate thickness and k is the metal thermal conductivity. The value of the heat transfer coefficient, h, is ~10^5 W/m^2.K typical for experimental measurements for contact with chill surfaces of most rapid solidification process methods [79-80]. As realized from this equation, Biot number depends on properties of both mold and liquid metal. Hence the data are inadequate for Fe-B-Nb and Fe-B-W systems, the calculations were performed for

only Fe83B17 alloy. The value of thermal conductivity of the metal can be calculated from,

$$k = \alpha C_p \rho \quad \textbf{(4.2)}$$

where α is the thermal diffusivity of metal, it has a value of 1 x 10^{-5} m^2/s for Fe83B17 alloy [47], C_p is the specific heat capacity of metal with a value of 50 J/mol.K [47] and ρ is the density. Density of Fe83B17 alloy can be calculated by using the additive rule of mixing as:

$$\rho = c_{Fe}\rho_{Fe} + c_B\rho_B \quad \textbf{(4.3)}$$

where c_i and ρ_i is the concentration and density of the element i.

When Bi << 1, Newtonian cooling conditions prevails, whereas for Bi >> 1, ideal cooling conditions prevails. For Newtonian cooling conditions, the temperature remains essentially uniform throughout the sample, where in ideal cooling conditions the temperature now depend on position in the sample [80].

By applying Equation 4.1, it can be realized that, for our system, Newtonian cooling prevails for thickness smaller than ~0,7 mm. For above thickness, ideal cooling condition is valid. However, in this study, it is assumed that the Newtonian cooling conditions valid throughout the thickness of the specimen, to calculate approximate cooling rate values achieved during casting. Hence, the cooling rate of the liquid metal in the mold cavity can be calculated by using Newton law's of cooling, Equation 4.4 [79-80].

$$\frac{dT}{dt} = \frac{h(T - T_0)}{l\rho C_p} \quad \textbf{(4.4)}$$

where $\frac{dT}{dt}$ is the rate of the temperature change of the liquid prior to solidification, T is the liquid temperature, T_0 is the mold temperature. Figure 4.32 shows the estimated cooling rate values with corresponding thickness, by using Equations (4.1)-(4.4) and thermophysical parameters available in literature [47,79,80], for Cu-mold casting experiments.

The calculated critical cooling rate values (R_C), based on Equations (2.48) and (2.60) given in section 2.2.2.3, required to obtain amorphous phase, are also shown on the figure for Fe83B17 binary system and, Fe82B17Nb1 and Fe82B17W1 ternary systems for comparison. The estimated cooling rate values, based on Newton law's of cooling (Equation (4.4)), are in good agreement with critical cooling rate values, calculated by using atomistic approach in this study. This result also supports the proposed model for investigation of the GFA of Fe-based alloy systems.

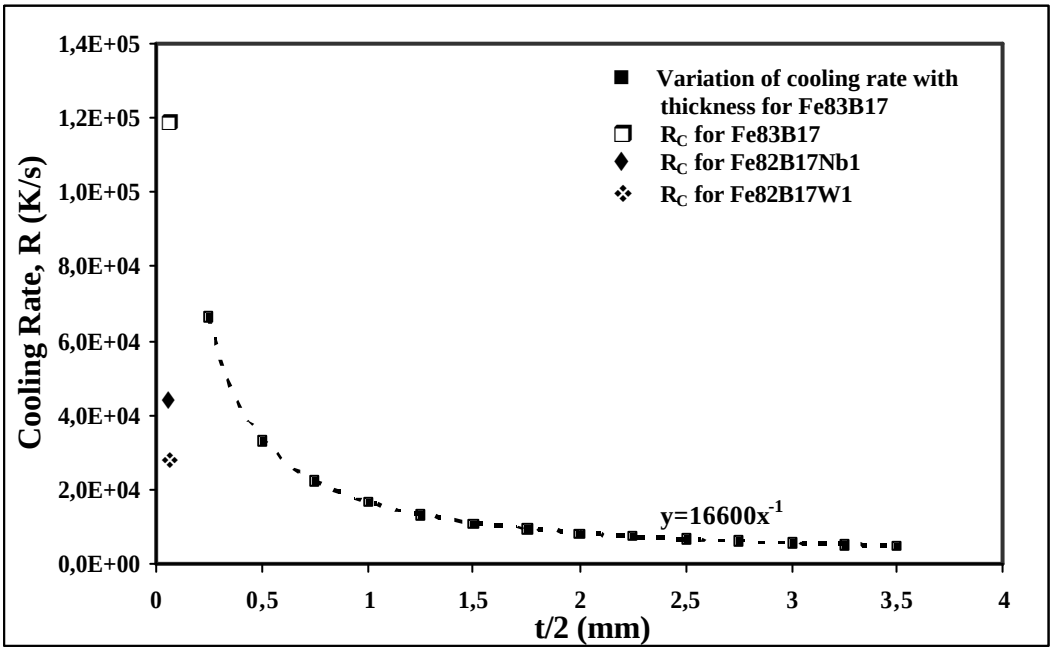

Figure 4.32 Calculated cooling rate (R) values, corresponding to sample thickness (t), attained during casting.

Results of the experiments conducted for Fe83B17 composition indicate that amorphous structure cannot be obtained even in the thinnest section of the cast sample. The result of the attained cooling rate calculations implies that this critical cooling rate can only be achieved at t ≅ 0,15 mm, for our system.

Furthermore, results of the experiments conducted for Fe-B-Nb and Fe-B-W systems, indicate that fully amorphous structure can be obtained for thickness ~0,6 mm and ~0,9 mm, respectively. The results of the conducted theoretical modeling studies suggest that Nb and W element addition to the Fe83B17 binary system improves GFA of the system and decrease the required cooling rate value to obtain amorphous structure. Regarding the results of the cooling rate calculations, it can be seen that it is possible to attain these theoretically predicted critical cooling rate values at approximately t ≅ 0,7 mm and t ≅ 1,1 mm for Fe-B-Nb and Fe-B-W systems, respectively.

As mentioned previously, structural features of the binary alloy Fe83B17 (S1), synthesized from commercial grade Fe-B alloy, reveals the fact that rapidly cooled structure exhibits a different structure than expected, such that, on the base of the microstructural findings of slowly cooled specimen of the same compositions Fe_2B intermetallic phase was expected to form, however formation of α-Fe primary phase was detected. This discrepancy probably resulted from the skewed eutectic coupled zone phenomena. A skewed eutectic coupled zone, normally associated with irregular eutectic growth, as in the case of alloy S1, Figure 4.9.a, b, is always skewed towards the faceted phase due to its growth problems and branching difficulty. Depending on the competitive growth between the primary phase and the eutectic, the solidification microstructure can be fully eutectic or dendrite plus eutectic. The phase selection is governed by the growth temperatures of the phases as a function of growth rate (V) or cooling rate (R) if the temperature gradient is constant.

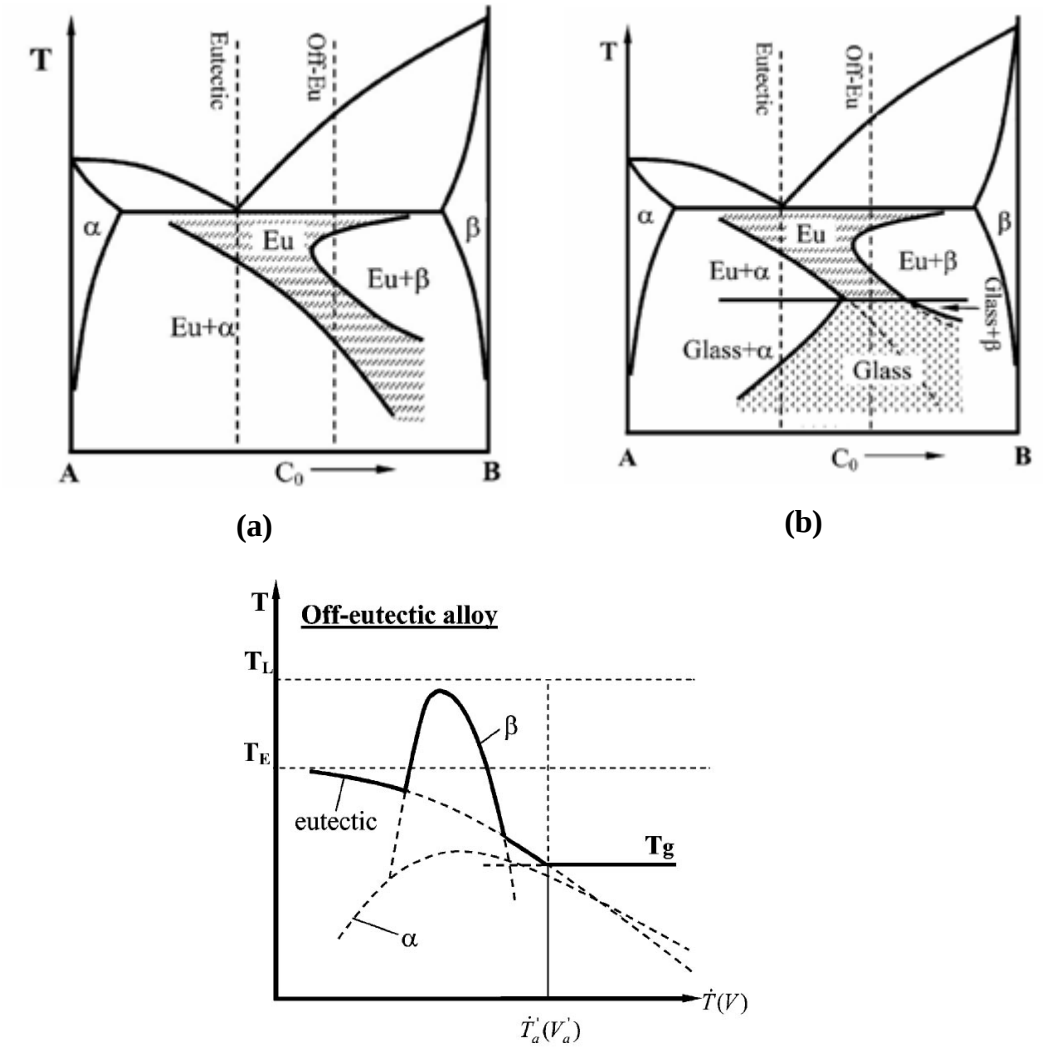

Figure 4.33 Schematic diagrams showing skewed coupled zone and its relation to GFA: a) a eutectic system with a skewed coupled zone, b) glass forming and composite forming regions related to the skewed coupled zone, c) growth temperature of the constituents as a function of growth rate (cooling rate, if temperature gradient is constant). Reproduced from [81].

For a system exhibiting skewed coupled zone, higher growth rates leads to the formation of α dendrites beside eutectic, whereas at sufficiently low growth rates fully eutectic structure will be obtained. For the off-eutectic alloy, Figure 4.33.a, only eutectic structure will be observed at sufficiently low growth rate, dendrites (β) and eutectic at intermediate rate, fully eutectic at higher growth rate, and finally α dendrites plus eutectic at extremely high growth rate [72, 81].

For Fe79B16Nb5 (S2), Fe79B16W5 (S3) and Fe79B16Nb5 (S5) ternary alloys, synthesized by using commercial grade Fe-B alloy and high purity materials, respectively, at least partial amorphous structure was obtained as mentioned previously. Structural features and the results of the DSC experiments indicate that these alloy systems exhibit common feature such that they all exhibit eutectic structure in their slowly cooled samples.

The comparison between the microstructures of the slowly cooled and the wedge cast specimens of these alloys reveal that attained high cooling rates suppress the equilibrium reactions, such as eutectic transformation, and stable phases, and favor the formation of metastable phase, such as Fe_3B intermetallic. On these account, the glass formation in alloys S2, S3 and S5 can be interpreted again on the basis of skewed coupled zone phenomena, Figure 4.33.b. If an alloy system exhibits high glass transition temperature relative to the eutectic temperature, rapid solidification will lead to fully glass or composite formation. In the case of skewed coupled zone, the eutectic in the eutectic or off-eutectic alloy will be replaced by glass when the growth rate is sufficiently higher, resulting in formation of a composite consisting of α or β dendrites plus glass, depending on the composition, as in the case of alloy S2, S3 and S5, Figures 4.14.b, c, d, 4.22.b, c, d and 4.30. If the cooling rate is higher than the critical cooling rate of the fully glass formation, fully amorphous structure will form, as it was observed in the thinnest section of the cast alloys of S2 and S3, Figures 4.14.a and 4.22.a [72, 81].

CHAPTER 5

CONCLUSIONS

In this study, theoretical modeling and computer simulations of GFA of Fe-based binary and ternary alloy systems were performed. In addition, to prove the result of the theoretical calculations, predicted binary and ternary systems with high GFA were synthesized by using raw materials of low grade commercial Fe-B alloy and high purity elements and then structurally characterized. The crucial points of these investigations can be summarized as follows:

(i) Based on the ordering energy calculations, it has been proposed that the third alloying elements of Re, Al, B, C, Mo, W, Ta, Zr and Nb, affect the ordering characteristics of binary Fe-based systems by increasing the ordering energy, and therefore these elements are potential candidates that tend to increase the glass forming ability of Fe-based binary systems.

(ii) Calculations of parameters characterizing GFA imply that Ca, Re, W, Mo, Nb, Ta, C, Zr, Hf, P, Si, B, Na, K, Al, Mn, Mg, Ga and Co are the potential candidate elements to improve the glass forming ability for almost all selected Fe-based systems and compositions.

(iii) Results of the theoretical calculations indicate that Fe-B system exhibits highest heat of mixing and lowest critical cooling rate values among the other theoretically modeled binary systems of Fe - C, Fe - Nb, Fe - Zr and Fe - W.

(iv) The results of the theoretical predictions on GFA are in good agreement with the previously conducted experimental studies reported in literature.

(v) It has been shown that Fe-B based bulk amorphous alloys can be produced directly from the melt more economically by using low grade commercial Fe - B alloy as a raw material and conventional centrifugal casting technique.

(vi) For ternary alloys of Fe79B16Nb5 (S2) and Fe79B16W5 (S3), synthesized by using commercial grade Fe-B alloy, formation of fully amorphous structure in the thinnest sections, whereas for middle sections, formation of a composite consisting of dendritic phase embedded in an amorphous matrix is detected.

(vii) Structural features of Fe79B16Nb5 ternary alloys, alloy S2 and S5 that were synthesized from commercial grade Fe-B alloy and from high purity elements, respectively, reveals that alloy S2 has higher GFA than alloy S5, which may be resulted from the positive effect of the presence of other impurity elements on GFA in commercial Fe-B alloy.

(viii) The experimental results of slowly cooled and wedge-cast samples indicate that cooling rate has an important effect on phase selection and on the final solidification structure such that high cooling rates may lead to the suppression of equilibrium reactions, i.e. eutectic transformation, and formation of metastable phases in the final structure.

(ix) Experimental observations indicate that formation of the amorphous phase occurs by easy suppression of the eutectic growth due to the growth problem and branching difficulty of its intermetallic constituent.

(x) Results of the experimental studies are in qualitative agreement with the theoretical predictions, such that addition of Nb and W element increase the GFA of Fe-B binary system.

REFERENCES

1. Inoue A., Takeuchi A., Materials Transactions, 43, 2002, 1892

2. Hu Y., Pan M.X., Liu L., Zhao Y.H., Zhao D.Q., W. H. Wang, Materials Letters 57, 2003, 2698

3. Inoue A., Makino A., Mizushima T., Journal of Magnetism and Magnetic Materials 215-216, 2000, 246

4. Fang S., Xiao X., Xia L., Li W., Dong Y., Journal of Non-Crystalline Solids, 321, 2003, 120

5. Inoue A., Mater. Trans., 36, 1995, 866

6. Basu J., Ranganathan S., Sadhana, 28, 2003, 783

7. Löffler J. F., Intermetallics, 11, 2003, 529

8. Inoue A., Yamaguchi H., Zhang T., Mater. Trans., JIM, 31, 1990, 104

9. Inoue A., Zhang T., Masumoto T., Mater. Trans., JIM, 31, 1990, 177

10. Inoue A., Zhang T., Masumoto T., Mater. Trans., JIM, 32, 1991, 1005

11. Inoue A., Masumoto T., Material Science and Engineering, A173, 1993, 1

12. Peker A. L., Johnson W. L., Appl. Phys. Lett., 63, 1993, 2342

13. Inoue A., Gook J.S., Mater. Trans., JIM, 36, 1995, 1180

14. Inoue A., Materials Science and Engineering., A 226-228, 1997, 357

15. Inoue A., Gook J. S., Mater. Trans., JIM, 36, 1995, 1282

16. Inoue A., Kimura H.M., and Gook J.S., Mater. Trans., JIM, 37, 1996, 32

17. Inoue A., Takeuchi A. Zhang T. Murakami A., Makino A. IEEE Trans. Mag., 32, 1996, 4866

18. Inoue A., Park R.E., Mat. Trans., JIM, 37, 1996, 1715

19. Inoue A., Zhang T., Itoi T., Mater. Trans., JIM, 37, 1996, 1731

20. Koshiba H., Inoue A., MakinoA., Nanostructured Materials, 8, 1997, 997

21. Inoue A. Zhang T., Itoi T., Takeuchi A., Mat. Trans., JIM, 38, 1997, 359

22. Inoue A., Koshiba M., Zhang T., Makino A., Mater. Trans., JIM, 38, 1997, 577

23. Inoue A., Zhang T., Takeuchi A., Appl. Phys. Lett., 71, 1997, 464

24. Gordon E.F., Journal of Applied Physics, 11, 1998, 6326

25. Chiriac H., Lupu N., Journal of Non-Cryst. Solids, 250-252, 1999, 751

26. Inoue A., Liqun M., Materials Letters, 38, 1999, 58

27. Chiriac H., Lupu N., Journal of Magnetism and Magnetic Materials, 215-216, 2000, 394

28. Ikarashi I., Mizushima T., Makino A., Inoue A., Materials Science and Enginerring, A304-306, 2001, 763

29. Schwarz R. B., Shen T. D., Acta Materialia, 49, 2001, 837

30. Jartchy E., Pekala K., Jaskiewicz P., Latuch J., Pekala M., Grabski J., Journal of Alloys and Compounds, 343, 2002, 211

31. Pang, S.J., Zhang T., Asami K., Inoue A., Acta Materialia, 50, 2002, 489

32. Xu M., Quan M.X., Hu Z.Q., Cheng L.Z., He K.Y., Physica B, 315, 2002, 96

33. Grahl H., Roth S., Eckert J., Schultz L., Journal of Magnetism and Magnetic Materials, 254-255, 2003, 23

34. Poon J., Shiflet J., Guo F., Ponnambalam V., Journal of Non-Crystalline Solids, 317, 2003, 1

35. Inoue A., Shinohara Y., Gook J. S., Mater. Trans., 36, 1995, 1427

36. Inoue A., Murakami A., Zhang T., Takeuchi A., Mater. Trans., 38, 1997, 189

37. Koshiba M., Inoue A., Makino, Journal of Applied Physics, 85, 1999, 5136

38. Zhang W., Inoue A., Mater. Trans., JIM, 40, 1999, 78

39. Pang S., Zhang T., Asami K., Inoue A., Mater. Trans., JIM, 42, 2001, 376

40. McHenry M. E., Willard M. A., Laughlin D. E., Progress in Materials Science, 44, 1999, 291

41. Mizushima T., Ikarashi K., Yoshida M., Makio A., Inoue a., Mater. Trans., JIM, 40, 1999, 1019

42. Chiriac H., Lupu N., Physica B, 299, 2001, 293

43. Inoue A., Wang X. M., Acta Materilia, 48, 2000, 1383

44. Chen A.W., Wang X. M.,Sakai A., Inoue A., Sakurai T., Scripta Mater., 43, 2000, 1021

45. Liu D.Y., Sun W.S., Wang A.M, Zhang H.F., Hu Z. Q., Journal of Alloys and Compounds, 370, 2004, 249

46. Palumbo M., Cacciamani G., Bosco E., Baricco M., Intermetallics, 11, 2003, 1293

47. Battezzati L., Antonione C., Baricco M, Journal of Alloys and Compounds, 247, 1997, 164

48. Matsubara E., Sato S., Imafuku M., Nakamura T., Koshiba H., Inoue A., Waseda Y., Materials Science and Engineering, A 312, 2001, 136

49. Yao B., Zhang Y., Si L., Tan H., Li Y., Journal of Alloys and Compounds, 370, 2004, 1

50. Zhichao L., Deren L., Junyi L., Journal of Magnetism and Magnetic Materials, 239, 2002, 502

51. Xu M., Quan M.X., Hu Z.Q., Cheng L.Z., He K. Y., Journal of Alloys and Compounds, 334, 2002, 238

52. Li Y., Ng S.C., Ong C.K., Hng H.H., Goh T.T., Scripta Mater., 36, 1997, 783

53. Liqun M., Wang L., Zhang T., Inoue A., Materials Research Bulletin, 34, 1999, 915

54. Lu Z.P., Li Y., Ng S.C., Journal of Non Crystalline Solids, 270, 2000, 103

55. Lu Z.P., Tan H., Li Y., Ng S.C., Scripta Mater., 42, 2000, 667

56. Miracle D.B., Senkov O.N., Material Science and Engineering, A347, 2003, 50

57. Liu C.T., Lu Z.P., Acta Materialia, 50, 2002, 3501

58. Inoue A., Bulk Amorphous Alloys, Trans. Tech. Publications, 1998

59. Warlimont H., Materials Science and Engineering, A304–306, 2001, 61

60. Takeuchi A., Inoue A., Material Science and Engineering, A304-306, 2001, 446

61. Singh R. N., Sommer F., Rep. Prog. Phys., 60, 1997, 57

62. Sommer F., Singh R. N., Witusiewiez V., Journal of Alloys and Compounds, 325, 2001, 118

63. Battezzati L., Greer A.L., Acta Materialia, 37, 1989, 1791

64. Akinlade O., Singh R. N. and Sommer F., Journal of Alloys and Compounds, 267, 1998, 195

65. Heine V., Cohen M. L., Weaine D., Solid State Physics, vol. 24 E. by H. Ehrenreich et al., Academic Press, New York, 1970

66. Mekhrabov A. O. and Akdeniz M. V., Metallurgical and Materials Transactions A, Volume 34A, March 2003, 721

67. Mekhrabov A. O. and Akdeniz M. V., Chemical Eng. Comm., Vol. 190, 2003, 898

68. Mekhrabov A. O. and Akdeniz M. V., Acta Materialica, vol. 47, no: 7, 1999, 2067

69. Mekhrabov A. O., Akdeniz M. V. and Arer M. M., Acta Materialica, vol. 45, no: 3, 1997, 1077

70. Akdeniz M. V., Mekhrabov A. O., Acta Materialica, vol. 46, no: 4, 1998, 1185

71. Senkov O.N., Miracle D. B., Materials Research Bulletin, 36, 2001, 2183

72. Kurz W., Fisher D. J., Fundamentals of Solidification, Trans. Tech. Publications, 1992

73. Evteev A. V., Kosilov A. T., Levtchenko E. V., Acta Metal., 51, 2003, 2665

74. Cowlam N., Journal of Non-Crystalline Solids, 205-207, 1996, 567

75. Portnoi K. I., Levinskaya M., Romashov V.M., Sov. Powder Metall. Met. Ceram., 8, 1969, 657

76. Voroshnin, L.G., Lyakhovich L. S., Panich G. G., Protasevich G. F., Met. Sci. Heat Treat. (USSR), 9, 1970, 732

77. Portnoi K.I., Romashov V.M., Poroshk. Metall., 113(5), 1972, 48

78. Khan Y., Kneller E., Sostarich M., Z. Metallkd., 73, 1982, 624

79. Clyne T. W., Metallurgical Transactions B, 15B, 1984, 369

80. Jones H., Rapid Solidification of Metals and Alloys, The Chameleon Press., 1982

81. Tan. H, Zhang Y., Ma D., Feng Y.P., Li Y., Acta Materialia, 51, 2003, 4551

APPENDIX A

BINARY PHASE DIAGRAMS

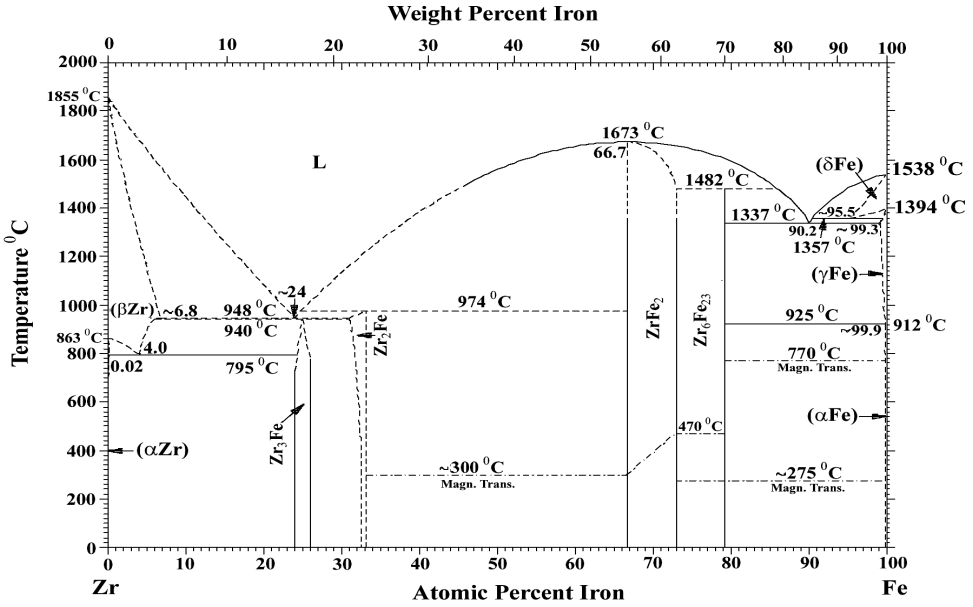

Figure A.1 Binary Phase Diagram of Fe-Zr

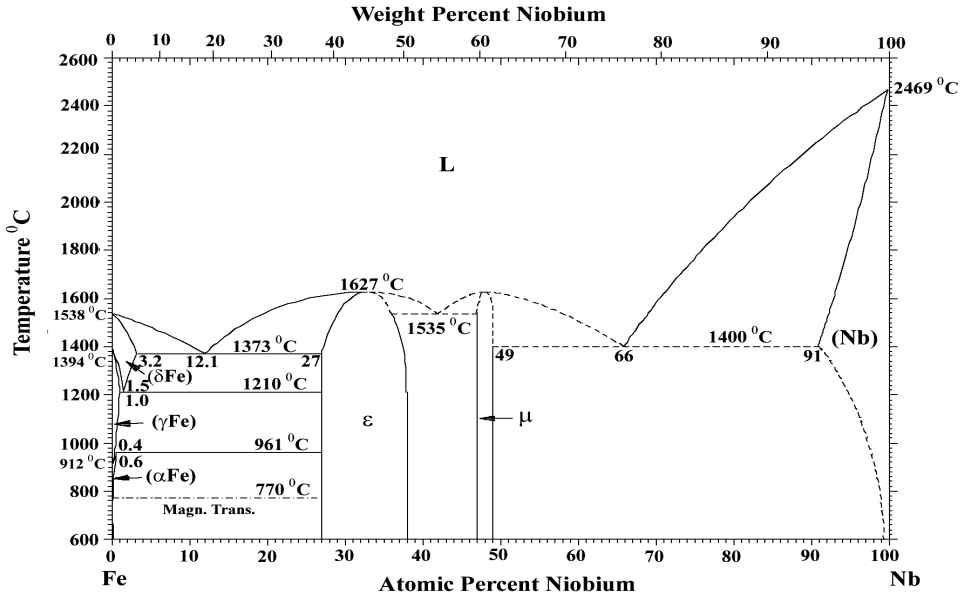

Figure A.2 Binary Phase Diagram of Fe-Nb

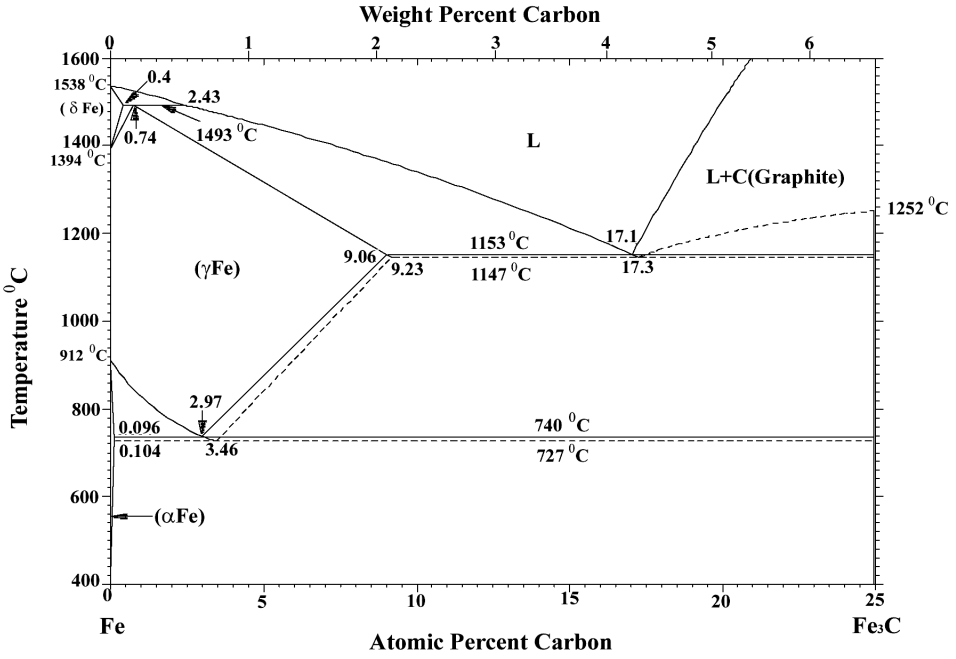

Figure A.3 Binary Phase Diagram of Fe-C

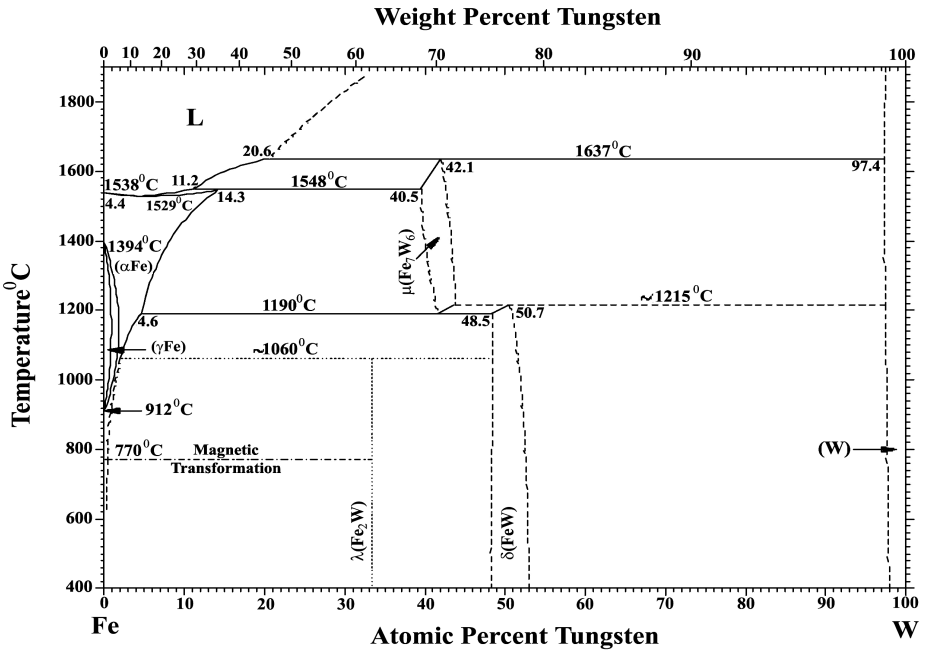

Figure A.4 Binary Phase Diagram of Fe-W

APPENDIX B

RESULTS OF THE ORDERING ENERGY CALCULATIONS FOR Fe-Zr, Fe-Nb, Fe-C AND Fe-W SYSTEMS

B.1 Fe-Zr System

Table B.1 Results of the ordering energy and interchange energy calculations for Fe72Zr27M1, in atomic unit.

Fe72Zr27M1						
M	**W_{Fe-Zr} a.u.**	**W_{Fe-M} a.u.**	**W_{Zr-M} a.u.**	**w_{Fe-Zr} a.u.**	**w_{Fe-M} a.u.**	**w_{Zr-M} a.u.**
None	0,0060	-	-	-0,0359	-	-
Al	0,0059	-0,0002	0,0097	-0,0356	0,0014	-0,0583
B	0,0061	0,0046	-0,0027	-0,0368	-0,0279	0,0160
Bi	0,0061	0,0043	0,0157	-0,0365	-0,0257	-0,0939
C	0,0060	0,0004	0,0123	-0,0359	-0,0027	-0,0736
Ca	0,0060	0,0011	0,0068	-0,0358	-0,0064	-0,0407
Co	0,0061	0,0112	-0,0003	-0,0364	-0,0670	0,0017
Cr	0,0059	-0,0006	0,0055	-0,0356	0,0033	-0,0330
Cu	0,0059	-0,0002	0,0097	-0,0357	0,0014	-0,0584
Ga	0,0060	0,0031	-0,0005	-0,0361	-0,0184	0,0029
Ge	0,0060	0,0026	-0,0007	-0,0361	-0,0158	0,0042
Hf	0,0059	-0,0017	-0,0003	-0,0353	0,0105	0,0019
K	0,0060	-0,0008	0,0119	-0,0357	0,0049	-0,0713
Mg	0,0059	0,0003	0,0085	-0,0354	-0,0018	-0,0512
Mn	0,0060	-0,0015	0,0076	-0,0363	0,0089	-0,0459
Mo	0,0061	0,0098	-0,0007	-0,0365	-0,0586	0,0040
Na	0,0059	0,0087	-0,0005	-0,0356	-0,0520	0,0030
Nb	0,0059	0,0003	0,0063	-0,0356	-0,0019	-0,0380
Ni	0,0056	0,0129	0,0927	-0,0338	-0,0775	-0,5561
P	0,0058	0,0216	-0,0222	-0,0351	-0,1297	0,1333
Re	0,0060	0,0124	0,0200	-0,0362	-0,0742	-0,1198
Se	0,0061	-0,0023	0,0133	-0,0365	0,0137	-0,0799
Si	0,0059	0,0013	0,0071	-0,0355	-0,0076	-0,0427
Ta	0,0053	0,0412	0,1244	-0,0318	-0,2469	-0,7462
Ti	0,0058	-0,0041	0,0169	-0,0350	0,0248	-0,1016
V	0,0056	-0,0008	0,0335	-0,0338	0,0050	-0,2007
W	0,0060	0,0022	0,0125	-0,0359	-0,0132	-0,0749
Y	0,0060	0,0035	0,0011	-0,0359	-0,0208	-0,0065
Zn	0,0058	0,0028	0,0004	-0,0347	-0,0167	-0,0022

Table B.2 Results of the ordering energy and interchange energy calculations for Fe72Zr27M1, in atomic unit.

Fe73Zr26M1						
M	**W_{Fe-Zr} a.u.**	**W_{Fe-M} a.u.**	**W_{Zr-M} a.u.**	**$^{W}Fe-Zr$ a.u.**	**$^{W}Fe-M$ a.u.**	**$^{W}Zr-M$ a.u.**
None	0,0060	-	-	-0,0359	-	-
Al	0,0061	-0,0023	0,0134	-0,0368	0,0137	-0,0801
B	0,0061	0,0123	0,0198	-0,0365	-0,0739	-0,1189
Bi	0,0059	0,0215	-0,0224	-0,0355	-0,1293	0,1344
C	0,0061	0,0043	0,0156	-0,0369	-0,0256	-0,0939
Ca	0,0057	0,0121	0,0923	-0,0341	-0,0724	-0,5539
Co	0,0060	-0,0002	0,0098	-0,0360	0,0014	-0,0586
Cr	0,0060	0,0004	0,0123	-0,0362	-0,0027	-0,0740
Cu	0,0059	-0,0017	-0,0003	-0,0357	0,0104	0,0015
Ga	0,0060	0,0013	0,0071	-0,0358	-0,0077	-0,0426
Ge	0,0060	0,0003	0,0063	-0,0359	-0,0020	-0,0381
Hf	0,0060	0,0087	-0,0005	-0,0359	-0,0524	0,0031
K	0,0054	0,0407	0,1241	-0,0322	-0,2442	-0,7446
Mg	0,0059	-0,0042	0,0170	-0,0353	0,0250	-0,1018
Mn	0,0060	-0,0006	0,0056	-0,0359	0,0033	-0,0334
Mo	0,0061	0,0113	-0,0003	-0,0368	-0,0677	0,0017
Na	0,0057	-0,0010	0,0334	-0,0342	0,0057	-0,2007
Nb	0,0061	0,0027	-0,0007	-0,0364	-0,0162	0,0042
Ni	0,0060	-0,0002	0,0098	-0,0360	0,0014	-0,0587
P	0,0060	0,0022	0,0125	-0,0362	-0,0134	-0,0748
Re	0,0062	0,0048	-0,0027	-0,0371	-0,0285	0,0159
Se	0,0060	0,0035	0,0010	-0,0362	-0,0209	-0,0062
Si	0,0060	-0,0008	0,0119	-0,0361	0,0048	-0,0714
Ta	0,0061	0,0032	-0,0005	-0,0364	-0,0189	0,0029
Ti	0,0060	0,0011	0,0068	-0,0362	-0,0065	-0,0407
V	0,0060	-0,0015	0,0077	-0,0363	0,0088	-0,0464
W	0,0061	0,0098	-0,0007	-0,0368	-0,0590	0,0040
Y	0,0058	0,0028	0,0004	-0,0350	-0,0171	-0,0022
Zn	0,0060	0,0003	0,0085	-0,0358	-0,0018	-0,0513

Table B.3 Results of the ordering energy and interchange energy calculations for Fe66Zr33M1, in atomic unit.

Fe66Zr33M1						
M	**W_{Fe-Zr} a.u.**	**W_{Fe-M} a.u.**	**W_{Zr-M} a.u.**	**w_{Fe-Zr} a.u.**	**w_{Fe-M} a.u.**	**w_{Zr-M} a.u.**
None	0,0056	-	-	-0,0337	-	-
Al	0,0057	-0,0023	0,0131	-0,0343	0,0137	-0,0786
B	0,0057	0,0126	0,0209	-0,0340	-0,0756	-0,1252
Bi	0,0055	0,0219	-0,0212	-0,0329	-0,1315	0,1271
C	0,0057	0,0044	0,0157	-0,0343	-0,0266	-0,0942
Ca	0,0053	0,0176	0,0942	-0,0315	-0,1055	-0,5653
Co	0,0056	-0,0002	0,0094	-0,0334	0,0014	-0,0563
Cr	0,0056	0,0005	0,0118	-0,0337	-0,0028	-0,0708
Cu	0,0055	-0,0018	-0,0006	-0,0331	0,0110	0,0036
Ga	0,0055	0,0011	0,0072	-0,0332	-0,0068	-0,0434
Ge	0,0056	0,0002	0,0062	-0,0334	-0,0015	-0,0375
Hf	0,0056	0,0083	-0,0005	-0,0334	-0,0498	0,0029
K	0,0049	0,0436	0,1253	-0,0296	-0,2614	-0,7520
Mg	0,0055	-0,0039	0,0167	-0,0327	0,0235	-0,1004
Mn	0,0056	-0,0006	0,0052	-0,0334	0,0034	-0,0312
Mo	0,0057	0,0105	-0,0003	-0,0343	-0,0632	0,0019
Na	0,0053	-0,0002	0,0334	-0,0316	0,0012	-0,2002
Nb	0,0056	0,0022	-0,0007	-0,0339	-0,0132	0,0044
Ni	0,0056	-0,0002	0,0094	-0,0334	0,0014	-0,0564
P	0,0056	0,0020	0,0125	-0,0337	-0,0117	-0,0751
Re	0,0058	0,0040	-0,0028	-0,0346	-0,0240	0,0168
Se	0,0056	0,0034	0,0014	-0,0337	-0,0202	-0,0085
Si	0,0056	-0,0010	0,0117	-0,0335	0,0058	-0,0704
Ta	0,0056	0,0026	-0,0005	-0,0339	-0,0157	0,0031
Ti	0,0056	0,0011	0,0068	-0,0336	-0,0063	-0,0406
V	0,0057	-0,0015	0,0071	-0,0341	0,0093	-0,0428
W	0,0057	0,0093	-0,0007	-0,0343	-0,0558	0,0042
Y	0,0054	0,0024	0,0004	-0,0324	-0,0144	-0,0023
Zn	0,0055	-0,0015	0,0085	-0,0332	0,0093	-0,0508

Table B.4 Results of the ordering energy and interchange energy calculations for Fe67Zr32M1, in atomic unit.

Fe67Zr32M1						
M	**W_{Fe-Zr} a.u.**	**W_{Fe-M} a.u.**	**W_{Zr-M} a.u.**	**$^{W}Fe-Zr$ a.u.**	**$^{W}Fe-M$ a.u.**	**$^{W}Zr-M$ a.u.**
None	0,0056	-	-	-0,0337	-	-
Al	0,0058	-0,0023	0,0131	-0,0346	0,0137	-0,0788
B	0,0057	0,0126	0,0207	-0,0343	-0,0754	-0,1243
Bi	0,0055	0,0219	-0,0214	-0,0332	-0,1312	0,1282
C	0,0058	0,0044	0,0157	-0,0347	-0,0265	-0,0942
Ca	0,0053	0,0169	0,0940	-0,0319	-0,1011	-0,5642
Co	0,0056	-0,0002	0,0094	-0,0338	0,0014	-0,0566
Cr	0,0057	0,0005	0,0119	-0,0340	-0,0028	-0,0713
Cu	0,0056	-0,0018	-0,0006	-0,0335	0,0110	0,0034
Ga	0,0056	0,0012	0,0072	-0,0336	-0,0070	-0,0433
Ge	0,0056	0,0003	0,0063	-0,0337	-0,0015	-0,0376
Hf	0,0056	0,0084	-0,0005	-0,0337	-0,0501	0,0029
K	0,0050	0,0432	0,1252	-0,0300	-0,2592	-0,7514
Mg	0,0055	-0,0040	0,0168	-0,0331	0,0237	-0,1006
Mn	0,0056	-0,0006	0,0052	-0,0337	0,0034	-0,0315
Mo	0,0058	0,0106	-0,0003	-0,0346	-0,0638	0,0019
Na	0,0053	-0,0003	0,0334	-0,0320	0,0018	-0,2004
Nb	0,0057	0,0023	-0,0007	-0,0342	-0,0136	0,0044
Ni	0,0056	-0,0002	0,0095	-0,0338	0,0014	-0,0568
P	0,0057	0,0020	0,0125	-0,0341	-0,0120	-0,0751
Re	0,0058	0,0041	-0,0028	-0,0350	-0,0247	0,0167
Se	0,0057	0,0034	0,0014	-0,0341	-0,0203	-0,0082
Si	0,0056	-0,0009	0,0118	-0,0339	0,0056	-0,0706
Ta	0,0057	0,0027	-0,0005	-0,0342	-0,0161	0,0030
Ti	0,0057	0,0011	0,0068	-0,0340	-0,0063	-0,0407
V	0,0057	-0,0015	0,0072	-0,0345	0,0092	-0,0433
W	0,0058	0,0094	-0,0007	-0,0346	-0,0563	0,0042
Y	0,0055	0,0025	0,0004	-0,0328	-0,0148	-0,0023
Zn	0,0056	0,0003	0,0085	-0,0336	-0,0017	-0,0509

Table B.5 Results of the ordering energy and interchange energy calculations for Fe32Zr67M1, in atomic unit.

Fe32Zr67M1						
M	**W_{Fe-Zr} a.u.**	**W_{Fe-M} a.u.**	**W_{Zr-M} a.u.**	**$^{W}_{Fe-Zr}$ a.u.**	**$^{W}_{Fe-M}$ a.u.**	**$^{W}_{Zr-M}$ a.u.**
None	0,0037	-	-	-0,0224	-	-
Al	0,0038	-0,0022	0,0116	-0,0230	0,0130	-0,0695
B	0,0038	0,0132	0,0252	-0,0227	-0,0795	-0,1512
Bi	0,0036	0,0216	-0,0160	-0,0219	-0,1294	0,0962
C	0,0038	0,0051	0,0159	-0,0231	-0,0303	-0,0955
Ca	0,0034	0,0337	0,0908	-0,0206	-0,2025	-0,5450
Co	0,0037	-0,0002	0,0076	-0,0222	0,0013	-0,0453
Cr	0,0037	0,0005	0,0089	-0,0225	-0,0027	-0,0532
Cu	0,0037	-0,0024	-0,0019	-0,0219	0,0142	0,0112
Ga	0,0037	0,0005	0,0078	-0,0221	-0,0031	-0,0467
Ge	0,0037	-0,0001	0,0058	-0,0222	0,0008	-0,0345
Hf	0,0037	0,0062	-0,0004	-0,0222	-0,0371	0,0022
K	0,0032	0,0509	0,1191	-0,0191	-0,3053	-0,7147
Mg	0,0036	-0,0029	0,0148	-0,0216	0,0175	-0,0889
Mn	0,0037	-0,0006	0,0036	-0,0222	0,0038	-0,0217
Mo	0,0038	0,0071	-0,0005	-0,0231	-0,0424	0,0033
Na	0,0034	0,0023	0,0303	-0,0207	-0,0136	-0,1819
Nb	0,0038	0,0002	-0,0008	-0,0227	-0,0013	0,0051
Ni	0,0037	-0,0002	0,0076	-0,0222	0,0014	-0,0455
P	0,0038	0,0008	0,0125	-0,0225	-0,0047	-0,0750
Re	0,0039	0,0008	-0,0034	-0,0234	-0,0050	0,0206
Se	0,0038	0,0024	0,0030	-0,0226	-0,0144	-0,0180
Si	0,0037	-0,0015	0,0108	-0,0224	0,0091	-0,0648
Ta	0,0038	0,0004	-0,0006	-0,0227	-0,0026	0,0039
Ti	0,0037	0,0009	0,0067	-0,0224	-0,0054	-0,0401
V	0,0038	-0,0019	0,0044	-0,0229	0,0113	-0,0266
W	0,0038	0,0069	-0,0008	-0,0231	-0,0411	0,0051
Y	0,0036	0,0005	0,0004	-0,0214	-0,0029	-0,0025
Zn	0,0037	0,0001	0,0081	-0,0220	-0,0008	-0,0486

Table B.6 Results of the ordering energy and interchange energy calculations for Fe33Zr66M1, in atomic unit.

Fe33Zr66M1 (M:Third Element)						
M	**W_{Fe-Zr} a.u.**	**W_{Fe-M} a.u.**	**W_{Zr-M} a.u.**	**w_{Fe-Zr} a.u.**	**w_{Fe-M} a.u.**	**w_{Zr-M} a.u.**
None	0,0037	-	-	-0,0224	-	-
Al	0,0039	-0,0022	0,0116	-0,0233	0,0131	-0,0698
B	0,0038	0,0132	0,0251	-0,0230	-0,0794	-0,1505
Bi	0,0037	0,0216	-0,0162	-0,0221	-0,1296	0,0970
C	0,0039	0,0050	0,0159	-0,0234	-0,0302	-0,0955
Ca	0,0035	0,0334	0,0911	-0,0209	-0,2006	-0,5466
Co	0,0037	-0,0002	0,0076	-0,0225	0,0013	-0,0456
Cr	0,0038	0,0005	0,0089	-0,0227	-0,0028	-0,0537
Cu	0,0037	-0,0024	-0,0018	-0,0222	0,0141	0,0111
Ga	0,0037	0,0005	0,0078	-0,0224	-0,0032	-0,0466
Ge	0,0038	-0,0001	0,0058	-0,0225	0,0007	-0,0346
Hf	0,0037	0,0062	-0,0004	-0,0225	-0,0374	0,0022
K	0,0032	0,0508	0,1195	-0,0193	-0,3047	-0,7168
Mg	0,0037	-0,0029	0,0149	-0,0219	0,0176	-0,0893
Mn	0,0037	-0,0006	0,0037	-0,0224	0,0038	-0,0219
Mo	0,0039	0,0072	-0,0005	-0,0233	-0,0430	0,0032
Na	0,0035	0,0022	0,0304	-0,0209	-0,0133	-0,1826
Nb	0,0038	0,0003	-0,0008	-0,0230	-0,0016	0,0050
Ni	0,0038	-0,0002	0,0076	-0,0225	0,0014	-0,0457
P	0,0038	0,0008	0,0125	-0,0228	-0,0049	-0,0750
Re	0,0039	0,0009	-0,0034	-0,0237	-0,0055	0,0205
Se	0,0038	0,0024	0,0030	-0,0228	-0,0145	-0,0178
Si	0,0038	-0,0015	0,0108	-0,0226	0,0091	-0,0650
Ta	0,0038	0,0005	-0,0006	-0,0230	-0,0029	0,0039
Ti	0,0038	0,0009	0,0067	-0,0227	-0,0054	-0,0401
V	0,0039	-0,0019	0,0045	-0,0232	0,0112	-0,0270
W	0,0039	0,0069	-0,0008	-0,0234	-0,0415	0,0050
Y	0,0036	0,0005	0,0004	-0,0217	-0,0032	-0,0025
Zn	0,0037	0,0001	0,0081	-0,0223	-0,0009	-0,0487

Table B.7 Results of the ordering energy and interchange energy calculations for Fe72B27M1, in SI units.

Fe72Zr27M1						
M	**W_{Fe-Zr} J/mol x10^4**	**W_{Fe-M} J/mol x10^4**	**W_{Zr-M} J/mol x10^4**	**$^{W}Fe-Zr$ J/mol x10^4**	**$^{W}Fe-M$ J/mol x10^4**	**$^{W}Zr-M$ J/mol x10^4**
None	1,569	-	-	-9,412	-	-
Al	1,559	-0,063	2,548	-9,356	0,376	-15,290
B	1,609	1,220	-0,702	-9,652	-7,321	4,209
Bi	1,598	1,126	4,109	-9,586	-6,756	-24,656
C	1,569	0,117	3,220	-9,415	-0,702	-19,317
Ca	1,567	0,282	1,781	-9,401	-1,690	-10,687
Co	1,594	2,932	-0,074	-9,565	-17,590	0,443
Cr	1,556	-0,145	1,445	-9,338	0,872	-8,673
Cu	1,560	-0,063	2,555	-9,359	0,377	-15,331
Ga	1,578	0,806	-0,127	-9,465	-4,837	0,761
Ge	1,578	0,690	-0,185	-9,465	-4,140	1,113
Hf	1,545	-0,457	-0,081	-9,271	2,743	0,486
K	1,563	-0,216	3,117	-9,375	1,296	-18,703
Mg	1,549	0,079	2,239	-9,293	-0,473	-13,435
Mn	1,588	-0,387	2,008	-9,526	2,325	-12,045
Mo	1,594	2,561	-0,176	-9,567	-15,368	1,054
Na	1,555	2,276	-0,133	-9,330	-13,655	0,799
Nb	1,556	0,084	1,662	-9,335	-0,503	-9,972
Ni	1,477	3,390	24,325	-8,863	-20,338	-145,948
P	1,535	5,673	-5,831	-9,209	-34,039	34,988
Re	1,582	3,244	5,240	-9,491	-19,463	-31,439
Se	1,595	-0,598	3,497	-9,571	3,589	-20,980
Si	1,551	0,331	1,868	-9,306	-1,984	-11,205
Ta	1,392	10,800	32,639	-8,352	-64,799	-195,831
Ti	1,529	-1,083	4,446	-9,177	6,499	-26,674
V	1,480	-0,219	8,780	-8,880	1,314	-52,678
W	1,570	0,575	3,275	-9,417	-3,452	-19,652
Y	1,569	0,912	0,286	-9,414	-5,471	-1,715
Zn	1,516	0,730	0,097	-9,097	-4,378	-0,583

Table B.8 Results of the ordering energy and interchange energy calculations for Fe73B26M1, in SI units.

Fe73Zr26M1						
M	**W_{Fe-Zr} J/mol x10^4**	**W_{Fe-M} J/mol x10^4**	**W_{Zr-M} J/mol x10^4**	**$^{W}Fe-Zr$ J/mol x10^4**	**$^{W}Fe-M$ J/mol x10^4**	**$^{W}Zr-M$ J/mol x10^4**
None	1,569	-	-	-9,412	-	-
Al	1,611	-0,598	3,506	-9,666	3,586	-21,033
B	1,598	3,232	5,199	-9,586	-19,392	-31,194
Bi	1,551	5,656	-5,877	-9,305	-33,933	35,263
C	1,613	1,119	4,107	-9,681	-6,715	-24,641
Ca	1,493	3,165	24,230	-8,961	-18,991	-145,381
Co	1,575	-0,063	2,562	-9,452	0,377	-15,375
Cr	1,585	0,116	3,238	-9,512	-0,697	-19,430
Cu	1,561	-0,453	-0,067	-9,369	2,717	0,404
Ga	1,567	0,336	1,862	-9,403	-2,015	-11,171
Ge	1,572	0,087	1,666	-9,432	-0,522	-9,994
Hf	1,571	2,292	-0,134	-9,427	-13,752	0,805
K	1,409	10,682	32,571	-8,451	-64,090	-195,425
Mg	1,546	-1,093	4,452	-9,274	6,555	-26,715
Mn	1,572	-0,145	1,459	-9,435	0,869	-8,753
Mo	1,610	2,959	-0,072	-9,658	-17,755	0,434
Na	1,496	-0,249	8,777	-8,978	1,496	-52,662
Nb	1,593	0,709	-0,184	-9,560	-4,256	1,106
Ni	1,576	-0,063	2,569	-9,455	0,377	-15,416
P	1,585	0,586	3,273	-9,512	-3,515	-19,641
Re	1,624	1,249	-0,696	-9,746	-7,491	4,174
Se	1,585	0,916	0,271	-9,509	-5,496	-1,625
Si	1,579	-0,210	3,123	-9,472	1,257	-18,738
Ta	1,593	0,827	-0,125	-9,560	-4,960	0,752
Ti	1,583	0,282	1,781	-9,497	-1,694	-10,688
V	1,588	-0,385	2,030	-9,526	2,307	-12,182
W	1,610	2,581	-0,174	-9,661	-15,487	1,047
Y	1,532	0,746	0,097	-9,194	-4,479	-0,581
Zn	1,565	0,080	2,242	-9,391	-0,480	-13,451

Table B.9 Results of the ordering energy and interchange energy calculations for Fe66B33M1, in SI units.

Fe66Zr33M1						
M	**W_{Fe-Zr} J/mol x10^4**	**W_{Fe-M} J/mol x10^4**	**W_{Zr-M} J/mol x10^4**	**W_{Fe-Zr} J/mol x10^4**	**W_{Fe-M} J/mol x10^4**	**W_{Zr-M} J/mol x10^4**
None	1,472	-	-	-8,834	-	-
Al	1,499	-0,599	3,438	-8,995	3,591	-20,628
B	1,486	3,306	5,478	-8,914	-19,838	-32,865
Bi	1,438	5,750	-5,561	-8,631	-34,500	33,367
C	1,502	1,165	4,121	-9,013	-6,990	-24,727
Ca	1,380	4,613	24,726	-8,278	-27,681	-148,355
Co	1,462	-0,062	2,461	-8,774	0,371	-14,765
Cr	1,473	0,122	3,098	-8,837	-0,730	-18,589
Cu	1,448	-0,483	-0,159	-8,688	2,900	0,955
Ga	1,454	0,299	1,900	-8,726	-1,794	-11,398
Ge	1,460	0,064	1,640	-8,758	-0,383	-9,839
Hf	1,459	2,177	-0,127	-8,753	-13,061	0,762
K	1,295	11,435	32,892	-7,768	-68,608	-197,353
Mg	1,432	-1,030	4,392	-8,594	6,178	-26,353
Mn	1,459	-0,149	1,364	-8,756	0,893	-8,185
Mo	1,499	2,764	-0,083	-8,994	-16,586	0,497
Na	1,382	-0,051	8,758	-8,293	0,307	-52,547
Nb	1,482	0,578	-0,192	-8,890	-3,465	1,154
Ni	1,463	-0,062	2,468	-8,778	0,372	-14,807
P	1,474	0,514	3,284	-8,843	-3,082	-19,703
Re	1,514	1,052	-0,735	-9,086	-6,311	4,412
Se	1,473	0,882	0,373	-8,841	-5,291	-2,240
Si	1,466	-0,252	3,081	-8,798	1,513	-18,483
Ta	1,482	0,686	-0,135	-8,890	-4,113	0,808
Ti	1,471	0,276	1,778	-8,824	-1,658	-10,665
V	1,492	-0,405	1,871	-8,954	2,430	-11,224
W	1,500	2,440	-0,183	-8,997	-14,642	1,097
Y	1,419	0,630	0,099	-8,514	-3,777	-0,593
Zn	1,452	-0,405	2,222	-8,712	2,430	-13,329

Table B.10 Results of the ordering energy and interchange energy calculations for Fe67B32M1, in SI units.

Fe67Zr32M1						
M	**W_{Fe-Zr} J/mol x10^4**	**W_{Fe-M} J/mol x10^4**	**W_{Zr-M} J/mol x10^4**	**$^{W}Fe-Zr$ J/mol x10^4**	**$^{W}Fe-M$ J/mol x10^4**	**$^{W}Zr-M$ J/mol x10^4**
None	1,472	-	-	-8,834	-	-
Al	1,515	-0,599	3,448	-9,091	3,593	-20,690
B	1,502	3,297	5,439	-9,010	-19,781	-32,633
Bi	1,454	5,740	-5,606	-8,726	-34,442	33,634
C	1,518	1,159	4,119	-9,109	-6,953	-24,717
Ca	1,396	4,423	24,677	-8,375	-26,539	-148,062
Co	1,478	-0,062	2,476	-8,870	0,373	-14,854
Cr	1,489	0,121	3,119	-8,933	-0,726	-18,716
Cu	1,464	-0,479	-0,147	-8,784	2,874	0,880
Ga	1,470	0,304	1,894	-8,822	-1,826	-11,367
Ge	1,476	0,067	1,644	-8,854	-0,403	-9,861
Hf	1,475	2,194	-0,128	-8,848	-13,161	0,768
K	1,311	11,337	32,867	-7,864	-68,024	-197,201
Mg	1,448	-1,039	4,402	-8,691	6,231	-26,413
Mn	1,475	-0,148	1,378	-8,853	0,890	-8,267
Mo	1,515	2,792	-0,081	-9,089	-16,754	0,488
Na	1,398	-0,078	8,766	-8,390	0,466	-52,594
Nb	1,498	0,596	-0,191	-8,986	-3,576	1,147
Ni	1,479	-0,062	2,483	-8,874	0,373	-14,895
P	1,490	0,524	3,283	-8,938	-3,142	-19,698
Re	1,530	1,080	-0,730	-9,181	-6,478	4,380
Se	1,489	0,887	0,359	-8,937	-5,324	-2,155
Si	1,482	-0,246	3,087	-8,893	1,478	-18,522
Ta	1,498	0,705	-0,133	-8,986	-4,233	0,800
Ti	1,487	0,277	1,778	-8,920	-1,663	-10,670
V	1,508	-0,402	1,893	-9,049	2,414	-11,360
W	1,515	2,461	-0,182	-9,092	-14,764	1,090
Y	1,435	0,646	0,099	-8,610	-3,878	-0,592
Zn	1,468	0,073	2,225	-8,808	-0,440	-13,347

Table B.11 Results of the ordering energy and interchange energy calculations for Fe32B67M1, in SI units.

Fe32Zr67M1						
M	**W_{Fe-Zr} J/mol x10^4**	**W_{Fe-M} J/mol x10^4**	**W_{Zr-M} J/mol x10^4**	**$^{W}Fe-Zr$ J/mol x10^4**	**$^{W}Fe-M$ J/mol x10^4**	**$^{W}Zr-M$ J/mol x10^4**
None	0,981	-	-	-5,888	-	-
Al	1,005	-0,571	3,040	-6,030	3,423	-18,238
B	0,993	3,477	6,613	-5,961	-20,863	-39,680
Bi	0,956	5,658	-4,207	-5,735	-33,948	25,243
C	1,009	1,326	4,178	-6,055	-7,958	-25,066
Ca	0,903	8,858	23,840	-5,419	-53,145	-143,042
Co	0,972	-0,059	1,982	-5,831	0,353	-11,890
Cr	0,982	0,120	2,325	-5,892	-0,722	-13,950
Cu	0,958	-0,621	-0,491	-5,749	3,727	2,949
Ga	0,966	0,136	2,041	-5,799	-0,815	-12,247
Ge	0,973	-0,034	1,511	-5,836	0,207	-9,066
Hf	0,971	1,621	-0,095	-5,828	-9,726	0,569
K	0,834	13,355	31,264	-5,007	-80,130	-187,583
Mg	0,947	-0,764	3,889	-5,680	4,586	-23,337
Mn	0,969	-0,166	0,949	-5,815	0,995	-5,696
Mo	1,009	1,855	-0,144	-6,052	-11,130	0,861
Na	0,904	0,595	7,957	-5,424	-3,567	-47,741
Nb	0,992	0,059	-0,221	-5,955	-0,354	1,325
Ni	0,972	-0,059	1,989	-5,834	0,355	-11,932
P	0,986	0,205	3,280	-5,916	-1,231	-19,679
Re	1,024	0,218	-0,901	-6,142	-1,308	5,403
Se	0,987	0,628	0,789	-5,923	-3,767	-4,732
Si	0,978	-0,400	2,834	-5,870	2,398	-17,005
Ta	0,992	0,114	-0,171	-5,955	-0,681	1,023
Ti	0,982	0,234	1,755	-5,890	-1,406	-10,531
V	1,002	-0,493	1,163	-6,010	2,957	-6,976
W	1,009	1,798	-0,221	-6,055	-10,788	1,328
Y	0,937	0,128	0,108	-5,620	-0,770	-0,648
Zn	0,963	0,037	2,127	-5,778	-0,220	-12,764

Table B.12 Results of the ordering energy and interchange energy calculations for Fe33B66M1, in SI units.

Fe33Zr66M1						
M	**W_{Fe-Zr} J/mol x10^4**	**W_{Fe-M} J/mol x10^4**	**W_{Zr-M} J/mol x10^4**	**$^{W}Fe-Zr$ J/mol x10^4**	**$^{W}Fe-M$ J/mol x10^4**	**$^{W}Zr-M$ J/mol x10^4**
None	0,981	-	-	-5,888	-	-
Al	0,981	0,981	0,981	-6,106	3,431	-18,308
B	1,018	-0,572	3,051	-6,035	-20,849	-39,505
Bi	1,006	3,475	6,584	-5,806	-34,006	25,455
C	0,968	5,668	-4,242	-6,130	-7,937	-25,053
Ca	1,022	1,323	4,176	-5,488	-52,660	-143,450
Co	0,915	8,777	23,908	-5,904	0,353	-11,964
Cr	0,984	-0,059	1,994	-5,967	-0,724	-14,083
Cu	0,994	0,121	2,347	-5,821	3,705	2,904
Ga	0,970	-0,618	-0,484	-5,872	-0,841	-12,225
Ge	0,979	0,140	2,037	-5,908	0,191	-9,085
Hf	0,985	-0,032	1,514	-5,902	-9,816	0,574
K	0,984	1,636	-0,096	-5,073	-79,955	-188,130
Mg	0,845	13,326	31,355	-5,752	4,627	-23,436
Mn	0,959	-0,771	3,906	-5,887	0,992	-5,758
Mo	0,981	-0,165	0,960	-6,126	-11,274	0,850
Na	1,021	1,879	-0,142	-5,494	-3,483	-47,929
Nb	0,916	0,581	7,988	-6,028	-0,428	1,322
Ni	1,005	0,071	-0,220	-5,907	0,356	-12,006
P	0,985	-0,059	2,001	-5,989	-1,279	-19,684
Re	0,998	0,213	3,281	-6,218	-1,433	5,378
Se	1,036	0,239	-0,896	-5,996	-3,817	-4,668
Si	0,999	0,636	0,778	-5,942	2,378	-17,047
Ta	0,990	-0,396	2,841	-6,028	-0,764	1,017
Ti	1,005	0,127	-0,169	-5,963	-1,413	-10,531
V	0,994	0,235	1,755	-6,084	2,944	-7,084
W	1,014	-0,491	1,181	-6,129	-10,888	1,321
Y	1,022	1,815	-0,220	-5,691	-0,845	-0,646
Zn	0,949	0,141	0,108	-5,850	-0,226	-12,776

B.2 Fe -Nb System

Table B.13 Results of the ordering energy and interchange energy calculations for Fe86,9Nb12,1M1, in atomic units.

Fe86,9Nb12,1M1						
M	**W_{Fe-Nb} a.u.**	**W_{Fe-M} a.u.**	**W_{Nb-M} a.u.**	**$^{W}Fe-Nb$ a.u.**	**$^{W}Fe-M$ a.u.**	**$^{W}Nb-M$ a.u.**
None	0,0075	-	-	-0,0471	-	-
Al	0,0076	-0,0037	0,0234	-0,0478	0,0232	-0,1476
B	0,0075	0,0245	0,0485	-0,0475	-0,1547	-0,3064
Bi	0,0073	0,0408	-0,0398	-0,0464	-0,2580	0,2517
C	0,0076	0,0105	0,0347	-0,0479	-0,0664	-0,2195
Ca	0,0071	0,0726	0,1837	-0,0451	-0,4589	-1,1609
Co	0,0074	0,0002	0,0157	-0,0470	-0,0013	-0,0994
Cr	0,0075	0,0005	0,0168	-0,0472	-0,0033	-0,1060
Cu	0,0074	-0,0025	-0,0025	-0,0466	0,0160	0,0156
Ga	0,0074	0,0007	0,0132	-0,0468	-0,0046	-0,0836
Ge	0,0074	0,0000	0,0110	-0,0469	0,0000	-0,0692
Hf	0,0074	0,0148	-0,0033	-0,0468	-0,0938	0,0210
K	0,0068	0,0618	0,1463	-0,0433	-0,3908	-0,9249
Mg	0,0073	-0,0034	0,0296	-0,0463	0,0212	-0,1873
Mn	0,0074	-0,0006	0,0073	-0,0469	0,0039	-0,0460
Mo	0,0075	0,0225	0,0014	-0,0477	-0,1424	-0,0088
Na	0,0071	0,0085	0,0543	-0,0452	-0,0537	-0,3429
Ni	0,0074	0,0002	0,0158	-0,0470	-0,0014	-0,0999
P	0,0075	0,0016	0,0247	-0,0472	-0,0102	-0,1560
Pb	0,0073	0,0231	-0,0645	-0,0464	-0,1458	0,4078
Pd	0,0074	0,0109	0,0236	-0,0467	-0,0690	-0,1494
Pt	0,0074	0,0085	0,0146	-0,0467	-0,0536	-0,0924
Re	0,0076	0,0139	0,0000	-0,0481	-0,0875	0,0001
Se	0,0075	0,0073	0,0072	-0,0472	-0,0463	-0,0454
Si	0,0074	-0,0028	0,0213	-0,0471	0,0176	-0,1346
Sn	0,0074	0,0043	-0,0031	-0,0466	-0,0274	0,0198
Ta	0,0075	0,0074	0,0000	-0,0473	-0,0469	-0,0002
Ti	0,0075	0,0018	0,0132	-0,0471	-0,0111	-0,0832
V	0,0075	-0,0019	0,0123	-0,0476	0,0123	-0,0775
W	0,0076	0,0219	0,0009	-0,0477	-0,1384	-0,0054
Y	0,0073	0,0041	-0,0008	-0,0459	-0,0257	0,0053
Zn	0,0074	0,0009	0,0163	-0,0467	-0,0060	-0,1033
Zr	0,0074	0,0116	-0,0012	-0,0468	-0,0736	0,0075

Table B.14 Results of the ordering energy and interchange energy calculations for Fe87,9Nb11,1M1, in atomic units.

Fe87,9Nb11,1M1						
M	**W_{Fe-Nb} a.u.**	**W_{Fe-M} a.u.**	**W_{Nb-M} a.u.**	**$^{W}Fe-Nb$ a.u.**	**$^{W}Fe-M$ a.u.**	**$^{W}Nb-M$ a.u.**
None	0,0075	-	-	-0,0471	-	-
Al	0,0075	-0,0037	0,0233	-0,0476	0,0232	-0,1474
B	0,0075	0,0245	0,0485	-0,0473	-0,1547	-0,3067
Bi	0,0073	0,0408	-0,0397	-0,0462	-0,2580	0,2512
C	0,0076	0,0105	0,0347	-0,0477	-0,0664	-0,2196
Ca	0,0071	0,0729	0,1837	-0,0449	-0,4608	-1,1608
Co	0,0074	0,0002	0,0157	-0,0467	-0,0013	-0,0991
Cr	0,0074	0,0005	0,0167	-0,0470	-0,0033	-0,1057
Cu	0,0073	-0,0025	-0,0025	-0,0464	0,0161	0,0160
Ga	0,0074	0,0007	0,0132	-0,0466	-0,0045	-0,0836
Ge	0,0074	0,0000	0,0109	-0,0467	0,0000	-0,0692
Hf	0,0074	0,0148	-0,0033	-0,0466	-0,0937	0,0210
K	0,0068	0,0620	0,1463	-0,0431	-0,3916	-0,9247
Mg	0,0073	-0,0033	0,0296	-0,0461	0,0211	-0,1870
Mn	0,0074	-0,0006	0,0072	-0,0467	0,0039	-0,0457
Mo	0,0075	0,0225	0,0014	-0,0475	-0,1420	-0,0088
Na	0,0071	0,0085	0,0542	-0,0450	-0,0539	-0,3425
Ni	0,0074	0,0002	0,0158	-0,0468	-0,0014	-0,0996
P	0,0074	0,0016	0,0300	-0,0470	-0,0101	-0,1894
Pb	0,0073	0,0231	-0,0644	-0,0462	-0,1460	0,4071
Pd	0,0074	0,0109	0,0235	-0,0465	-0,0690	-0,1487
Pt	0,0074	0,0085	0,0147	-0,0465	-0,0535	-0,0926
Re	0,0076	0,0138	0,0000	-0,0479	-0,0871	0,0001
Se	0,0074	0,0073	0,0072	-0,0470	-0,0462	-0,0456
Si	0,0074	-0,0028	0,0213	-0,0469	0,0176	-0,1345
Sn	0,0073	0,0043	-0,0031	-0,0464	-0,0274	0,0198
Ta	0,0083	0,0074	0,0000	-0,0523	-0,0467	-0,0002
Ti	0,0074	0,0018	0,0132	-0,0469	-0,0111	-0,0832
V	0,0075	-0,0020	0,0122	-0,0474	0,0123	-0,0774
W	0,0075	0,0219	0,0009	-0,0475	-0,1381	-0,0054
Y	0,0072	0,0040	-0,0008	-0,0457	-0,0256	0,0053
Zn	0,0074	0,0009	0,0163	-0,0465	-0,0060	-0,1031
Zr	0,0074	0,0116	-0,0012	-0,0466	-0,0734	0,0075

Table B.15 Results of the ordering energy and interchange energy calculations for Fe56Nb43M1, in atomic units.

Fe56Nb43M1						
M	**W_{Fe-Nb} a.u.**	**W_{Fe-M} a.u.**	**W_{Nb-M} a.u.**	**w_{Fe-Nb} a.u.**	**w_{Fe-M} a.u.**	**w_{Nb-M} a.u.**
None	0,0083	-	-	-0,0525	-	-
Al	0,0084	-0,0037	0,0241	-0,0531	0,0235	-0,1522
B	0,0084	0,0242	0,0472	-0,0529	-0,1532	-0,2984
Bi	0,0082	0,0405	-0,0422	-0,0519	-0,2562	0,2669
C	0,0084	0,0103	0,0346	-0,0532	-0,0648	-0,2186
Ca	0,0080	0,0639	0,1826	-0,0508	-0,4040	-1,1543
Co	0,0083	0,0002	0,0169	-0,0524	-0,0015	-0,1068
Cr	0,0083	0,0005	0,0177	-0,0526	-0,0030	-0,1121
Cu	0,0082	-0,0023	-0,0011	-0,0521	0,0148	0,0068
Ga	0,0083	0,0009	0,0132	-0,0522	-0,0059	-0,0836
Ge	0,0083	0,0002	0,0111	-0,0523	-0,0010	-0,0702
Hf	0,0083	0,0155	-0,0033	-0,0523	-0,0981	0,0210
K	0,0078	0,0579	0,1459	-0,0493	-0,3658	-0,9218
Mg	0,0079	-0,0038	0,0306	-0,0499	0,0239	-0,1937
Mn	0,0083	-0,0006	0,0084	-0,0523	0,0037	-0,0529
Mo	0,0084	0,0241	0,0014	-0,0529	-0,1520	-0,0087
Na	0,0081	0,0075	0,0555	-0,0509	-0,0473	-0,3510
Ni	0,0083	0,0003	0,0170	-0,0524	-0,0016	-0,1073
P	0,0083	0,0021	0,0244	-0,0526	-0,0131	-0,1540
Pb	0,0082	0,0221	-0,0671	-0,0519	-0,1398	0,4241
Pd	0,0083	0,0105	0,0264	-0,0522	-0,0667	-0,1667
Pt	0,0083	0,0087	0,0138	-0,0522	-0,0547	-0,0873
Re	0,0084	0,0156	0,0001	-0,0533	-0,0984	-0,0007
Se	0,0083	0,0078	0,0061	-0,0526	-0,0491	-0,0387
Si	0,0083	-0,0026	0,0216	-0,0525	0,0162	-0,1363
Sn	0,0082	0,0045	-0,0029	-0,0521	-0,0284	0,0183
Ta	0,0083	0,0083	0,0000	-0,0527	-0,0526	-0,0002
Ti	0,0083	0,0018	0,0131	-0,0525	-0,0114	-0,0828
V	0,0084	-0,0018	0,0128	-0,0529	0,0116	-0,0809
W	0,0084	0,0231	0,0009	-0,0530	-0,1462	-0,0055
Y	0,0082	0,0046	-0,0006	-0,0515	-0,0294	0,0041
Zn	0,0083	0,0010	0,0170	-0,0522	-0,0065	-0,1075
Zr	0,0086	0,0122	-0,0011	-0,0541	-0,0774	0,0071

Table B.16 Results of the ordering energy and interchange energy calculations for Fe57Nb42M1, in atomic units.

Fe57Nb42M1						
M	**W_{Fe-Nb} a.u.**	**W_{Fe-M} a.u.**	**W_{Nb-M} a.u.**	**$^{W}Fe-Nb$ a.u.**	**$^{W}Fe-M$ a.u.**	**$^{W}Nb-M$ a.u.**
None	0,0083	-	-	-0,0525	-	-
Al	0,0087	-0,0038	0,0247	-0,0548	0,0239	-0,1564
B	0,0086	0,0250	0,0500	-0,0545	-0,1581	-0,3161
Bi	0,0085	0,0419	-0,0421	-0,0536	-0,2646	0,2659
C	0,0087	0,0107	0,0364	-0,0548	-0,0676	-0,2299
Ca	0,0083	0,0700	0,1881	-0,0526	-0,4423	-1,1885
Co	0,0086	0,0003	0,0175	-0,0541	-0,0017	-0,1105
Cr	0,0086	0,0005	0,0181	-0,0543	-0,0031	-0,1147
Cu	0,0085	-0,0024	-0,0009	-0,0538	0,0153	0,0056
Ga	0,0085	0,0008	0,0140	-0,0539	-0,0053	-0,0884
Ge	0,0085	0,0001	0,0116	-0,0540	-0,0006	-0,0734
Hf	0,0085	0,0158	-0,0034	-0,0539	-0,0998	0,0213
K	0,0081	0,0594	0,1467	-0,0511	-0,3755	-0,9272
Mg	0,0085	-0,0036	0,0315	-0,0535	0,0226	-0,1990
Mn	0,0085	-0,0006	0,0087	-0,0540	0,0038	-0,0550
Mo	0,0086	0,0246	0,0015	-0,0546	-0,1554	-0,0093
Na	0,0083	0,0083	0,0568	-0,0527	-0,0524	-0,3589
Ni	0,0086	0,0003	0,0176	-0,0541	-0,0018	-0,1110
P	0,0086	0,0019	0,0253	-0,0543	-0,0118	-0,1601
Pb	0,0085	0,0230	-0,0674	-0,0536	-0,1457	0,4261
Pd	0,0085	0,0110	0,0262	-0,0539	-0,0698	-0,1653
Pt	0,0085	0,0087	0,0153	-0,0539	-0,0551	-0,0967
Re	0,0087	0,0160	0,0002	-0,0549	-0,1012	-0,0010
Se	0,0086	0,0079	0,0070	-0,0542	-0,0500	-0,0441
Si	0,0086	-0,0027	0,0223	-0,0542	0,0173	-0,1407
Sn	0,0085	0,0046	-0,0029	-0,0538	-0,0291	0,0184
Ta	0,0086	0,0085	0,0000	-0,0544	-0,0539	-0,0002
Ti	0,0086	0,0018	0,0139	-0,0542	-0,0115	-0,0875
V	0,0086	-0,0019	0,0132	-0,0546	0,0120	-0,0832
W	0,0086	0,0238	0,0009	-0,0547	-0,1505	-0,0059
Y	0,0084	0,0046	-0,0006	-0,0532	-0,0290	0,0037
Zn	0,0085	0,0011	0,0179	-0,0539	-0,0067	-0,1130
Zr	0,0085	0,0125	-0,0012	-0,0539	-0,0793	0,0073

Table B.17 Results of the ordering energy and interchange energy calculations for Fe86,9Nb12,1M1, in SI units.

Fe86,9Nb12,1M1						
M	**W_{Fe-Nb} J/mol x10^4**	**W_{Fe-M} J/mol x10^4**	**W_{Nb-M} J/mol x10^4**	**$^{W}Fe-Nb$ J/mol x10^5**	**$^{W}Fe-M$ J/mol x10^5**	**$^{W}Nb-M$ J/mol x10^5**
None	1,957	-	-	-1,237	-	-
Al	1,987	-0,965	6,128	-1,256	0,610	-3,873
B	1,974	6,423	12,723	-1,248	-4,059	-8,041
Bi	1,926	10,712	-10,454	-1,217	-6,770	6,607
C	1,990	2,756	9,117	-1,258	-1,742	-5,762
Ca	1,872	19,056	48,209	-1,183	-12,043	-30,468
Co	1,950	0,055	4,129	-1,232	-0,035	-2,610
Cr	1,960	0,137	4,400	-1,238	-0,086	-2,781
Cu	1,936	-0,666	-0,649	-1,224	0,421	0,410
Ga	1,943	0,191	3,471	-1,228	-0,121	-2,194
Ge	1,948	0,002	2,874	-1,231	-0,001	-1,817
Hf	1,944	3,897	-0,874	-1,229	-2,463	0,552
K	1,797	16,229	38,409	-1,136	-10,257	-24,274
Mg	1,922	-0,880	7,778	-1,215	0,556	-4,916
Mn	1,946	-0,162	1,910	-1,230	0,102	-1,207
Mo	1,981	5,912	0,366	-1,252	-3,737	-0,231
Na	1,876	2,228	14,240	-1,186	-1,408	-9,000
Ni	1,951	0,059	4,149	-1,233	-0,037	-2,622
P	1,962	0,423	6,479	-1,240	-0,268	-4,095
Pb	1,926	6,054	-16,933	-1,217	-3,826	10,702
Pd	1,941	2,864	6,204	-1,227	-1,810	-3,921
Pt	1,940	2,225	3,839	-1,226	-1,406	-2,426
Re	1,997	3,635	-0,002	-1,262	-2,298	0,001
Se	1,961	1,922	1,884	-1,239	-1,215	-1,191
Si	1,955	-0,729	5,588	-1,235	0,461	-3,532
Sn	1,935	1,138	-0,821	-1,223	-0,719	0,519
Ta	1,966	1,948	0,009	-1,243	-1,231	-0,006
Ti	1,957	0,460	3,455	-1,237	-0,291	-2,184
V	1,977	-0,511	3,218	-1,249	0,323	-2,034
W	1,983	5,749	0,226	-1,253	-3,633	-0,143
Y	1,908	1,068	-0,219	-1,206	-0,675	0,139
Zn	1,939	0,249	4,289	-1,226	-0,157	-2,710
Zr	1,942	3,056	-0,311	-1,227	-1,931	0,197

Table B.18 Results of the ordering energy and interchange energy calculations for Fe87,9Nb11,1M1, in SI units.

Fe87,9Nb11,1M1						
M	**W_{Fe-Nb} J/mol x10^4**	**W_{Fe-M} J/mol x10^4**	**W_{Nb-M} J/mol x10^4**	**$^{W}Fe-Nb$ J/mol x10^5**	**$^{W}Fe-M$ J/mol x10^5**	**$^{W}Nb-M$ J/mol x10^5**
None	1,957	-	-	-1,237	-	-
Al	1,978	-0,965	6,120	-1,250	0,610	-3,868
B	1,966	6,425	12,736	-1,242	-4,060	-8,049
Bi	1,917	10,713	-10,430	-1,211	-6,771	6,592
C	1,982	2,758	9,118	-1,252	-1,743	-5,763
Ca	1,863	19,135	48,206	-1,177	-12,093	-30,466
Co	1,941	0,055	4,117	-1,227	-0,035	-2,602
Cr	1,951	0,137	4,390	-1,233	-0,087	-2,774
Cu	1,927	-0,668	-0,663	-1,218	0,422	0,419
Ga	1,934	0,189	3,471	-1,222	-0,119	-2,194
Ge	1,939	0,000	2,873	-1,226	0,000	-1,816
Hf	1,936	3,889	-0,874	-1,223	-2,458	0,552
K	1,788	16,263	38,400	-1,130	-10,278	-24,269
Mg	1,913	-0,876	7,767	-1,209	0,553	-4,909
Mn	1,937	-0,162	1,898	-1,224	0,103	-1,200
Mo	1,972	5,896	0,366	-1,246	-3,726	-0,231
Na	1,867	2,237	14,224	-1,180	-1,414	-8,989
Ni	1,942	0,058	4,137	-1,227	-0,037	-2,615
P	1,953	0,419	7,865	-1,234	-0,265	-4,971
Pb	1,917	6,061	-16,906	-1,211	-3,831	10,685
Pd	1,932	2,865	6,174	-1,221	-1,811	-3,902
Pt	1,931	2,223	3,847	-1,220	-1,405	-2,431
Re	1,989	3,618	-0,003	-1,257	-2,286	0,002
Se	1,952	1,917	1,895	-1,234	-1,212	-1,198
Si	1,946	-0,732	5,585	-1,230	0,462	-3,530
Sn	1,926	1,136	-0,824	-1,217	-0,718	0,521
Ta	2,170	1,939	0,009	-1,372	-1,225	-0,006
Ti	1,948	0,460	3,456	-1,231	-0,290	-2,184
V	1,968	-0,512	3,212	-1,244	0,324	-2,030
W	1,974	5,736	0,226	-1,248	-3,625	-0,143
Y	1,899	1,063	-0,221	-1,200	-0,672	0,140
Zn	1,931	0,248	4,282	-1,220	-0,157	-2,706
Zr	1,933	3,050	-0,312	-1,222	-1,927	0,197

Table B.19 Results of the ordering energy and interchange energy calculations for Fe56Nb43M1, in SI units.

Fe56Nb43M1						
M	**W_{Fe-Nb} J/mol x10^4**	**W_{Fe-M} J/mol x10^4**	**W_{Nb-M} J/mol x10^4**	**$^{W}Fe-Nb$ J/mol x10^5**	**$^{W}Fe-M$ J/mol x10^5**	**$^{W}Nb-M$ J/mol x10^5**
None	2,181	-	-	-1,379	-	-
Al	2,205	-0,977	6,321	-1,394	0,618	-3,995
B	2,195	6,361	12,393	-1,387	-4,020	-7,832
Bi	2,154	10,638	-11,082	-1,361	-6,724	7,004
C	2,208	2,691	9,078	-1,395	-1,701	-5,737
Ca	2,111	16,776	47,932	-1,334	-10,603	-30,293
Co	2,176	0,062	4,435	-1,375	-0,039	-2,803
Cr	2,183	0,125	4,655	-1,380	-0,079	-2,942
Cu	2,165	-0,615	-0,283	-1,368	0,389	0,179
Ga	2,170	0,244	3,470	-1,371	-0,154	-2,193
Ge	2,173	0,041	2,914	-1,374	-0,026	-1,842
Hf	2,170	4,075	-0,874	-1,372	-2,575	0,552
K	2,048	15,190	38,280	-1,294	-9,600	-24,193
Mg	2,070	-0,992	8,043	-1,308	0,627	-5,083
Mn	2,173	-0,154	2,198	-1,373	0,098	-1,389
Mo	2,199	6,313	0,362	-1,390	-3,990	-0,228
Na	2,115	1,963	14,575	-1,337	-1,241	-9,212
Ni	2,177	0,066	4,456	-1,376	-0,042	-2,816
P	2,184	0,545	6,393	-1,380	-0,344	-4,041
Pb	2,155	5,804	-17,611	-1,362	-3,668	11,130
Pd	2,168	2,768	6,923	-1,370	-1,749	-4,376
Pt	2,168	2,270	3,624	-1,370	-1,435	-2,291
Re	2,212	4,087	0,031	-1,398	-2,583	-0,019
Se	2,183	2,039	1,609	-1,379	-1,289	-1,017
Si	2,179	-0,671	5,661	-1,377	0,424	-3,578
Sn	2,162	1,180	-0,761	-1,366	-0,746	0,481
Ta	2,187	2,185	0,008	-1,382	-1,381	-0,005
Ti	2,180	0,475	3,440	-1,378	-0,300	-2,174
V	2,196	-0,484	3,359	-1,388	0,306	-2,123
W	2,201	6,072	0,229	-1,391	-3,837	-0,145
Y	2,140	1,220	-0,169	-1,353	-0,771	0,107
Zn	2,167	0,270	4,464	-1,370	-0,171	-2,821
Zr	2,247	3,215	-0,296	-1,420	-2,032	0,187

Table B.20 Results of the ordering energy and interchange energy calculations for Fe57Nb42M1, in SI units.

Fe57Nb42M1						
M	**W_{Fe-Nb} J/mol x10^4**	**W_{Fe-M} J/mol x10^4**	**W_{Nb-M} J/mol x10^4**	**$^{W}Fe-Nb$ J/mol x10^5**	**$^{W}Fe-M$ J/mol x10^5**	**$^{W}Nb-M$ J/mol x10^5**
None	2,181	-	-	-1,379	-	-
Al	2,275	-0,993	6,495	-1,438	0,628	-4,105
B	2,265	6,567	13,126	-1,431	-4,150	-8,295
Bi	2,225	10,987	-11,042	-1,406	-6,944	6,979
C	2,277	2,805	9,546	-1,439	-1,773	-6,033
Ca	2,183	18,368	49,355	-1,379	-11,609	-31,193
Co	2,246	0,071	4,590	-1,419	-0,045	-2,901
Cr	2,253	0,129	4,761	-1,424	-0,081	-3,009
Cu	2,235	-0,637	-0,235	-1,413	0,402	0,148
Ga	2,240	0,219	3,672	-1,415	-0,138	-2,321
Ge	2,244	0,026	3,048	-1,418	-0,016	-1,926
Hf	2,240	4,145	-0,886	-1,416	-2,619	0,560
K	2,121	15,592	38,504	-1,341	-9,854	-24,335
Mg	2,223	-0,937	8,262	-1,405	0,592	-5,222
Mn	2,243	-0,156	2,283	-1,417	0,099	-1,443
Mo	2,268	6,455	0,384	-1,434	-4,080	-0,243
Na	2,187	2,175	14,904	-1,382	-1,375	-9,420
Ni	2,246	0,076	4,612	-1,420	-0,048	-2,914
P	2,254	0,492	6,650	-1,424	-0,311	-4,203
Pb	2,225	6,048	-17,694	-1,406	-3,823	11,183
Pd	2,238	2,900	6,864	-1,415	-1,833	-4,338
Pt	2,238	2,289	4,014	-1,414	-1,447	-2,537
Re	2,281	4,204	0,043	-1,442	-2,657	-0,027
Se	2,253	2,075	1,830	-1,424	-1,311	-1,156
Si	2,249	-0,720	5,841	-1,421	0,455	-3,692
Sn	2,233	1,209	-0,762	-1,411	-0,764	0,482
Ta	2,257	2,238	0,009	-1,427	-1,415	-0,006
Ti	2,250	0,479	3,636	-1,422	-0,303	-2,298
V	2,266	-0,499	3,454	-1,432	0,315	-2,183
W	2,270	6,249	0,245	-1,435	-3,950	-0,155
Y	2,211	1,204	-0,153	-1,397	-0,761	0,097
Zn	2,237	0,279	4,691	-1,414	-0,176	-2,965
Zr	2,238	3,292	-0,305	-1,415	-2,081	0,193

B.3 Fe -C System

Table B.21 Results of the ordering energy and interchange energy calculations for Fe82C17M1, in atomic units.

Fe82C17M1						
M	**W_{Fe-C} a.u.**	**W_{Fe-M} a.u.**	**W_{C-M} a.u.**	**$^{W}Fe-C$ a.u.**	**$^{W}Fe-M$ a.u.**	**$^{W}C-M$ a.u.**
None	0,0218	-	-	-0,0715	-	-
Al	0,0224	0,0078	0,0755	-0,0733	-0,0257	-0,2477
B	0,0220	0,0345	-0,0098	-0,0723	-0,1132	0,0322
Bi	0,0208	0,0462	0,1715	-0,0683	-0,1517	-0,5625
Ca	0,0199	0,0462	0,2313	-0,0651	-0,1517	-0,7586
Co	0,0216	0,0097	-0,0076	-0,0710	-0,0320	0,0250
Cr	0,0218	0,0013	0,0281	-0,0714	-0,0044	-0,0922
Cu	0,0214	-0,0080	-0,0685	-0,0703	0,0261	0,2246
Ga	0,0213	-0,0045	0,0334	-0,0700	0,0146	-0,1095
Ge	0,0214	-0,0055	0,0680	-0,0700	0,0180	-0,2229
Hf	0,0214	0,0816	0,2274	-0,0702	-0,2677	-0,7459
K	0,0182	-0,1086	-0,1462	-0,0597	0,3563	0,4794
Mg	0,0210	0,0209	0,0553	-0,0688	-0,0687	-0,1815
Mn	0,0216	0,0000	-0,0103	-0,0708	-0,0001	0,0338
Mo	0,0221	0,2306	0,4947	-0,0726	-0,7565	-1,6225
Na	0,0200	-0,0007	-0,0330	-0,0655	0,0023	0,1083
Nb	0,0218	0,1749	0,4087	-0,0716	-0,5736	-1,3407
Ni	0,0217	0,0100	-0,0081	-0,0710	-0,0329	0,0267
P	0,0216	-0,0493	0,0594	-0,0707	0,1617	-0,1950
Pb	0,0209	0,0712	0,0401	-0,0687	-0,2334	-0,1316
Pd	0,0214	-0,0293	-0,0305	-0,0703	0,0960	0,1000
Pt	0,0214	0,0030	-0,0293	-0,0703	-0,0097	0,0961
Re	0,0224	0,2766	0,5879	-0,0734	-0,9072	-1,9284
Se	0,0215	-0,0187	0,1122	-0,0704	0,0614	-0,3679
Si	0,0215	-0,0128	0,0796	-0,0705	0,0420	-0,2612
Sn	0,0211	0,0283	0,1196	-0,0693	-0,0928	-0,3924
Ta	0,0218	0,1567	0,3832	-0,0716	-0,5139	-1,2570
Ti	0,0216	-0,0118	0,0403	-0,0710	0,0388	-0,1322
V	0,0220	-0,0156	0,0641	-0,0723	0,0512	-0,2102
W	0,0221	0,2515	0,5148	-0,0726	-0,8248	-1,6885
Y	0,0206	0,0340	0,1418	-0,0676	-0,1114	-0,4650
Zn	0,0214	0,0129	-0,0064	-0,0703	-0,0422	0,0211
Zr	0,0213	0,1149	0,2882	-0,0700	-0,3768	-0,9454

Table B.22 Results of the ordering energy and interchange energy calculations for Fe83C16M1, in atomic units.

Fe83C16M1						
M	**W_{Fe-C} a.u.**	**W_{Fe-M} a.u.**	**W_{C-M} a.u.**	**$^{W}Fe-C$ a.u.**	**$^{W}Fe-M$ a.u.**	**$^{W}C-M$ a.u.**
None	0,0218	-	-	-0,0715	-	-
Al	0,0219	0,0079	0,0749	-0,0717	-0,0259	-0,2458
B	0,0215	0,0340	-0,0097	-0,0706	-0,1114	0,0318
Bi	0,0203	0,1281	0,1700	-0,0667	-0,4203	-0,5575
Ca	0,0194	0,0416	0,2238	-0,0635	-0,1364	-0,7340
Co	0,0211	0,0097	-0,0082	-0,0694	-0,0319	0,0269
Cr	0,0213	0,0013	0,0273	-0,0698	-0,0041	-0,0896
Cu	0,0209	-0,0080	-0,0691	-0,0686	0,0262	0,2268
Ga	0,0209	-0,0044	0,0331	-0,0684	0,0144	-0,1087
Ge	0,0209	-0,0055	0,0677	-0,0684	0,0179	-0,2221
Hf	0,0209	0,0819	0,2271	-0,0685	-0,2685	-0,7448
K	0,0177	-0,1089	-0,1464	-0,0582	0,3572	0,4803
Mg	0,0205	0,0208	0,0543	-0,0671	-0,0681	-0,1779
Mn	0,0211	0,0000	-0,0109	-0,0692	0,0000	0,0359
Mo	0,0216	0,2314	0,4949	-0,0710	-0,7588	-1,6233
Na	0,0195	-0,0009	-0,0340	-0,0639	0,0030	0,1115
Nb	0,0213	0,1758	0,4089	-0,0699	-0,5765	-1,3411
Ni	0,0212	0,0100	-0,0087	-0,0694	-0,0328	0,0286
P	0,0211	-0,0493	0,0596	-0,0691	0,1616	-0,1954
Pb	0,0205	0,0695	0,0388	-0,0671	-0,2280	-0,1272
Pd	0,0209	-0,0297	-0,0322	-0,0687	0,0975	0,1057
Pt	0,0209	0,0030	-0,0292	-0,0686	-0,0099	0,0956
Re	0,0219	0,2776	0,5885	-0,0717	-0,9105	-1,9302
Se	0,0210	-0,0191	0,1120	-0,0688	0,0628	-0,3674
Si	0,0210	-0,0126	0,0795	-0,0689	0,0414	-0,2607
Sn	0,0206	0,0283	0,1191	-0,0677	-0,0929	-0,3908
Ta	0,0213	0,1575	0,3834	-0,0699	-0,5166	-1,2575
Ti	0,0211	-0,0119	0,0401	-0,0694	0,0391	-0,1316
V	0,0215	-0,0157	0,0639	-0,0706	0,0514	-0,2095
W	0,0216	0,2522	0,5149	-0,0709	-0,8271	-1,6887
Y	0,0201	0,0343	0,1414	-0,0660	-0,1124	-0,4639
Zn	0,0209	0,0129	-0,0068	-0,0686	-0,0422	0,0222
Zr	0,0208	0,1154	0,2879	-0,0684	-0,3784	-0,9445

Table B.23 Results of the ordering energy and interchange energy calculations for Fe74C25M1, in atomic units.

Fe74C25M1						
M	**W_{Fe-C} a.u.**	**W_{Fe-M} a.u.**	**W_{C-M} a.u.**	**w_{Fe-C} a.u.**	**w_{Fe-M} a.u.**	**w_{C-M} a.u.**
None	0,0260	-	-	-0,1117	-	-
Al	0,0266	0,0072	0,0800	-0,1144	-0,0308	-0,3442
B	0,0262	0,0396	-0,0107	-0,1128	-0,1701	0,0462
Bi	0,0249	0,0887	0,1858	-0,1070	-0,3815	-0,7988
Ca	0,0239	0,0887	0,2971	-0,1026	-0,3815	-1,2777
Co	0,0258	0,0099	-0,0027	-0,1111	-0,0427	0,0117
Cr	0,0260	0,0020	0,0347	-0,1116	-0,0087	-0,1493
Cu	0,0256	-0,0075	-0,0631	-0,1101	0,0324	0,2713
Ga	0,0255	-0,0049	0,0352	-0,1096	0,0211	-0,1515
Ge	0,0255	-0,0058	0,0699	-0,1096	0,0251	-0,3005
Hf	0,0255	0,0801	0,2305	-0,1097	-0,3442	-0,9914
K	0,0221	-0,1050	-0,1427	-0,0948	0,4517	0,6137
Mg	0,0251	0,0225	0,0641	-0,1078	-0,0969	-0,2758
Mn	0,0258	0,0002	-0,0051	-0,1108	-0,0008	0,0220
Mo	0,0263	0,2255	0,4933	-0,1132	-0,9698	-2,1210
Na	0,0240	0,0015	-0,0244	-0,1032	-0,0066	0,1049
Nb	0,0260	0,1681	0,4078	-0,1117	-0,7227	-1,7536
Ni	0,0258	0,0102	-0,0032	-0,1111	-0,0439	0,0139
P	0,0257	-0,0494	0,0584	-0,1105	0,2124	-0,2510
Pb	0,0250	0,0860	0,0526	-0,1077	-0,3698	-0,2261
Pd	0,0256	-0,0251	-0,0156	-0,1101	0,1081	0,0671
Pt	0,0256	0,0028	-0,0301	-0,1100	-0,0119	0,1296
Re	0,0266	0,2687	0,5839	-0,1142	-1,1555	-2,5106
Se	0,0256	-0,0148	0,1135	-0,1100	0,0637	-0,4880
Si	0,0256	-0,0142	0,0808	-0,1103	0,0612	-0,3474
Sn	0,0252	0,0282	0,1237	-0,1085	-0,1213	-0,5320
Ta	0,0260	0,1504	0,3822	-0,1117	-0,6465	-1,6435
Ti	0,0258	-0,0112	0,0416	-0,1109	0,0480	-0,1790
V	0,0262	-0,0152	0,0658	-0,1128	0,0655	-0,2831
W	0,0263	0,2463	0,5146	-0,1131	-1,0592	-2,2128
Y	0,0247	0,0317	0,1447	-0,1061	-0,1363	-0,6221
Zn	0,0256	0,0128	-0,0036	-0,1100	-0,0549	0,0157
Zr	0,0255	0,1112	0,2907	-0,1095	-0,4784	-1,2501

Table B.24 Results of the ordering energy and interchange energy calculations for Fe75C24M1, in atomic units.

Fe75C24M1						
M	**W_{Fe-C} a.u.**	**W_{Fe-M} a.u.**	**W_{C-M} a.u.**	**w_{Fe-C} a.u.**	**w_{Fe-M} a.u.**	**w_{C-M} a.u.**
None	0,0260	-	-	-0,1117	-	-
Al	0,0261	0,0073	0,0073	-0,1120	-0,0312	-0,0312
B	0,0257	0,0389	0,0389	-0,1105	-0,1672	-0,1672
Bi	0,0244	0,1441	0,1441	-0,1048	-0,6198	-0,6198
Ca	0,0233	0,0829	0,0829	-0,1004	-0,3564	-0,3564
Co	0,0253	0,0099	0,0099	-0,1087	-0,0426	-0,0426
Cr	0,0254	0,0019	0,0019	-0,1093	-0,0083	-0,0083
Cu	0,0251	-0,0076	-0,0076	-0,1078	0,0326	0,0326
Ga	0,0250	-0,0048	-0,0048	-0,1073	0,0208	0,0208
Ge	0,0249	-0,0058	-0,0058	-0,1073	0,0249	0,0249
Hf	0,0250	0,0802	0,0802	-0,1074	-0,3449	-0,3449
K	0,0216	-0,1056	-0,1056	-0,0927	0,4542	0,4542
Mg	0,0245	0,0223	0,0223	-0,1055	-0,0960	-0,0960
Mn	0,0252	0,0002	0,0002	-0,1085	-0,0007	-0,0007
Mo	0,0258	0,2261	0,2261	-0,1109	-0,9722	-0,9722
Na	0,0235	0,0012	0,0012	-0,1010	-0,0052	-0,0052
Nb	0,0254	0,1689	0,1689	-0,1094	-0,7263	-0,7263
Ni	0,0253	0,0102	0,0102	-0,1088	-0,0438	-0,0438
P	0,0252	-0,0494	-0,0494	-0,1082	0,2124	0,2124
Pb	0,0245	0,0840	0,0840	-0,1054	-0,3611	-0,3611
Pd	0,0251	-0,0257	-0,0257	-0,1078	0,1106	0,1106
Pt	0,0250	0,0028	0,0028	-0,1077	-0,0119	-0,0119
Re	0,0260	0,2697	0,2697	-0,1119	-1,1595	-1,1595
Se	0,0251	-0,0154	-0,0154	-0,1077	0,0660	0,0660
Si	0,0251	-0,0141	-0,0141	-0,1080	0,0604	0,0604
Sn	0,0247	0,0282	0,0282	-0,1062	-0,1213	-0,1213
Ta	0,0254	0,1511	0,1511	-0,1094	-0,6498	-0,6498
Ti	0,0253	-0,0113	-0,0113	-0,1086	0,0484	0,0484
V	0,0257	-0,0153	-0,0153	-0,1104	0,0657	0,0657
W	0,0258	0,2469	0,2469	-0,1108	-1,0618	-1,0618
Y	0,0241	0,0320	0,0320	-0,1038	-0,1374	-0,1374
Zn	0,0250	0,0128	0,0128	-0,1077	-0,0550	-0,0550
Zr	0,0249	0,1117	0,1117	-0,1072	-0,4802	-0,4802

Table B.25 Results of the ordering energy and interchange energy calculations for Fe82C17M1, in SI units.

Fe82C17M1						
M	**W_{Fe-C} J/mol x10^4**	**W_{Fe-M} J/mol x10^4**	**W_{C-M} J/mol x10^4**	**$^{W}_{Fe-C}$ J/mol x10^5**	**$^{W}_{Fe-M}$ J/mol x10^5**	**$^{W}_{C-M}$ J/mol x10^5**
None	5,721	-	-	-1,877	-	-
Al	5,868	2,057	19,820	-1,925	-0,675	-6,501
B	5,781	9,060	-2,578	-1,896	-2,972	0,846
Bi	5,467	12,136	45,011	-1,793	-3,981	-14,764
Ca	5,210	12,136	60,696	-1,709	-3,981	-19,908
Co	5,681	2,559	-2,000	-1,863	-0,839	0,656
Cr	5,716	0,349	7,376	-1,875	-0,115	-2,419
Cu	5,623	-2,087	-17,973	-1,844	0,684	5,895
Ga	5,603	-1,171	8,759	-1,838	0,384	-2,873
Ge	5,604	-1,443	17,833	-1,838	0,473	-5,849
Hf	5,614	21,419	59,682	-1,841	-7,025	-19,576
K	4,777	-28,508	-38,363	-1,567	9,351	12,583
Mg	5,502	5,497	14,520	-1,805	-1,803	-4,762
Mn	5,667	0,006	-2,708	-1,859	-0,002	0,888
Mo	5,812	60,529	129,827	-1,906	-19,853	-42,583
Na	5,242	-0,182	-8,662	-1,719	0,060	2,841
Nb	5,725	45,900	107,275	-1,878	-15,055	-35,186
Ni	5,683	2,633	-2,135	-1,864	-0,864	0,700
P	5,661	-12,940	15,600	-1,857	4,244	-5,117
Pb	5,498	18,679	10,528	-1,803	-6,127	-3,453
Pd	5,627	-7,684	-8,000	-1,846	2,520	2,624
Pt	5,622	0,777	-7,687	-1,844	-0,255	2,521
Re	5,869	72,587	154,303	-1,925	-23,808	-50,611
Se	5,635	-4,912	29,434	-1,848	1,611	-9,654
Si	5,642	-3,358	20,901	-1,851	1,101	-6,855
Sn	5,544	7,429	31,397	-1,818	-2,437	-10,298
Ta	5,725	41,122	100,582	-1,878	-13,488	-32,991
Ti	5,681	-3,108	10,575	-1,863	1,019	-3,468
V	5,784	-4,097	16,822	-1,897	1,344	-5,518
W	5,806	65,999	135,107	-1,904	-21,648	-44,315
Y	5,408	8,910	37,208	-1,774	-2,923	-12,204
Zn	5,622	3,375	-1,688	-1,844	-1,107	0,554
Zr	5,599	30,149	75,644	-1,836	-9,889	-24,811

Table B.26 Results of the ordering energy and interchange energy calculations for Fe83C16M1, in SI units.

Fe83C16M1						
M	**W_{Fe-C} J/mol x10^4**	**W_{Fe-M} J/mol x10^4**	**W_{C-M} J/mol x10^4**	**w_{Fe-C} J/mol x10^5**	**w_{Fe-M} J/mol x10^5**	**w_{C-M} J/mol x10^5**
None	5,721	-	-	-1,877	-	-
Al	5,735	2,076	19,670	-1,881	-0,681	-6,452
B	5,649	8,910	-2,543	-1,853	-2,923	0,834
Bi	5,339	33,631	44,608	-1,751	-11,031	-14,631
Ca	5,084	10,914	58,727	-1,668	-3,580	-19,263
Co	5,549	2,553	-2,155	-1,820	-0,837	0,707
Cr	5,585	0,329	7,170	-1,832	-0,108	-2,352
Cu	5,492	-2,100	-18,144	-1,801	0,689	5,951
Ga	5,472	-1,156	8,699	-1,795	0,379	-2,853
Ge	5,475	-1,431	17,771	-1,796	0,469	-5,829
Hf	5,484	21,486	59,594	-1,799	-7,047	-19,547
K	4,655	-28,582	-38,432	-1,527	9,375	12,606
Mg	5,372	5,447	14,239	-1,762	-1,787	-4,670
Mn	5,535	0,001	-2,873	-1,816	0,000	0,942
Mo	5,680	60,718	129,890	-1,863	-19,916	-42,604
Na	5,115	-0,243	-8,926	-1,678	0,080	2,928
Nb	5,595	46,128	107,308	-1,835	-15,130	-35,197
Ni	5,552	2,628	-2,290	-1,821	-0,862	0,751
P	5,531	-12,933	15,632	-1,814	4,242	-5,127
Pb	5,370	18,246	10,176	-1,761	-5,985	-3,338
Pd	5,496	-7,800	-8,454	-1,803	2,559	2,773
Pt	5,491	0,791	-7,653	-1,801	-0,260	2,510
Re	5,738	72,857	154,443	-1,882	-23,897	-50,657
Se	5,505	-5,024	29,401	-1,806	1,648	-9,644
Si	5,512	-3,312	20,859	-1,808	1,086	-6,842
Sn	5,415	7,436	31,270	-1,776	-2,439	-10,257
Ta	5,595	41,337	100,619	-1,835	-13,558	-33,003
Ti	5,550	-3,128	10,532	-1,820	1,026	-3,455
V	5,653	-4,109	16,767	-1,854	1,348	-5,500
W	5,675	66,182	135,125	-1,861	-21,708	-44,321
Y	5,280	8,992	37,119	-1,732	-2,949	-12,175
Zn	5,491	3,378	-1,778	-1,801	-1,108	0,583
Zr	5,469	30,278	75,570	-1,794	-9,931	-24,787

Table B.27 Results of the ordering energy and interchange energy calculations for Fe74C25M1, in SI units.

Fe74C25M1						
M	**W_{Fe-C} J/mol x10^4**	**W_{Fe-M} J/mol x10^4**	**W_{C-M} J/mol x10^4**	**$^{W}_{Fe-C}$ J/mol x10^5**	**$^{W}_{Fe-M}$ J/mol x10^5**	**$^{W}_{C-M}$ J/mol x10^5**
None	6,819	-	-	-2,932	-	-
Al	6,982	1,881	21,008	-3,002	-0,809	-9,033
B	6,886	10,385	-2,818	-2,961	-4,466	1,212
Bi	6,533	23,286	48,752	-2,809	-10,013	-20,963
Ca	6,261	23,286	77,983	-2,692	-10,013	-33,533
Co	6,778	2,604	-0,715	-2,915	-1,120	0,307
Cr	6,814	0,533	9,113	-2,930	-0,229	-3,919
Cu	6,718	-1,977	-16,557	-2,889	0,850	7,120
Ga	6,689	-1,285	9,247	-2,876	0,553	-3,976
Ge	6,688	-1,532	18,341	-2,876	0,659	-7,887
Hf	6,698	21,009	60,507	-2,880	-9,034	-26,018
K	5,789	-27,568	-37,455	-2,489	11,854	16,106
Mg	6,582	5,913	16,834	-2,830	-2,542	-7,239
Mn	6,763	0,050	-1,343	-2,908	-0,022	0,577
Mo	6,909	59,191	129,454	-2,971	-25,452	-55,665
Na	6,299	0,401	-6,402	-2,709	-0,173	2,753
Nb	6,817	44,113	107,028	-2,931	-18,968	-46,022
Ni	6,781	2,679	-0,851	-2,916	-1,152	0,366
P	6,746	-12,966	15,320	-2,901	5,575	-6,588
Pb	6,570	22,568	13,799	-2,825	-9,704	-5,933
Pd	6,720	-6,599	-4,098	-2,889	2,838	1,762
Pt	6,714	0,728	-7,909	-2,887	-0,313	3,401
Re	6,969	70,524	153,236	-2,997	-30,325	-65,891
Se	6,715	-3,886	29,785	-2,887	1,671	-12,807
Si	6,729	-3,737	21,205	-2,894	1,607	-9,118
Sn	6,621	7,404	32,470	-2,847	-3,184	-13,962
Ta	6,817	39,459	100,311	-2,931	-16,967	-43,134
Ti	6,771	-2,929	10,926	-2,912	1,260	-4,698
V	6,882	-4,001	17,282	-2,959	1,720	-7,431
W	6,903	64,649	135,055	-2,968	-27,799	-58,074
Y	6,474	8,320	37,972	-2,784	-3,577	-16,328
Zn	6,714	3,352	-0,956	-2,887	-1,441	0,411
Zr	6,681	29,197	76,298	-2,873	-12,555	-32,808

Table B.28 Results of the ordering energy and interchange energy calculations for Fe75C24M1, in SI units.

Fe75C24M1						
M	**W_{Fe-C} J/mol x10^4**	**W_{Fe-M} J/mol x10^4**	**W_{C-M} J/mol x10^4**	**W_{Fe-C} J/mol x10^5**	**W_{Fe-M} J/mol x10^5**	**W_{C-M} J/mol x10^5**
None	6,819	-	-	-2,932	-	-
Al	6,837	1,906	1,906	-2,940	-0,819	-0,819
B	6,743	10,206	10,206	-2,900	-4,388	-4,388
Bi	6,395	37,828	37,828	-2,750	-16,266	-16,266
Ca	6,125	21,752	21,752	-2,634	-9,353	-9,353
Co	6,637	2,598	2,598	-2,854	-1,117	-1,117
Cr	6,672	0,508	0,508	-2,869	-0,218	-0,218
Cu	6,577	-1,991	-1,991	-2,828	0,856	0,856
Ga	6,549	-1,272	-1,272	-2,816	0,547	0,547
Ge	6,548	-1,522	-1,522	-2,816	0,655	0,655
Hf	6,558	21,048	21,048	-2,820	-9,051	-9,051
K	5,658	-27,720	-27,720	-2,433	11,919	11,919
Mg	6,442	5,859	5,859	-2,770	-2,519	-2,519
Mn	6,621	0,045	0,045	-2,847	-0,019	-0,019
Mo	6,767	59,340	59,340	-2,910	-25,516	-25,516
Na	6,163	0,318	0,318	-2,650	-0,137	-0,137
Nb	6,676	44,332	44,332	-2,871	-19,063	-19,063
Ni	6,639	2,673	2,673	-2,855	-1,149	-1,149
P	6,606	-12,966	-12,966	-2,841	5,575	5,575
Pb	6,432	22,041	22,041	-2,766	-9,477	-9,477
Pd	6,578	-6,750	-6,750	-2,829	2,903	2,903
Pt	6,573	0,728	0,728	-2,826	-0,313	-0,313
Re	6,827	70,771	70,771	-2,936	-30,432	-30,432
Se	6,575	-4,029	-4,029	-2,827	1,732	1,732
Si	6,589	-3,688	-3,688	-2,833	1,586	1,586
Sn	6,482	7,404	7,404	-2,787	-3,184	-3,184
Ta	6,676	39,661	39,661	-2,871	-17,054	-17,054
Ti	6,631	-2,954	-2,954	-2,851	1,270	1,270
V	6,740	-4,013	-4,013	-2,898	1,726	1,726
W	6,761	64,806	64,806	-2,907	-27,867	-27,867
Y	6,337	8,387	8,387	-2,725	-3,606	-3,606
Zn	6,572	3,355	3,355	-2,826	-1,443	-1,443
Zr	6,541	29,308	29,308	-2,813	-12,603	-12,603

B.4 Fe -W System

Table B.29 Results of the ordering energy and interchange energy calculations for Fe79W20M1, in atomic units.

Fe79W20M1						
M	**W_{Fe-W} a.u.**	**W_{Fe-M} a.u.**	**W_{W-M} a.u.**	**$^{W}_{Fe-W}$ a.u.**	**$^{W}_{Fe-M}$ a.u.**	**$^{W}_{W-M}$ a.u.**
None	0,0286	-	-	-0,1432	-	-
Al	0,0288	-0,0043	0,0462	-0,1439	0,0215	-0,2310
B	0,0287	0,0290	0,0838	-0,1436	-0,1449	-0,4189
Bi	0,0285	0,0480	-0,0458	-0,1423	-0,2401	0,2291
C	0,0288	0,0128	0,0705	-0,1440	-0,0638	-0,3525
Ca	0,0282	0,0862	0,0296	-0,1410	-0,4311	-0,1479
Co	0,0286	0,0004	0,0411	-0,1430	-0,0022	-0,2053
Cr	0,0286	0,0005	0,0394	-0,1432	-0,0023	-0,1972
Cu	0,0285	-0,0026	0,0182	-0,1427	0,0128	-0,0910
Ga	0,0286	0,0008	0,0321	-0,1428	-0,0038	-0,1607
Ge	0,0286	0,0001	0,0296	-0,1429	-0,0005	-0,1479
Hf	0,0286	0,0184	-0,0002	-0,1428	-0,0921	0,0010
K	0,0278	0,0604	0,1692	-0,1388	-0,3021	-0,8460
Mg	0,0285	-0,0034	0,0545	-0,1423	0,0172	-0,2726
Mn	0,0286	-0,0006	0,0288	-0,1429	0,0030	-0,1441
Mo	0,0287	0,0295	0,0004	-0,1437	-0,1476	-0,0019
Na	0,0282	0,0105	0,0842	-0,1411	-0,0524	-0,4210
Nb	0,0287	0,0109	0,0012	-0,1433	-0,0544	-0,0060
Ni	0,0286	0,0005	0,0412	-0,1430	-0,0023	-0,2060
P	0,0286	0,0020	0,0466	-0,1432	-0,0098	-0,2332
Pb	0,0285	0,0258	-0,0723	-0,1424	-0,1288	0,3616
Pd	0,0286	0,0125	0,0486	-0,1428	-0,0624	-0,2430
Pt	0,0286	0,0094	0,0354	-0,1428	-0,0469	-0,1769
Re	0,0288	0,0203	-0,0008	-0,1440	-0,1013	0,0041
Si	0,0286	-0,0033	0,0425	-0,1431	0,0164	-0,2127
Sn	0,0032	0,0054	0,0080	-0,0161	-0,0271	-0,0400
Ta	0,0287	0,0107	0,0018	-0,1433	-0,0534	-0,0090
Ti	0,0286	0,0021	0,0346	-0,1431	-0,0105	-0,1731
V	0,0287	-0,0020	0,0359	-0,1436	0,0099	-0,1796
Y	0,0284	0,0055	0,0062	-0,1419	-0,0276	-0,0309
Zn	0,0286	0,0013	0,0412	-0,1428	-0,0066	-0,2061
Zr	0,0286	0,0150	0,0012	-0,1428	-0,0750	-0,0059

Table B.30 Results of the ordering energy and interchange energy calculations for Fe80W19M1, in atomic units.

Fe80W19M1						
M	**W_{Fe-W} a.u.**	**W_{Fe-M} a.u.**	**W_{W-M} a.u.**	**$^{W}Fe-W$ a.u.**	**$^{W}Fe-M$ a.u.**	**$^{W}W-M$ a.u.**
None	0,0286	-	-	-0,1432	-	-
Al	0,0287	0,0007	0,0461	-0,1434	-0,0036	-0,2305
B	0,0286	0,0055	0,0840	-0,1431	-0,0273	-0,4201
Bi	0,0283	0,0290	-0,0454	-0,1417	-0,1450	0,2271
C	0,0287	0,0128	0,0696	-0,1434	-0,0639	-0,3482
Ca	0,0281	0,0481	0,2420	-0,1404	-0,2406	-1,2099
Co	0,0285	0,0004	0,0409	-0,1425	-0,0022	-0,2046
Cr	0,0285	0,0005	0,0393	-0,1427	-0,0023	-0,1967
Cu	0,0243	-0,0026	0,0180	-0,1214	0,0129	-0,0902
Ga	0,0286	0,0260	0,0322	-0,1428	-0,1298	-0,1608
Ge	0,0285	0,0876	0,0296	-0,1424	-0,4380	-0,1478
Hf	0,0285	0,0149	-0,0002	-0,1423	-0,0747	0,0010
K	0,0276	-0,0033	0,1694	-0,1382	0,0167	-0,8472
Mg	0,0283	0,0278	0,0544	-0,1417	-0,1390	-0,2721
Mn	0,0285	-0,0006	0,0287	-0,1424	0,0030	-0,1434
Mo	0,0286	0,0294	0,0004	-0,1431	-0,1468	-0,0019
Na	0,0281	0,0609	0,0841	-0,1405	-0,3047	-0,4206
Nb	0,0286	0,0108	0,0012	-0,1428	-0,0541	-0,0061
Ni	0,0285	0,0005	0,0411	-0,1425	-0,0023	-0,2053
P	0,0285	0,0054	0,0467	-0,1427	-0,0270	-0,2333
Pb	0,0284	0,0284	-0,0719	-0,1418	-0,1421	0,3593
Pd	0,0284	0,0093	0,0482	-0,1422	-0,0467	-0,2410
Pt	0,0284	0,0106	0,0356	-0,1422	-0,0532	-0,1778
Re	0,0287	0,0201	-0,0008	-0,1435	-0,1005	0,0041
Si	0,0285	0,0013	0,0425	-0,1425	-0,0066	-0,2124
Sn	0,0284	-0,0033	0,0080	-0,1420	0,0166	-0,0398
Ta	0,0286	0,0106	0,0018	-0,1428	-0,0530	-0,0090
Ti	0,0285	0,0021	0,0346	-0,1426	-0,0104	-0,1731
V	0,0286	0,0183	0,0373	-0,1431	-0,0917	-0,1863
Y	0,0283	0,0125	0,0061	-0,1413	-0,0624	-0,0307
Zn	0,0284	-0,0020	0,0412	-0,1422	0,0100	-0,2059
Zr	0,0284	0,0001	0,0012	-0,1422	-0,0004	-0,0058

Table B.31 Results of the ordering energy and interchange energy calculations for Fe66W33M1, in atomic units.

Fe66W33M1						
M	**W_{Fe-W} a.u.**	**W_{Fe-M} a.u.**	**W_{W-M} a.u.**	**$^{W}Fe-W$ a.u.**	**$^{W}Fe-M$ a.u.**	**$^{W}W-M$ a.u.**
None	0,0298	-	-	-0,1490	-	-
Al	0,0299	-0,0044	0,0470	-0,1494	0,0222	-0,2348
B	0,0298	0,0285	0,0808	-0,1492	-0,1424	-0,4039
Bi	0,0297	0,0459	-0,0505	-0,1484	-0,2294	0,2524
C	0,0299	0,0124	0,0700	-0,1495	-0,0620	-0,3498
Ca	0,0295	0,0660	0,0298	-0,1476	-0,3300	-0,1488
Co	0,0298	0,0004	0,0423	-0,1489	-0,0021	-0,2116
Cr	0,0298	0,0003	0,0402	-0,1490	-0,0014	-0,2008
Cu	0,0297	-0,0023	0,0200	-0,1487	0,0113	-0,1000
Ga	0,0298	0,0011	0,0317	-0,1488	-0,0057	-0,1583
Ge	0,0298	0,0004	0,0298	-0,1488	-0,0019	-0,1488
Hf	0,0297	0,0192	0,0000	-0,1487	-0,0962	0,0002
K	0,0292	0,0527	0,1618	-0,1460	-0,2634	-0,8091
Mg	0,0297	-0,0045	0,0549	-0,1484	0,0224	-0,2746
Mn	0,0298	-0,0006	0,0302	-0,1488	0,0028	-0,1508
Mo	0,0298	0,0312	0,0004	-0,1492	-0,1560	-0,0020
Na	0,0295	0,0082	0,0836	-0,1477	-0,0411	-0,4179
Nb	0,0298	0,0116	0,0012	-0,1491	-0,0581	-0,0058
Ni	0,0298	0,0005	0,0425	-0,1489	-0,0023	-0,2124
P	0,0298	0,0031	0,0463	-0,1490	-0,0153	-0,2314
Pb	0,0297	0,0224	-0,0775	-0,1484	-0,1122	0,3875
Pd	0,0297	0,0120	0,0522	-0,1487	-0,0599	-0,2609
Pt	0,0297	0,0095	0,0331	-0,1487	-0,0473	-0,1654
Re	0,0299	0,0221	-0,0007	-0,1495	-0,1103	0,0034
Si	0,0298	-0,0028	0,0429	-0,1489	0,0140	-0,2143
Sn	0,0297	0,0056	0,0085	-0,1486	-0,0279	-0,0423
Ta	0,0298	0,0116	0,0018	-0,1491	-0,0580	-0,0090
Ti	0,0298	0,0023	0,0344	-0,1489	-0,0113	-0,1719
V	0,0298	-0,0018	0,0370	-0,1492	0,0088	-0,1848
Y	0,0296	0,0063	0,0065	-0,1482	-0,0314	-0,0324
Zn	0,0297	0,0014	0,0417	-0,1487	-0,0070	-0,2084
Zr	0,0297	0,0156	0,0013	-0,1487	-0,0780	-0,0067

Table B.32 Results of the ordering energy and interchange energy calculations for Fe67W32M1, in atomic units.

Fe67W32M1						
M	**W_{Fe-W} a.u.**	**W_{Fe-M} a.u.**	**W_{W-M} a.u.**	**$^{W}Fe-W$ a.u.**	**$^{W}Fe-M$ a.u.**	**$^{W}W-M$ a.u.**
None	0,0298	-	-	-0,1490	-	-
Al	0,0298	-0,0044	0,0469	-0,1491	0,0221	-0,2347
B	0,0298	0,0285	0,0810	-0,1489	-0,1427	-0,4050
Bi	0,0296	0,0461	-0,0502	-0,1481	-0,2305	0,2508
C	0,0298	0,0124	0,0700	-0,1491	-0,0621	-0,3500
Ca	0,0294	0,0677	0,2332	-0,1471	-0,3385	-1,1659
Co	0,0297	0,0004	0,0423	-0,1485	-0,0021	-0,2113
Cr	0,0297	0,0003	0,0401	-0,1487	-0,0015	-0,2007
Cu	0,0297	-0,0023	0,0199	-0,1483	0,0114	-0,0994
Ga	0,0298	0,0011	0,0317	-0,1488	-0,0056	-0,1585
Ge	0,0297	0,0004	0,0297	-0,1485	-0,0018	-0,1487
Hf	0,0297	0,0192	-0,0001	-0,1484	-0,0960	0,0003
K	0,0291	0,0533	0,1626	-0,1456	-0,2667	-0,8132
Mg	0,0296	-0,0044	0,0549	-0,1481	0,0220	-0,2747
Mn	0,0297	-0,0006	0,0301	-0,1485	0,0028	-0,1504
Mo	0,0298	0,0311	0,0004	-0,1489	-0,1555	-0,0020
Na	0,0295	0,0084	0,0837	-0,1473	-0,0420	-0,4186
Nb	0,0297	0,0116	0,0012	-0,1487	-0,0579	-0,0058
Ni	0,0297	0,0005	0,0424	-0,1485	-0,0023	-0,2120
P	0,0297	0,0030	0,0463	-0,1487	-0,0149	-0,2316
Pb	0,0296	0,0227	-0,0771	-0,1481	-0,1136	0,3857
Pd	0,0297	0,0120	0,0520	-0,1484	-0,0602	-0,2600
Pt	0,0297	0,0095	0,0332	-0,1484	-0,0473	-0,1662
Re	0,0298	0,0219	-0,0007	-0,1492	-0,1097	0,0034
Si	0,0297	-0,0028	0,0429	-0,1486	0,0142	-0,2143
Sn	0,0296	0,0056	0,0084	-0,1482	-0,0279	-0,0421
Ta	0,0297	0,0115	0,0018	-0,1487	-0,0577	-0,0090
Ti	0,0297	0,0022	0,0344	-0,1486	-0,0112	-0,1720
V	0,0298	-0,0018	0,0369	-0,1489	0,0089	-0,1845
Y	0,0296	0,0062	0,0065	-0,1478	-0,0312	-0,0323
Zn	0,0297	0,0014	0,0417	-0,1484	-0,0070	-0,2083
Zr	0,0297	0,0156	0,0013	-0,1484	-0,0778	-0,0067

Table B.33 Results of the ordering energy and interchange energy calculations for Fe59W40M1, in atomic units.

Fe59W40M1						
M	**W_{Fe-W} a.u.**	**W_{Fe-M} a.u.**	**W_{W-M} a.u.**	**$^{W}Fe-W$ a.u.**	**$^{W}Fe-M$ a.u.**	**$^{W}W-M$ a.u.**
None	0,0302	-	-	-0,1510	-	-
Al	0,0303	-0,0045	0,0471	-0,1513	0,0224	-0,2354
B	0,0302	0,0281	0,0793	-0,1512	-0,1404	-0,3964
Bi	0,0301	0,0441	-0,0527	-0,1507	-0,2207	0,2635
C	0,0299	0,0122	0,0696	-0,1495	-0,0609	-0,3480
Ca	0,0300	0,0537	0,0297	-0,1500	-0,2686	-0,1487
Co	0,0302	0,0004	0,0427	-0,1509	-0,0021	-0,2136
Cr	0,0302	0,0002	0,0401	-0,1510	-0,0009	-0,2006
Cu	0,0302	-0,0021	0,0208	-0,1508	0,0107	-0,1040
Ga	0,0302	0,0013	0,0313	-0,1509	-0,0066	-0,1567
Ge	0,0302	0,0005	0,0297	-0,1509	-0,0026	-0,1487
Hf	0,0302	0,0195	0,0000	-0,1509	-0,0975	-0,0001
K	0,0298	0,0479	0,1552	-0,1489	-0,2393	-0,7759
Mg	0,0301	-0,0050	0,0546	-0,1507	0,0250	-0,2730
Mn	0,0302	-0,0005	0,0307	-0,1509	0,0027	-0,1533
Mo	0,0302	0,0318	0,0004	-0,1512	-0,1589	-0,0020
Na	0,0300	0,0069	0,0822	-0,1501	-0,0343	-0,4108
Nb	0,0302	0,0119	0,0011	-0,1511	-0,0597	-0,0057
Ni	0,0302	0,0004	0,0429	-0,1510	-0,0022	-0,2143
P	0,0302	0,0036	0,0460	-0,1511	-0,0179	-0,2302
Pb	0,0301	0,0202	-0,0798	-0,1507	-0,1011	0,3990
Pd	0,0302	0,0115	0,0531	-0,1508	-0,0576	-0,2655
Pt	0,0302	0,0094	0,0320	-0,1508	-0,0468	-0,1600
Re	0,0303	0,0228	-0,0006	-0,1513	-0,1141	0,0030
Si	0,0302	-0,0025	0,0429	-0,1510	0,0127	-0,2144
Sn	0,0302	0,0056	0,0086	-0,1508	-0,0281	-0,0432
Ta	0,0302	0,0120	0,0018	-0,1511	-0,0599	-0,0089
Ti	0,0302	0,0023	0,0342	-0,1510	-0,0115	-0,1710
V	0,0302	-0,0017	0,0373	-0,1512	0,0084	-0,1865
Y	0,0301	0,0066	0,0066	-0,1505	-0,0329	-0,0331
Zn	0,0302	0,0014	0,0418	-0,1508	-0,0072	-0,2089
Zr	0,0302	0,0158	0,0014	-0,1508	-0,0790	-0,0070

Table B.34 Results of the ordering energy and interchange energy calculations for Fe60W39M1, in atomic units.

Fe60W39M1						
M	**W_{Fe-W} a.u.**	**W_{Fe-M} a.u.**	**W_{W-M} a.u.**	**$^{W}Fe-W$ a.u.**	**$^{W}Fe-M$ a.u.**	**$^{W}W-M$ a.u.**
None	0,0302	-	-	-0,1510	-	-
Al	0,0302	-0,0045	0,0471	-0,1662	0,0246	-0,2589
B	0,0302	0,0281	0,0795	-0,1812	-0,1689	-0,4770
Bi	0,0301	0,0444	-0,0524	-0,1955	-0,2886	0,3405
C	0,0302	0,0122	0,0696	-0,2116	-0,0855	-0,4875
Ca	0,0299	0,0555	0,2243	-0,2246	-0,4164	-1,6826
Co	0,0301	0,0004	0,0427	-0,2411	-0,0034	-0,3414
Cr	0,0302	0,0002	0,0401	-0,2563	-0,0016	-0,3412
Cu	0,0301	-0,0022	0,0207	-0,1505	0,0108	-0,1035
Ga	0,0302	0,0013	0,0314	-0,1509	-0,0065	-0,1569
Ge	0,0301	0,0005	0,0298	-0,1507	-0,0025	-0,1488
Hf	0,0301	0,0195	0,0000	-0,1506	-0,0974	-0,0001
K	0,0297	0,0486	0,1562	-0,1485	-0,2428	-0,7811
Mg	0,0301	-0,0049	0,0547	-0,1504	0,0247	-0,2734
Mn	0,0301	-0,0005	0,0306	-0,1506	0,0027	-0,1530
Mo	0,0302	0,0317	0,0004	-0,1509	-0,1586	-0,0020
Na	0,0300	0,0071	0,0824	-0,1498	-0,0353	-0,4120
Nb	0,0302	0,0119	0,0011	-0,1508	-0,0595	-0,0057
Ni	0,0301	0,0004	0,0428	-0,1507	-0,0022	-0,2141
P	0,0302	0,0035	0,0461	-0,1508	-0,0176	-0,2304
Pb	0,0301	0,0205	-0,0795	-0,1504	-0,1027	0,3975
Pd	0,0301	0,0116	0,0530	-0,1506	-0,0580	-0,2651
Pt	0,0301	0,0094	0,0322	-0,1506	-0,0469	-0,1608
Re	0,0302	0,0227	-0,0006	-0,1511	-0,1136	0,0031
Si	0,0302	-0,0026	0,0429	-0,1508	0,0129	-0,2144
Sn	0,0301	0,0056	0,0086	-0,1505	-0,0281	-0,0431
Ta	0,0302	0,0119	0,0018	-0,1508	-0,0597	-0,0089
Ti	0,0301	0,0023	0,0342	-0,1507	-0,0115	-0,1711
V	0,0302	-0,0017	0,0369	-0,1509	0,0084	-0,1845
Y	0,0300	0,0065	0,0066	-0,1502	-0,0327	-0,0330
Zn	0,0301	0,0014	0,0418	-0,1506	-0,0072	-0,2088
Zr	0,0301	0,0158	0,0014	-0,1506	-0,0789	-0,0070

Table B.35 Results of the ordering energy and interchange energy calculations for Fe79W20M1, in SI units.

Fe79W20M1						
M	**W_{Fe-W} J/mol x10^4**	**W_{Fe-M} J/mol x10^4**	**W_{W-M} J/mol x10^4**	**w_{Fe-W} J/mol x10^5**	**w_{Fe-M} J/mol x10^5**	**w_{W-M} J/mol x10^5**
None	7,515	-	-	-3,758	-	-
Al	7,553	-1,128	12,125	-3,777	0,564	-6,063
B	7,538	7,603	21,988	-3,769	-3,802	-10,994
Bi	7,470	12,604	-12,024	-3,735	-6,302	6,012
C	7,556	3,347	18,503	-3,778	-1,673	-9,252
Ca	7,400	22,628	7,763	-3,700	-11,314	-3,882
Co	7,507	0,114	10,774	-3,754	-0,057	-5,387
Cr	7,519	0,118	10,352	-3,759	-0,059	-5,176
Cu	7,491	-0,672	4,778	-3,745	0,336	-2,389
Ga	7,497	0,197	8,433	-3,748	-0,098	-4,217
Ge	7,503	0,025	7,763	-3,751	-0,013	-3,882
Hf	7,497	4,835	-0,050	-3,749	-2,417	0,025
K	7,288	15,858	44,407	-3,644	-7,929	-22,204
Mg	7,470	-0,901	14,308	-3,735	0,450	-7,154
Mn	7,502	-0,155	7,562	-3,751	0,078	-3,781
Mo	7,541	7,748	0,101	-3,771	-3,874	-0,051
Na	7,408	2,750	22,097	-3,704	-1,375	-11,048
Nb	7,524	2,857	0,318	-3,762	-1,429	-0,159
Ni	7,508	0,120	10,812	-3,754	-0,060	-5,406
P	7,519	0,514	12,239	-3,759	-0,257	-6,119
Pb	7,472	6,762	-18,979	-3,736	-3,381	9,489
Pd	7,495	3,273	12,755	-3,748	-1,637	-6,377
Pt	7,494	2,460	9,284	-3,747	-1,230	-4,642
Re	7,561	5,319	-0,213	-3,781	-2,659	0,107
Si	7,511	-0,862	11,162	-3,756	0,431	-5,581
Sn	0,844	1,422	2,098	-0,422	-0,711	-1,049
Ta	7,524	2,805	0,471	-3,762	-1,402	-0,236
Ti	7,513	0,551	9,084	-3,757	-0,276	-4,542
V	7,538	-0,519	9,425	-3,769	0,260	-4,713
Y	7,449	1,450	1,620	-3,724	-0,725	-0,810
Zn	7,493	0,347	10,820	-3,747	-0,174	-5,410
Zr	7,494	3,937	0,310	-3,747	-1,968	-0,155

Table B.36 Results of the ordering energy and interchange energy calculations for Fe80W19M1, in SI units.

Fe80W19M1						
M	**W_{Fe-W} J/mol x10^4**	**W_{Fe-M} J/mol x10^4**	**W_{W-M} J/mol x10^4**	**w_{Fe-W} J/mol x10^5**	**w_{Fe-M} J/mol x10^5**	**w_{W-M} J/mol x10^5**
None	7,515	-	-	-3,758	-	-
Al	7,525	0,188	12,101	-3,762	-0,094	-6,050
B	7,509	1,432	22,052	-3,754	-0,716	-11,026
Bi	7,440	7,609	-11,921	-3,720	-3,805	5,960
C	7,528	3,354	18,279	-3,764	-1,677	-9,140
Ca	7,367	12,629	63,510	-3,684	-6,314	-31,755
Co	7,477	0,114	10,739	-3,739	-0,057	-5,370
Cr	7,489	0,121	10,325	-3,744	-0,061	-5,163
Cu	6,372	-0,679	4,737	-3,186	0,339	-2,368
Ga	7,497	6,815	8,441	-3,748	-3,408	-4,221
Ge	7,472	22,991	7,757	-3,736	-11,495	-3,879
Hf	7,467	3,921	-0,053	-3,734	-1,960	0,027
K	7,253	-0,879	44,469	-3,626	0,439	-22,235
Mg	7,439	7,295	14,284	-3,720	-3,647	-7,142
Mn	7,472	-0,156	7,527	-3,736	0,078	-3,764
Mo	7,512	7,706	0,101	-3,756	-3,853	-0,050
Na	7,375	15,992	22,076	-3,688	-7,996	-11,038
Nb	7,495	2,840	0,318	-3,747	-1,420	-0,159
Ni	7,479	0,120	10,778	-3,739	-0,060	-5,389
P	7,489	1,418	12,245	-3,744	-0,709	-6,122
Pb	7,441	7,459	-18,860	-3,721	-3,729	9,430
Pd	7,465	2,453	12,652	-3,732	-1,227	-6,326
Pt	7,464	2,791	9,335	-3,732	-1,396	-4,667
Re	7,533	5,276	-0,216	-3,766	-2,638	0,108
Si	7,481	0,345	11,150	-3,741	-0,173	-5,575
Sn	7,454	-0,872	2,087	-3,727	0,436	-1,044
Ta	7,495	2,783	0,471	-3,747	-1,392	-0,235
Ti	7,484	0,547	9,087	-3,742	-0,274	-4,543
V	7,509	4,812	9,780	-3,755	-2,406	-4,890
Y	7,417	3,276	1,612	-3,709	-1,638	-0,806
Zn	7,463	-0,524	10,807	-3,732	0,262	-5,403
Zr	7,464	0,019	0,306	-3,732	-0,009	-0,153

Table B.37 Results of the ordering energy and interchange energy calculations for Fe66W33M1, in SI units.

Fe66W33M1						
M	**W_{Fe-W} J/mol x10^4**	**W_{Fe-M} J/mol x10^4**	**W_{W-M} J/mol x10^4**	**$^{W}Fe-W$ J/mol x10^5**	**$^{W}Fe-M$ J/mol x10^5**	**$^{W}W-M$ J/mol x10^5**
None	7,819	-	-	-3,909	-	-
Al	7,843	-1,164	12,326	-3,921	0,582	-6,163
B	7,834	7,476	21,200	-3,917	-3,738	-10,600
Bi	7,791	12,043	-13,249	-3,896	-6,022	6,625
C	7,845	3,253	18,359	-3,923	-1,626	-9,180
Ca	7,745	17,323	7,808	-3,873	-8,662	-3,904
Co	7,814	0,112	11,108	-3,907	-0,056	-5,554
Cr	7,821	0,074	10,538	-3,911	-0,037	-5,269
Cu	7,804	-0,595	5,251	-3,902	0,297	-2,625
Ga	7,808	0,299	8,307	-3,904	-0,150	-4,153
Ge	7,813	0,102	7,808	-3,906	-0,051	-3,904
Hf	7,808	5,052	-0,012	-3,904	-2,526	0,006
K	7,666	13,827	42,469	-3,833	-6,913	-21,235
Mg	7,792	-1,174	14,416	-3,896	0,587	-7,208
Mn	7,811	-0,146	7,917	-3,905	0,073	-3,959
Mo	7,833	8,186	0,103	-3,917	-4,093	-0,052
Na	7,751	2,155	21,934	-3,876	-1,077	-10,967
Nb	7,824	3,051	0,305	-3,912	-1,526	-0,153
Ni	7,815	0,118	11,147	-3,908	-0,059	-5,574
P	7,822	0,804	12,146	-3,911	-0,402	-6,073
Pb	7,792	5,887	-20,339	-3,896	-2,944	10,170
Pd	7,807	3,147	13,697	-3,904	-1,573	-6,848
Pt	7,806	2,483	8,683	-3,903	-1,242	-4,342
Re	7,846	5,792	-0,178	-3,923	-2,896	0,089
Si	7,818	-0,735	11,250	-3,909	0,368	-5,625
Sn	7,800	1,465	2,219	-3,900	-0,732	-1,110
Ta	7,824	3,045	0,470	-3,912	-1,522	-0,235
Ti	7,818	0,591	9,022	-3,909	-0,296	-4,511
V	7,833	-0,464	9,700	-3,916	0,232	-4,850
Y	7,777	1,648	1,703	-3,889	-0,824	-0,851
Zn	7,806	0,370	10,939	-3,903	-0,185	-5,469
Zr	7,806	4,094	0,352	-3,903	-2,047	-0,176

Table B.38 Results of the ordering energy and interchange energy calculations for Fe67W32M1, in SI units.

Fe67W32M1						
M	**W_{Fe-W} J/mol x10^4**	**W_{Fe-M} J/mol x10^4**	**W_{W-M} J/mol x10^4**	**$^{W}Fe-W$ J/mol x10^5**	**$^{W}Fe-M$ J/mol x10^5**	**$^{W}W-M$ J/mol x10^5**
None	7,819	-	-	-3,909	-	-
Al	7,825	-1,162	12,317	-3,913	0,581	-6,159
B	7,816	7,489	21,257	-3,908	-3,744	-10,629
Bi	7,771	12,101	-13,162	-3,886	-6,050	6,581
C	7,828	3,260	18,372	-3,914	-1,630	-9,186
Ca	7,723	17,766	61,197	-3,862	-8,883	-30,598
Co	7,796	0,112	11,090	-3,898	-0,056	-5,545
Cr	7,803	0,078	10,534	-3,901	-0,039	-5,267
Cu	7,785	-0,600	5,219	-3,892	0,300	-2,609
Ga	7,808	0,292	8,318	-3,904	-0,146	-4,159
Ge	7,794	0,096	7,807	-3,897	-0,048	-3,904
Hf	7,789	5,040	-0,014	-3,894	-2,520	0,007
K	7,642	14,000	42,683	-3,821	-7,000	-21,342
Mg	7,772	-1,154	14,420	-3,886	0,577	-7,210
Mn	7,792	-0,147	7,895	-3,896	0,073	-3,948
Mo	7,816	8,160	0,103	-3,908	-4,080	-0,051
Na	7,730	2,204	21,973	-3,865	-1,102	-10,986
Nb	7,806	3,038	0,306	-3,903	-1,519	-0,153
Ni	7,797	0,118	11,128	-3,898	-0,059	-5,564
P	7,804	0,783	12,154	-3,902	-0,392	-6,077
Pb	7,772	5,965	-20,246	-3,886	-2,982	10,123
Pd	7,788	3,161	13,648	-3,894	-1,581	-6,824
Pt	7,787	2,485	8,726	-3,894	-1,242	-4,363
Re	7,829	5,761	-0,181	-3,915	-2,880	0,090
Si	7,799	-0,745	11,247	-3,900	0,373	-5,624
Sn	7,781	1,462	2,211	-3,890	-0,731	-1,106
Ta	7,806	3,029	0,470	-3,903	-1,514	-0,235
Ti	7,799	0,589	9,028	-3,900	-0,295	-4,514
V	7,815	-0,468	9,684	-3,908	0,234	-4,842
Y	7,757	1,635	1,697	-3,878	-0,818	-0,849
Zn	7,787	0,368	10,933	-3,893	-0,184	-5,467
Zr	7,787	4,085	0,349	-3,893	-2,043	-0,175

Table B.39 Results of the ordering energy and interchange energy calculations for Fe59W40M1, in SI units.

Fe59W40M1						
M	**W_{Fe-W} J/mol x10^4**	**W_{Fe-M} J/mol x10^4**	**W_{W-M} J/mol x10^4**	**$^{W}Fe-W$ J/mol x10^5**	**$^{W}Fe-M$ J/mol x10^5**	**$^{W}W-M$ J/mol x10^5**
None	7,925	-	-	-3,963	-	-
Al	7,942	-1,174	12,356	-3,971	0,587	-6,178
B	7,937	7,371	20,809	-3,969	-3,685	-10,405
Bi	7,908	11,583	-13,829	-3,954	-5,791	6,915
C	7,845	3,199	18,265	-3,923	-1,600	-9,133
Ca	7,875	14,097	7,807	-3,937	-7,048	-3,904
Co	7,923	0,111	11,212	-3,961	-0,055	-5,606
Cr	7,928	0,046	10,531	-3,964	-0,023	-5,265
Cu	7,916	-0,560	5,458	-3,958	0,280	-2,729
Ga	7,920	0,345	8,223	-3,960	-0,173	-4,111
Ge	7,923	0,136	7,807	-3,962	-0,068	-3,904
Hf	7,919	5,119	0,007	-3,959	-2,559	-0,004
K	7,815	12,560	40,728	-3,907	-6,280	-20,364
Mg	7,908	-1,314	14,332	-3,954	0,657	-7,166
Mn	7,920	-0,142	8,046	-3,960	0,071	-4,023
Mo	7,935	8,342	0,102	-3,967	-4,171	-0,051
Na	7,880	1,798	21,561	-3,940	-0,899	-10,780
Nb	7,930	3,133	0,298	-3,965	-1,566	-0,149
Ni	7,924	0,117	11,251	-3,962	-0,058	-5,626
P	7,930	0,941	12,082	-3,965	-0,470	-6,041
Pb	7,908	5,304	-20,944	-3,954	-2,652	10,472
Pd	7,918	3,025	13,937	-3,959	-1,513	-6,969
Pt	7,918	2,458	8,399	-3,959	-1,229	-4,200
Re	7,944	5,988	-0,160	-3,972	-2,994	0,080
Si	7,927	-0,667	11,253	-3,963	0,333	-5,627
Sn	7,914	1,476	2,269	-3,957	-0,738	-1,134
Ta	7,930	3,145	0,468	-3,965	-1,572	-0,234
Ti	7,926	0,605	8,974	-3,963	-0,303	-4,487
V	7,936	-0,439	9,790	-3,968	0,219	-4,895
Y	7,898	1,725	1,738	-3,949	-0,863	-0,869
Zn	7,917	0,379	10,963	-3,959	-0,190	-5,481
Zr	7,917	4,149	0,370	-3,959	-2,074	-0,185

Table B.40 Results of the ordering energy and interchange energy calculations for Fe60W39M1, in SI units.

Fe60W39M1						
M	**W_{Fe-W} J/mol x10^4**	**W_{Fe-M} J/mol x10^4**	**W_{W-M} J/mol x10^4**	**$^{W}Fe-W$ J/mol x10^5**	**$^{W}Fe-M$ J/mol x10^5**	**$^{W}W-M$ J/mol x10^5**
None	7,925	-	-	-3,963	-	-
Al	7,930	-1,173	12,355	-4,361	0,645	-6,795
B	7,924	7,387	20,864	-4,755	-4,432	-12,518
Bi	7,894	11,654	-13,750	-5,131	-7,575	8,937
C	7,932	3,207	18,279	-5,553	-2,245	-12,796
Ca	7,858	14,571	58,878	-5,894	-10,928	-44,159
Co	7,910	0,111	11,200	-6,328	-0,089	-8,960
Cr	7,915	0,050	10,536	-6,728	-0,042	-8,956
Cu	7,902	-0,565	5,430	-3,951	0,282	-2,715
Ga	7,920	0,339	8,235	-3,960	-0,169	-4,118
Ge	7,910	0,131	7,808	-3,955	-0,066	-3,904
Hf	7,905	5,111	0,005	-3,952	-2,556	-0,002
K	7,796	12,746	41,000	-3,898	-6,373	-20,500
Mg	7,894	-1,294	14,349	-3,947	0,647	-7,175
Mn	7,907	-0,143	8,030	-3,953	0,071	-4,015
Mo	7,922	8,323	0,103	-3,961	-4,161	-0,051
Na	7,863	1,850	21,624	-3,932	-0,925	-10,812
Nb	7,917	3,122	0,299	-3,958	-1,561	-0,149
Ni	7,910	0,117	11,239	-3,955	-0,058	-5,620
P	7,917	0,922	12,092	-3,958	-0,461	-6,046
Pb	7,894	5,392	-20,862	-3,947	-2,696	10,431
Pd	7,904	3,045	13,913	-3,952	-1,522	-6,956
Pt	7,904	2,463	8,438	-3,952	-1,232	-4,219
Re	7,932	5,962	-0,163	-3,966	-2,981	0,081
Si	7,914	-0,676	11,254	-3,957	0,338	-5,627
Sn	7,900	1,475	2,262	-3,950	-0,738	-1,131
Ta	7,917	3,132	0,468	-3,958	-1,566	-0,234
Ti	7,912	0,603	8,981	-3,956	-0,302	-4,491
V	7,923	-0,443	9,684	-3,962	0,221	-4,842
Y	7,883	1,715	1,733	-3,941	-0,858	-0,867
Zn	7,903	0,378	10,961	-3,952	-0,189	-5,480
Zr	7,904	4,142	0,367	-3,952	-2,071	-0,184

APPENDIX C

CALCULATED VALUES OF ΔH^M, ΔS^M, S^s, $\Delta h/h_0$, R_c AND a_1 FOR Fe-Zr, Fe-Nb, Fe-C AND Fe-W SYSTEMS

C.1 Fe-Zr System

Table C.1 Calculated values of enthalpy of mixing (ΔH^M), mismatch entropy (S^σ), entropy of mixing (ΔS^M), change in viscosity ($\Delta\eta/\eta_0$), critical cooling rate (R_c) and short range order parameter (α_1) for Fe72Zr27M1.

Fe72Zr27M1						
M	ΔH^M **J/mol x10^4**	S^s **J/mol.K**	ΔS^M **J/mol.K**	$\Delta h/h_0$	R_C **K/s x10^8**	a_1
None	-1,855	0,482	5,329	1,171	1,966	-0,370
Al	-1,857	2,580	7,866	1,173	1,397	
B	-1,918	8,445	13,731	1,211	0,583	
Bi	-1,979	3,553	8,839	1,249	1,131	
C	-1,888	14,520	19,806	1,192	0,246	
Ca	-1,869	0,356	5,642	1,180	1,914	
Co	-1,985	-0,300	4,986	1,253	1,989	
Cr	-1,832	2,723	8,009	1,157	1,382	
Cu	-1,858	2,717	8,003	1,173	1,366	
Ga	-1,873	2,708	7,994	1,182	1,357	
Ge	-1,867	2,725	8,011	1,179	1,358	
Hf	-1,781	2,750	8,036	1,125	1,398	
K	-1,864	3,840	9,126	1,177	1,160	
Mg	-1,846	2,761	8,047	1,166	1,369	
Mn	-1,868	2,709	7,995	1,179	1,362	
Mo	-1,968	2,708	7,994	1,242	1,295	
Na	-1,910	2,973	8,259	1,206	1,288	
Nb	-1,845	2,711	7,997	1,165	1,372	
Ni	-2,264	2,724	8,010	1,429	1,127	
P	-1,941	2,793	8,079	1,225	1,302	
Re	-2,070	2,708	7,994	1,307	1,226	
Se	-1,891	2,709	7,994	1,194	1,344	
Si	-1,854	2,753	8,039	1,170	1,365	
Ta	-2,619	2,711	7,997	1,653	0,945	
Ti	-1,809	2,715	8,001	1,142	1,400	
V	-1,859	2,712	7,998	1,174	1,368	
W	-1,909	2,708	7,994	1,205	1,323	
Y	-1,874	2,911	8,197	1,183	1,315	
Zn	-1,801	2,708	7,994	1,137	1,404	

Table C.2 Calculated values of enthalpy of mixing (ΔH^M), mismatch entropy (S^σ), entropy of mixing (ΔS^M), change in viscosity ($\Delta\eta/\eta_0$), critical cooling rate (R_c) and short range order parameter (α_1) for Fe73Zr26M1.

Fe73Zr26M1						
M	DH^M **J/mol x10^4**	S^s **J/mol.K**	DS^M **J/mol.K**	Dh/h_0	R_C **K/s x10^8**	a_1
None	-1,855	0,482	5,329	1,171	1,966	-0,370
Al	-1,863	2,542	7,744	1,176	1,416	
B	-2,042	8,324	13,526	1,289	0,565	
Bi	-1,922	3,507	8,709	1,214	1,181	
C	-1,950	14,311	19,513	1,231	0,249	
Ca	-2,217	0,366	5,568	1,400	1,637	
Co	-1,831	-0,295	4,907	1,156	2,160	
Cr	-1,861	2,683	7,886	1,175	1,386	
Cu	-1,757	2,678	7,880	1,109	1,456	
Ga	-1,828	2,669	7,872	1,154	1,408	
Ge	-1,820	2,686	7,888	1,149	1,410	
Hf	-1,887	2,713	7,915	1,192	1,350	
K	-2,580	3,821	9,023	1,629	0,837	
Mg	-1,782	2,725	7,927	1,125	1,433	
Mn	-1,807	2,670	7,872	1,141	1,424	
Mo	-1,962	2,669	7,871	1,238	1,320	
Na	-1,830	2,941	8,143	1,155	1,358	
Nb	-1,843	2,672	7,874	1,163	1,396	
Ni	-1,832	2,684	7,886	1,157	1,404	
P	-1,882	2,753	7,955	1,188	1,361	
Re	-1,894	2,669	7,871	1,196	1,354	
Se	-1,849	2,670	7,872	1,167	1,394	
Si	-1,837	2,712	7,915	1,160	1,398	
Ta	-1,849	2,672	7,875	1,167	1,383	
Ti	-1,843	2,677	7,879	1,163	1,400	
V	-1,823	2,672	7,875	1,151	1,414	
W	-1,944	2,669	7,871	1,227	1,322	
Y	-1,779	2,878	8,081	1,123	1,397	
Zn	-1,821	2,670	7,872	1,150	1,414	

Table C.3 Calculated values of enthalpy of mixing (ΔH^M), mismatch entropy (S^σ), entropy of mixing (ΔS^M), change in viscosity ($\Delta\eta/\eta_0$), critical cooling rate (R_c) and short range order parameter (α_1) for Fe66Zr33M1.

Fe66Zr33M1						
M	DH^M **J/mol x10^4**	S^s **J/mol.K**	DS^M **J/mol.K**	Dh/h_0	R_C **K/s x10^8**	a_1
None	-1,953	0,513	5,783	1,224	1,857	-0,493
Al	-2,004	2,744	8,446	1,256	1,267	
B	-2,181	8,962	14,664	1,367	0,475	
Bi	-1,997	3,752	9,454	1,252	1,084	
C	-2,091	15,411	21,113	1,310	0,195	
Ca	-2,475	0,308	6,010	1,551	1,441	
Co	-1,957	-0,317	5,384	1,227	2,009	
Cr	-1,991	2,893	8,594	1,248	1,245	
Cu	-1,870	2,886	8,588	1,172	1,318	
Ga	-1,950	2,872	8,574	1,222	1,271	
Ge	-1,942	2,895	8,597	1,217	1,271	
Hf	-1,990	2,902	8,604	1,247	1,232	
K	-2,796	3,896	9,598	1,752	0,738	
Mg	-1,918	2,912	8,614	1,202	1,287	
Mn	-1,928	2,874	8,576	1,208	1,285	
Mo	-2,067	2,873	8,575	1,295	1,201	
Na	-1,978	3,099	8,801	1,239	1,219	
Nb	-1,955	2,872	8,574	1,226	1,266	
Ni	-1,958	2,893	8,595	1,227	1,263	
P	-2,011	2,967	8,669	1,261	1,222	
Re	-2,006	2,872	8,574	1,257	1,227	
Se	-1,968	2,872	8,574	1,233	1,260	
Si	-1,967	2,924	8,626	1,233	1,255	
Ta	-1,961	2,872	8,574	1,229	1,254	
Ti	-1,968	2,875	8,577	1,234	1,262	
V	-1,971	2,879	8,581	1,235	1,259	
W	-2,053	2,873	8,575	1,286	1,201	
Y	-1,881	3,044	8,745	1,179	1,279	
Zn	-1,925	2,872	8,574	1,207	1,286	

Table C.4 Calculated values of enthalpy of mixing (ΔH^M), mismatch entropy (S^σ), entropy of mixing (ΔS^M), change in viscosity ($\Delta\eta/\eta_0$), critical cooling rate (R_c) and short range order parameter (α_1) for Fe67Zr32M1.

Fe67Zr32M1						
M	**ΔH^M J/mol x10^4**	**S^s J/mol.K**	**ΔS^M J/mol.K**	**$\Delta h/h_0$**	**R_C K/s x10^8**	**a_1**
None	-1,953	0,513	5,783	1,224	1,857	-0,493
Al	-1,991	2,724	8,366	1,248	1,288	
B	-2,169	8,900	14,542	1,359	0,486	
Bi	-1,994	3,728	9,370	1,250	1,098	
C	-2,079	15,303	20,946	1,303	0,201	
Ca	-2,447	0,315	5,957	1,534	1,471	
Co	-1,947	-0,315	5,327	1,220	2,035	
Cr	-1,980	2,872	8,515	1,241	1,265	
Cu	-1,861	2,865	8,508	1,167	1,338	
Ga	-1,940	2,852	8,495	1,216	1,291	
Ge	-1,932	2,875	8,517	1,211	1,291	
Hf	-1,983	2,885	8,527	1,243	1,249	
K	-2,773	3,893	9,536	1,738	0,753	
Mg	-1,906	2,894	8,537	1,195	1,308	
Mn	-1,919	2,855	8,497	1,202	1,305	
Mo	-2,059	2,854	8,496	1,291	1,218	
Na	-1,964	3,085	8,727	1,231	1,239	
Nb	-1,947	2,853	8,496	1,220	1,284	
Ni	-1,948	2,873	8,515	1,221	1,283	
P	-2,000	2,946	8,588	1,254	1,242	
Re	-1,998	2,853	8,495	1,252	1,246	
Se	-1,959	2,852	8,495	1,228	1,279	
Si	-1,956	2,904	8,546	1,226	1,276	
Ta	-1,952	2,853	8,496	1,224	1,273	
Ti	-1,958	2,856	8,499	1,227	1,282	
V	-1,960	2,859	8,501	1,229	1,279	
W	-2,045	2,853	8,496	1,282	1,218	
Y	-1,874	3,029	8,671	1,174	1,296	
Zn	-1,934	2,852	8,495	1,212	1,295	

Table C.5 Calculated values of enthalpy of mixing (ΔH^M), mismatch entropy (S^σ), entropy of mixing (ΔS^M), change in viscosity ($\Delta\eta/\eta_0$), critical cooling rate (R_c) and short range order parameter (α_1) for Fe32Zr67M1.

Fe32Zr67M1						
M	ΔH^M **J/mol x10^4**	S^s **J/mol.K**	ΔS^M **J/mol.K**	$\Delta h/h_0$	R_C **K/s x10^8**	a_1
None	-1,302	0,397	5,667	1,088	1,453	-0,492
Al	-1,404	2,160	7,803	1,173	1,024	
B	-1,611	6,983	12,626	1,346	0,449	
Bi	-1,169	3,046	8,689	0,977	1,032	
C	-1,492	11,968	17,611	1,247	0,235	
Ca	-2,290	0,252	5,894	1,914	0,773	
Co	-1,329	-0,241	5,402	1,110	1,515	
Cr	-1,359	2,222	7,864	1,136	1,042	
Cu	-1,201	2,212	7,854	1,003	1,152	
Ga	-1,328	2,182	7,824	1,110	1,068	
Ge	-1,311	2,225	7,868	1,096	1,072	
Hf	-1,277	2,172	7,814	1,067	1,096	
K	-2,587	2,802	8,444	2,162	0,444	
Mg	-1,359	2,175	7,817	1,136	1,051	
Mn	-1,282	2,191	7,833	1,071	1,099	
Mo	-1,327	2,188	7,830	1,109	1,065	
Na	-1,494	2,271	7,913	1,249	0,952	
Nb	-1,269	2,176	7,818	1,060	1,107	
Ni	-1,330	2,223	7,865	1,111	1,061	
P	-1,404	2,309	7,951	1,174	1,002	
Re	-1,285	2,185	7,827	1,074	1,088	
Se	-1,314	2,180	7,823	1,098	1,077	
Si	-1,365	2,262	7,904	1,141	1,034	
Ta	-1,272	2,175	7,818	1,063	1,099	
Ti	-1,338	2,172	7,814	1,118	1,064	
V	-1,326	2,200	7,842	1,108	1,067	
W	-1,324	2,187	7,829	1,106	1,062	
Y	-1,212	2,239	7,881	1,013	1,137	
Zn	-1,325	2,181	7,824	1,107	1,070	

Table C.6 Calculated values of enthalpy of mixing (ΔH^M), mismatch entropy (S^σ), entropy of mixing (ΔS^M), change in viscosity ($\Delta\eta/\eta_0$), critical cooling rate (R_c) and short range order parameter (α_1) for Fe33Zr66M1.

Fe33Zr66M1						
M	ΔH^M **J/mol x10^4**	S^s **J/mol.K**	ΔS^M **J/mol.K**	$\Delta h/h_0$	R_C **K/s x10^8**	a_1
None	-1,302	0,397	5,667	1,088	1,453	-0,492
Al	-1,439	2,204	7,906	1,203	0,992	
B	-1,644	7,129	12,831	1,374	0,429	
Bi	-1,209	3,100	8,802	1,010	0,996	
C	-1,527	12,220	17,922	1,276	0,221	
Ca	-2,316	0,250	5,951	1,935	0,759	
Co	-1,364	-0,246	5,456	1,140	1,478	
Cr	-1,395	2,271	7,972	1,166	1,009	
Cu	-1,236	2,260	7,962	1,033	1,115	
Ga	-1,362	2,231	7,933	1,139	1,034	
Ge	-1,346	2,274	7,976	1,125	1,038	
Hf	-1,314	2,222	7,924	1,098	1,060	
K	-2,610	2,859	8,561	2,181	0,433	
Mg	-1,392	2,225	7,927	1,163	1,019	
Mn	-1,317	2,240	7,942	1,101	1,064	
Mo	-1,366	2,237	7,939	1,141	1,029	
Na	-1,525	2,323	8,024	1,274	0,925	
Nb	-1,306	2,225	7,927	1,091	1,071	
Ni	-1,365	2,272	7,974	1,140	1,027	
P	-1,439	2,357	8,059	1,202	0,970	
Re	-1,323	2,234	7,936	1,106	1,051	
Se	-1,349	2,229	7,931	1,128	1,042	
Si	-1,399	2,311	8,012	1,169	1,002	
Ta	-1,309	2,225	7,927	1,094	1,063	
Ti	-1,373	2,221	7,923	1,147	1,030	
V	-1,362	2,249	7,951	1,138	1,033	
W	-1,362	2,236	7,938	1,138	1,026	
Y	-1,247	2,290	7,992	1,042	1,101	
Zn	-1,359	2,230	7,932	1,136	1,036	

C.2 Fe-Nb System

Table C.7 Calculated values of enthalpy of mixing (ΔH^M), mismatch entropy (S^σ), entropy of mixing (ΔS^M), change in viscosity ($\Delta\eta/\eta_0$), critical cooling rate (R_c) and short range order parameter (α_1) for Fe86,9Nb12,1M1.

Fe86,9Nb12,1M1						
M	ΔH^M **J/mol x10^4**	S^s **J/mol.K**	ΔS^M **J/mol.K**	$\Delta\eta/\eta_0$	R_C **K/s x10^8**	α_1
None	-1,316	0,462	3,528	0,962	2,826	-0,138
Al	-1,314	0,493	4,014	0,961	2,709	
B	-1,762	0,646	4,166	1,288	2,076	
Bi	-1,788	0,886	4,406	1,307	1,945	
C	-1,544	0,681	4,201	1,129	2,328	
Ca	-2,659	1,195	4,715	1,944	1,170	
Co	-1,330	0,462	3,982	0,973	2,690	
Cr	-1,343	0,462	3,982	0,982	2,673	
Cu	-1,245	0,462	3,982	0,910	2,818	
Ga	-1,328	0,479	4,000	0,971	2,684	
Ge	-1,317	0,462	3,983	0,963	2,707	
Hf	-1,499	0,584	4,104	1,096	2,386	
K	-2,379	2,195	5,715	1,740	1,180	
Mg	-1,288	0,605	4,125	0,942	2,704	
Mn	-1,299	0,469	3,989	0,950	2,735	
Mo	-1,644	0,472	3,992	1,202	2,255	
Na	-1,478	0,951	4,471	1,081	2,319	
Ni	-1,331	0,462	3,982	0,973	2,689	
P	-1,376	0,507	4,027	1,006	2,612	
Pb	-1,483	0,777	4,297	1,084	2,336	
Pd	-1,495	0,475	3,995	1,093	2,444	
Pt	-1,441	0,478	3,998	1,053	2,498	
Re	-1,527	0,475	3,995	1,116	2,386	
Se	-1,423	0,482	4,002	1,040	2,545	
Si	-1,302	0,476	3,997	0,952	2,734	
Sn	-1,342	0,622	4,142	0,981	2,599	
Ta	-1,414	0,493	4,013	1,033	2,533	
Ti	-1,352	0,507	4,027	0,988	2,644	
V	-1,310	0,464	3,984	0,958	2,721	
W	-1,635	0,473	3,993	1,195	2,250	
Y	-1,325	0,856	4,376	0,968	2,543	
Zn	-1,335	0,480	4,000	0,976	2,674	
Zr	-1,456	0,606	4,126	1,064	2,453	

Table C.8 Calculated values of enthalpy of mixing (ΔH^M), mismatch entropy (S^σ), entropy of mixing (ΔS^M), change in viscosity ($\Delta\eta/\eta_0$), critical cooling rate (R_c) and short range order parameter (α_1) for Fe87,9Nb11,1M1.

Fe87,9Nb11,1M1						
M	**ΔH^M J/mol x10^4**	**S^s J/mol.K**	**ΔS^M J/mol.K**	**$\Delta h/h_0$**	**R_C K/s x10^8**	**a_1**
None	-1,316	0,462	3,528	0,962	2,826	-0,138
Al	-1,209	0,463	3,816	0,884	2,935	
B	-1,658	0,614	3,967	1,212	2,248	
Bi	-1,704	0,861	4,213	1,246	2,082	
C	-1,439	0,649	4,001	1,052	2,522	
Ca	-2,550	1,172	4,524	1,864	1,269	
Co	-1,229	0,431	3,783	0,898	2,909	
Cr	-1,241	0,431	3,783	0,908	2,891	
Cu	-1,147	0,431	3,783	0,838	3,043	
Ga	-1,227	0,449	3,802	0,897	2,902	
Ge	-1,216	0,431	3,784	0,889	2,926	
Hf	-1,403	0,555	3,908	1,026	2,571	
K	-2,275	2,180	5,532	1,663	1,276	
Mg	-1,186	0,576	3,929	0,867	2,926	
Mn	-1,199	0,438	3,791	0,877	2,955	
Mo	-1,546	0,441	3,794	1,130	2,434	
Na	-1,375	0,926	4,278	1,006	2,507	
Ni	-1,230	0,431	3,783	0,899	2,908	
P	-1,283	0,475	3,828	0,938	2,813	
Pb	-1,400	0,751	4,103	1,024	2,498	
Pd	-1,394	0,444	3,797	1,019	2,642	
Pt	-1,341	0,448	3,800	0,981	2,698	
Re	-1,427	0,444	3,797	1,044	2,577	
Se	-1,324	0,452	3,804	0,968	2,749	
Si	-1,199	0,445	3,797	0,876	2,960	
Sn	-1,245	0,594	3,947	0,910	2,803	
Ta	-1,446	0,463	3,815	1,057	2,545	
Ti	-1,251	0,477	3,830	0,915	2,858	
V	-1,208	0,433	3,786	0,883	2,944	
W	-1,538	0,442	3,795	1,124	2,427	
Y	-1,228	0,830	4,182	0,898	2,741	
Zn	-1,234	0,450	3,802	0,902	2,891	
Zr	-1,359	0,577	3,930	0,994	2,645	

Table C.9 Calculated values of enthalpy of mixing (ΔH^M), mismatch entropy (S^σ), entropy of mixing (ΔS^M), change in viscosity ($\Delta\eta/\eta_0$), critical cooling rate (R_c) and short range order parameter (α_1) for Fe56Nb43M1.

Fe56Nb43M1						
M	**ΔH^M J/mol x10^4**	**S^s J/mol.K**	**ΔS^M J/mol.K**	**$\Delta h/h_0$**	**R_C K/s x10^8**	**a_1**
None	-3,379	0,916	6,594	2,249	0,924	-0,754
Al	-3,494	0,917	7,014	2,325	0,842	
B	-3,903	1,121	7,218	2,598	0,667	
Bi	-3,353	1,198	7,294	2,232	0,857	
C	-3,702	1,155	7,252	2,464	0,734	
Ca	-5,109	1,439	7,536	3,401	0,348	
Co	-3,434	0,914	7,011	2,286	0,866	
Cr	-3,454	0,915	7,011	2,299	0,858	
Cu	-3,265	0,911	7,007	2,173	0,942	
Ga	-3,405	0,911	7,007	2,266	0,879	
Ge	-3,388	0,916	7,013	2,255	0,885	
Hf	-3,423	0,974	7,071	2,278	0,856	
K	-4,694	2,249	8,346	3,124	0,381	
Mg	-3,334	0,989	7,085	2,219	0,903	
Mn	-3,361	0,908	7,004	2,237	0,899	
Mo	-3,580	0,908	7,005	2,382	0,804	
Na	-3,685	1,247	7,344	2,452	0,730	
Ni	-3,436	0,915	7,012	2,287	0,865	
P	-3,516	0,977	7,073	2,340	0,825	
Pb	-3,006	1,115	7,211	2,001	1,031	
Pd	-3,586	0,909	7,006	2,387	0,801	
Pt	-3,478	0,910	7,007	2,315	0,840	
Re	-3,512	0,909	7,006	2,337	0,826	
Se	-3,438	0,912	7,009	2,288	0,864	
Si	-3,446	0,939	7,036	2,294	0,860	
Sn	-3,312	1,001	7,098	2,204	0,905	
Ta	-3,406	0,917	7,014	2,267	0,870	
Ti	-3,428	0,925	7,021	2,282	0,868	
V	-3,417	0,908	7,004	2,274	0,875	
W	-3,570	0,908	7,005	2,376	0,803	
Y	-3,296	1,174	7,271	2,194	0,892	
Zn	-3,429	0,911	7,008	2,282	0,868	
Zr	-3,526	0,989	7,086	2,347	0,816	

Table C.10 Calculated values of enthalpy of mixing (ΔH^M), mismatch entropy (S^σ), entropy of mixing (ΔS^M), change in viscosity ($\Delta\eta/\eta_0$), critical cooling rate (R_c) and short range order parameter (α_1) for Fe57Nb42M1.

Fe57Nb42M1						
M	**ΔH^M J/mol x10^4**	**S^s J/mol.K**	**ΔS^M J/mol.K**	**$\Delta h/h_0$**	**R_C K/s x10^8**	**a_1**
None	-3,379	0,916	6,594	2,249	0,924	-0,754
Al	-3,579	0,917	6,990	2,382	0,811	
B	-4,012	1,119	7,192	2,670	0,635	
Bi	-3,469	1,200	7,273	2,309	0,812	
C	-3,800	1,154	7,227	2,529	0,703	
Ca	-5,274	1,443	7,516	3,510	0,322	
Co	-3,522	0,913	6,986	2,344	0,833	
Cr	-3,540	0,913	6,986	2,356	0,826	
Cu	-3,352	0,909	6,982	2,231	0,907	
Ga	-3,494	0,910	6,983	2,325	0,845	
Ge	-3,476	0,915	6,988	2,314	0,851	
Hf	-3,515	0,974	7,047	2,340	0,822	
K	-4,793	2,258	8,331	3,190	0,364	
Mg	-3,550	0,989	7,062	2,363	0,815	
Mn	-3,448	0,907	6,980	2,295	0,865	
Mo	-3,675	0,907	6,980	2,446	0,771	
Na	-3,783	1,250	7,323	2,518	0,698	
Ni	-3,524	0,914	6,987	2,345	0,832	
P	-3,604	0,975	7,048	2,399	0,794	
Pb	-3,115	1,116	7,189	2,073	0,981	
Pd	-3,673	0,908	6,981	2,445	0,770	
Pt	-3,575	0,909	6,982	2,379	0,804	
Re	-3,604	0,908	6,981	2,399	0,793	
Se	-3,532	0,911	6,984	2,351	0,828	
Si	-3,532	0,937	7,010	2,351	0,828	
Sn	-3,401	1,002	7,075	2,264	0,870	
Ta	-3,496	0,916	6,989	2,327	0,836	
Ti	-3,518	0,924	6,997	2,342	0,834	
V	-3,502	0,907	6,980	2,331	0,842	
W	-3,666	0,907	6,980	2,440	0,769	
Y	-3,385	1,176	7,249	2,253	0,857	
Zn	-3,520	0,910	6,983	2,343	0,834	
Zr	-3,497	0,990	7,063	2,328	0,832	

C.3 Fe-C System

Table C.11 Calculated values of enthalpy of mixing (ΔH^M), mismatch entropy (S^σ), entropy of mixing (ΔS^M), change in viscosity ($\Delta\eta/\eta_0$), critical cooling rate (R_c) and short range order parameter (α_1) for Fe82C17M1.

Fe82C17M1						
M	ΔH^M **J/mol x10^4**	S^s **J/mol.K**	ΔS^M **J/mol.K**	$\Delta\eta/\eta_0$	R_C **K/s x10^7**	a_1
None	-2,648	3,356	7,144	2,234	4,886	-0,205
Al	-2,849	3,427	7,665	2,404	4,102	
B	-2,873	3,508	7,746	2,424	4,000	
Bi	-3,077	3,964	8,202	2,597	3,224	
Ca	-3,047	4,357	8,596	2,571	3,159	
Co	-2,655	3,357	7,595	2,241	4,668	
Cr	-2,664	3,357	7,595	2,248	4,645	
Cu	-2,415	3,361	7,599	2,038	5,429	
Ga	-2,579	3,403	7,641	2,176	4,861	
Ge	-2,623	3,356	7,594	2,214	4,758	
Hf	-3,476	3,561	7,799	2,933	2,664	
K	-1,204	5,589	9,828	1,016	8,492	
Mg	-2,744	3,590	7,828	2,316	4,281	
Mn	-2,576	3,383	7,621	2,174	4,891	
Mo	-5,009	3,388	7,626	4,227	1,043	
Na	-2,344	4,047	8,286	1,978	5,165	
Nb	-4,450	3,425	7,663	3,756	1,479	
Ni	-2,657	3,356	7,594	2,243	4,662	
P	-2,327	3,379	7,617	1,964	5,743	
Pb	-3,075	3,822	8,060	2,595	3,296	
Pd	-2,322	3,394	7,632	1,959	5,706	
Pt	-2,549	3,400	7,638	2,151	4,894	
Re	-5,496	3,394	7,632	4,638	0,759	
Se	-2,608	3,407	7,645	2,201	4,764	
Si	-2,606	3,357	7,595	2,199	4,831	
Sn	-2,910	3,614	7,853	2,455	3,805	
Ta	-4,285	3,425	7,664	3,616	1,628	
Ti	-2,573	3,448	7,686	2,171	4,859	
V	-2,628	3,371	7,609	2,218	4,743	
W	-5,183	3,390	7,628	4,374	0,926	
Y	-2,920	3,925	8,163	2,464	3,626	
Zn	-2,652	3,404	7,642	2,238	4,643	
Zr	-3,793	3,591	7,830	3,201	2,189	

Table C.12 Calculated values of enthalpy of mixing (ΔH^M), mismatch entropy (S^σ), entropy of mixing (ΔS^M), change in viscosity ($\Delta\eta/\eta_0$), critical cooling rate (R_c) and short range order parameter (α_1) for Fe83C16M1.

Fe83C16M1						
M	**ΔH^M J/mol x10^4**	**S^s J/mol.K**	**ΔS^M J/mol.K**	**$\Delta h/h_0$**	**R_C K/s x10^7**	**a_1**
None	-2,648	3,356	7,144	2,234	4,886	-0,205
Al	-2,658	3,237	7,342	2,243	4,794	
B	-2,690	3,321	7,426	2,270	4,648	
Bi	-3,475	3,769	7,873	2,933	2,598	
Ca	-2,820	4,159	8,263	2,380	3,782	
Co	-2,475	3,169	7,273	2,089	5,416	
Cr	-2,479	3,169	7,273	2,092	5,406	
Cu	-2,240	3,173	7,277	1,890	6,279	
Ga	-2,398	3,214	7,318	2,024	5,645	
Ge	-2,439	3,168	7,272	2,058	5,535	
Hf	-3,286	3,369	7,474	2,773	3,111	
K	-1,048	5,382	9,486	0,884	9,729	
Mg	-2,563	3,398	7,503	2,163	4,973	
Mn	-2,396	3,194	7,299	2,022	5,676	
Mo	-4,809	3,199	7,304	4,058	1,227	
Na	-2,175	3,851	7,956	1,835	5,957	
Nb	-4,256	3,235	7,340	3,591	1,732	
Ni	-2,478	3,168	7,273	2,091	5,408	
P	-2,139	3,192	7,296	1,805	6,697	
Pb	-2,889	3,628	7,733	2,438	3,843	
Pd	-2,137	3,205	7,310	1,804	6,639	
Pt	-2,373	3,211	7,315	2,003	5,663	
Re	-5,293	3,205	7,310	4,467	0,894	
Se	-2,416	3,218	7,322	2,038	5,573	
Si	-2,420	3,170	7,274	2,042	5,625	
Sn	-2,725	3,422	7,527	2,300	4,430	
Ta	-4,090	3,236	7,340	3,452	1,906	
Ti	-2,388	3,258	7,363	2,015	5,658	
V	-2,438	3,182	7,287	2,058	5,537	
W	-4,983	3,201	7,306	4,205	1,089	
Y	-2,739	3,730	7,834	2,312	4,213	
Zn	-2,474	3,215	7,319	2,088	5,379	
Zr	-3,603	3,400	7,504	3,041	2,557	

Table C.13 Calculated values of enthalpy of mixing (ΔH^M), mismatch entropy (S^σ), entropy of mixing (ΔS^M), change in viscosity ($\Delta\eta/\eta_0$), critical cooling rate (R_c) and short range order parameter (α_1) for Fe74C25M1.

Fe74C25M1						
M	DH^M **J/mol x10^4**	S^s **J/mol.K**	DS^M **J/mol.K**	Dh/h_0	R_C **K/s x10^7**	a_1
None	-5,498	4,804	9,477	3,136	3,373	-0,333
Al	-5,840	4,890	10,004	3,330	2,776	
B	-5,778	4,943	10,058	3,295	2,833	
Bi	-6,462	5,480	10,594	3,685	1,914	
Ca	-6,560	5,903	11,017	3,741	1,760	
Co	-5,467	4,806	9,920	3,118	3,283	
Cr	-5,536	4,805	9,920	3,157	3,191	
Cu	-5,104	4,812	9,926	2,911	3,830	
Ga	-5,380	4,862	9,977	3,068	3,376	
Ge	-5,468	4,804	9,918	3,119	3,277	
Hf	-6,647	5,040	10,154	3,791	1,891	
K	-3,325	7,216	12,330	1,896	5,808	
Mg	-5,605	5,072	10,186	3,196	2,990	
Mn	-5,367	4,839	9,953	3,061	3,412	
Mo	-8,771	4,845	9,960	5,002	0,791	
Na	-4,955	5,570	10,684	2,826	3,675	
Nb	-7,977	4,888	10,002	4,550	1,105	
Ni	-5,470	4,805	9,919	3,120	3,279	
P	-5,119	4,819	9,933	2,919	3,815	
Pb	-6,093	5,326	10,440	3,475	2,292	
Pd	-5,091	4,852	9,967	2,904	3,809	
Pt	-5,279	4,859	9,973	3,011	3,478	
Re	-9,435	4,852	9,966	5,381	0,589	
Se	-5,538	4,867	9,982	3,158	3,150	
Si	-5,462	4,801	9,915	3,115	3,303	
Sn	-5,852	5,099	10,213	3,337	2,652	
Ta	-7,757	4,888	10,003	4,424	1,202	
Ti	-5,411	4,914	10,028	3,086	3,315	
V	-5,533	4,824	9,938	3,156	3,186	
W	-9,000	4,848	9,962	5,133	0,710	
Y	-5,823	5,437	10,552	3,321	2,565	
Zn	-5,437	4,864	9,978	3,101	3,295	
Zr	-7,064	5,074	10,188	4,029	1,589	

Table C.14 Calculated values of enthalpy of mixing (ΔH^M), mismatch entropy (S^σ), entropy of mixing (ΔS^M), change in viscosity ($\Delta\eta/\eta_0$), critical cooling rate (R_c) and short range order parameter (α_1) for Fe75C24M1.

Fe75C24M1						
M	**ΔH^M J/mol x10^4**	**S^s J/mol.K**	**ΔS^M J/mol.K**	**$\Delta\eta/\eta_0$**	**R_C K/s x10^7**	**a_1**
None	-5,498	4,804	9,477	3,136	3,373	-0,333
Al	-5,373	4,712	9,734	3,065	3,488	
B	-5,654	4,770	9,792	3,224	3,074	
Bi	-6,560	5,295	10,317	3,741	1,892	
Ca	-5,667	5,715	10,736	3,232	2,658	
Co	-5,247	4,630	9,652	2,993	3,712	
Cr	-5,186	4,630	9,652	2,958	3,814	
Cu	-5,006	4,636	9,658	2,855	4,111	
Ga	-5,014	4,685	9,707	2,860	4,064	
Ge	-5,003	4,629	9,650	2,853	4,116	
Hf	-5,972	4,860	9,882	3,406	2,600	
K	-3,199	7,017	12,038	1,825	6,329	
Mg	-5,235	4,892	9,914	2,986	3,606	
Mn	-5,127	4,662	9,684	2,924	3,892	
Mo	-7,763	4,669	9,691	4,428	1,253	
Na	-4,784	5,384	10,406	2,728	4,076	
Nb	-7,054	4,710	9,732	4,023	1,688	
Ni	-5,252	4,629	9,651	2,996	3,705	
P	-4,561	4,644	9,666	2,601	4,983	
Pb	-5,917	5,143	10,165	3,374	2,548	
Pd	-4,804	4,676	9,697	2,740	4,434	
Pt	-5,118	4,682	9,704	2,919	3,836	
Re	-8,297	4,675	9,697	4,732	0,987	
Se	-4,917	4,690	9,712	2,805	4,228	
Si	-4,943	4,626	9,648	2,819	4,245	
Sn	-5,332	4,919	9,941	3,041	3,411	
Ta	-6,856	4,711	9,733	3,910	1,820	
Ti	-5,006	4,736	9,758	2,855	4,058	
V	-5,046	4,648	9,670	2,878	4,039	
W	-7,992	4,671	9,693	4,558	1,126	
Y	-5,262	5,253	10,275	3,001	3,361	
Zn	-5,230	4,687	9,709	2,983	3,707	
Zr	-6,311	4,894	9,916	3,599	2,260	

C.4 Fe-W System

Table C.15 Calculated values of enthalpy of mixing (ΔH^M), mismatch entropy (S^σ), entropy of mixing (ΔS^M), change in viscosity ($\Delta\eta/\eta_0$), critical cooling rate (R_c) and short range order parameter (α_1) for Fe79W20M1.

Fe79W20M1						
M	**ΔH^M J/mol x10^4**	**S^s J/mol.K**	**ΔS^M J/mol.K**	**$\Delta h/h_0$**	**R_C K/s x10^7**	**a_1**
None	-6,012	0,760	4,918	3,788	3,403	-0,250
Al	-6,044	2,873	7,478	3,808	2,377	
B	-6,475	8,875	13,480	4,079	0,816	
Bi	-6,279	3,903	8,508	3,956	1,813	
C	-6,287	15,056	19,661	3,961	0,365	
Ca	-6,817	0,758	5,364	4,295	2,237	
Co	-6,043	-0,032	4,573	3,807	3,611	
Cr	-6,048	0,242	4,847	3,810	3,464	
Cu	-5,939	0,332	4,937	3,742	3,598	
Ga	-6,014	0,319	4,925	3,789	3,477	
Ge	-6,006	0,303	4,908	3,784	3,499	
Hf	-6,113	0,423	5,029	3,852	3,247	
K	-6,828	2,032	6,637	4,302	1,852	
Mg	-6,009	0,444	5,049	3,786	3,433	
Mn	-5,996	0,309	4,914	3,778	3,515	
Mo	-6,265	0,312	4,917	3,947	3,087	
Na	-6,182	0,790	5,395	3,895	3,010	
Nb	-6,060	0,332	4,937	3,818	3,391	
Ni	-6,044	0,302	4,907	3,808	3,438	
P	-6,082	0,348	4,953	3,832	3,361	
Pb	-5,980	0,617	5,222	3,768	3,356	
Pd	-6,178	0,315	4,920	3,892	3,213	
Pt	-6,111	0,318	4,923	3,850	3,297	
Re	-6,181	0,315	4,920	3,894	3,193	
Si	-6,011	0,317	4,922	3,787	3,492	
Sn	-0,744	0,462	5,067	0,469	40,975	
Ta	-6,059	0,333	4,938	3,818	3,374	
Ti	-6,048	0,347	4,952	3,811	3,413	
V	-6,029	0,304	4,909	3,798	3,464	
Y	-5,958	0,695	5,300	3,754	3,378	
Zn	-6,042	0,320	4,925	3,807	3,432	
Zr	-6,079	0,445	5,050	3,830	3,307	

Table C.16 Calculated values of enthalpy of mixing (ΔH^M), mismatch entropy (S^σ), entropy of mixing (ΔS^M), change in viscosity ($\Delta\eta/\eta_0$), critical cooling rate (R_c) and short range order parameter (α_1) for Fe80W19M1.

Fe80W19M1						
M	ΔH^M **J/mol x10^4**	S^s **J/mol.K**	ΔS^M **J/mol.K**	$\Delta h/h_0$	R_C **K/s x10^7**	a_1
None	-6,012	0,760	4,918	3,788	3,403	-0,250
Al	-5,841	2,774	7,262	3,680	2,704	
B	-5,973	8,571	13,059	3,763	1,101	
Bi	-5,845	3,783	8,271	3,683	2,307	
C	-6,029	14,537	19,025	3,799	0,453	
Ca	-6,708	0,762	5,250	4,226	2,398	
Co	-5,789	-0,031	4,457	3,647	4,146	
Cr	-5,794	0,234	4,722	3,651	3,982	
Cu	-4,861	0,320	4,809	3,062	6,110	
Ga	-6,050	0,309	4,798	3,812	3,487	
Ge	-6,672	0,292	4,780	4,204	2,605	
Hf	-5,831	0,414	4,903	3,674	3,783	
K	-5,899	2,031	6,520	3,717	2,926	
Mg	-6,081	0,435	4,924	3,831	3,384	
Mn	-5,744	0,299	4,787	3,619	4,039	
Mo	-6,019	0,302	4,790	3,792	3,538	
Na	-6,455	0,783	5,271	4,067	2,698	
Nb	-5,813	0,323	4,811	3,662	3,888	
Ni	-5,791	0,292	4,780	3,648	3,954	
P	-5,865	0,337	4,825	3,695	3,801	
Pb	-5,775	0,609	5,097	3,638	3,772	
Pd	-5,892	0,305	4,793	3,712	3,752	
Pt	-5,873	0,308	4,796	3,700	3,763	
Re	-5,934	0,305	4,793	3,739	3,660	
Si	-5,806	0,306	4,794	3,658	3,926	
Sn	-5,650	0,453	4,942	3,560	4,114	
Ta	-5,812	0,323	4,811	3,662	3,868	
Ti	-5,796	0,337	4,825	3,652	3,922	
V	-5,992	0,294	4,782	3,775	3,596	
Y	-5,784	0,688	5,176	3,644	3,740	
Zn	-5,754	0,310	4,799	3,625	4,012	
Zr	-5,676	0,437	4,925	3,576	4,080	

Table C.17 Calculated values of enthalpy of mixing (ΔH^M), mismatch entropy (S^σ), entropy of mixing (ΔS^M), change in viscosity ($\Delta\eta/\eta_0$), critical cooling rate (R_c) and short range order parameter (α_1) for Fe66W33M1.

Fe66W33M1						
M	**ΔH^M J/mol x10^4**	**S^s J/mol.K**	**ΔS^M J/mol.K**	**$\Delta h/h_0$**	**R_C K/s x10^7**	**a_1**
None	-8,643	1,006	6,276	4,888	1,434	-0,493
Al	-8,705	5,112	10,814	4,923	0,744	
B	-9,128	6,644	12,346	5,162	0,499	
Bi	-8,663	6,897	12,599	4,899	0,580	
C	-8,954	9,488	15,190	5,063	0,356	
Ca	-9,135	0,832	6,534	5,166	1,149	
Co	-8,697	0,002	5,704	4,918	1,558	
Cr	-8,694	1,457	7,159	4,916	1,265	
Cu	-8,566	0,133	5,835	4,844	1,616	
Ga	-8,650	0,411	6,113	4,892	1,497	
Ge	-8,640	0,401	6,103	4,886	1,506	
Hf	-8,669	0,503	6,205	4,902	1,458	
K	-9,505	2,012	7,714	5,375	0,828	
Mg	-8,684	0,522	6,223	4,911	1,456	
Mn	-8,632	0,403	6,105	4,881	1,512	
Mo	-8,802	0,405	6,107	4,978	1,403	
Na	-8,874	0,841	6,543	5,018	1,283	
Nb	-8,626	0,422	6,124	4,878	1,509	
Ni	-8,699	0,400	6,102	4,919	1,470	
P	-8,746	0,451	6,153	4,946	1,433	
Pb	-8,344	0,680	6,382	4,718	1,629	
Pd	-8,832	0,407	6,109	4,994	1,385	
Pt	-8,726	0,410	6,112	4,935	1,441	
Re	-8,733	0,407	6,109	4,938	1,438	
Si	-8,675	0,418	6,120	4,906	1,483	
Sn	-8,579	0,538	6,240	4,851	1,511	
Ta	-8,629	0,422	6,124	4,879	1,500	
Ti	-8,682	0,434	6,136	4,910	1,474	
V	-8,675	0,399	6,101	4,905	1,486	
Y	-8,552	0,753	6,455	4,836	1,485	
Zn	-8,693	0,412	6,113	4,916	1,471	
Zr	-8,641	0,523	6,224	4,887	1,477	

Table C.18 Calculated values of enthalpy of mixing (ΔH^M), mismatch entropy (S^σ), entropy of mixing (ΔS^M), change in viscosity ($\Delta\eta/\eta_0$), critical cooling rate (R_c) and short range order parameter (α_1) for Fe67W32M1.

Fe67W32M1						
M	DH^M **J/mol x10^4**	S^s **J/mol.K**	DS^M **J/mol.K**	Dh/h_0	R_C **K/s x10^7**	a_1
None	-8,643	1,006	5,270	4,888	1,434	-0,493
Al	-8,547	4,983	5,642	4,833	0,820	
B	-8,970	6,627	5,642	5,072	0,541	
Bi	-8,526	6,726	5,642	4,821	0,637	
C	-8,795	9,490	5,642	4,973	0,385	
Ca	-9,854	0,833	5,642	5,572	0,857	
Co	-8,538	0,002	5,642	4,828	1,687	
Cr	-8,536	1,418	5,642	4,827	1,377	
Cu	-8,409	0,136	5,642	4,755	1,747	
Ga	-8,513	0,406	5,642	4,814	1,607	
Ge	-8,483	0,396	5,642	4,797	1,630	
Hf	-8,518	0,499	5,642	4,817	1,574	
K	-9,344	2,016	5,642	5,284	0,897	
Mg	-8,524	0,518	5,642	4,820	1,578	
Mn	-8,475	0,398	5,642	4,792	1,637	
Mo	-8,653	0,400	5,642	4,893	1,514	
Na	-8,712	0,839	5,642	4,926	1,391	
Nb	-8,475	0,417	5,642	4,792	1,629	
Ni	-8,540	0,395	5,642	4,829	1,592	
P	-8,587	0,445	5,642	4,856	1,552	
Pb	-8,208	0,677	5,642	4,641	1,747	
Pd	-8,673	0,403	5,642	4,905	1,500	
Pt	-8,571	0,405	5,642	4,847	1,558	
Re	-8,583	0,402	5,642	4,854	1,552	
Si	-8,516	0,412	5,642	4,816	1,607	
Sn	-8,425	0,534	5,642	4,764	1,633	
Ta	-8,477	0,418	5,642	4,794	1,620	
Ti	-8,525	0,430	5,642	4,821	1,595	
V	-8,517	0,394	5,642	4,816	1,609	
Y	-8,397	0,751	5,642	4,749	1,605	
Zn	-8,535	0,407	5,642	4,826	1,593	
Zr	-8,490	0,519	5,642	4,801	1,595	

Table C.19 Calculated values of enthalpy of mixing (ΔH^M), mismatch entropy (S^σ), entropy of mixing (ΔS^M), change in viscosity ($\Delta\eta/\eta_0$), critical cooling rate (R_c) and short range order parameter (α_1) for Fe59W40M1.

Fe59W40M1						
M	**ΔH^M J/mol x10^4**	**S^s J/mol.K**	**ΔS^M J/mol.K**	**$\Delta h/h_0$**	**R_C K/s x10^7**	**a_1**
None	-9,510	1,068	6,661	5,035	1,325	-0,667
Al	-9,584	5,953	11,968	5,074	0,613	
B	-9,999	6,601	12,616	5,294	0,473	
Bi	-9,397	8,037	14,052	4,975	0,484	
C	-9,717	9,267	15,283	5,144	0,360	
Ca	-9,864	0,830	6,845	5,222	1,148	
Co	-9,577	0,002	6,017	5,070	1,449	
Cr	-9,567	1,722	7,737	5,065	1,135	
Cu	-9,433	0,104	6,119	4,994	1,511	
Ga	-9,520	0,432	6,448	5,040	1,392	
Ge	-9,509	0,426	6,441	5,035	1,399	
Hf	-9,495	0,518	6,533	5,027	1,381	
K	-10,406	1,978	7,994	5,509	0,784	
Mg	-9,580	0,536	6,551	5,072	1,342	
Mn	-9,503	0,425	6,441	5,031	1,404	
Mo	-9,611	0,427	6,442	5,088	1,342	
Na	-9,782	0,843	6,858	5,179	1,185	
Nb	-9,455	0,442	6,458	5,006	1,424	
Ni	-9,578	0,425	6,440	5,071	1,362	
P	-9,627	0,478	6,493	5,097	1,327	
Pb	-9,069	0,688	6,703	4,801	1,594	
Pd	-9,711	0,429	6,444	5,141	1,288	
Pt	-9,583	0,431	6,447	5,074	1,349	
Re	-9,548	0,429	6,444	5,055	1,370	
Si	-9,559	0,444	6,459	5,061	1,371	
Sn	-9,427	0,551	6,567	4,991	1,416	
Ta	-9,459	0,442	6,458	5,008	1,416	
Ti	-9,550	0,454	6,469	5,056	1,373	
V	-9,547	0,423	6,438	5,054	1,380	
Y	-9,405	0,758	6,773	4,979	1,389	
Zn	-9,573	0,433	6,448	5,068	1,363	
Zr	-9,472	0,537	6,552	5,015	1,396	

Table C.20 Calculated values of enthalpy of mixing (ΔH^M), mismatch entropy (S^σ), entropy of mixing (ΔS^M), change in viscosity ($\Delta\eta/\eta_0$), critical cooling rate (R_c) and short range order parameter (α_1) for Fe60W39M1.

Fe60W39M1						
M	**ΔH^M J/mol x10^4**	**S^s J/mol.K**	**ΔS^M J/mol.K**	**$\Delta h/h_0$**	**R_C K/s x10^7**	**a_1**
Fe60W40	-9,510	1,068	6,661	5,035	1,325	-0,667
Al	-10,432	4,016	9,998	5,523	0,584	
B	-11,880	12,372	18,354	6,290	0,098	
Bi	-12,112	5,310	11,291	6,412	0,246	
C	-13,627	21,007	26,988	7,214	0,014	
Ca	-16,170	0,701	6,683	8,560	0,097	
Co	-15,162	-0,045	5,937	8,027	0,160	
Cr	-16,094	0,340	6,321	8,521	0,105	
Cu	-9,334	0,462	6,443	4,942	1,506	
Ga	-9,437	0,430	6,412	4,996	1,452	
Ge	-9,410	0,423	6,405	4,982	1,469	
Hf	-9,402	0,517	6,498	4,978	1,446	
K	-10,303	1,984	7,965	5,455	0,824	
Mg	-9,477	0,535	6,516	5,017	1,411	
Mn	-9,403	0,423	6,404	4,978	1,474	
Mo	-9,521	0,425	6,406	5,041	1,404	
Na	-9,677	0,844	6,825	5,123	1,246	
Nb	-9,362	0,440	6,422	4,956	1,492	
Ni	-9,478	0,423	6,404	5,018	1,431	
P	-9,526	0,475	6,456	5,043	1,395	
Pb	-8,990	0,688	6,669	4,760	1,660	
Pd	-9,611	0,427	6,408	5,088	1,353	
Pt	-9,486	0,429	6,411	5,022	1,416	
Re	-9,457	0,427	6,408	5,007	1,433	
Si	-9,458	0,441	6,422	5,007	1,440	
Sn	-9,331	0,550	6,532	4,940	1,485	
Ta	-9,366	0,441	6,422	4,958	1,484	
Ti	-9,451	0,452	6,433	5,003	1,441	
V	-9,446	0,420	6,402	5,001	1,450	
Y	-9,308	0,758	6,739	4,928	1,456	
Zn	-9,472	0,431	6,412	5,015	1,432	
Zr	-9,379	0,536	6,517	4,965	1,462	